Deeply Virtual Compton Scattering off a Deuterium Target at the HERMES Experiment

Aram Movsisyan

Yerevan Physics Institute

Yerevan - 2010

Thesis for acquiring the degree of candidate of physical-mathematical science in the division 01.04.16 “nuclear, elementary particles and cosmic ray physics”

Research Director: Dr. H. Marukyan

Yerevan - 2010

Contents

Chapter 1

Introduction

Throughout many decades the scattering experiments serve as a useful source of information about the structure of matter. To our present knowledge the matter is composed of atoms. In 1913 E. Rutherford investigating the scattering of the alpha particles from a gold, showed that the atoms have substructure. They are composed of massive nucleus, surrounded by negatively charged electrons. In a number of subsequent experiments from 1919-1932, when a positively charged proton and a neutral neutron, were discovered, it became clear that the nucleus itself is a composite object, i.e. a bound state of protons and neutrons. Up to now, the structure of nucleons (protons and neutrons) and their different bound states are a subject of intense investigations. Until recently, the nucleon structure was described by two categories of objects - elastic form factors and parton distribution functions. Nucleon form factors measured in the elastic lepton-nucleon scattering experiments describe the difference of the electromagnetic structure of nucleons from that of point-like particle. Thus they represent transverse spatial distribution of charge and magnetization in the nucleon. Parton distribution functions are distributions in longitudinal momentum fraction of partons in the nucleon, and are extracted from measurements of inclusive and semi-inclusive deep-inelastic scattering. Form factors and parton distribution functions are one-dimensional spatial and momentum distributions, respectively.

In the framework of recently developed formalism of generalized parton distributions (GPD), a more comprehensive multidimensional description of the nucleon is possible. GPDs embody parton distribution functions as limiting cases, and the elastic form factors appear as certain GPD moments. A strong interest to GPDs is motivated also by their relation to the total angular momentum carried by partons in the nucleon. The latter is of special importance due to the fact, that according to the recent experimental measurements, in decomposition of the z-component of the nucleons spin through spins of quarks $\Delta\Sigma$ and gluons Δg and respectively to their orbital angular momenta L_z^q and L_z^g

$$s_z = \frac{1}{2}\Delta\Sigma + L_z^q + \Delta g + L_z^g = \frac{1}{2}, \tag{1.1}$$

the contribution from the quarks spin is about 20-25%. Hence one of the most exciting quests in the hadronic physics is the determination of different contributions to the spin of the nucleon.

From the experimental point of view, the GPDs can be accessed through hard exclusive processes, where the target stays intact after the scattering. One of the most promising hard exclusive processes is the Deeply Virtual Compton Scattering (DVCS), i.e. hard

leptoproduction of a real photon, where the quark absorbs a hard virtual photon, emits a real one and rejoins the target. Beside DVCS, there is another process with the same initial and final states, Bethe-Heitler, where the final photon is radiated by the incoming or outgoing lepton. These processes are experimentally indistinguishable, and due to the same final state they interfere at the level of production amplitudes, resulting in an interference term in the cross section for exclusive leptoproduction of real photons. Although in a kinematic conditions of fixed target experiments the DVCS cross section is much smaller than that of Bethe-Heitler, the presence of interference allows to access DVCS amplitude.

In this report the DVCS measurements on an unpolarized and longitudinally polarized deuterium targets are presented. For DVCS off deuteron, one can consider two types of processes. The Coherent process, when the deuteron stays intact after the scattering, allows to consider the structure of deuteron at partonic degrees of freedom, while the incoherent process, when deuteron breaks up to proton and neutron, may provide an information about the GPDs of neutron.

Chapter 2

Generalized Parton Distributions

In this chapter the framework of generalized parton distributions is discussed. The chapter starts from general introduction to the formalism of deep inelastic scattering. In section 2.1 an interpretation of deep inelastic scattering in terms of quark-parton model is considered. Its cross section is represented through forward Compton amplitude, which in tern is described by parton distribution functions. Further, more general case of non-forward Compton amplitude is considered, where the generalized parton distributions appear. A detailed description of the properties and interpretation of generalized parton distributions is given in sections 2.2 - 2.4, while their parameterization and various models are considered in sections 2.5 - 2.8.

2.1 From DIS to DVCS

A theoretical framework of Generalized Parton Distributions (GPDs) was introduced in last decade and was found to be a universal tool for the description of hadron structure in quark and gluon degrees of freedom. At present GPDs appear in the description of large amount of hard exclusive processes which leave the target intact, such as hard leptoproduction of real photons or mesons. Exclusivity in this case means that the final state of the process is determined and consists of three particles, scattered lepton, recoiled nucleon or nuclei and produced photon or meson. An introduction to framework of GPDs is reasonable to begin with consideration of inclusive deep inelastic lepton[1]-nucleon scattering (DIS) $ep \to eX$. The deep-inelastic scattering of leptons off a nucleon is a process where due to the interaction the nucleon breaks up into a hadronic state X. At moderate values of squared four momentum transfers to the nucleon, the dominant mechanism of lepton-nucleon interaction is the single virtual photon exchange. Since the typical center of mass energy at HERMES kinematic conditions is about $7\,GeV$, any contribution from other mechanisms of interaction is negligible. Within single-photon exchange approximation the leading order diagram of inclusive DIS is depicted in Figure 2.1. Experimental measurements of DIS, where only the scattered lepton is detected at the final state, refer to as inclusive. The relevant kinematic variables of inclusive DIS are expressed through energies and momenta of initial and final state lepton. They are listed below and are expressed in laboratory (lab.) frame, which in the case of fixed target experiments corresponds to the target rest frame.

[1]Further in this report the lepton will refer to either electron or positron.

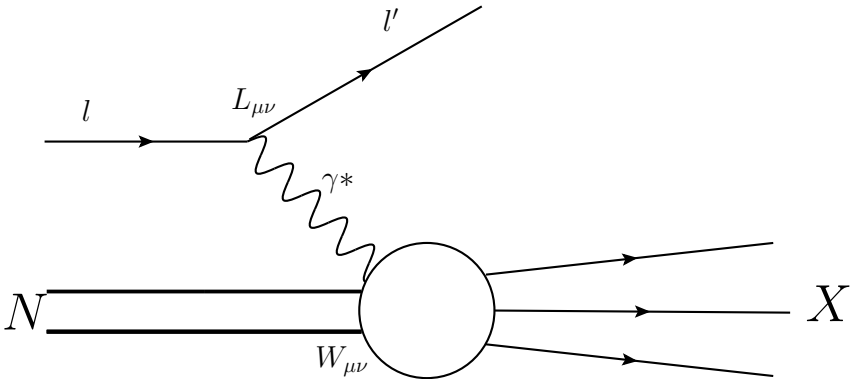

Figure 2.1: Deep inelastic lepton-nucleon scattering process in one-photon exchange approximation.

- The four momentum of the virtual photon q

$$-q^2 = Q^2 = -(k-k')^2 \overset{lab.}{=} 4EE'\sin^2(\theta/2) \tag{2.1}$$

  where $k(E)$ and $k'(E')$ are the four-momenta (energies) of incoming and outgoing lepton, and θ - is the lepton scattering angle in the laboratory frame.

- The energy of virtual photon ν (i.e. the energy transfer from the lepton to the virtual photon)

$$\nu \equiv \frac{p\cdot q}{M_N} \overset{lab.}{=} E - E' \tag{2.2}$$

  where M_N is the target nucleon mass.

- The squared invariant mass of virtual photon-target system (or final hadronic system) W^2

$$W^2 \equiv (p+q)^2 \overset{lab.}{=} M_N^2 + 2M_N\nu - Q^2 \tag{2.3}$$

- The Bjorken variable x_B

$$x_B \equiv \frac{Q^2}{2p\cdot q} \overset{lab.}{=} \frac{Q^2}{2M_N\nu} \tag{2.4}$$

- The fractional energy transfer from a lepton to the target nucleon y

$$y \equiv \frac{p\cdot q}{p\cdot k} \overset{lab.}{=} \frac{\nu}{E} \tag{2.5}$$

The differential cross section of inclusive DIS can be presented as a convolution of leptonic and hadronic tensors [Ans95], where the first one describes a radiation of virtual photon by a lepton and can be calculated in Quantum Electrodynamics (QED), while the hadronic tensor which describes a virtual photon-proton interaction and contains an information about unknown inner structure of proton can be parameterized in terms of structure functions. At present there is no rule for the calculation of hadronic tensor from basic principles, hence the inclusive DIS or $\gamma^* p$ interaction is described by means of optical

theorem. It relates the cross section of the process $\gamma^* p \to X$ to the imaginary part of forward Compton amplitude $\gamma^* p \to \gamma^* p$, shown on the left side of Figure 2.2. In the case of polarized leptons scattering off polarized spin-1/2 nucleons, there are four structure functions entering the parameterization of hadronic tensor. Two of them $F_1(x_B, Q^2)$ and $F_2(x_B, Q^2)$ are spin independent and often are referred to as unpolarized structure functions. The unpolarized cross section of inclusive DIS reads

$$\frac{d^2\sigma_{unpol}}{dx_B dy} = \frac{4\pi\alpha^2}{s x_B^2 y^2}\left\{ x_B y^2 F_1(x_B, Q^2) + \left(1 - y - \frac{\gamma^2 y^2}{4}\right) F_2(x_B, Q^2)\right\}, \tag{2.6}$$

where $\gamma = (2Mx_B)/(Q)$ and s is the center of mass energy. The structure functions $F_1(x_B, Q^2)$ and $F_2(x_B, Q^2)$ and the ratio R of longitudinal σ_L and transverse σ_T virtual photo-absorption cross sections are related according to

$$R(x_B, Q^2) = \frac{\sigma_L(x_B, Q^2)}{\sigma_T(x_B, Q^2)} = \frac{(1+\gamma^2)F_2(x_B, Q^2) - 2x_B F_1(x_B, Q^2)}{2x_B F_1(x_B, Q^2)}. \tag{2.7}$$

Experimental measurements of unpolarized DIS had been carried out in variety of experiments. The first measurements of structure function F_2 were performed by SLAC experiment [Whi90b], and continued by number of experiments up to the resent measurements by H1 [Adl03] and ZEUS [Che01]. An overview of the proton structure function F_2 can be found in [Yao06].

When the lepton beam is polarized longitudinally, i.e. the spin of the lepton is aligned parallel or antiparallel with its momentum, the cross section of inclusive DIS depends on azimuthal ϕ_s and polar θ_s angles of the target spin vector $\vec{S}$ with respect to the lepton scattering plane. In order to obtain polarization dependent part of the cross section, it is common to consider the difference between two target polarization states $\pm S_z$, so that the unpolarized cross section cancels and the polarization dependent cross section is parameterized in terms of structure functions $g_1(x_B, Q^2)$ and $g_2(x_B, Q^2)$

$$\begin{aligned}
\frac{d^3\sigma_{pol}}{dx_B dy d\phi_s} =& \frac{d^3\sigma(-S)}{dx_B dy d\phi_s} - \frac{d^3\sigma(S)}{dx_B dy d\phi_s} \\
=& \frac{4\alpha^2}{s x_B y}\Big\{\Big[\Big(2 - y - \frac{\gamma^2 y^2}{2}\Big) g_1(x_B, Q^2) - \gamma^2 y g_2(x_B, Q^2)\Big]\cos\theta_s + \\
& \gamma\sqrt{1 - y - \frac{\gamma^2 y^2}{4}}[\gamma g_1(x_B, Q^2 + 2g_2(x_B, Q^2))]\sin\theta_s\cos\phi_s\Big\}.
\end{aligned} \tag{2.8}$$

The above equation shows how an information about both structure functions can be revealed experimentally. For this purpose, measurements with both longitudinally and transversely polarized targets are important. If the target is longitudinally polarized, i.e. $\theta_s = 0$, the cross section receives dominant contribution from structure function $g_1(x_B, Q^2)$, as the contribution from $g_2(x_B, Q^2)$ is suppressed by the factor $\gamma^2 \sim 1/Q^2$. In the case when the target is polarized transversely with respect to the lepton beam, both structure functions contribute in the cross section with the similar weights. Hence, the combination of measurements on longitudinally and transversely polarized targets allows the extraction of both polarized structure functions g_1 and g_2. The separate measurement of these functions is important due to the fact, that their is no trivial relation between polarized structure functions, as in the case of unpolarized ones from Eq. 2.7 [WW77]. The most recent experimental measurements of structure function g_1 are presented in [Air07a]. Currently also the first measurements of structure function g_2 exist [Ant03].

The decomposition of hadronic tensor in terms of linearly independent structure functions can be applied also in the case of deep inelastic scattering of leptons from a spin-one hadrons. Detailed description of this parameterization is given in [Hoo89]. The hadronic tensor for a spin-one target depends on eight structure functions. Four additional structure functions denoted as $b_{1-4}(x_B, Q^2)$ contribute to the cross section. Two of them $b_1(x_B, Q^2)$ and $b_2(x_B, Q^2)$ satisfy a relation

$$R(x_B, Q^2) = \frac{(1+\gamma^2)b_2(x_B, Q^2) - 2x_B b_1(x_B, Q^2)}{2x_B b_1(x_B, Q^2)}\,, \tag{2.9}$$

which has the same physical basis as the analogues relation for proton structure functions from Eq. 2.7. Compared to $b_1(x, Q^2)$ and $b_2(x, Q^2)$, the contribution of two other structure functions $b_3(x, Q^2)$ and $b_4(x, Q^2)$ to the total cross section vanishes faster by one power of Q^2.

The early experimental data on inclusive DIS performed by SLAC [Whi90b] indicated that despite of the fact that dynamics of DIS is handled by two variables Q^2 and ν, the structure functions $F_1(x_B, Q^2)$ and $F_2(x_B, Q^2)$ under certain kinematic conditions depend on one variable x_B. This phenomenon, known as Bjorken scaling, brought a significant contribution in further consideration and development of quark-parton model. In order to explain the scale invariance, Bjorken and Feynman [Bjo69a, Bjo69b, Fey69] suggested a model according to which in the so-called infinite momentum frame, where nucleon moves fast in the z-direction, it can be regarded as being composed of free constituents, partons. These partons were further recognized to be quarks with the spins 1/2, whose existence had been proposed earlier by Gell-Mann and Zweig, based on the symmetry properties of the mesons and baryons multiplets [Gel64, Zwe64]. In the simple quark-parton model interpretation of DIS, an electron scatters off a point-like parton in the proton in an elastic manner. Within the chosen frame for the proton momentum $P^\mu = (P, 0, 0, P)$ one has $P = |\mathbf{P}| \gg M_N$. Meanwhile for partons in the nucleon $p^\mu \simeq (p, 0, 0, p)$, $p \equiv |p| \equiv xP \gg |p_\perp|$. Here $p_\perp$ is the parton momentum in the transverse direction and $x = p/P$ is the momentum fraction of the nucleon carried by the parton. Requiring the parton to stay in its mass-shell implies for the Bjorken scaling variable to be identical to parton momentum fraction $x = x_B$ in the infinite momentum frame of the nucleon. Then the cross section is presented as an elastic lepton-quark (antiquark) scattering cross section summed over all quark (antiquark) flavors q ($\bar{q}$) and multiplied by Parton Distribution Functions (PDFs) $q(x)$ for each quark flavor. PDFs $q(x)$ multiplied by the differential momentum fraction dx give the probability to find a quark of flavor q carrying a fraction of the nucleon momentum in the range $[x, x + dx]$. The PDFs can be split up in two parts $q(x) = q_\rightarrow(x) + q_\leftarrow(x)$, where $q_\rightarrow(x)$ ($q_\leftarrow(x)$) is the PDF of a quark with spin aligned parallel (antiparallel) with respect to the nucleon spin. Hence the PDF $q(x)$ represents the distributions of partons summed over the spin states. Similarly one can define helicity distributions as a difference between PDFs of partons with different helicity states $\Delta q(x) = q_\rightarrow(x) - q_\leftarrow(x)$.

Such an interpretation of DIS described the early experimental features, like scale invariance or famous Callan-Gross relation $F_2(x_B) = 2x_B F_1(x_B)$, which is a sequence of helicity conservation. Further DIS experiments on fixed targets [Fox74] found a scaling violation at relatively smaller values of x_B. Also the violation from Callan-Gross relation were observed at the beginning of 90's [Whi90a]. These observations can not be explained in a model which does not take into account interactions among the partons inside the nucleon. The latter is carried out in the framework of quantum chromodynamics (QCD). QCD is a non-Abelian gauge theory that models a strong interaction among color charged quarks. Quarks couple to gluons and the latter ones mediate the strong interaction.

Compared with QED, where the photons dose not bear electric charge, the gluons in QCD carry color charge, which causes a scale dependence of strong coupling constant α_s:

$$\alpha_s(Q^2) = \frac{12\pi}{(33 - 2n_f)ln(Q^2/\Lambda^2_{QCD})}. \tag{2.10}$$

Here, n_f is the number of active quark flavors and the parameter $\Lambda_{QCD} \approx 300MeV$ represents the strength of the coupling. At relatively large values of Q^2 ($Q^2 > \Lambda^2_{QCD}$) the coupling decreases with increasing Q^2 and the quarks are asymptotically free, while at lower values of Q^2 quarks are confined to hadrons. Taking into account an interaction between quarks, they can be assumed to be dressed with a cloud of gluons and virtual quark-antiquark pairs (so-called sea quarks). Corrections of DIS cross section with terms rising due to the radiation of gluons by quarks and splitting of gluons into quark-antiquark pairs are applied in a so-called QCD-improved quark-parton model. This contributions lead to violation of Bjorken scaling.

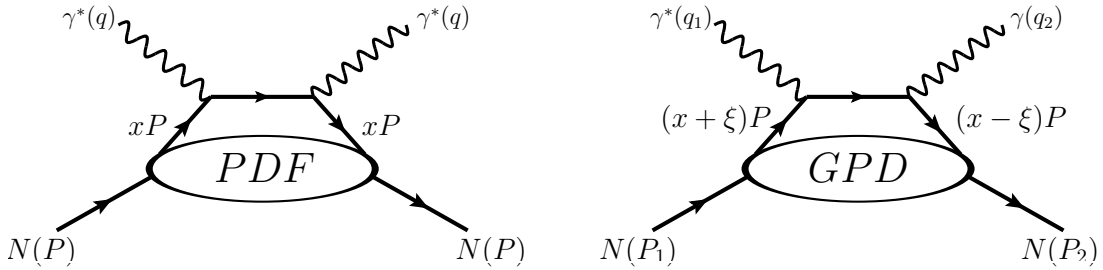

Figure 2.2: Left: Leading order handbag diagram of forward Compton amplitude, whose imaginary part determines the DIS cross section. Right: The non-forward Compton amplitude appearing in DVCS.

Deep-inelastic scattering can be interpreted using the factorization theorem [Col88], that is based on the separation of the cross-section into a short-distance and a long-distance parts. The short-distance part is calculated in perturbative QCD. The long-distance part cannot be calculated, but it is described by the parton distributions which evolve logarithmically in Q^2. The structure functions are related to parton densities accordingly:

$$\begin{array}{lcc} & Nucleon & Deuteron \\ F_1 & \frac{1}{2}\sum_q e_q^2\left[q^{1/2}_{\rightarrow} + q^{1/2}_{\leftarrow}\right] & \frac{1}{3}\sum_q e_q^2\left[q^{1}_{\rightarrow} + q^{-1}_{\rightarrow} + q^{0}_{\rightarrow}\right] \\ g_1 & \frac{1}{2}\sum_q e_q^2\left[q^{1/2}_{\rightarrow} - q^{1/2}_{\leftarrow}\right] & \frac{1}{2}\sum_q e_q^2\left[q^{1}_{\rightarrow} - q^{1}_{\leftarrow}\right] \\ b_1 & \cdots & \frac{1}{2}\sum_q e_q^2\left[2q^{0}_{\rightarrow} - q^{-1}_{\rightarrow} - q^{-1}_{\rightarrow}\right] \end{array} \tag{2.11}$$

where $q^{\Lambda}_{\rightarrow[\leftarrow]}$ is the number density of quarks with spin aligned parallel[antiparallel] to the z axis in the hadron(nucleus) with helicity Λ moving with infinite momentum along the z axis. The sums run over quark and antiquark flavors q with a charge e_q in units of the elementary charge e. The reflection symmetry implies for the number density of quarks $q^{\Lambda}_{\rightarrow} = q^{-\Lambda}_{\leftarrow}$.

It was proven [Rad96, CF99, JiO98] that the factorization into hard and soft parts similar to that for forward Compton amplitude, can be applied also in more general case of non-forward Compton amplitude (see right diagram in Figure 2.2 for special case of

DVCS). However for general Compton amplitude, when one does not require a reality or virtuality of initial or final photon, the factorization is valid in a so-called generalized Bjorken limit of

$$|q_1^2| + |q_2^2| \to \infty, \qquad \text{at fixed} \qquad q_1^2/W^2, q_2^2/W^2, \, t$$

where $t = \Delta^2 = (p_1 - p_2)^2 = (q_2 - q_1)^2$ is the squared four-momentum transfer to the proton with $p_1(q_1)$ and $p_2(q_2)$ being four-momenta of initial and final proton(photon) respectively. A non-vanishing four-momentum transfer to the proton requires two scaling variables for the process, generalized Bjorken variable and skewness

$$\eta = -\frac{(q_1 + q_2)^2}{2(p_1 + p_2) \cdot (q_1 + q_2)}, \qquad \xi = \frac{(p_1 - p_2) \cdot (q_1 + q_2)}{(p_1 + p_2) \cdot (q_1 + q_2)}. \tag{2.12}$$

The most important limiting cases are summarized below up to the terms of an order $\Delta^2/q_{1,2}^2$ with the relevant processes where they appear.

- Deep Inelastic scattering $\gamma^* p \to \gamma^* p$

$$\begin{aligned} \Delta = 0, \qquad \xi = 0 \qquad \eta = x_B \\ -q_1^2 = -q_2^2 \to \infty \end{aligned} \tag{2.13}$$

- Deeply Virtual Compton scattering $\gamma^* p_1 \to \gamma p_2$

$$\begin{aligned} q_2^2 = 0, \qquad \xi = \eta = \frac{x_B}{2 - x_B} \\ -q_1^2 \to \infty, \qquad -\Delta^2 \ll W^2 \end{aligned} \tag{2.14}$$

- Timelike Compton scattering $\gamma p_1 \to \gamma^* p_2$

$$\begin{aligned} q_1^2 = 0, \qquad \xi = -\eta \\ q_2^2 \to \infty, \qquad -\Delta^2 \ll W^2 \end{aligned} \tag{2.15}$$

- Double deeply virtual Compton scattering $\gamma^* p_1 \to \gamma^* p_2$

$$\begin{aligned} q_1^2 < 0, \qquad q_2^2 > 0, \xi > \eta \\ -q_1^2 \sim q_2^2 \to \infty, \qquad -\Delta^2 \ll W^2 \end{aligned} \tag{2.16}$$

Another possible limiting case, extensively discussed in literature is the wide-angle Compton scattering [Rad98, DFJK99], where both photons are real and $-\Delta^2$ is large. Nevertheless, the factorization of this process is still a subject for further investigations.

2.2 Properties of GPDs

The non-perturbative part of non-forward Compton amplitude of the reaction $\gamma^* p_1 \to \gamma p_2$, describing the nucleon structure, is parameterized in terms of generalized parton distributions (GPDs). GPDs depend on four kinematic variables. Compared with PDFs they depend in addition on squared four momentum transfer t to the nucleon and ξ which represents half the difference of the longitudinal momentum fraction carried by probed parton in the nucleon. In quantum field theory approach the GPDs are defined in analogy

to PDFs, through matrix elements of bilocal operators of quark and gluon fields. As can be seen from right side diagram of Figure 2.2 the parton and nucleon momenta are different in the initial and final state, hence GPDs do not correspond to squared amplitudes and can not be treated as probability densities. They rather describe interferences of amplitudes. GPDs evolve logarithmically with Q^2 in analogy with PDFs. The evolution of GPDs is considered in the following three regions (see Figure 2.3).

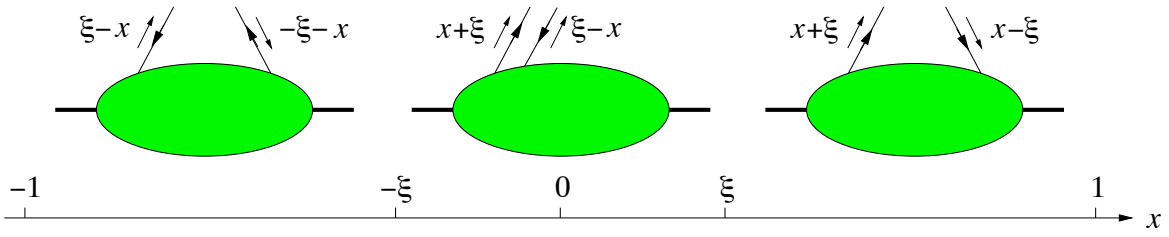

Figure 2.3: The parton interpretation of the coordinates x and ξ in the x-intervals

- For $-1 < x < -\xi$, corresponding to emission of an anti-quark with longitudinal momentum fraction $\xi - x$ and absorption of an anti-quark with longitudinal momentum fraction $-x - \xi$.
- For $-\xi < x < \xi$, corresponding to emission of quark and anti-quark with longitudinal momentum fractions $x + \xi$ and $\xi - x$ respectively.
- For $\xi < x < 1$, corresponding to emission of a quark with longitudinal momentum fraction $x + \xi$ and absorption of a quark with longitudinal momentum fraction $x - \xi$.

The evolution of GPDs in the first and third regions is described by DGLAP evolution equation named after the authors Dokshitzer, Gribov, Lipatov, Altarelli, Parisi [AlPa77, Dok77, GrLi72, Lip75]. While the second case refers to as ERBL(Efremov-Radyuskin-Brodsky-Lepage) region [LeBr79, EfRa80]. More details on the evolution of GPDs in leading order in α_s can be found in [Mul94, Ji97a, Rad99] and in next-to leading order in [Bel00a, Bel00b] .

The non-forward Compton amplitude for spin-1/2 nucleons is described by four leading-twist (twist-two) quark-chirality conserving GPDs for each quark flavor q (and also for gluons g), namely the GPDs H^q, E^q, $\widetilde{H}^q$ and $\widetilde{E}^q$. The twist is defined as the dimension minus spin of the operator defining the GPD [Jaf96]. The twist of a term is usually identified to its suppression in orders of M_N/Q. The GPDs H^q and $\widetilde{H}^q$ conserve the nucleon-helicity, while Eq and $\widetilde{E}^q$ are associated with a helicity flip of the nucleon. Their are also parton helicity flip GPDs, which will not be considered in the following. For the case of spin-1 deuteron, the non-forward Compton amplitude is described by nine GPDs, denoted as H_1^q, H_2^q, H_3^q, H_4^q, H_5^q, $\widetilde{H}_1^q$, $\widetilde{H}_2^q$, $\widetilde{H}_3^q$, $\widetilde{H}_4^q$.

In the following discussion the Q^2 dependence of the GPDs and PDFs will be omitted.

In the forward limit of vanishing momentum difference between the initial and final hadronic states ($t \to 0$, $\xi \to 0$), the GPDs reduce to ordinary quark helicity distributions.

In the case of spin-1/2 nucleons [Rad96, Ji97a]:

$$H^q(x,t=0,\xi=0) = q(x), \tag{2.17}$$

$$\widetilde{H}^q(x,t=0,\xi=0) = \Delta q(x), \tag{2.18}$$

and for spin-1 deuteron [Ber01]:

$$H_1^q(x,t=0,\xi=0) = \frac{q^1(x)+q^{-1}(x)+q^0(x)}{3}, \tag{2.19}$$

$$\widetilde{H}_1^q(x,t=0,\xi=0) = q_{\rightarrow}^1(x) - q_{\leftarrow}^{-1}, \tag{2.20}$$

$$H_5^q(x,t=0,\xi=0) = q^0(x) - \frac{q^1(x)+q^{-1}(x)}{2}. \tag{2.21}$$

Here, $q^{\Lambda}_{\rightarrow[\leftarrow]}(x)$ represents the probability to find a quark with longitudinal momentum fraction x and positive [negative] helicity in a rapidly moving target with longitudinal spin projection Λ. The above relations for $x<0$ involve the anti-quark distributions, with an overall minus sign in the expressions for $\widetilde{H}^q$, H_1 and H_5. In the forward limit the remaining GPDs both for nucleons and deuteron decouple from the Compton amplitude, as in the parameterization of Compton amplitude these GPDs are multiplied by a factor proportional to Δ.

Certain properties of GPDs directly follow from hermiticity and time reversal invariance. First of all those apply for GPDs to be a real valued functions. In addition the following symmetry properties take place:

$$\begin{array}{ll}
\text{Spin}=1/2 & \text{Spin}=1 \\
H^q(x,t,\xi) = H^q(x,t,-\xi) & H_i^q(x,t,\xi) = H_i^q(x,t,-\xi) \qquad i=(1,2,3,5) \\
\widetilde{H}^q(x,t,\xi) = \widetilde{H}^q(x,t,-\xi) & H_4^q(x,t,\xi) = -H_4^q(x,t,-\xi) \\
E^q(x,t,\xi) = E^q(x,t,-\xi) & \widetilde{H}_i^q(x,t,\xi) = \widetilde{H}_i^q(x,t,-\xi) \qquad i=(1,2,4) \\
\widetilde{E}^q(x,t,\xi) = \widetilde{E}^q(x,t,-\xi) & \widetilde{H}_3^q(x,t,\xi) = -\widetilde{H}_3^q(x,t,-\xi).
\end{array} \tag{2.22}$$

Note that the implication of time reversal changes the sign of ξ because the initial and final states are interchanged.

Various features of GPDs are related to the moments in momentum fraction x. First of all it is important to mention that as a consequence of Lorentz invariance the integrals of GPDs over x do not depend on ξ anymore. For instance, the first moments of GPDs are connected to electromagnetic form factors of hadrons. For the case of nucleons [Ji97a]

$$\int_{-1}^{+1} dx H^q(x,t,\xi) = F_1^q(t), \tag{2.23}$$

$$\int_{-1}^{+1} dx \widetilde{H}^q(x,t,\xi) = g_A^q(t), \tag{2.24}$$

$$\int_{-1}^{+1} dx E^q(x,t,\xi) = F_2^q(t), \tag{2.25}$$

$$\int_{-1}^{+1} dx \widetilde{E}^q(x,t,\xi) = h_A^q(t)\,. \tag{2.26}$$

Here, the quantities F_1^q and F_2^q can be expressed through well known Dirac and Pauli form factors of proton and neutron using isospin-symmetry. The axial g_A^q and pseudo-scalar h_A^q form factors (defined for given quark flavor) can be investigated in week reactions [Cho93].

Similar relations exist also for deuteron GPDs [Ber01]

$$\int_{-1}^{+1} dx H_i^q(x,t,\xi) = G_i^q(t) \qquad i = (1,2,3) \tag{2.27}$$

$$\int_{-1}^{+1} dx H_i^q(x,t,\xi) = 0 \qquad i = (4,5) \tag{2.28}$$

$$\int_{-1}^{+1} dx \widetilde{H}_i^q(x,t,\xi) = \widetilde{G}_i^q(t) \qquad i = (1,2) \tag{2.29}$$

$$\int_{-1}^{+1} dx \widetilde{H}_3^q(x,t,\xi) = 0\,. \tag{2.30}$$

The form factors G_1, G_2 and G_3 can be derived from charge monopole G_E, magnetic dipole G_M and charge quadrupole G_C form factors.

$$G_C(\Delta^2) = \Big(1 + \frac{2\tau}{3}\Big) G_1(\Delta^2) - \frac{2\tau}{3}\big[G_2(\Delta^2) - (1-\tau)G_3(\Delta^2)\big], \tag{2.31}$$

$$G_M(\Delta^2) = G_2(\Delta^2), \tag{2.32}$$

$$G_Q(\Delta^2) = G_1(\Delta^2) - G_2(\Delta^2) + (1+\tau)G_3(\Delta^2), \tag{2.33}$$

with $\tau = -\Delta^2/(4M_d^2)$, where $M_d = 1.84\,GeV$ is the mass of deuteron. The normalization of these form factors is given by

$$G_C(0) = 1, \qquad G_M(0) = \mu_d = 1.714 \qquad G_Q(0) = Q_d = 25.83\,,$$

where μ_d denotes the magnetic moment and Q_d denotes the quadrupole moment of the deuteron. The three form factors G_1, G_2 and G_3 are shown in Figure 2.4. They are obtained using the parameterization suggested in [Kob95], and the fitting parameters are taken from [Abb00]. No experimental measurements exist for the axial form factors $\widetilde{G_1}$

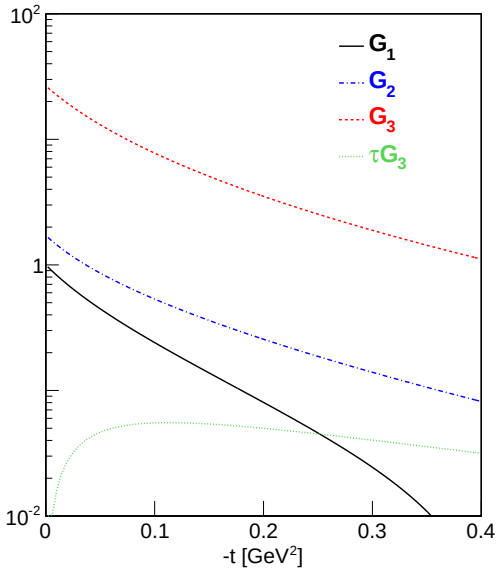

Figure 2.4: The electromagnetic form factors of deuteron .

and $\widetilde{G_2}$, although certain linear combinations with respect to the flavor number can be measured in the weak interactions.

The relations between GPDs and form factors are a special case of more general property of GPDs, i.e. polynomiality . In [Ji98] it was shown, that Mellin moments of GPDs H and E can be expressed as a polynomials in ξ with maximal power of N for even N and $N+1$ for odd N.

$$\int_{-1}^{+1} dx x^N H^q(x,\xi,t) = h_0^{q(N)} + h_2^{q(N)}\xi^2 + \cdots + h_{N+1}^{q(N)}\xi^{N+1}, \tag{2.34}$$

$$\int_{-1}^{+1} dx x^N E^q(x,\xi,t) = e_0^{q(N)} + e_2^{q(N)}\xi^2 + \cdots + e_{N+1}^{q(N)}\xi^{N+1}\,. \tag{2.35}$$

For the case of odd N, the coefficients in front of the highest power of ξ are related to each other as [GPV01]

$$e_{N+1}^{q(N)} = -h_{N+1}^{q(N)}. \tag{2.36}$$

The GPDs $\widetilde{H}$ and $\widetilde{E}$ satisfy to similar polynomiality conditions as GPDs H and E, whereas in this case, the highest power of the polynomial is $N-1$ for odd N and N for even N. The coefficients in the polynomials are interpreted as form factors.

2.3 Relation to quark angular momentum

An interest to GPDs significantly raised after the discovery of their rich spin structure. Particularly in 1996 it was shown by Ji [Ji97b], that GPDs fulfill a sum rule which provides an access to total angular momentum of quarks in a nucleon. In the naive quark-parton model the nucleon is considered to consist of three spin-1/2 quarks, and its spin is a vector sum of the quark spins. In late 80's measurements on polarized DIS provided by European Muon Collaboration (EMC) [Ash88], showed that the contribution of quarks spins into nucleon spin is abut 20%. Later this result was conformed by number of experiments (see for instance [Air07a]). In order to understand this discrepancy, one needs to consider the spin structure of nucleon in QCD-improved parton model. Here the nucleon spin is decomposed into sum of quark and gluon total angular momenta:

$$1/2 = J_q + J_g, \tag{2.37}$$

where J_q and J_g are the contributions from quarks and gluons respectively. J_q and J_g can be expressed as a matrix elements of the QCD energy-momentum tensor, which in turn is decomposed on form factors [Ji97b]. As was mentioned in previous section the form factors can be represented in terms of the moments of GPDs. This is expressed in a Ji's famous sum rule [Ji97b]

$$J_q = \frac{1}{2}\lim_{t\to 0}\int_{-1}^{+1}(H^q(x,\xi,t) + E^q(x,\xi,t))x dx\,. \tag{2.38}$$

2.4 Impact parameter space representation

In an alternative presentation the GPDs are introduced as a generalized Wigner distributions. The generalization of the concept of phase-space distributions to the case of

relativistic quarks and gluons is described in details in [BelR05]. In this context it is obvious that GPDs do not have probabilistic interpretation. Nevertheless, in particular case of zero skewness the GPDs acquire a probabilistic interpretation. This is obtained in an impact parameter space, when keeping the longitudinal momentum (momentum in a light-cone + direction) and Fourier transforming the transverse momentum to transverse position [Bur00]. For a particular case of GPD H^q the impact parameter distribution reads:

$$q(x,|b|) = \int \frac{d^2\Delta}{(2\pi)^2} e^{-i\Delta_\perp b} H^q(x,\xi=0,t=-\Delta_\perp). \tag{2.39}$$

Here, $\Delta_\perp$ is the transverse component of the nucleon momentum difference (the zero value of skewness $\xi = 0$ implies for a longitudinal component of the nucleon momentum difference to be equal to zero) and b indicates a position in the transverse plane and is defined as: $b = \sum_i x_i b_i$, where the sum goes over all partons with longitudinal momentum fraction x_i and transverse location b_i. This kind of mixed representation allows for a three-dimensional probabilistic interpretation of fast moving nucleon in one-dimensional momentum and two-dimensional coordinate space.

Fourier transform to impact parameter space could be applied also for other GPDs. For GPD E^q one obtains a function $e(x,|b|)$, which has no direct interpretation, since it refers to the nucleon helicity flip, and thus is non-diagonal. Same holds also for GPD $\widetilde{E}^q$, while for GPD $\widetilde{H}^q$ the impact parameter space distribution $\Delta q(x,|b|)$ is interpreted as the polarized analogue of $q(x,|b|)$.

2.5 Parameterization of GPDs

Various parameterization models of GPDs are available in the literature. The starting point for modeling of GPDs, are the properties discussed in previous sections. Especially the forward limit, where the PDFs are used as an input. From the other side, it is important to generate the non-trivial ξ dependence of GPDs in a way, that will comply the polynomiality condition. Very often, for the consistent parameterization of GPDs the so-called double-distributions (DD) are considered. DDs were introduced in [Mul94, Rad96] and are discussed in details in [Rad99, Rad01]. The relation between DDs $f(\beta,\alpha,t)$ and GPDs $F(x,\xi,t)$ is given by:

$$F^q(x,\xi,t) = \int_{-1}^{+1} d\beta \int_{-1+|\beta|}^{1-|\beta|} \alpha\delta(x-\beta-\alpha\xi) f(\beta,\alpha,t) \tag{2.40}$$

The DD function satisfies to polynomiality conditions, but always have $e_{N+1}^{q(N)} = h_{N+1}^{q(N)} = 0$. In order to complete the parameterization, the so-called D-term was introduced.

$$H^q(x,\xi,t) = \int_{-1}^{+1} d\beta \int_{-1+|\beta|}^{1-|\beta|} \alpha\delta(x-\beta-\alpha\xi) f(\beta,\alpha,t) + \theta\Big[1-\frac{x^2}{\xi^2}\Big] D^q\Big(\frac{x}{\xi}t\Big), \tag{2.41}$$

$$E^q(x,\xi,t) = \int_{-1}^{+1} d\beta \int_{-1+|\beta|}^{1-|\beta|} \alpha\delta(x-\beta-\alpha\xi) k(\beta,\alpha,t) + \theta\Big[1-\frac{x^2}{\xi^2}\Big] D^q\Big(\frac{x}{\xi}t\Big). \tag{2.42}$$

The dependence on both x and ξ is projected out by the delta function and the support region for the α and β integration is determined from the condition $|\alpha| + |\beta| \leq 1$. One of the advantages of DDs is that independent of the kind of model used for their parameterization, the polynomiality condition is fulfilled automatically. The contribution of the

D-term to GPDs H and E are of the same magnitude, but opposite sign. It contributes only in ERBL region and does not contribute in a forward limit. It drops out also in the integration of GPDs over x, which does not allows for any constraint of its t dependence by nucleon form factors. The GPDs $\widetilde{H}$ and $\widetilde{E}$ do not have a D-term.

2.6 The VGG model

One of the most direct GPD models commonly used for the comparison with the experimental results was suggested by Vanderhaeghen, Guichon and Guidal (VGG model) [VGG99]. It is based on double distribution formalism and satisfies to the requirements discussed in section 2.2 .

For the parameterization of GPD H^q, first the t independent part of GPD $H^q(x,\xi) = H^q(x,\xi,t=0)$ is modeled using the factorized representation of DDs discussed in [Rad99].

$$f^q(\beta,\alpha) = h(\beta,\alpha)q(\beta). \tag{2.43}$$

Here $q(\beta)$ is an ordinary parton density for positive values of β corresponding to quark PDF and with negative values to antiquark PDF. The profile function $h(\beta,\alpha)$ is parameterized through a one-parameter ansatz, following [Rad99]

$$h(\beta,\alpha) = \frac{\Gamma(2b+2)}{2^{2b+1}\Gamma^2(b+1)} \frac{\left[(1-|b|)^2-\alpha^2\right]^b}{(1-|\beta|)^{2b+1}}. \tag{2.44}$$

The parameter b in Eq. 2.44 characterizes the dependence of GPD on skewness ξ. It is a free parameter for both valence and sea quark contributions and needs to be determined from the fits to experimental data. The limiting case $b \to \infty$ corresponds to the vanishing skewness dependence for the GPD, and reduces it to parton density $H^q(x,\xi,t=0)_{b\to\infty} = q(x)$. In the considered VGG model, the parameterization of quark distributions was taken from [MRST98], however the results in the valence region practically do not change when using another parameterization.

The parameterization of the t dependence of GPD H^q is modeled in a two alternative approaches, which fulfill the sum rules in Eqs. 2.23 - 2.26. The simplest parameterization is the so-called factorized ansatz:

$$H^u(x,\xi,t) = H^u(x,\xi)F_1^u(t)/2, \tag{2.45}$$
$$H^d(x,\xi,t) = H^d(x,\xi)F_1^d(t), \tag{2.46}$$
$$H^s(x,\xi,t) = 0\,. \tag{2.47}$$

In this form the GPDs satisfy to correct forward limit for $u-$ and $d-$quark distributions.

Another approach of modeling the t dependence at small $-t$ region is the Regge-theory motivated ansatz. In this case the t dependence is encoded in parameterization of double distribution as:

$$f^q(\beta,\alpha,t) = h(\beta,\alpha)q(\beta)\frac{q}{|\beta|^{\alpha' t}}, \tag{2.48}$$

where α' is the slope of the Regge trajectory. It can be determined from the cross section measurements of hadron-hadron reactions [Col77]. For the complete parameterization of GPD H^q also the D-term needs to be specified. Various features of it are taken into account. Based on the chiral quark-soliton model calculations, it is assumed that contributions of $u-$ and $d-$quarks in the D-term are the same, thus allowing for the consideration

of reduced quantity $D^q(\frac{x}{\xi}) = \frac{1}{2}D(\frac{x}{\xi})$. Further, taking into account the odd nature of t independent part of the D-term , it is expanded in a Gegenbauer polynomial up to the fifth order in x/ξ. The coefficients of the expansion are estimated using the calculation of GPDs in chiral quark-soliton model [Pet98]. The t dependence of the D-term is assumed to be the same as for double distribution part of GPDs.

The parameterization of GPD E^q, similar to that of H^q, is more complicated as in the forward limit it has no DIS constraint. In this case the only constraint is provided by Eq. 2.25. In addition, the total quark angular momentum J_q from Eq. 2.38 is used as a free parameter in the construction of the forward limit of GPD E^q, allowing a model dependent constraint of J^q to be made using experimental data. The contribution of the D-term is the same as for H^q, but with opposite sign.

As it was mentioned above the GPDs $\widetilde{H}^q$ and $\widetilde{E}^q$ do not contain a D-term. Hence the GPD $\widetilde{H}^q$ is parametrized in a full analogy with H^q, without a D-term and with an appropriate forward limit. While for GPD $\widetilde{E}^q$ the only constraint is the sum rule from Eq. 2.26. Its parameterization is based on the findings of quark-soliton model, which suggest that in wide range of t and ξ the GPD $\widetilde{E}^q$ gets a dominant contribution from pion pole [GPV01].

2.7 The Dual-GT model

Another model used in this report is based on dual parameterization of GPDs. It was introduced by Guzey and Teckentrup in [GT06] based on the initial work of Polyakov and Shuvaev [PS02]. In this model only the unpolarized GPDs H^q and E^q are considered. They are parameterized using a decomposition into infinite sum of t-channel resonances.

$$H^q(x,\xi,t) = \sum_{\substack{n=1\\odd}}^{\infty}\sum_{\substack{l=0\\even}}^{n+1} B^q_{nl}(t)\theta(\xi-|x|)\Big(1-\frac{x^2}{\xi^2}\Big)C_n^{3/2}\Big(\frac{x}{\xi}\Big)P_l\Big(\frac{1}{\xi}\Big), \tag{2.49}$$

$$E^q(x,\xi,t) = \sum_{\substack{n=1\\odd}}^{\infty}\sum_{\substack{l=0\\even}}^{n+1} C^q_{nl}(t)\theta(\xi-|x|)\Big(1-\frac{x^2}{\xi^2}\Big)C_n^{3/2}\Big(\frac{x}{\xi}\Big)P_l\Big(\frac{1}{\xi}\Big), \tag{2.50}$$

In the Eqs. 2.49 - 2.50 the B^q_{nl} and C^q_{nl} denote the unknown form factors, $C_n^{3/2}$ and P_l are Gegenbauer and Legendre polynomials respectively. As it is discussed in [GT06] a set of generating functions is introduced, whose Mellin moments are related to unknown form factors B^q_{nl} and C^q_{nl}. The constraints on generating functions follow from the properties of GPDs like, relation to electromagnetic form factors, reduction in forward limit, polynomility, etc.. For the case of GPD E^q, the same approach as in VGG-model is applied.

The t dependence of GPDs is included in factorized or Regge ansatz like in the case of VGG-model. The Regge slope parameter is determined from the comparison of the model predictions with the DVCS cross section measurements [Akt05, Che03].

Note, that in the original version of the model a factor of two in the DVCS amplitude was missing, which was corrected later in [GT09], while the agreement of the prediction of the original version with the experimental measurements was much better.

2.8 Models for deuteron GPDs

In the scattering process where an electron scatters off a deuteron, one can consider two types of processes. First, when deuteron acts as a single particle and stays intact after scattering, the process is called coherent, while in the case when the deuteron breaks up into proton and neutron it is called incoherent. In addition one can consider a break up of deuteron to more complicated final states. In the context of GPDs an investigation of coherent process serves as useful source of information about partonic behavior in a nuclei and nuclear binding forces, while the incoherent process can provide an access to neutron GPDs. For instance, the GPDs H_3 and H_5 are associated with the 5% D-wave component of the deuteron wave function in terms of nucleons [Lac81]. H_3 is related to isoscalar currents and probes the binding forces in the deuteron, and H_5 involves a tensor term [Ber01, KM04], the analog of which has no relationship to any local current due to Lorentz invariance.

Most of the GPD models for deuteron are based on simple approach of impulse approximation. In this approximation the scattering takes place on one of the quarks of one of the quasi-free nucleons, while the other nucleon is considered as a spectator. Thus, the deuteron GPDs are convolutions of nucleon GPDs and two body wave functions describing the physical state of deuteron with an appropriate momentum and spin dependences.

One of the simplified models for deuteron GPDs in context of impulse approximation is described in [KM04]. It is based on double distribution ansatz for nucleonic GPDs, combined with factorized t dependence, and with the D-term set to zero. In a discussed model only the GPDs H_1, H_3, H_5 and $\widetilde{H}_1$ are considered, as in the DVCS amplitude the rest of the GPDs are kinematically suppressed. The GPDs H_1 and $\widetilde{H}_1$ are related to corresponding proton GPDs (H, $\widetilde{H}$) and the reduction to parton densities is satisfied by implementation of double distribution representation. The GPD H_3 is assumed to be sensitive to binding forces between partons that carry either large or small momentum fractions. Hence in a moderate values of x_B, relevant for present fixed target experiments, they can be set to zero. Alternatively the GPD H_3 can be equated to H_1, as in a convolution model both of them are determined by isoscalar GPD H^{iso} [CP03]. Finally, the simplest choice for modeling the GPD H_5 is to set it to zero. This is according to the fact that in forward limit H_5 reduces to parton density δq (see Eq. 2.21), which in turn is related to structure function b_1. Measurement on tensor polarized deuterium target [Air05] suggest, that in a valence quark region (moderate values of x_B) the structure function b_1 is zero. In addition, the GPD H_5 can be equated to an antisymmetric function in x that in the forward limit will reduce to an experimental constraints for δq. Another model for deuteron GPDs was suggested in [CP04]. This model is based on double distributions, where only the polarizations of the valence quarks are considered for the nucleonic GPDs. A factorized ansatz for the t dependence of the nucleonic GPDs is employed and the strange quark contribution is neglected. Again the impulse approximation is used to combine the nucleonic GPDs, without including the particular contribution from the D-term.

Chapter 3

Deeply Virtual Compton Scattering

In this chapter the hard exclusive leptoproduction of real photon off a nucleon or nuclear targets is discussed. The relevant kinematics of the process and the interpretation of the cross section in terms of factorization theorem is discussed in section 3.1. In section 3.2 the azimuthal dependence of the cross section is considered, which further is extended for the case of polarized spin-1/2 and spin-1 targets. In section 3.4 various experimental observables are defined for both unpolarized and longitudinally polarized deuterium targets. And finally in section 3.5 the relations between experimental observables and Compton form factors are discussed.

3.1 Exclusive leptoproduction of real photons

Exclusive leptoproduction of a real photon on nucleon or nuclear target A is denoted as

$$l(k) + A(p) \rightarrow l(k') + A(p') + \gamma(q'), \tag{3.1}$$

where $k(k')$ and $p(p')$ are the four-momenta of initial(final) lepton and target respectively, and q' is the four-momentum of real photon. The reaction given in Eq. 3.1 includes contributions from certain processes: the Bethe - Heitler(BH) process, where the real photon is radiated by an initial or final state lepton, the Deeply Virtual Compton Scattering(DVCS), where the photon is emitted by a struck parton in the target, and the radiation of real photon by an initial or final state target.

The first process is exactly calculable in leading order of QED. It can be treated as first order radiative correction to the elastic lepton nucleon or nuclei scattering. It was studied theoretically in certain works. One of the first calculations were done by Mo and Tsai [MT69]. Further theoretical investigations of the process can be found also in [Ent01] and the case of polarized beam and target was considered in [Aku97, BMK02]. For higher order radiative correction one can see [Van00, Afa06]. Although this investigations where done for a kinematic conditions not directly relevant to HERMES, one can expect that all the possible two-photon exchange contributions are suppressed. In current report we will be interested mainly in BH from a spin-1 target, which was considered in [KM04].

The second process which contributes to the reaction 3.1 is the DVCS. DVCS refers to the generalized Bjorken region. In this region the quark absorbs a hardly virtual photon, emits a real energetic one, and joins the target remnant. The amplitude of DVCS is parameterized in terms of GPDs. At present the effects of next-to-leading order in strong coupling constant α_s [Bel98, JiO98] and next-to-leading twist [KPV01, BMK02] were investigated.

Finally the last process mentioned above refers to as Virtual Compton Scattering (VCS), i.e. the process of radiation of a photon by target, in which an intermediate target propagates between two photon vertexes. Below the pion emission threshold the amplitude of this process is parametrized in terms of generalized polarizabilities. VCS was investigated both theoretically [Gui98] and experimentally in MAMI [Roc00]. It is expected that VCS process is suppressed at the Bjorken region, relevant for DVCS.

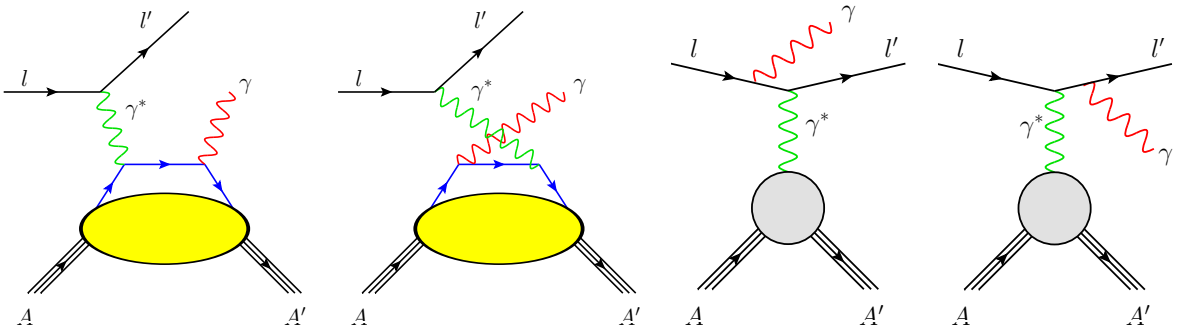

Figure 3.1: Leading order Feynman diagrams for deeply virtual Compton scattering from the left and for the Bethe - Heitler process from the right.

Further we will consider the BH and DVCS processes in a single photon exchange approximation. The handbag diagrams of these processes are depicted in Figure 3.1, which are expected to have a dominant contribution to the reaction from Eq. 3.1 at Bjorken limit [Mul94]. Due to the different physical insight of BH and DVCS processes, the kinematic variables used for their description require different interpretation. In the following only the case of DVCS will be considered.

For the description of inclusive part of the DVCS the same kinematic variables can be considered, as for DIS:

$$\begin{aligned} -q^2 &\equiv Q^2 = -(k-k')^2 \overset{lab.}{=} 4EE'\sin^2(\theta/2) \\ \nu &\equiv \frac{p\cdot q}{M_A} \overset{lab.}{=} E - E' \\ W^2 &\equiv (p+q)^2 \overset{lab.}{=} M_A^2 + 2M_A\nu - Q^2 \\ x_A &\equiv \frac{Q^2}{2p\cdot q} \overset{lab.}{=} \frac{Q^2}{2M_A\nu} \\ y &\equiv \frac{p\cdot q}{p\cdot k} \overset{lab.}{=} \frac{\nu}{E}\,. \end{aligned} \tag{3.2}$$

Here we do not specify the target and denote its mass through M_A. Due to the exclusivity of the DVCS process, an additional variable is needed to fix the reaction kinematics. It is convenient for such an additional variable to take the squared four-momentum transfer to the target t. If the mass of the target is unchanged, then it reads:

$$t = \Delta^2 = (p-p')^2 \overset{lab.}{=} 2M_A(M_A - E'), \tag{3.3}$$

where E' is the energy of final state target. The four-fold differential cross-section of the

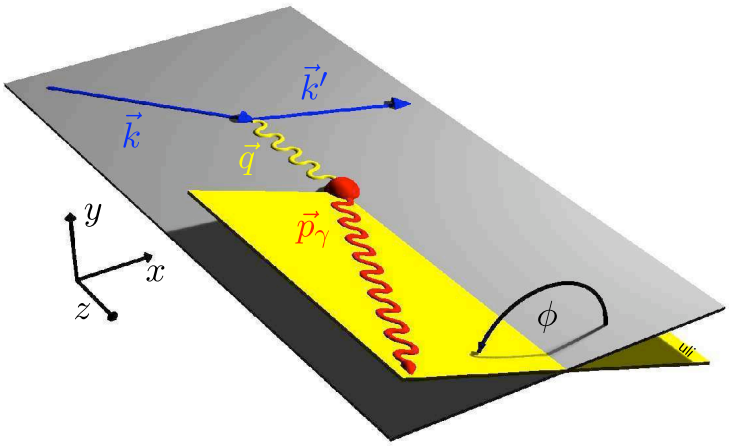

Figure 3.2: Definition of the azimuthal angle ϕ between the lepton scattering plane and photon production plane.

reaction 3.1 is given according to [DGPR97, KM04] as:

$$\frac{d\sigma}{dx_A dQ^2 d|t| d\phi} = \frac{\alpha^2 x_A y}{16\pi^2 Q^2 \sqrt{1+\epsilon^2}} \cdot \frac{2\pi y}{Q^2} \cdot \left|\frac{\mathcal{T}}{e^3}\right|^2 , \tag{3.4}$$

where $\epsilon^2 = (2x_A M_A)^2/Q^2$, $\mathcal{T}$ is the total amplitude of the reaction, and ϕ is the azimuthal angle between lepton scattering plane and photon production plane as depicted in Figure 3.2. As the final states of BH and DVCS are the same and are experimentally indistinguishable, the squared amplitude $\mathcal{T}^2$ will contain coherent sum of the amplitudes of two processes $\mathcal{T}_{\rm BH}$ and $\mathcal{T}_{\rm DVCS}$:

$$\begin{aligned} |\mathcal{T}|^2 &= |\mathcal{T}_{\rm BH} + \mathcal{T}_{\rm DVCS}|^2 \\ &= |\mathcal{T}_{\rm BH}|^2 + |\mathcal{T}_{\rm DVCS}|^2 + \mathcal{T}_{\rm DVCS}\mathcal{T}^*_{\rm BH} + \mathcal{T}^*_{\rm DVCS}\mathcal{T}_{\rm BH} \\ &= |\mathcal{T}_{\rm BH}|^2 + |\mathcal{T}_{\rm DVCS}|^2 + {\rm I}. \end{aligned} \tag{3.5}$$

Here, I denotes the interference term between the amplitudes of these processes. The three terms in Eq. 3.5 can be presented by the contraction of hadronic tensor

$$T_{\mu\nu} = \frac{i}{e^2}\int dx e^{ix(q+q')/2}\langle p', S'|T(j_\mu(x/2)j_\nu(-x/2))|p, S\rangle \tag{3.6}$$

with the electromagnetic current

$$J_\alpha = \frac{1}{e}\langle p', S'|j_\alpha(0)|p, S\rangle\,, \tag{3.7}$$

and a corresponding leptonic tensor $L^{\mu\nu}$.

$$|\mathcal{T}_{\rm DVCS}|^2 = \frac{e^6}{q^4}(-g^{\alpha\beta})L^{\mu\nu}_{\rm DVCS}\sum_{S'} T_{\alpha\mu}(T_{\beta\nu})^\dagger, \tag{3.8}$$

$$|\mathcal{T}_{\rm BH}| = \frac{e^6}{t^2}L^{\mu\nu}_{\rm BH}\sum_{S'} J_\mu J^\dagger_\nu, \tag{3.9}$$

$${\rm I} = \frac{\pm e^6}{q^2 t}L^{\alpha\mu\nu}\sum_{S'}\left[J_\mu(T_{\alpha\nu})^\dagger + h.c.\right] \tag{3.10}$$

Here (±) sign refers to a charge of the beam. The hadronic tensor is presented as a time-ordered product of quark electromagnetic currents with the flavor i and charge e_i

$$j_\alpha = \sum_{i=u,d,s} e_i \bar{\psi} \gamma_\alpha \psi \,, \tag{3.11}$$

sandwiched between hadron states of different momenta and spin $S(S')$. As can be seen from Eqs. 3.8 - 3.10, at the limit $t << Q^2$, the BH cross section dominates over DVCS cross section and the contribution from interference term has a size between BH and DVCS. In addition, one can see from Eq. 3.10 that the sign of interference term is defined by the charge of lepton beam. This allows to measure a wide number of cross section asymmetries with respect to the beam charge. For further evaluation of the cross section, the hadronic tensor can be parameterized in terms of Compton Form Factors (CFFs) $\mathcal{F}(\eta, t, Q^2)$, which appear as a coefficients in front of independent Lorentz structures. The CFFs depend on three variables t, Q^2 and generalized Bjorken variable η which in the case of DVCS can be considered to be equal to skewness variable ξ[1]. To the virtue of the factorization theorem, the CFFs in turn can be presented as convolutions of perturbative hard scattering amplitudes and corresponding GPDs F

$$\mathcal{F}(\eta, t, Q^2) = \sum_{i=u,d,s..} \int_{-1}^{1} dx C_i^{(\mp)}(x, \eta, Q^2) F_i(x, \xi, t, Q^2)\big|_{\xi=\eta} \,. \tag{3.12}$$

In an above equation the hard scattering amplitude have been calculated in next to leading order in QCD coupling constant α_s. At leading order it reads:

$$\eta C^{(\mp)} = \frac{Q^2}{1 - x/\eta - i0} \mp \frac{Q^2}{1 + x/\eta - i0}. \tag{3.13}$$

In the case of DVCS observables one can not directly measure the GPDs. They can be accessed in convolution integrals over x. As can be seen from Eq. 3.13 the measurement of the imaginary parts of CFFs probes GPDs along the trajectory $|x| = \xi$, while from the real part of CFFs one can project out GPDs in an integral over x. This leads to a fact, that in DVCS it is impossible to investigate two dimensional (in x and ξ) dependencies of GPDs.

3.2 Azimuthal Dependence

At HERMES kinematic conditions the DVCS cross sections is much smaller than that of BH. Fortunately, the DVCS amplitudes can be accessed through the Interference term. The three terms of the cross section, given in Eqs. 3.5, can be expanded into Fourier series in azimuthal angle ϕ. In general case, when the beam and target might be polarized, excluding transverse target polarization, they read [BMK02]:

[1] In reference [BMK02] the relation between generalized Bjorken variable and skewness is given with the minus sign, which depends on a definition of variable $\Delta = \pm(p - p')$. Meanwhile the given relation up to the terms of higher order than Δ^2/Q^2 read as $\eta = \xi(1 + \frac{\Delta^2}{2Q^2})^2$

$$|\mathcal{T}_{\rm BH}|^2 = \frac{K_{BH}}{\mathcal{P}_1(\phi)\mathcal{P}_2(\phi)} \times \sum_{n=0}^{2} c_n^{BH}\cos(n\phi), \qquad K_{BH} = \frac{1}{x_A^2 y^2 t(1+\epsilon^2)^2} \quad (3.14)$$

$$|\mathcal{T}_{\rm DVCS}|^2 = K_{DVCS}\Big\{\sum_{n=0}^{2} c_n^{DVCS}\cos(n\phi) + \sum_{n=1}^{2} s_n^{DVCS}\sin(n\phi)\Big\}, \qquad K_{DVCS} = \frac{1}{y^2Q^2}, \quad (3.15)$$

$$I = \frac{K_I e_\ell}{\mathcal{P}_1(\phi)\mathcal{P}_2(\phi)}\Big\{\sum_{n=0}^{3} c_n^{I}\cos(n\phi) + \sum_{n=1}^{3} s_n^{I}\sin(n\phi)\Big\}, \qquad K_I = \frac{1}{x_A y^3 t}. \quad (3.16)$$

Here, e_ℓ is the beam charge in the units of elementary charge and $\mathcal{P}_1(\phi), \mathcal{P}_2(\phi)$ are the lepton propagators, which contribute only in BH and interference terms and introduce an additional ϕ dependence. In the case of transversely polarized target an additional odd harmonics appear in the Fourier decomposition of BH term. The explicit dependence of lepton propagators on ϕ read

$$\mathcal{P}_1(\phi) = -\frac{1}{y(1+\epsilon^2)}\{J + 2K\cos(\phi)\}, \quad \mathcal{P}_2(\phi) = 1 - \frac{t}{Q^2} + \frac{1}{y(1+\epsilon^2)}\{J + 2K\cos(\phi)\}$$

where

$$K^2 = \frac{t}{Q^2}(1-x_A)\left(1 - y - \frac{y\epsilon^2}{2}\right)\left(1 - \frac{t_0}{t}\right)\left\{\sqrt{1+\epsilon^2} + \frac{4x_A(1-x_A)+\epsilon^2}{4(1-x_A)}\frac{t_0 - t}{Q^2}\right\} \quad (3.17)$$

$$J = \left(1 - y - \frac{y\epsilon^2}{2}\right)\left(1 - \frac{t}{Q^2}\right) + (1-x_A)(2-y)\frac{t}{Q^2} \quad (3.18)$$

$$t_0 = Q^2\frac{2(1-x_A)\big(1-\sqrt{1+\epsilon^2}+\epsilon^2\big)}{4x_A(1-x_A)+\epsilon^2}. \quad (3.19)$$

Here, t_0 is the minimum allowed value of four-momentum transfer to the target $|t| > |t_0|$. The kinematic factor K behaves like $\sqrt{-t}/Q^2$ and further appears also in the decomposition of Fourier coefficient from Eqs. 3.15 - 3.16 through CFFs. For the coherent scattering on a spin-1 deuteron, polarized longitudinally with respect to the virtual photon, the following decomposition of Fourier coefficients from Eqs. 3.14 - 3.16 can be introduced

$$\begin{aligned} c_n(\Lambda,\lambda) &= \frac{3}{2}\Lambda^2 c_{n,unp} + \lambda\Lambda c_{n,LP} + (1 - \frac{3}{2}\Lambda^2)c_{n,LLP} \\ s_n(\Lambda,\lambda) &= \frac{3}{2}\lambda\Lambda^2 s_{n,unp} + \Lambda s_{n,LP} + (1 - \frac{3}{2}\Lambda^2)\lambda s_{n,LLP}\,. \end{aligned} \quad (3.20)$$

Here, the $\Lambda = +1, -1, 0$ is the spin projection of deuteron and λ is the beam helicity. The coefficients $c/s_{n,unp}$ are ascribed for an unpolarized and coefficients $c/s_{n,LP}$, $c/s_{n,LLP}$ for a longitudinally polarized parts of the cross section. The coefficients c/s_{LLP} appear due to tensor polarization of deuteron. Hence, the analogous decomposition for a spin-1/2 nucleon reduces to

$$\begin{aligned} c_n(\Lambda,\lambda) &= c_{n,unp} + \lambda\Lambda c_{n,LP} \\ s_n(\Lambda,\lambda) &= \lambda s_{n,unp} + \Lambda s_{n,LP}. \end{aligned} \quad (3.21)$$

Note that the above equations are written for a pure longitudinal polarization of the target with respect to the virtual photon and all the transverse components of target polarization are zero.

3.3 Treatment of Target Polarization

The Fourier coefficients from the decomposition of BH, DVCS and interference terms in Eqs. 3.14 - 3.16 encompass the dependence of total leptopruduction cross section on beam helicity λ and target spin projection Λ. These dependences for spin-1 deuteron and spin-1/2 nucleon are given in Eqs. 3.20 - 3.21. These equations are applicable for purely polarized states with $\Lambda = \pm 1, 0$ for deuteron ($\Lambda = \pm 1$ for nucleon). In a real experiment, the polarized target contains a mixture of these pure polarized states, and also the beam has certain time averaged polarization value. Hence, from experimental point of view it is more convenient to represent the cross section through experimentally measured quantities. Let us first consider the case of spin-1/2 nucleon. Here the z-component of the spin of individual particle can have two projections along the quantization direction z, namely $+\frac{1}{2}$ or $-\frac{1}{2}$. If one considers an ensemble of spin-1/2 particles, then the vector polarization of an ensemble is defined as

$$P_z = \frac{n^+ - n^-}{n^+ + n^-}, \tag{3.22}$$

where $n^+(n^-)$ is the population of the state with spin projection $\Lambda = 1(-1)$. In other words n^+ and n^- are the probabilities to find a particle with certain spin projection from an ensemble. The total number of particles is normalized to one, $n^+ + n^- = 1$. Hence, one can represent the populations of the states through polarization values as

$$n^+ = \frac{1}{2}(1 + P_z) \tag{3.23}$$

$$n^- = \frac{1}{2}(1 - P_z)\,. \tag{3.24}$$

The absolute value of vector polarization varies between -1 and +1. When each of the states $\Lambda = 1$ and $\Lambda = -1$ is populated by $\frac{1}{2}$ of the particles then the longitudinal polarization vanishes $P_z = 0$, like in an unpolarized case.

For the case of deuteron, the situation is more complicated. For the spin-1 particle, the z-component of the spin can have three projections along the quantization direction, namely +1, 0, −1. So, in the total ensemble the particles are distributed in $\Lambda = \pm 1$, 0 states with the probabilities n^+, n^- and n^0, respectively. The vector (P_z) and tensor (P_{zz}) polarizations are defined as

$$P_z = \frac{n^+ - n^-}{n^+ + n^- + n^0}, \tag{3.25}$$

$$P_{zz} = \frac{n^+ + n^- - 2n^0}{n^+ + n^- + n^0}. \tag{3.26}$$

Again with the common normalization $n^+ + n^- + n^0 = 1$, the probabilities read

$$n^+ = \frac{1}{6}(2 + P_{zz} + 3P_z), \tag{3.27}$$

$$n^- = \frac{1}{6}(2 + P_{zz} - 3P_z), \tag{3.28}$$

$$n^0 = \frac{1}{3}(1 - P_{zz}). \tag{3.29}$$

The largest (absolute) value of vector polarization is achieved, when only $\Lambda = 1$ or $\Lambda = -1$ states are populated. In that case $|P_z| = 1$ ($n^- = 0$ or $n^+ = 0$) and $P_{zz} = +1$. When only

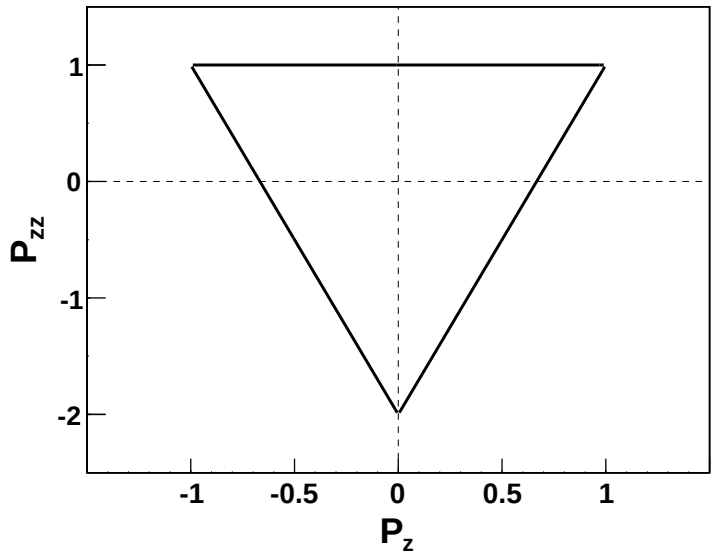

Figure 3.3: Schematic representation of the allowed range of vector and tensor polarization of the spin-one particle.

the $\Lambda = 0$ state is populated, then $P_{zz} = -2$ and $P_z = 0$. The allowed range of vector and tensor polarizations is shown in Figure 3.3.

In sense of above defined probabilities of population, the unpolarized ensemble requires equal population of each state. For spin-1/2 nucleons this yields in $n^+ = n^- = \frac{1}{2}$ and for spin-1 deuterons $n^+ = n^- = n^0 = \frac{1}{3}$.

3.4 Definition of Observables

From an experimental point of view the DVCS observables can be categorized in certain groups. An information about a process of interest with an underling physical objects like CFFs or GPDs can be gained through measurement of absolute cross sections. It requires precise knowledge of the luminosity of the experiment together with perfectly aligned detector with sufficiently large acceptance. In addition, it is important to provide a measurement in a kinematic range, where the DVCS cross section is larger or comparable with that of BH. The ratio of DVCS and BH cross sections behaves like $(1-y)t/(yQ^2)^2$ and at present fixed target experiments BH dominates over DVCS. Another possibility is to measure cross section differences or cross section asymmetries. In the latter case one can assume that the possible systematic effects will be relatively small. At HERMES experiment the DVCS was accessed through measurement of the cross section asymmetries with respect to beam charge, beam polarization and target polarization.

Presently a number of experimental measurements of DVCS are available. The first measurements of beam-helicity asymmetries on a proton target were reported in 2001 by HERMES [Air01] and CLASS [Step01] collaborations. Later, asymmetries with respect to longitudinal [Chen06, Air10a] and transverse [Air08] target polarization, as well as beam charge [Air07b] and, with greater precision, beam helicity [Cam06, Gir08, Gav09, Air09], were also measured on the proton.

The DVCS cross section measurements were performed by collider experiments H1 and ZEUS [Akt05, Che03].

3.4.1 Observables from Scattering off Unpolarized Deuterium

Here we will define the observables for the scattering of longitudinally polarized electron or positron beam from an unpolarized deuterium target. The azimuthal angular dependence of three terms from Eqs. 3.14 - 3.16 for a total leptopruduction cross section in the case of longitudinally polarized lepton beam with polarization P_ℓ and unpolarized target of atomic mass number A read:

$$|\mathcal{T}_{\rm BH}|^2 = \frac{K_{BH}}{\mathcal{P}_1(\phi)\mathcal{P}_2(\phi)} \times \sum_{n=0}^{2} c^{BH}_{n,unp}\cos(n\phi), \tag{3.30}$$

$$|\mathcal{T}_{\rm DVCS}|^2 = K_{DVCS}\Big\{\sum_{n=0}^{2} c^{DVCS}_{n,unp}\cos(n\phi) + P_\ell s^{DVCS}_{1,unp}\sin(\phi)\Big\}, \tag{3.31}$$

$$I = \frac{K_I e_\ell}{\mathcal{P}_1(\phi)\mathcal{P}_2(\phi)}\Big\{\sum_{n=0}^{3} c^{I}_{n,unp}\cos(n\phi) + P_\ell \sum_{n=1}^{2} s^{I}_{n,unp}\sin(n\phi)\Big\}. \tag{3.32}$$

In an above equations we have two sets of coefficient $c^{BH}_{n,unp}$ and $c^{DVCS}_{n,unp}$, which do not represent dependences on either beam polarization or beam charge. The coefficient $s^{DVCS}_{1,unp}$ represents depends on polarization of the beam, while $s^{I}_{n,unp}$ from an interference term represent the dependence on both beam polarization and beam charge. Finally, $c^{I}_{n,unp}$ represent the dependence of the cross section only on beam charge.

One of the observables further discussed in this report is the beam-helicity asymmetry defined either for positron or for electron beams (so called single-charge beam-helicity asymmetry).

$$\mathcal{A}_{\rm LU}(e_\ell,\phi) \equiv \frac{d\sigma^{\rightarrow} - d\sigma^{\leftarrow}}{d\sigma^{\rightarrow} + d\sigma^{\leftarrow}} \tag{3.33}$$

$$= \frac{\frac{K_I e_\ell}{\mathcal{P}_1(\phi)\mathcal{P}_2(\phi)}\Big[\sum_{n=1}^{2} s^{I}_{n,unp}\sin(n\phi)\Big] + K_{DVCS}\, s^{DVCS}_{1,unp}\sin(\phi)}{\frac{1}{\mathcal{P}_1(\phi)\mathcal{P}_2(\phi)}\Big[K_{BH}\sum_{n=0}^{2} c^{BH}_{n,unp}\cos(n\phi) + e_\ell K_I \sum_{n=0}^{3} c^{I}_{n,unp}\cos(n\phi)\Big] + K_{DVCS}\sum_{n=0}^{2} c^{DVCS}_{n,unp}\cos(n\phi)}$$

Here, the arrows $\rightarrow$ ($\leftarrow$) denote the positive (negative) beam helicity. The $d\sigma^{\rightarrow}$ and $d\sigma^{\leftarrow}$ in Eq. 3.33 are the cross sections (or normalized yields) of scattering a longitudinally polarized lepton beam with given charge and helicity on au unpolarized target. Due to the fact that this asymmetry is defined for given beam charge, it contains in denominator the coefficients $c^{I}_{n,unp}$. In the numerator both coefficients $s^{I}_{n,unp}$ and $s^{DVCS}_{1,unp}$ contribute.

In order to provide a cleaner access to coefficients $s^{I}_{n,unp}$ and $s^{DVCS}_{1,unp}$, it is possible to define the beam helicity asymmetries with combination of charge, so called charge-difference beam-helicity asymmetry and charge-averaged beam helicity asymmetry, which read

$$\mathcal{A}^{\rm I}_{\rm LU}(\phi) \equiv \frac{\big[d\sigma^{+\rightarrow} + d\sigma^{-\leftarrow}\big] - \big[d\sigma^{-\rightarrow} + d\sigma^{+\leftarrow}\big]}{\big[d\sigma^{+\rightarrow} + d\sigma^{-\leftarrow}\big] + \big[d\sigma^{-\rightarrow} + d\sigma^{+\leftarrow}\big]} \tag{3.34}$$

$$= \frac{-\frac{K_I}{\mathcal{P}_1(\phi)\mathcal{P}_2(\phi)}\Big[\sum_{n=1}^{2} s^{I}_{n,unp}\sin(n\phi)\Big]}{\frac{K_{BH}}{\mathcal{P}_1(\phi)\mathcal{P}_2(\phi)}\Big[\sum_{n=0}^{2} c^{BH}_{n,unp}\cos(n\phi)\Big] + K_{DVCS}\sum_{n=0}^{2} c^{DVCS}_{n,unp}\cos(n\phi)},$$

$$\mathcal{A}_{\rm LU}^{\rm DVCS}(\phi) \equiv \frac{\left[d\sigma^{+\rightarrow} + d\sigma^{+\rightarrow}\right] - \left[d\sigma^{-\leftarrow} + d\sigma^{-\leftarrow}\right]}{\left[d\sigma^{+\rightarrow} + d\sigma^{+\rightarrow}\right] + \left[d\sigma^{-\leftarrow} + d\sigma^{-\leftarrow}\right]} \tag{3.35}$$
$$= \frac{K_{DVCS}\, s_{1,unp}^{DVCS} \sin(\phi)}{\frac{K_{BH}}{\mathcal{P}_1(\phi)\mathcal{P}_2(\phi)}\Big[\sum_{n=0}^{2} c_{n,unp}^{BH} \cos(n\phi)\Big] + K_{DVCS} \sum_{n=0}^{2} c_{n,unp}^{DVCS} \cos(n\phi)}.$$

Comparing the asymmetries $\mathcal{A}_{\rm LU}$ and $\mathcal{A}_{\rm LU}^{\rm I}$, one can see that in the latter case we have direct sensitivity to an odd coefficients from interference term in the numerator. The odd coefficient from squared DVCS term $s_{1,unp}^{DVCS}$ now appears in the numerator of $\mathcal{A}_{\rm LU}^{\rm DVCS}$. Such a separation of contributions from interference and squared DCVS terms is possible, when data collected with both beam charges are available. In addition, it is important to mention that the denominators of $\mathcal{A}_{\rm LU}^{\rm I}$ and $\mathcal{A}_{\rm LU}^{\rm DVCS}$ differ from that of $\mathcal{A}_{\rm LU}$. In a latter case there exists an additional contribution from pure charge dependent part of the cross section in terms of $c_{n,unp}^{I}$ coefficients.

Presence of data with both beam charges allows to measure one more asymmetry with respect to beam charge

$$\mathcal{A}_{\rm C}(\phi) \equiv \frac{\left[d\sigma^{+\rightarrow} + d\sigma^{+\leftarrow}\right] - \left[d\sigma^{-\rightarrow} + d\sigma^{-\leftarrow}\right]}{\left[d\sigma^{+\rightarrow} + d\sigma^{+\leftarrow}\right] + \left[d\sigma^{-\rightarrow} + d\sigma^{-\leftarrow}\right]} \tag{3.36}$$
$$= \frac{-\frac{K_I}{\mathcal{P}_1(\phi)\mathcal{P}_2(\phi)}\Big[\sum_{n=0}^{3} c_{n,unp}^{I} \cos(n\phi)\Big]}{\frac{K_{BH}}{\mathcal{P}_1(\phi)\mathcal{P}_2(\phi)}\Big[\sum_{n=0}^{2} c_{n,unp}^{BH} \cos(n\phi)\Big] + K_{DVCS} \sum_{n=0}^{2} c_{n,unp}^{DVCS} \cos(n\phi)},$$

which is defined as a cross section difference between opposite beam charges, averaged over beam polarizations. This asymmetry is sensitive to $c_{n,unp}^{I}$ coefficients from interference, and in contrast to beam-helicity asymmetries, contains a cosinusoidal modulation in the numerator. Note that Fourier decomposition of squared BH, DVCS and interference terms for unpolarized targets is independent of target particle. The specific features of various targets appear later in the treatment of Fourier coefficients in terms of nucleon or nucleus electromagnetic form factors and Compton form factors.

In general expression of the azimuthal dependence of the cross section from Eqs. 3.14 - 3.16, the Fourier coefficients c_0^I, c_1^I, s_1^I and c_0^{DVCS} arise at twist-two level, while the rest harmonics from squared DVCS and interference term appear at twist-three level or from twist-two gluon GPDs. In addition they can be affected by twist-four quark GPDs. Meanwhile the coefficients from squared BH term can be exactly calculated, and as an example the t dependences of various coefficients from squared BH term are shown in the left side plot of Figure 3.4. They were evaluated for the proton at the typical kinematics of HERMES experiment $Q^2 = 2.5\,GeV^2$, $x_B = 0.1$. Figure 3.4 shows, that the dominant contribution to the squared BH term originates from coefficient c_0^{BH}. Same holds true also for deuteron (not shown here). Therefore, the above defined asymmetries at leading twist approximation can be simplified to

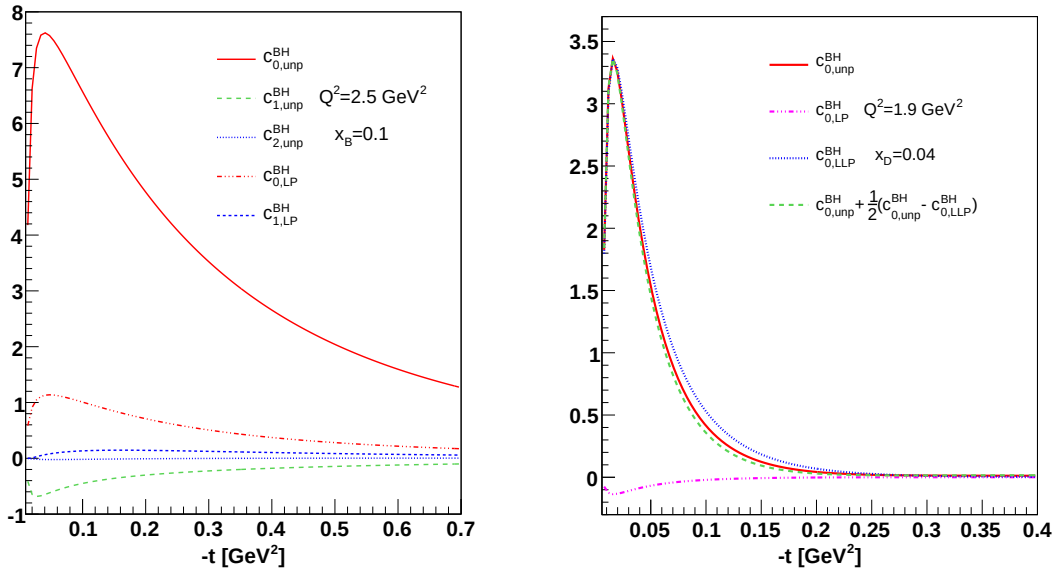

Figure 3.4: On the left side the $-t$ dependences of Fourier coefficients from squared BH term for proton at kinematics $x_B = 0.1$, $Q^2 = 2.5\,GeV^2$. On the right side the $-t$ dependences of Fourier coefficients from squared BH term for deuteron at kinematics $x_D = 0.04$, $Q^2 = 1.9\,GeV^2$.

$$\mathcal{A}^{\mathrm{I}}_{\mathrm{LU}}(\phi) \approx -\frac{K_I s^I_{1,unp}\sin(\phi)}{K_{BH}c^{BH}_{0,unp}} \tag{3.37}$$

$$\mathcal{A}_{\mathrm{C}}(\phi) \approx -\frac{K_I(c^I_{0,unp}+c^I_{1,unp}\cos(\phi))}{K_{BH}c^{BH}_{0,unp}} \tag{3.38}$$

$$\mathcal{A}^{\mathrm{DVCS}}_{\mathrm{LU}}(\phi) \approx \frac{K_{DVCS}s^{DVCS}_{1,unp}\sin(\phi)}{\frac{K_{BH}}{\mathcal{P}_1(\phi)\mathcal{P}_2(\phi)}c^{BH}_{0,unp}}\,. \tag{3.39}$$

The asymmetry $\mathcal{A}^{\mathrm{DVCS}}_{\mathrm{LU}}$ is sensitive to the twist-three contributions and therefore is expected to be small in magnitude, and in addition it will provide a measure of possible contributions from higher twist effects. A simplified expression can be written also for the single-charge beam-helicity asymmetry $\mathcal{A}_{\mathrm{LU}}$. In this particular case, an additional contributions from leading twist coefficients $c^I_{0,unp}$ and $c^I_{1,unp}$ to the denominator of the asymmetry are not expected to be negligible. Nevertheless, within the assumption that the dominant contribution to denominator of the asymmetry $\mathcal{A}_{\mathrm{LU}}$ (see Eq. 3.33) arises from $c^{BH}_{0,unp}$ coefficient, a trivial relation between beam-helicity asymmetries can be deduced

$$\mathcal{A}_{\mathrm{LU}} \approx e_\ell \mathcal{A}^{\mathrm{I}}_{\mathrm{LU}} + \mathcal{A}^{\mathrm{DVCS}}_{\mathrm{LU}}\,. \tag{3.40}$$

3.4.2 Observables from Scattering off Longitudinally Polarized Deuterium

Longitudinal polarization of the target provides an additional degree of freedom in the azimuthal decomposition of the cross section. It allows to access the target polarization

dependent parts of the cross section through measurements of various asymmetries with respect to target polarization. There are certain observables that can be measured on spin-1 targets and have no analogues for spin-1/2 targets. The latter is due to the completely different spin structure of spin-1 particles compared with that of spin-1/2 particles.

In order to emphasize the dependence of the cross section on polarization of deuteron, one needs to apply the decomposition of Fourier coefficients from Eq. 3.20 separately to BH, DVCS and interference terms from Eqs. 3.14 - 3.16. It is important to take into account, that in the real experiment the polarized deuterium target contains a mixture of all $\Lambda = \pm 1, 0$ states, hence the cross sections should be weighted with an appropriate populations of the spin states n^+, n^- and n^0

$$\sigma_{pol} = \sigma(\Lambda = 1)n^+ + \sigma(\Lambda = -1)n^- + \sigma(\Lambda = 0)n^0. \tag{3.41}$$

This yield in the following decompositions of the reaction amplitude for spin-1 deuteron

$$\begin{aligned}
|\mathcal{T}_{\rm BH}|^2 = \frac{K_{\rm BH}}{\mathcal{P}_1(\phi)\mathcal{P}_2(\phi)}\Bigg\{ & \sum_{n=0}^{2} c^{\rm BH}_{n,\rm unp}\cos(n\phi) \\
& + P_z\left[P_\ell \sum_{n=0}^{1} c^{\rm BH}_{n,\rm LP}\cos(n\phi)\right] + \frac{1}{2}P_{zz}\left[\sum_{n=0}^{2}(c^{\rm BH}_{n,\rm unp} - c^{\rm BH}_{n,\rm LLP})\cos(n\phi)\right]\Bigg\},
\end{aligned} \tag{3.42}$$

$$\begin{aligned}
|\mathcal{T}_{\rm DVCS}|^2 = K_{\rm DVCS}\Bigg\{ & \sum_{n=0}^{2} c^{\rm DVCS}_{n,\rm unp}\cos(n\phi) + P_\ell\, s^{\rm DVCS}_{1,\rm unp}\sin\phi \\
& + P_z\left[P_\ell \sum_{n=0}^{1} c^{\rm DVCS}_{n,\rm LP}\cos(n\phi) + \sum_{n=1}^{2} s^{\rm DVCS}_{n,\rm LP}\sin(n\phi)\right] \\
& + \frac{1}{2}P_{zz}\left[\sum_{n=0}^{2}(c^{\rm DVCS}_{n,\rm unp} - c^{\rm DVCS}_{n,\rm LLP})\cos(n\phi) + P_\ell\,(s^{\rm DVCS}_{1,\rm unp} - s^{\rm DVCS}_{1,\rm LLP})\sin\phi\right]\Bigg\},
\end{aligned} \tag{3.43}$$

$$\begin{aligned}
\mathrm{I} = -\frac{K_{\rm I} e_\ell}{\mathcal{P}_1(\phi)\mathcal{P}_2(\phi)}\Bigg\{ & \sum_{n=0}^{3} c^{\rm I}_{n,\rm unp}\cos(n\phi) + P_\ell \sum_{n=1}^{2} s^{\rm I}_{n,\rm unp}\sin(n\phi) \\
& + P_z\left[P_\ell \sum_{n=0}^{3} c^{\rm I}_{n,\rm LP}\cos(n\phi) + \sum_{n=1}^{3} s^{\rm I}_{n,\rm LP}\sin(n\phi)\right] \\
& + \frac{1}{2}P_{zz}\left[\sum_{n=0}^{3}(c^{\rm I}_{n,\rm unp} - c^{\rm I}_{n,\rm LLP})\cos(n\phi) + P_\ell \sum_{n=1}^{2}(s^{\rm I}_{n,\rm unp} - s^{\rm I}_{n,\rm LLP})\sin(n\phi)\right]\Bigg\}.
\end{aligned} \tag{3.44}$$

A similar decomposition can be obtained for longitudinally polarized spin-1/2 nucleons requiring the $P_{zz} = 0$. For further definitions of the observables it is convenient to introduce the following notations: $\rightarrow$ ($\leftarrow$) to denote positive (negative) beam helicity and $\Rightarrow$ ($\Leftarrow$) to denote the vector polarization direction of deuteron target parallel (anti-parallel) to the beam momentum direction in the target rest frame.

As in the case of unpolarized target, here also one can define combined asymmetries. First we define asymmetries with respect to beam and target polarizations for the given beam charge. According to Eqs. 3.42 - 3.44 , the cross section for the production of real photon by an unpolarized positrons on a tensor polarized deuterium target with vanishing vector polarization is given by

$$d\sigma_{\mathrm{U}^{\Leftarrow}_{\Rightarrow}}(e_\ell = +1, P_{zz}, \phi) \equiv \frac{1}{4}\left[d\sigma^{\vec{\Rightarrow}+} + d\sigma^{\vec{\Leftarrow}+} + d\sigma^{\vec{\Rightarrow}+} + d\sigma^{\vec{\Leftarrow}+}\right] \tag{3.45}$$

$$= K_0\Bigg\{\frac{K_{BH}}{\mathcal{P}_1(\phi)\mathcal{P}_2(\phi)}\left[\sum_{n=0}^{2} c^{BH}_{n,\mathrm{unp}}\cos(n\phi) + \frac{1}{2}P_{zz}\sum_{n=0}^{2}(c^{BH}_{n,\mathrm{unp}} - c^{BH}_{n,LLP})\cos(n\phi)\right]$$

$$+ K_{DVCS}\left[\sum_{n=0}^{2} c^{DVCS}_{n,\mathrm{unp}}\cos(n\phi) + \frac{1}{2}P_{zz}\sum_{n=0}^{2}(c^{DVCS}_{n,\mathrm{unp}} - c^{DVCS}_{n,LLP})\cos(n\phi)\right]$$

$$- \frac{K_I}{\mathcal{P}_1(\phi)\mathcal{P}_2(\phi)}\left[\sum_{n=0}^{3} c^{I}_{n,\mathrm{unp}}\cos(n\phi) + \frac{1}{2}P_{zz}\sum_{n=0}^{3}(c^{I}_{n,\mathrm{unp}} - c^{I}_{n,LLP})\cos(n\phi)\right]\Bigg\},$$

where $K_0 = \frac{x_D e^6}{32(2\pi)^4 Q^4\sqrt{1+\epsilon^2}}$ is a common kinematic factor. One of the most interesting observables is the bem-helicity-averaged target-spin asymmetry

$$\mathcal{A}_{\mathrm{UL}}(e_\ell = +1, P_{zz}, \phi) \equiv \frac{\left[d\sigma^{\vec{\Rightarrow}+} + d\sigma^{\vec{\Rightarrow}+}\right] - \left[d\sigma^{\vec{\Leftarrow}+} + d\sigma^{\vec{\Leftarrow}+}\right]}{\left[d\sigma^{\vec{\Rightarrow}+} + d\sigma^{\vec{\Rightarrow}+}\right] + \left[d\sigma^{\vec{\Leftarrow}+} + d\sigma^{\vec{\Leftarrow}+}\right]} \tag{3.46}$$

$$= \frac{K_0}{\sigma_{\mathrm{U}^{\Leftarrow}_{\Rightarrow}}(e_\ell = +1, P_{zz}, \phi)}\left\{K_{DVCS}\sum_{n=1}^{2} s^{DVCS}_{n,LP}\sin(n\phi) - \frac{K_I}{\mathcal{P}_1(\phi)\mathcal{P}_2(\phi)}\sum_{n=1}^{3} s^{I}_{n,LP}\sin(n\phi)\right\}.$$

The numerator of this asymmetry is sensitive to both interference and squared DVCS terms, while the denominator contains an additional Fourier coefficients, ascribed by 'LLP'. These additional coefficients are relevant only for spin-1 targets and they vanish when one defines a similar asymmetry for spin-1/2. Together with target-spin asymmetry one can define also double-spin asymmetry as a difference between cross sections with parallel and antiparallel spin orientations of target and beam

$$\mathcal{A}_{\mathrm{LL}}(e_\ell = +1, P_{zz}, \phi) \equiv \frac{\left[d\sigma^{\vec{\Rightarrow}+} + d\sigma^{\vec{\Leftarrow}+}\right] - \left[d\sigma^{\vec{\Leftarrow}+} + d\sigma^{\vec{\Rightarrow}+}\right]}{\left[d\sigma^{\vec{\Rightarrow}+} + d\sigma^{\vec{\Leftarrow}+}\right] + \left[d\sigma^{\vec{\Leftarrow}+} + d\sigma^{\vec{\Rightarrow}+}\right]} \tag{3.47}$$

$$= \frac{K_0}{\sigma_{\mathrm{U}^{\Leftarrow}_{\Rightarrow}}(e_\ell = +1, P_{zz}, \phi)}\Bigg\{\frac{K_{BH}}{\mathcal{P}_1(\phi)\mathcal{P}_2(\phi)}\sum_{n=0}^{1} c^{BH}_{n,LP} cos(n\phi) + K_{DVCS}\sum_{n=0}^{1} c^{DVCS}_{n,LP} cos(n\phi)$$

$$- \frac{K_I}{\mathcal{P}_1(\phi)\mathcal{P}_2(\phi)}\sum_{n=0}^{2} c^{I}_{n,LP} cos(n\phi)\Bigg\}.$$

In contrast to all other asymmetries, the double-spin asymmetry is the only one which contains in the numerator a contribution from squared BH term together with contributions from interference and squared DVCS terms. That is due to the fact that time reversal and parity conservation lows does not allow for BH process to contribute in beam-charge or single beam(target)-spin asymmetries, but only in double-spin asymmetry. The above mentioned asymmetries can be obtained for both spin-1/2 and spin-1 targets, while there are certain asymmetries which can be defined only for spin-1 target. They may be classified according to whether the cross section for $\Lambda = 0$ appears explicitly in the definition of this asymmetries or not. An example of such an asymmetry is the so-called incomplete beam-helicity asymmetry, defined as

$$\mathcal{A}_{\overleftarrow{\Rightarrow}}(e_\ell=+1,P_{zz},\phi) \equiv \frac{\left[d\sigma^{\overrightarrow{\Rightarrow}+}+d\sigma^{\overleftarrow{\Leftarrow}+}\right]-\left[d\sigma^{\overleftarrow{\Rightarrow}+}+d\sigma^{\overleftarrow{\Leftarrow}+}\right]}{\left[d\sigma^{\overrightarrow{\Rightarrow}+}+d\sigma^{\overleftarrow{\Leftarrow}+}\right]+\left[d\sigma^{\overleftarrow{\Rightarrow}+}+d\sigma^{\overleftarrow{\Leftarrow}+}\right]} \tag{3.48}$$

$$= \frac{K_0}{\sigma_{\mathrm{U}\overleftarrow{\Rightarrow}}(e_\ell=+1,P_{zz},\phi)}\Bigg\{K_{DVCS}\Big[s^{DVCS}_{1,\mathrm{unp}}\sin\phi+\frac{1}{2}P_{zz}\,(s^{DVCS}_{1,\mathrm{unp}}-s^{DVCS}_{1,LLP})\sin\phi\Big]$$

$$-\frac{K_I}{\mathcal{P}_1(\phi)\mathcal{P}_2(\phi)}\Big[\sum_{n=1}^{2}s^I_{n,\mathrm{unp}}\sin(n\phi)+\frac{1}{2}P_{zz}\sum_{n=1}^{2}(s^I_{n,\mathrm{unp}}-s^I_{n,LLP})\sin(n\phi)\Big]\Bigg\},$$

where compared with the similar beam-helicity asymmetry defined for unpolarized target $\mathcal{A}^{\mathrm{I}}_{\mathrm{LU}}$, an additional terms appear in both numerator and denominator of the asymmetry $\mathcal{A}_{\overleftarrow{\Rightarrow}}$. These terms, ascribed by 'LLP' are relevant to tensor effects in a spin-1 deuteron. As in the case of asymmetries from unpolarized target, one can write a simplified expressions also for the above defined asymmetries $\mathcal{A}_{\mathrm{UL}}$, $\mathcal{A}_{\mathrm{LL}}$ and $\mathcal{A}_{\mathrm{L}\overleftarrow{\Rightarrow}}$:

$$\mathcal{A}_{\mathrm{UL}}(e_\ell=+1,P_{zz},\phi)\approx -\frac{K_I s^I_{1,LP}\sin(\phi)}{K_{BH}\Big[c^{BH}_{0,unp}+\frac{1}{2}P_{zz}(c^{BH}_{0,unp}-c^{BH}_{0,LLP})\Big]}, \tag{3.49}$$

$$\mathcal{A}_{\mathrm{LL}}(e_\ell=+1,P_{zz},\phi)\approx \frac{\Big[K_{BH}c^{BH}_{0,LP}-K_I c^I_{0,LP}\Big]+\Big[K_{BH}c^{BH}_{1,LP}-K_I c^I_{1,LP}\Big]\cos(\phi)}{K_{BH}\Big[c^{BH}_{0,unp}+\frac{1}{2}P_{zz}(c^{BH}_{0,unp}-c^{BH}_{0,LLP})\Big]}, \tag{3.50}$$

$$\mathcal{A}_{\mathrm{L}\overleftarrow{\Rightarrow}}(e_\ell=+1,P_{zz},\phi)\approx -\frac{K_I\Big[s^I_{1,unp}+\frac{1}{2}P_{zz}(s^I_{1,unp}-s^I_{1,LLP})\Big]\sin(\phi)}{K_{BH}\Big[c^{BH}_{0,unp}+\frac{1}{2}P_{zz}(c^{BH}_{0,unp}-c^{BH}_{0,LLP})\Big]}. \tag{3.51}$$

Here we neglect the contributions appearing from non-leading twist coefficients and in addition also from the leading twist coefficients in the denominator of asymmetries, i.e. in Eq. 3.45. As can be seen from the right side plot of Figure 3.4, the contribution from Fourier coefficient $c^{BH}_{0,LLP}$ is compatible with that of $c^{BH}_{0,unp}$, therefore they can not be neglected. It is expected that also the contributions from coefficients $c^I_{0,LLP}$, $c^1_{1,LLP}$ and $s^I_{1,LLP}$ are not necessarily small. The Fourier coefficients from squared BH term shown in the right side plot of Figure 3.4 were evaluated according to their representation through electromagnetic form factors of deuteron given in [KM04].

The three asymmetries $\mathcal{A}_{\overleftarrow{\Rightarrow}}$, $\mathcal{A}_{\mathrm{UL}}$, and $\mathcal{A}_{\mathrm{LL}}$ with respect to beam helicity and target vector polarization were defined for a single beam charge. This dependence for a particular case of positron beam is encoded in the negative sign of the contribution from interference term to the asymmetries in Eqs. 3.46 - 3.48. In order to extract more information on various combinations of Fourier coefficients, it is possible to use data collected with negative polarization of the electron beam in conjunction with the subset of positron data with the same sign of the beam polarization. In this case, another set of Fourier coefficients can be accessed through single-beam-helicity asymmetries $\mathcal{A}_{\overset{\mathrm{C}}{\leftarrow}\overleftarrow{\Rightarrow}}(P_\ell,P_{zz},\phi)$, $\mathcal{A}_{\overset{\mathrm{C}}{\leftarrow}\mathrm{L}}(P_\ell,P_{zz},\phi)$ and $\mathcal{A}_{\overset{0}{\leftarrow}\mathrm{L}}(P_\ell,P_{zz},\phi)$, which are defined with respect to the beam charge and longitudinal vector polarization of the deuterium target. Here, the subscript $\overset{\mathrm{C}}{\leftarrow}\overleftarrow{\Rightarrow}$ indicates the charge asymmetry for a lepton beam with only negative polarization on a longitudinally polarized deuterium target with vanishing net vector polarization. The subscript $\overset{0}{\leftarrow}\mathrm{L}$ indicates the asymmetry with respect to longitudinal vector target polarization for a charge-averaged lepton beam with negative beam polarization. The subscript $\overset{\mathrm{C}}{\leftarrow}\mathrm{L}$ indicates the double

asymmetry with respect to the lepton charge and longitudinal vector polarization of the target. Denoting the cross section for the production of real photons by a charge averaged lepton beam with a single helicity on a tensor polarized deuterium target with vanishing vector polarization as

$$\begin{aligned}\sigma_{\substack{\mathrm{C}\\ \leftarrow\\ \Rightarrow}}(P_\ell,P_{zz},\phi) &\equiv \frac{1}{4}\left[\mathrm{d}\sigma^{\substack{\leftarrow\\ \Rightarrow}+} + \mathrm{d}\sigma^{\substack{\leftarrow\\ \Leftarrow}+} + \mathrm{d}\sigma^{\substack{\leftarrow\\ \Rightarrow}-} + \mathrm{d}\sigma^{\substack{\leftarrow\\ \Leftarrow}-}\right] \\ &= K_0\Bigg\{\frac{K_{BH}}{\mathcal{P}_1(\phi)\mathcal{P}_2(\phi)}\Bigg\{\sum_{n=0}^{2} c^{BH}_{n,\mathrm{unp}}\cos(n\phi) + \frac{1}{2}P_{zz}\sum_{n=0}^{2}(c^{BH}_{n,\mathrm{unp}} - c^{BH}_{n,LLP})\cos(n\phi)\Bigg\} \\ &\quad + K_{DVCS}\Bigg\{\sum_{n=0}^{2} c^{DVCS}_{n,\mathrm{unp}}\cos(n\phi) + P_\ell\sum_{n=1}^{2} s^{DVCS}_{n,\mathrm{unp}}\sin(n\phi) \\ &\quad + \frac{1}{2}P_{zz}\Bigg[\sum_{n=0}^{2}(c^{DVCS}_{n,\mathrm{unp}} - c^{DVCS}_{n,LLP})\cos(n\phi) + P_\ell\sum_{n=1}^{2}(s^{DVCS}_{n,\mathrm{unp}} - s^{DVCS}_{n,LLP})\sin(n\phi)\Bigg]\Bigg\}\Bigg\},\end{aligned} \tag{3.52}$$

the single-helicity beam-charge asymmetry $\mathcal{A}_{\substack{\mathrm{C}\\ \leftarrow\\ \Rightarrow}}(P_\ell, P_{zz}, \phi)$ can be defined as a difference between cross sections for positrons and electrons averaged over the longitudinal vector polarization of the target for scattering of a negatively polarized beam

$$\begin{aligned}\mathcal{A}_{\substack{\mathrm{C}\\ \leftarrow\\ \Rightarrow}}(P_\ell, P_{zz}, \phi) &\equiv \frac{\left[d\sigma^{\substack{\leftarrow\\ \Rightarrow}+} + d\sigma^{\substack{\leftarrow\\ \Leftarrow}+}\right] - \left[d\sigma^{\substack{\leftarrow\\ \Rightarrow}-} + d\sigma^{\substack{\leftarrow\\ \Leftarrow}-}\right]}{\left[d\sigma^{\substack{\leftarrow\\ \Rightarrow}+} + d\sigma^{\substack{\leftarrow\\ \Leftarrow}+}\right] + \left[d\sigma^{\substack{\leftarrow\\ \Rightarrow}-} + d\sigma^{\substack{\leftarrow\\ \Leftarrow}-}\right]} \\ &= \frac{K_0}{\mathrm{d}\sigma_{\substack{\mathrm{C}\\ \leftarrow\\ \Rightarrow}}(P_\ell, P_{zz}, \phi)} \times \Bigg\{ - \frac{K_I}{\mathcal{P}_1(\phi)\mathcal{P}_2(\phi)}\Bigg\{\sum_{n=0}^{3} c^{I}_{n,\mathrm{unp}}\cos(n\phi) + P_\ell\sum_{n=1}^{2} s^{I}_{n,\mathrm{unp}}\sin(n\phi) \\ &\quad + \frac{1}{2}P_{zz}\Bigg[\sum_{n=0}^{3}(c^{I}_{n,\mathrm{unp}} - c^{I}_{n,LLP})\cos(n\phi) + P_\ell\sum_{n=1}^{2}(s^{I}_{n,\mathrm{unp}} - s^{I}_{n,LLP})\sin(n\phi)\Bigg]\Bigg\}\Bigg\}.\end{aligned} \tag{3.53}$$

The single-helicity charge-averaged target-spin asymmetry $\mathcal{A}_{\substack{0\\ \leftarrow\\ \mathrm{L}}}(P_\ell, P_{zz}, \phi)$ is defined as a difference between cross sections of scattering a negatively polarized lepton beam off a positively and negatively vector polarized deuterium target, averaged over both beam charges

$$\begin{aligned}\mathcal{A}_{\substack{0\\ \leftarrow\\ \mathrm{L}}}(P_\ell, P_{zz}, \phi) &\equiv \frac{\left[\sigma^{\substack{\leftarrow\\ \Rightarrow}+} + \sigma^{\substack{\leftarrow\\ \Rightarrow}-}\right] - \left[\sigma^{\substack{\leftarrow\\ \Leftarrow}+} + \sigma^{\substack{\leftarrow\\ \Leftarrow}-}\right]}{\left[\sigma^{\substack{\leftarrow\\ \Rightarrow}+} + \sigma^{\substack{\leftarrow\\ \Rightarrow}-}\right] + \left[\sigma^{\substack{\leftarrow\\ \Leftarrow}+} + \sigma^{\substack{\leftarrow\\ \Leftarrow}-}\right]} \\ &= \frac{K_0}{\mathrm{d}\sigma_{\substack{\mathrm{C}\\ \leftarrow\\ \Rightarrow}}(P_\ell, P_{zz}, \phi)} \times \Bigg\{\frac{K_{BH}}{\mathcal{P}_1(\phi)\mathcal{P}_2(\phi)}\Big\{P_\ell\sum_{n=0}^{1} c^{BH}_{n,LP}\cos(n\phi)\Big\} \\ &\quad + K_{DVCS}\Big\{P_\ell\sum_{n=0}^{1} c^{DVCS}_{n,LP}\cos(n\phi) + \sum_{n=1}^{2} s^{DVCS}_{n,LP}\sin(n\phi)\Big\}\Bigg\}.\end{aligned} \tag{3.54}$$

And finally the single-helicity charge-difference target-spin asymmetry $\mathcal{A}_{\substack{\mathrm{C}\\ \leftarrow\\ \mathrm{L}}}(P_\ell, P_{zz}, \phi)$ is defined as:

$$\begin{aligned}\mathcal{A}_{\substack{\mathrm{C}\\ \leftarrow\\ \mathrm{L}}}(P_\ell, P_{zz}, \phi) &\equiv \frac{\left[\sigma^{\substack{\leftarrow\\ \Rightarrow}+} + \sigma^{\substack{\leftarrow\\ \Leftarrow}+}\right] - \left[\sigma^{\substack{\leftarrow\\ \Rightarrow}-} + \sigma^{\substack{\leftarrow\\ \Leftarrow}-}\right]}{\left[\sigma^{\substack{\leftarrow\\ \Rightarrow}+} + \sigma^{\substack{\leftarrow\\ \Leftarrow}+}\right] + \left[\sigma^{\substack{\leftarrow\\ \Rightarrow}-} + \sigma^{\substack{\leftarrow\\ \Leftarrow}-}\right]} \\ &= \frac{K_0}{\mathrm{d}\sigma_{\substack{\mathrm{C}\\ \leftarrow\\ \Rightarrow}}(P_\ell, P_{zz}, \phi)} \times \Bigg\{ - \frac{K_I}{\mathcal{P}_1(\phi)\mathcal{P}_2(\phi)}\Big\{P_\ell\sum_{n=0}^{2} c^{I}_{n,LP}\cos(n\phi) + \sum_{n=1}^{3} s^{I}_{n,LP}\sin(n\phi)\Big\}\Bigg\}.\end{aligned} \tag{3.55}$$

All the asymmetries defined for longitudinally polarized deuteron depend on tensor polarization of the target P_{zz}, while the single-helicity asymmetries have an additional dependence on beam polarization both in numerator and in denominator. As can be seen from Eqs. 3.53 - 3.55 the beam polarization dependent parts in the numerators of the asymmetries have different azimuthal dependences (even for $\mathcal{A}_{\underset{\leftarrow}{\mathrm{C}}_{\mathrm{L}}}(P_\ell, P_{zz}, \phi)\,, \mathcal{A}_{\underset{\leftarrow}{0}_{\mathrm{L}}}(P_\ell, P_{zz}, \phi)$ and odd for $\mathcal{A}_{\underset{\leftarrow}{\mathrm{C}}\underset{\Rightarrow}{\Leftarrow}}(P_\ell, P_{zz}, \phi)$) compared with beam polarization independent parts. Meanwhile, in the denominator, i.e. Eq. 3.52, mainly the higher twist contributions are sensitive to beam polarization. This feature allows to separate the contributions appearing in the asymmetries from beam polarization dependent and independent parts. Within the leading-order and leading twist approximation the simplified expressions for a single-helicity asymmetries read as:

$$\mathcal{A}_{\underset{\leftarrow}{\mathrm{C}}\underset{\Rightarrow}{\Leftarrow}}(P_\ell, P_{zz}, \phi) \approx -\frac{K_I\Big[c^I_{0,unp} + \frac{1}{2}P_{zz}(c^I_{0,unp} - c^I_{0,LLP})\Big]}{K_{BH}\Big[c^{BH}_{0,unp} + \frac{1}{2}P_{zz}(c^{BH}_{0,unp} - c^{BH}_{0,LLP})\Big]} \tag{3.56}$$
$$-\frac{K_I\Big[c^I_{1,unp} + \frac{1}{2}P_{zz}(c^I_{1,unp} - c^I_{1,LLP})\Big]\cos(\phi) + P_\ell K_I\Big[s^I_{1,unp} + \frac{1}{2}P_{zz}(s^I_{1,unp} - s^I_{1,LLP})\Big]\sin(\phi)}{K_{BH}\Big[c^{BH}_{0,unp} + \frac{1}{2}P_{zz}(c^{BH}_{0,unp} - c^{BH}_{0,LLP})\Big]},$$

$$\mathcal{A}_{\underset{\leftarrow}{0}_{\mathrm{L}}}(P_\ell, P_{zz}, \phi) \approx \frac{K_{BH}P_\ell\Big[c^{BH}_{0,LP} + c^{BH}_{1,LP}\cos(\phi)\Big] + K_{DVCS}s^{DVCS}_{1,LP}\sin(\phi)}{K_{BH}\Big[c^{BH}_{0,unp} + \frac{1}{2}P_{zz}(c^{BH}_{0,unp} - c^{BH}_{0,LLP})\Big]}, \tag{3.57}$$

$$\mathcal{A}_{\underset{\leftarrow}{\mathrm{C}}_{\mathrm{L}}}(P_\ell, P_{zz}, \phi) \approx -\frac{K_I P_\ell\Big[c^I_{0,LP} + c^I_{1,LP}\cos(\phi)\Big] + K_I s^I_{n,LP}\sin(\phi)}{K_{BH}\Big[c^{BH}_{0,unp} + \frac{1}{2}P_{zz}(c^{BH}_{0,unp} - c^{BH}_{0,LLP})\Big]} \tag{3.58}$$

From the comparison of the simplified expressions, one can see that the cosinusoidal modulations in the single-helicity asymmetries $\mathcal{A}_{\underset{\leftarrow}{\mathrm{C}}_{\mathrm{L}}}$, $\mathcal{A}_{\underset{\leftarrow}{0}_{\mathrm{L}}}$ and single-charge double-spin asymmetry $\mathcal{A}_{\mathrm{LL}}$ are not independent.Similarly the sinusoidal harmonics in the asymmetries $\mathcal{A}_{\underset{\leftarrow}{\mathrm{C}}_{\mathrm{L}}}$ and $\mathcal{A}_{\underset{\leftarrow}{0}_{\mathrm{L}}}$ are related to the ones in the single-charge target-spin asymmetry $\mathcal{A}_{\mathrm{UL}}$.

3.5 Relations between asymmetries and Compton form factors

In previous sections various asymmetries were defined, that appear in the azimuthal distributions of the real photons. Azimuthal dependencies of the asymmetries were given through Fourier decomposition of the DVCS/BH cross section. As can be seen from the definition of the asymmetries, their is no direct accesses to certain Fourier coefficient, rather than to their complicated combination. On the other hand the Fourier coefficients themselves have a very complicated relation to Compton Form Factors. Nevertheless within certain assumptions and approximations one can represent a simplified connection between asymmetries and Compton form factors. For the coherent process on the deuteron, the coefficients can be expanded in powers of x_D, the Bjorken variable for the deuteron target, and $\tau = t/(4M_D^2)$, where M_D is the deuteron mass [KM04]. Since at the HERMES kinematic conditions the average Bjorken variable is $x_D = 0.04$ and the $-t = 0.1\,GeV^2$, one can neglect the contributions proportional to x_D and τ. Then the

leading Fourier coefficients from squared BH and interference term are presented as:

$$\begin{aligned}
\left\{ \begin{array}{c} c^I_{1,unp} \\ s^I_{1,unp} \end{array} \right\} &= \left\{ \begin{array}{c} -8K(2-2y-y^2) \\ 8Ky(2-y) \end{array} \right\} \left\{ \begin{array}{c} \mathcal{R}e \\ \mathcal{I}m \end{array} \right\} \times \frac{1}{9}\Big[G_1(9\mathcal{H}_1 - 6\tau\mathcal{H}_3) + G_3(-6\tau\mathcal{H}_1 + 2\tau\mathcal{H}_5)\Big] \\
\left\{ \begin{array}{c} c^I_{1,LP} \\ s^I_{1,LP} \end{array} \right\} &= \left\{ \begin{array}{c} -8Ky(2-y) \\ 8K(2-2y-y^2) \end{array} \right\} \left\{ \begin{array}{c} \mathcal{R}e \\ \mathcal{I}m \end{array} \right\} \times \frac{1}{6}\Big[6G_1\widetilde{\mathcal{H}}_1 - 6\tau G_3\widetilde{\mathcal{H}}_1\Big] \\
\left\{ \begin{array}{c} c^I_{1,LLP} \\ s^I_{1,LLP} \end{array} \right\} &= \left\{ \begin{array}{c} -8K(2-2y-y^2) \\ 8Ky(2-y) \end{array} \right\} \left\{ \begin{array}{c} \mathcal{R}e \\ \mathcal{I}m \end{array} \right\} \times \frac{1}{3}\Big[G_1(3\widetilde{\mathcal{H}}_1 + 2\widetilde{\mathcal{H}}_5)\Big] \qquad (3.59) \\
c^{BH}_{0,unp} &= \big\{8(2-2y+y^2)\big\} \times \frac{1}{3}\Big[3G_1^2 - 4\tau G_1 G_3\Big] \\
c^{BH}_{0,LLP} &= \big\{8(2-2y+y^2)\big\} \times G_1^2
\end{aligned}$$

Here the terms proportional to G_3 are given up to order $O(\tau)$, because G_3 is about 20 times larger than other form factors and the product τG_3 is not negligible (see Figure 2.4). The complete expressions for the Fourier coefficients are given in [KM04] for deuterium and in [BMK02] for nucleons. Substituting the Eqs. 3.59 into the simplified representation of the asymmetries one can get the approximate relations between asymmetries and Compton form factors. The latters are summarized in Table 3.1.

		Lepton charge			Target population (deuterons)				Beam helicity			
					$\Lambda = +1$		$\Lambda = -1$	$\Lambda = 0$	$\lambda = +1$		$\lambda = -1$	Coherent
		$+1$		-1	$\Rightarrow$		$\Leftarrow$	0	$\rightarrow$		$\leftarrow$	sensitivity
Unpol. traget	$\mathcal{A}_{\mathrm{C}}$	■	−	■					■	+	■	$\Re\mathrm{e}(\mathcal{H}_1)$
	$\mathcal{A}^{\mathrm{I}}_{\mathrm{LU}}$	■	−	■					■	−	■	$\Im\mathrm{m}(\mathcal{H}_1)$
	$\mathcal{A}^{\mathrm{DVCS}}_{\mathrm{LU}}$	■	+	■					■	−	■	h. twist
Single-charge	$\mathcal{A}_{\mathrm{L}\overleftrightarrows}$	■			■	+	■		■	−	■	$\Im\mathrm{m}(\mathcal{H}_1, \mathcal{H}_5)$
	$\mathcal{A}_{\mathrm{UL}}$	■			■	−	■		■	+	■	$\Im\mathrm{m}(\widetilde{\mathcal{H}}_1)$
	$\mathcal{A}_{\mathrm{LL}}$	■			■	−	■		■	−	■	BH+$\Re\mathrm{e}(\widetilde{\mathcal{H}}_1)$
Single-helicity	$\mathcal{A}_{\overleftarrow{\mathrm{C}}\overleftrightarrows}$	■	−	■	■	+	■				■	$\Im\mathrm{m}/\Re\mathrm{e}(\mathcal{H}_1, \mathcal{H}_5)$
	$\mathcal{A}_{\overleftarrow{\mathrm{C}}_{\mathrm{L}}}$	■	−	■	■	−	■				■	$\Im\mathrm{m}/\Re\mathrm{e}(\widetilde{\mathcal{H}}_1)$
	$\mathcal{A}_{\overleftarrow{0}_{\mathrm{L}}}$	■	+	■	■	−	■				■	BH+h. twist

Table 3.1: The sensitivity of the asymmetries on both unpolarized and polarized deuterium target to the corresponding Compton form factors or BH amplitude for coherent scattering. The symbol ■ marks which data taken under certain experimental conditions (beam polarization, beam charge and target polarization state) are available for the construction of the respective asymmetry. The − or + indicates the sign with which the corresponding yield enters the numerator of the asymmetry.

Chapter 4

The HERMES Experiment

The HERMES (HERa MEasurement of Spin) experiment is one of four experiments operated on HERA (Hadron Elektron Ring Anlage) electron/positron-proton collider, located at DESY (Deutsches Elektronen-Synchrotron) in Hamburg, Germany. HERMES is a fixed target experiment and uses only lepton (electron or positron) beam. The longitudinally polarized lepton beam scatters off an internally polarized or unpolarized gas target. The products of scattering are detected in forward spectrometer. The HERMES experiment was designed to investigate the spin structure of nucleon through polarized deep inelastic scattering (DIS). It started operation in 1995 and continued collecting data up to 2007. During its operation HERMES has collected data on an unpolarized Hydrogen, Deuterium, Helium, Nitrogen, Neon, Krypton, Xenon targets in addition with longitudinally polarized Helium-3 and with longitudinally/transversely polarized Hydrogen targets, and longitudinally vector/tensor polarized Deuterium target. In this chapter the HERMES experimental setup will be discussed in details, especially parts relevant for DVCS analysis.

4.1 The Polarized Lepton Beam at HERA

HERA collider consists of two rings with a circumference of $6.3\,km$ (see Figure 4.1). One ring is for protons with energy of $920\,GeV$ and the second for electrons/positrons with energy of $27.57\,GeV$. The typical current of the lepton beam is about $40\,mA$ at injection. It decreases exponentially with the lifetime of about 8 hours. When the beam current decreases to about $10\,mA$, the beam is dumped and the accelerator is refilled. Up to 220 bunches of leptons were injected in the storage ring, with the length of $27\,ps$ and separated by a time interval of $96\,ns$. Each bunch contains about $3.8 \cdot 10^{10}$ leptons.

During operation of HERA, the lepton ring was mostly filled by positrons. Electrons were injected only in 1998, 2005 and some period of 2006. The injected lepton beam is initially unpolarized, i.e the number of leptons with spins aligned parallel to the magnetic field of ring magnets is equal to those aligned anti-parallel. Fortunately the emission of synchrotron radiation of charged particles rotating in the storage ring causes an asymmetric spin-flip of particles, i.e. the probability of spin-flip in one direction is not equal to that in opposite direction. This phenomenon, known as Sokolov-Ternov effect [ST64], leads to a total disbalance of particles with spin orientation 'up' and 'down'. The dependence of this self polarization effect on polarization built-up time can be qualitatively described by

$$P_{ST}(t) = \frac{8}{5\sqrt{3}}(1 - e^{-\frac{t}{\tau_{ST}}})\,, \tag{4.1}$$

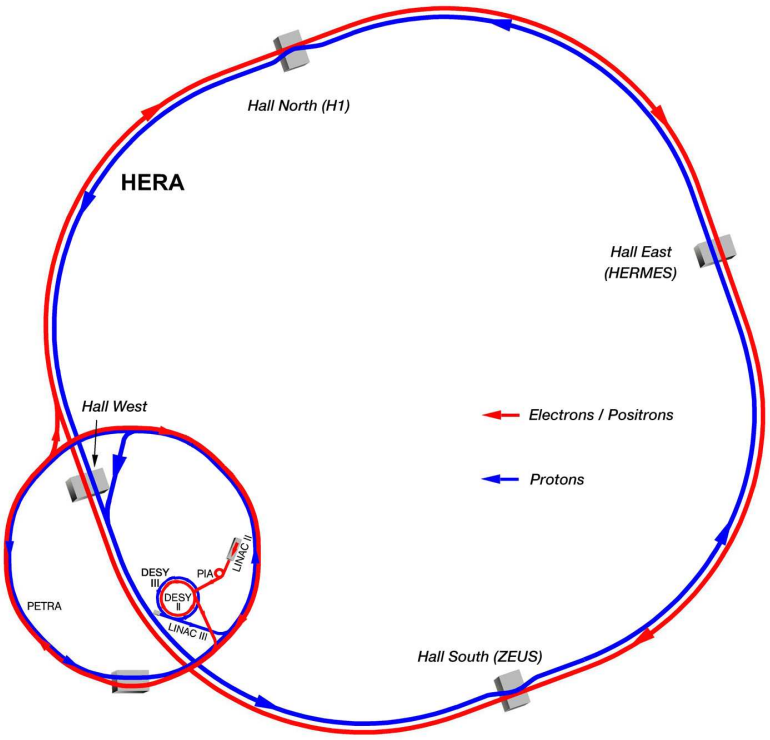

Figure 4.1: The HERA accelerator facility at DESY and its system of preaccelerators, with the location of four experiments (HERMES, H1, ZEUS and HERA-B).

where

$$\tau_{ST} = \frac{8}{5\sqrt{3}} \frac{2\pi m_e \rho^3}{r_e \hbar \gamma^5}. \tag{4.2}$$

Here m_e and r_e are electron mass and Bohr radius, ρ is the bending radius of the orbit and $\gamma = \sqrt{1 - v^2/c^2}$ is the Lorentz factor. For the HERA ring parameters the polarization build-up time is about 25 minutes. The possible maximum polarization value is 92%. For evaluation of the polarization, several depolarizing effects like beam-beam interaction, misalignment of binding magnets and depolarizing resonances, should be taken into account. All the above mentioned depolarizing effects can be described by introducing single time constant τ_D, and the effective polarization can be written as:

$$P_{eff} = \frac{8}{5\sqrt{3}} \frac{\tau_D}{\tau_{ST} + \tau_D}. \tag{4.3}$$

Thus depolarizing effects yield in total decrease of the average polarization of the lepton beam. Despite of the fact that due to the Sokoov-Ternov effect the lepton beam is naturally polarized in the transverse direction, the most interesting observables at HERMES require a longitudinally polarized beam. The longitudinally polarized beam was achieved through spin-rotators, implemented just before and after HERMES experimental setup. They consist of six horizontal and vertical bending dipole magnets. Passing through these magnets the spin vector of the lepton precesses around the magnetic field direction, so that finally the combination of all bending magnets rotates the spin vector of the lepton by 90 degrees. The second spin rotator installed after experimental setup changes the spin direction of the beam particles from longitudinal to transverse, in order to take an advantage of self polarization due to Sokolov-Ternov effect.

The polarization of the beam was continuously monitored during data taking period by two polarimeters. The operation of the polarimeters is based on the asymmetries in the cross section for Compton back-scattering of left and right circularly polarized laser light off the polarized lepton beam. The transverse polarimeter (TPOL) [Bar93] was located in the west side of HERA storage ring, where no spin rotators were implemented.

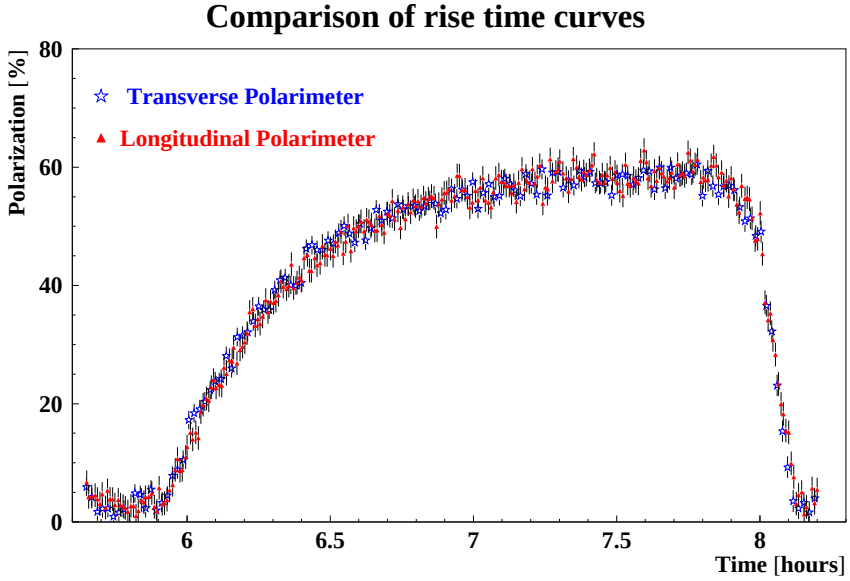

Figure 4.2: Beam polarization values measured by longitudinal and transverse polarimeters

The source of polarized light for the transverse polarimeter is a $10\,W$ argon-ion laser, which provides a continuous photon beam of energy $2.41\,eV$. The linear polarization of the photons is converted into circularly polarized light using a Pockels cell. The beam helicity was switched at a frequency of $90\,Hz$ to reduce any systematic effects. The energies and positions of the backscattered photons are measured by a tungsten scintillator calorimeter situated $65\,m$ downstream from the interaction point. The calorimeter is divided horizontally into two segments, symmetric around lepton plane. Flipping the polarization of photon beam leads to an energy dependent asymmetry in the vertical position of backscattered photons. The polarization can then be determined by the difference in the mean vertical position of left and right circularly polarized light measured in the calorimeter.

At the location of the HERMES experiment in the east hall where the beam is longitudinally polarized, the longitudinal polarimeter was located. For the LPOL [Bec02] a ND:YAG pulse laser was used, providing a photon beam with an energy of $2.33\,eV$. As in the case of TPOL, the linear polarization of the photon beam was converted into circularly polarized one by means of Pockels cell. In the LPOL the backscattered photons were detected by a calorimeter consisting of a 2×2 array of four Cherenkov $NaBi(WO_4)_2$ crystals. An operation of LPOL is based on the measurement of an asymmetry in the energy distribution of the backscattered photons in the calorimeter. This asymmetry is proportional to the longitudinal polarization of the lepton beam and thus provides a measure for the lepton beam polarization.

An example of typical beam polarization rise time curve for the leptons is shown in Figure 4.2.

4.2 The HERMES Target

HERMES experiment was running in parallel with three other experiments on HERA ring, two of them H1 and ZUES being a collider experiments. Hence, it was very important to collect data without significantly reducing the lifetime of the electron/positron beam. This implies certain limitations and requirements on the construction and usage of a target system. At first any usage of target from solid material or other with high areal density was excluded. In addition, for the realization of proposed measurements of deep inelastic scattering from polarized targets it was essential to perform high and stable polarization of the target. For these reasons an internal gas target was chosen. Although the gaseous targets operate with much lower areal density compared to solid material targets, they have also certain advantages. One of them is the small dilution factor and possibility to provide high polarization, which is the key point for the polarization observables. Also the polarization of the gas can be easily flipped within a short time interval of about 2-3 milliseconds, which significantly reduces the systematic uncertainties of the measurements. The schematic view of the HERMES target is shown in Figure 4.3. The main components of it are the atomic beam source (ABS), storage cell, target gas analyzer (TGA) and Brit-Rabi polarimeter. Not shown in the figure is the target magnet, which provides a holding field to define the polarization axis and to prevent spin relaxation by effectively decoupling the magnetic moments of electrons and nucleons.

An additional important feature of gaseous targets is the possibility to detect the re-

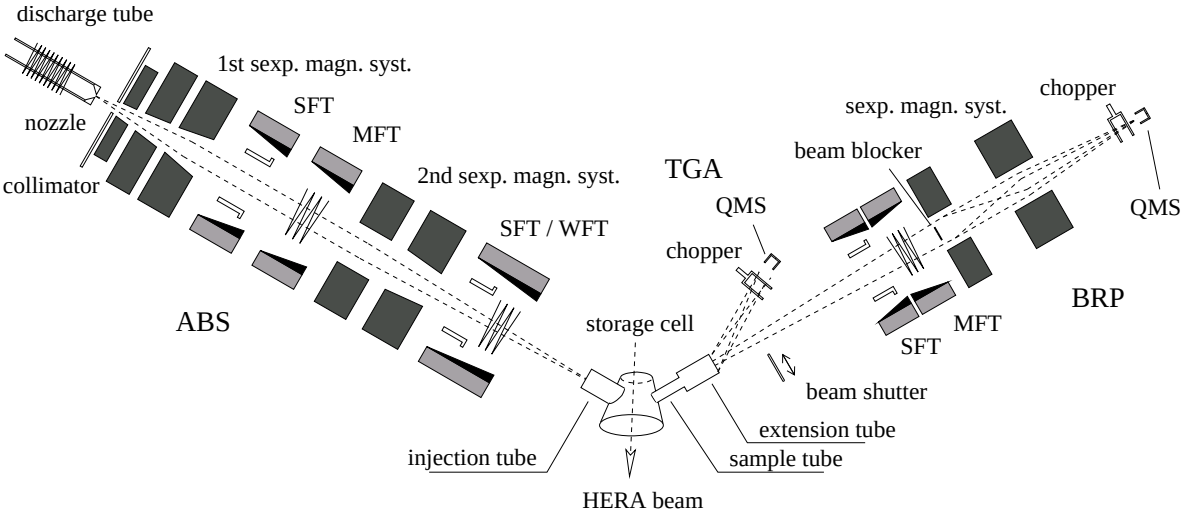

Figure 4.3: The schematic view of HERMES Target.

coiling fragments of the target after interaction. This was done during 2006-2007 data taking period, when the recoil detector was operating. The details about construction and operation of HERMES target can be found in [Air05a]

4.2.1 Atomic Beam Source

The nuclear beams of polarized hydrogen and deuterium atoms were generated by ABS [Nas03]. An operation of ABS is based on Stern-Gerlach separation of hydrogen/deuterium atoms with radio-frequency hyperfine transitions. ABS consists of a dis-

sociator, an atomic beam formation system (a nozzle, a skimmer and a collimator), a sextupole magnet systems to focus atoms with certain electron polarization into the storage cell and several high frequency transition units to transfer the polarization from electrons to nucleons. The schematic view of ABS is shown on the left side of Figure 4.3.

At first the molecular hydrogen or deuterium gas is dissociated by a radio frequency discharge in the glass tube with a dissociation degree up to 80%. The dissociated gas then expands through nozzle into the vacuum of dissociator chamber, supported by a pumping system with a nominal pumping speed of more than 15000 ls^{-1}, which ensures that the scattering of the atomic beam is suppressed. The nozzle is cooled to temperature of 100 K and the water produced during discharge creates an ice layer on the nozzle surface, which helps to prevent recombination.

The atoms of hydrogen/deuterium in the magnetic field can be found in certain hyperfine states. The hyperfine splitting of the states appears due to the interaction of external magnetic field with the magnetic moments of electron and proton/nucleus in the atoms. Taking the magnetic field direction as a quantization axis for the electron spin S and proton spin I, the four possible hyperfine states of hydrogen atom are defined through spin projections of electron $m_s = \pm\frac{1}{2}$ and proton $m_I = \pm\frac{1}{2}$. At weak magnetic field ($B \ll B_C = 11.7\ mT$) S and I couple, and total magnetic moment $F = S + I$ and its projection m_F are used. The dependence of splitting of hydrogen and deuterium as a function of magnetic field is shown in Figure 4.4, with corresponding quantum numbers for each eigenstate. In the case of deuterium atom the hyperfine splitting differs from that of hydrogen. This is due to the nuclear spin $I = 1$. So the total angular momentum is $F = \frac{3}{2}$ or $F = \frac{1}{2}$. Thus in the external magnetic field there are six possible hyperfine states for the deuterium.

In the atomic beam from the dissociator chamber all possible hyperfine states are equally populated. Further passing through sextupole magnet systems, the hydrogen atoms in two spin states $|1>= |+\frac{1}{2}, +\frac{1}{2}$ and $|2>= |+\frac{1}{2}, -\frac{1}{2}$, with the same electron spin and opposite nuclear spin are focused, while the other two states are defocused and pumped out. Further transition between $|1> \rightarrow |3>$ and $|2> \rightarrow |4>$ is obtained by high-frequency transition (HFT) units. Hence, by usage of different combination of HFT units it is possible to populate two states with the same nuclear spin orientation, and finally inject polarized atomic beam into the storage cell. In addition, it is possible to invert the nuclear polarization every 120 seconds. Similar procedure can be applied for deuterium, while in this case the injection mods are different.

4.2.2 The Storage Cell

As was mentioned above, the typical areal density of gaseous targets ($\leq 2 \times 10^{11}$ atoms/cm^2) is much lower from that of solid targets. Nevertheless it is possible to significantly improve the areal density, confining the polarized target atoms in a small volume around the path of the beam, by injecting them into an open-ended storage cell. Such a storage cell was used for HERMES internal gas target [Bau03]. The storage cell was constructed from pure aluminum, 75 μm thick. It had an elliptical cross-section like HERA lepton beam with diameters 29 mm and 9.8 mm. The interior of the cell was coated with drifilm, to minimize the depolarization of the atoms caused by the wall collisions. The spectrometer acceptance limits the usable target length to 400 mm. The polarized atomic beam was injected into a storage cell through feed tube, mounted under 30 °. In addition to feed tube a smaller sampling tube is mounted under 160 °. About 5% of the gas passes through sampling tube to TGA and BRP for further analysis of the gas conditions in the

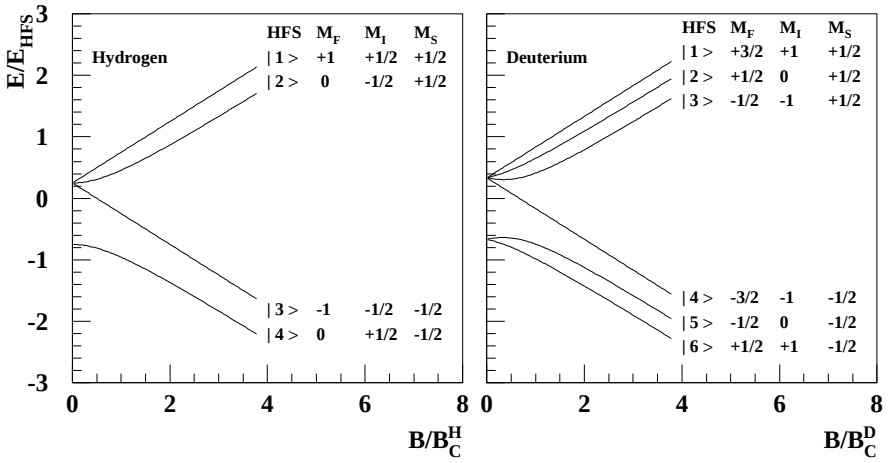

Figure 4.4: The energy splitting of hyperfine-levels for hydrogen and deuterium as a function of the magnetic field. For deuterium $E_{HFS} = 1.35 \cdot 10^{-6} eV$ and $B_C = 11.7 mT$.

storage cell.

Under typical running conditions the flux of $6.6\,(5.0) \times 10^{16}$ atoms/s of polarized hydrogen (deuterium) was injected into a storage cell and the areal density of $7.6 \times 10^{13}\,(2.1 \times 10^{14})$ nucleons/cm^2 was achieved for hydrogen (deuterium). During the operation the storage cell was cooled to a temperature of $100\,(60)\,K$ for hydrogen (deuterium), which suppresses the recombination and spin relaxation during wall collisions. The target was cooled by pumping cold helium gas through the cooling rails. Storage cell with its supporting cooling rails was build in a target chamber (see Figure 4.5), surrounded by superconducting magnet. The pressure in a target chamber was kept in a $10^{-7} mbar$ range by turbo pumping system.

A $0.3\,mm$ thick stainless steel exit window on the downstream end of the target cham-

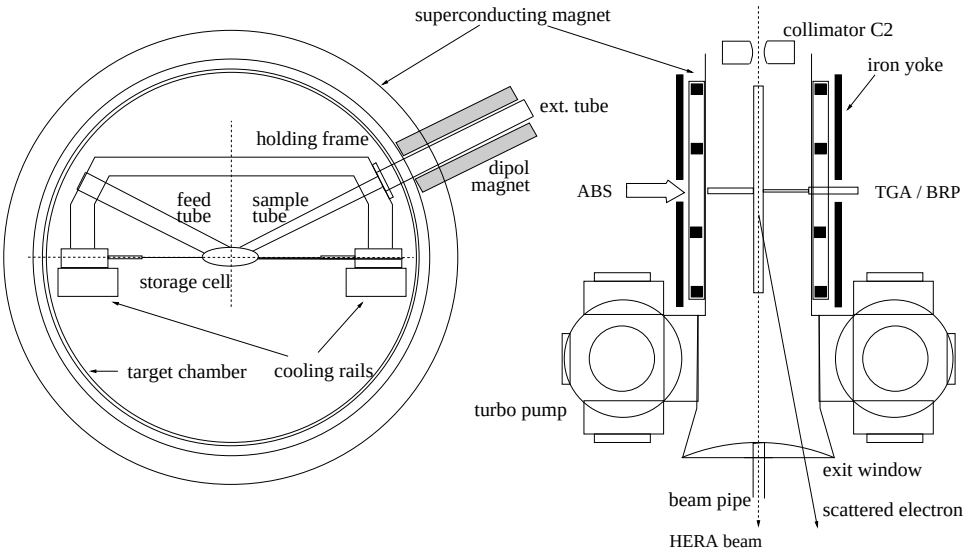

Figure 4.5: A Cross sectional (left) and top (right) view of longitudinal target chamber and superconducting magnets.

ber allows the scattered electrons and hadronic fragments to leave the target chamber and enter the HERMES spectrometer. On the upstream of the target chamber two collimators were installed, in order to reduce the amount of synchrotron radiation entering the target cell and further the spectrometer (in Figure 4.5 only one collimator is shown).

4.2.3 The Target Gas Analyzer (TGA)

One of the essential requirements for HERMES measurements is the precise determination of effective target polarization value seen by the HERA beam. The average target polarization receives contribution from the molecules from recombination of atomic hydrogen or deuterium, together from an unpolarized molecules due to ballistic flow of undissociated hydrogen (deuterium) in the dissociator of ABS, and in addition from residual molecular gas in the target chamber. All these contributions need to be measured in order to obtain the polarization of target gas. For this purpose a TGA was developed and installed at HERMES [Bau03a]. The main components of TGA are a chopper, a 90 ° off-axis quadrupole mass spectrometer (QMS) with a cross-beam ionizer, and a channel electron multiplier (CEM). The atomic and molecular gas entering the TGA is ionized by $70\,eV$ electron beam. Then the ions are filtered in QMS and detected by CEM. The chopper in front of QMS rotates at $5.5\,Hz$ frequency, periodically interrupting the sample beam. This allows to subtract the residual gas signal. The TGA is tilted by 7 ° with respect to sampling tube and BRP, in order to avoid an interference with the beam entering BRP (right-hand side of Figure 4.3).

The contribution of molecules in gas sample is expressed it terms of the degree of dissociation α, which is defined as a ratio of number of nuclei in atoms divided by the total number of nuclei in the sample, and which is measured roughly once per minute. Presenting the total flux of the gas ϕ_{tot}, that flows into the target, as a sum of fluxes of polarized atoms ϕ_a and molecules $\phi_m = \phi_r + \phi_{ball} + \phi_{rg}$, (here ϕ_r, ϕ_{ball} and ϕ_{rg} are respectively the fluxes of molecules from recombination, ballistic flow and residual gas)

$$\phi_{tot} = \phi_a + \phi_r + \phi_{ball} + \phi_{rg}, \tag{4.4}$$

one can define the fraction of atoms in absence of recombination

$$\alpha_0 = \frac{\phi_a + \phi_r}{\phi_{tot}}, \tag{4.5}$$

and the fraction of atoms surviving recombination

$$\alpha_r = \frac{\phi_a}{\phi_a + \phi_r}. \tag{4.6}$$

The fraction of atoms undergoing recombination then will be $1 - \alpha_r$. Meanwhile one can present the fraction of polarized nuclei in the atoms as $\alpha_0\alpha_r = \frac{\phi_a}{\phi_{tot}}$ and the fraction of polarized nuclei in the molecules as $\alpha_0(1 - \alpha_r) = \frac{\phi_r}{\phi_{tot}}$. A precise knowledge of above mentioned two fractions is necessary as the polarization of protons/deuterons is different inside atoms and molecules. The measurement of atomic and molecular fluxes is not enough for calculation of α_0 and α_r. One needs also to determine various components to the molecular flow. The measurement of residual gas contribution ϕ_{rg} was carried out using the fact that it is linearly proportional to the pressure in the target chamber. Hence injecting an increasing quantities of molecules into target chamber with controlled flow system, the coefficient of proportionality was determined. The contribution of ballistic

flux ϕ_{ball} was measured by varying atomic flux of the injected beam, while keeping the molecular flux constant. As the probability of recombination inside the cell was found to be independent of the injected beam intensity, the ϕ_{ball} can be extracted and the remaining contribution ϕ_r is found from Eq. 4.4.

By the measurement of different flow rates the quantities α_0 and α_r are extracted for the sample beam in TGA, while in order to obtain the α_0 and α_r for the gas in the storage cell, sampling correction factor needs to be applied. This was calculated by Monte Carlo simulation of stochastic motion of particles in the storage cell.

4.2.4 Breit-Rabi Polarimeter

Beside the measurements of atomic and molecular content of the gas provided by TGA, the polarization degree of the target also needs to be determined. For this reason the Breit-Rabi Polarimeter [Bau02] (BRP) was installed at HERMES. It consists of sextupole magnet system, radio-frequency transitions and beam detection system. BRP measures the relative populations of the hyperfine states of atomic hydrogen or deuterium gas. The gas from sampling tube passes through strong and medium field radio-frequency units , which can be tuned for exchange between different hyperfine states. Further, the sextupole magnet system provides a filtering of gas, by focusing the atoms with $m_s = +\frac{1}{2}$ along the BRP axis and defocussing the atoms with $m_s = -\frac{1}{2}$. Additionally the beam blocker in front of magnets prevents the atoms with $m_s = -\frac{1}{2}$ to reach the detector system, which is similar to that used in TGA. It consists of a cross-beam ionizer, a quadrupole magnet spectrometer (QMS) and a channel electron multiplier (CEM). In contrast to the TGA, only atoms (no molecules) are analyzed by BRP. From the measured relative populations of the hyperfine states of atoms, the atomic polarization P_a can be deduced, which corresponds to the polarization of atoms in the center of target cell. In order to obtain the polarization averaged along the cell, sampling corrections need to be applied as in the case of quantities α_0 and α_r.

Using the measurements of BRP and TGA, the average polarization of the target gas as seen by HERA lepton beam reads

$$P_{target} = \alpha_0\alpha_r P_a + \alpha_0(1-\alpha_r)P_m. \tag{4.7}$$

Here P_a is the atomic polarization measured by BRP and P_m is the nuclear polarization of molecules from recombination. The actual value of P_m is not possible to measure at HERMES, hence one has to allow the range $1 \leq \beta \leq 1$, for the ratio of the nuclear polarization of molecules produced by recombination and the nuclear polarization of the atoms $\beta = P_m/P_a$. However the range of β can be restricted to $\beta = [0.45, 0.83]$. The upper limit is determined according to the measurement of β at higher cell temperature of $260\,K$ (the nominal temperature was $100\,K$), resulting in $\beta^{260K} = 0.68 \pm 0.09_{stat} \pm 0.06_{syst}$. With an assumption that recombination mechanism at 100 and $260\,K$ is the same, the β at $100\,K$ can not exceed the value measured at $260\,K$ as the recombination probability is smaller at lower temperatures. The lower limit on β is derived from a simple argument that surface recombination involves target atoms ($P_a \approx 1.0$) and totally depolarized surface atoms, plus accounting for depolarization of molecules while colliding with the walls. The remaining uncertainty of β further contributes into total systematic uncertainty of measured target polarization value. The average target polarization values obtained with polarized deuterium (hydrogen) from 1998 to 2000 (1996 to 19997) are given in Table 4.1.

Year	Target	Target Polarization			
		P_z	ΔP_z	P_{zz}	ΔP_{zz}
1996	Hydrogen	± 0.759	±0.042	–	–
1997	Hydrogen	± 0.850	±0.032	–	–
1998	Deuterium	± 0.856	±0.064	0.827	± 0.027
1999	Deuterium	± 0.832	±0.058	0.827	± 0.027
2000	Deuterium	−0.840/+0.851	±0.031/0.028	0.827	± 0.027
2000	Deuterium	− 0.010	±0.026	− 1.656	±0.049

Table 4.1: The average values of the target vector and tensor polarizations.

4.2.5 Unpolarized Gas Feeding System

Apart from data collected with polarized targets, HERMES has collected large amount of data on an unpolarized targets (H, De, He, Ni, Ne, Kr, Xe). The unpolarized gas feed system (UGFS) was used to fill the storage cell with unpolarized molecular gas. Unlike polarized gases, where the technological limitations do not allow to increase the target density in the storage cell to more than $10^{13}-10^{14}\ atoms/cm^2$, the UGFS allows to achieve a target densities of about $10^{15}-10^{17}\ atoms/cm^2$. The UGFS had no technical limitations like the Stern-Gerlach setup of ABS, however the allowed target density is limited by the lifetime of the HERA lepton beam, which under normal running conditions was more than 10 hours. The total lifetime τ can be expressed as

$$\frac{1}{\tau} = \frac{1}{\tau_{HERA}} + \frac{1}{\tau_{HERMES}}. \tag{4.8}$$

During normal running the contribution of τ_{HERMES} had to be greater than 45 hours. This leads to a typical areal densities of about $10^{16}\ atoms/cm^2$, however HERMES was allowed to increase the areal density whenever the lepton beam current fell below $15\,mA$. In this case the areal densities of about $10^{17}\ atoms/cm^2$ were achieved. Another limit on the density of an unpolarized gas target arises from the requirements of HERMES data acquisition system (DAQ), which had a maximum trigger rate of $500\,Hz$. With the increase of a target density the background of Møller electrons in the HERMES front region would also increase resulting in a total increase of DAQ deadtime.

4.3 The HERMES Spectrometer

The fragments of interaction in the storage cell were detected in the HERMES spectrometer. HERMES had a typical for a fixed target experiments forward angle spectrometer. It consists of two identical parts, arranged below and above the HERA lepton beam plane. The coordinate system used at HERMES has the z-axis along the electron/positron beam direction, y-axis vertical upwards, and the x-axis in horizontal direction, forming an orthogonal right-handed coordinate system, which originates at interaction point (center of target cell). The spectrometer consists of several detector components, which provide high efficient tracking and identification of scattered and produced particles. The schematic view of HERMES spectrometer is shown in Figure 4.6. The front region before the spectrometer magnet consists of a silicon strip detector, drift vertex and two front chambers (DVC, FC1/2), and a trigger hodoscope (H0 at $145\,cm$ distance from the

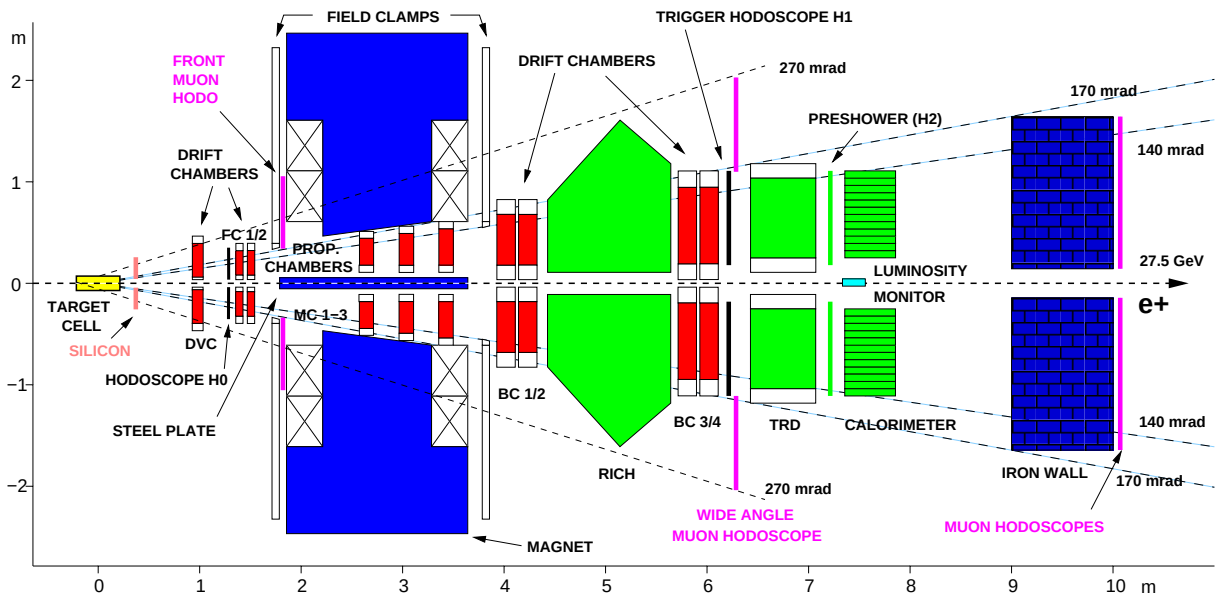

Figure 4.6: The schematic view of HERMES Spectrometer

center of target cell). At the region behind the magnet four backward drift chambers (BC1/2, BC3/4) were mounted, with a ring-imaging cherenkov detector (RICH) between them. The latter are followed by a trigger hodoscope (H1), a transition-radiation detector (TRD), a preshower detector (H2), a luminosity detector, and a lead-glass calorimeter (CALO). In the gap of magnet three multi-wire proportional chambers (MWPC) (MC1-3) were installed . A number of muon hodoscopes were also installed between the field clamps and the body of the magnet, and directly behind hodoscope H1, as well as behind a one meter thick iron wall.

The spectrometer magnet is a H-type dipole magnet, with a deflecting power of $1.3\,Tm$. It creates a vertical dipole magnetic field, which bends charged particle tracks mainly in the horizontal direction. The shielding of lepton/proton beam is provided by $11\,cm$ thick iron plate (septum plate) located in a x-z plane. Further the fringe field in the septum plate was corrected by a correction coil with a deflecting power of $0.08\,Tm$. The filed clamps in front and behind the magnet reduce the outer fringe field below $0.1\,T$. The magnet and the septum plate limit the geometrical acceptance of the spectrometer to $\pm 170\,mrad$ in the horizontal direction and from $\pm 40\,mrad$ to $\pm 140\,mrad$ in the vertical direction.

4.3.1 The tracking system

The purpose of tracking system is the three-dimensional reconstruction of the tracks of the charged particles and precise determination of particle trajectories, i.e. the scattering angles (θ and ϕ) and momenta. The detector components of tracking system are the silicon detector, the drift chambers (DVC, FC1/2) in front of magnet, four drift chambers (BC1/2, BC3/4) behind the magnet and proportional wire chambers (MCs) in the magnet gap. The variety of tracking devices serve to solve certain requirements. The silicon strip detector installed in 2002 was aimed to improve the detection of long living particles (Λ, K_s ...) that decay outside the target cell. It is described in details in [Ste00]. For the analysis discussed in this report it was not used. Also an information from MCs is not

essential in this report, as they were used for momentum determination of low energy particles that do not reach the back region, i.e. BCs. The main information for tracking comes from DVC, FCs and BCs. They are conventional drift chambers of horizontal type. Each chamber consists of six layers of drift cells. The cells are organized in three pairs, a vertical X, X' pair of planes, together with U,U' and V,V' planes which are at an angle of $\pm 30^\circ$ with respect to the vertical plane. The two layers of one pair are used with an offset of half the cell size in order to help resolve ambiguities. Each layer in its tern is made of a plane of alternating anode and cathode wires between the cathode foils. The cathode wires and foils are at negative high voltage of a few thousand volts, while the anode wires at ground potential. All drift chambers were filled with the same gas mixture $Ar/CO_2/CF_4$ with proportions 90/5/5.

4.3.2 The Particle Identification Detectors

The particle identification at HERMES is achieved by means of four detectors. First, leptons and hadrons are separated using an information from transition radiation detector (TRD) in combination with lead-glass electromagnetic calorimeter and preshower detector. Further charged pions, kaons and protons can be identified by ring imaging cherenkov detector (RICH), which was installed in 1998, instead of conventional cherenkov detector used in 1996 and 1997. RICH can also be used for lepton hadron separation in a momentum range up to $4\,GeV$, while for present analysis the typical lepton momenta are above that threshold. Therefore the RICH was not used for DVCS analysis.

The transition radiation detector was chosen to provide a pion rejection factor of above 100 for particles at energies above $5\,GeV$. It's operation is based on a radiation of X-rays by ultra-relativistic charged particles passing through boundary of two materials with different dielectric coefficients of refraction. The transition radiation is emitted in a cone with opening angle θ proportional to $1/\gamma$, where γ is the Lorenz factor ($\gamma = \sqrt{1 + v^2/c^2}$). The mean radiated energy for a single transition between dielectric material with plasma-frequency ω_{pf} is given by

$$E_{TR} = \frac{2}{3}\alpha\gamma\omega_{pf}. \tag{4.9}$$

The emitted energy is proportional to γ, which is about 270 times larger for electrons/positrons than for pions with the same energy. This enables a separation of leptons from hadrons in the sense that at typical HERMES energies mainly electrons/positrons emit a transition radiation photon. For practical usage of TRD it is essential to provide a multiple medium/vacuum transitions, as the intensity of radiation is low for single transition.

The HERMES TRD consists of six modules per detector half. Each module consists of $6.35\,cm$ thick poly-propylene/ethylene fiber radiator and $2.54\,cm$ thick proportional multi-wire chambers (MWPC). The MWPCs are built out of 256 vertical wires and filled with a gas mixture of Xe/CH_4 (90/10), which provides an efficient X-ray absorption. Traversing through MWPCs all particles deposit some energy due to ionization of the gas. Although it is difficult to distinguish between ionization signal from the charged particles, it is possible to separate leptons from hadrons, taking into account the fact that leptons in contrast to hadrons produce transition radiation. Therefore leptons in average deposit approximately 2.5 times more energy than hadrons. In order to obtain a good hadron rejection factor, an information from several modules was combined by the "truncated mean" method: the largest signal from the 6 modules was discarded while the average of the other five was taken (see [Van06] for details).

The preshower detector consists of a passive radiator, and a scintillator counter (H_2 hodoscope). The radiator is made of 11 mm (two radiation length) thick lead, sandwiched between 1.3 mm stainless steel sheets. Passing through radiator the leptons have much higher probability to produce electromagnetic showers then hadrons. Therefore leptons deposit more energy in the scintillator than hadrons, which lose energy mainly due to the ionization. The scintillator itself consists of 42 vertical paddles per detector half. Each paddle is made of 1 cm thick fast scintillation material BC-412 and have an area of 9.3×91 cm^2. The scintillation light was detected by a photomultiplier tube installed at the outer edges of the scintillator paddles. A pion rejection factor of about 10 was achieved by the preshower detector with 95% efficiency for lepton detection.

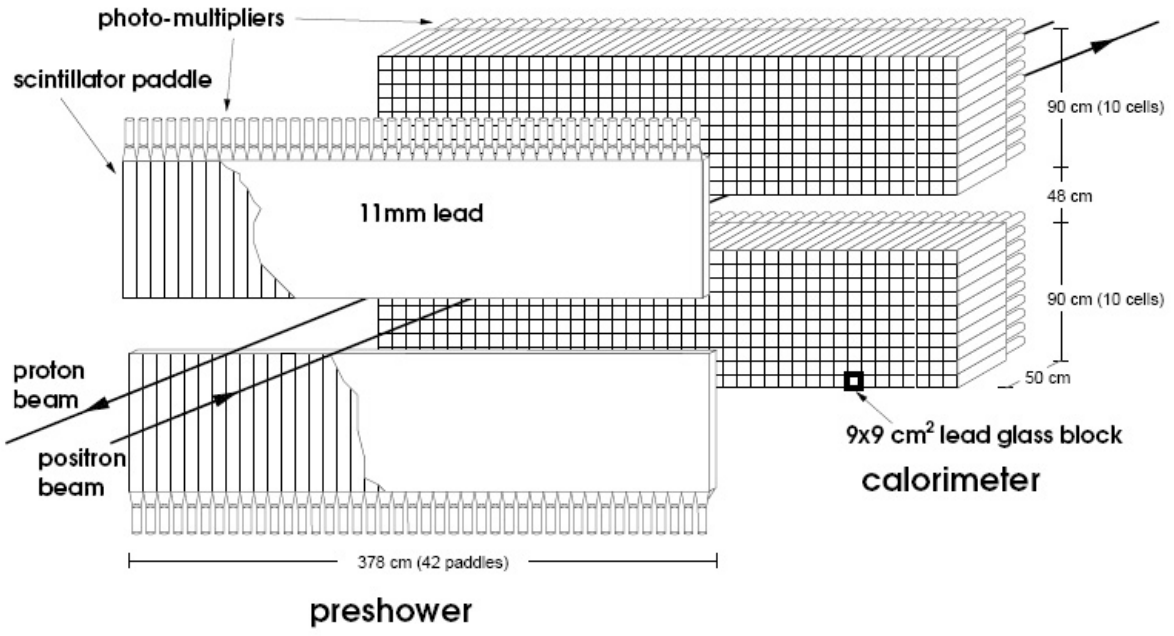

Figure 4.7: Schematic view of the calorimeter and preshower detector.

The last detector of the HERMES PID system is the electromagnetic calorimeter. It consists of an array of 42 × 10 F101 lead-glass blocks in each detector half. Each block have a front area of 9 × 9 cm^2 and 50 cm depth, corresponding to 18 radiation lengths. The blocks are optically connected to a photomultiplier tubes as shown in Figure 4.7. The surface area of blocks was chosen in a way that 90% of electromagnetic shower is contained in a block, while the matrix of 3 × 3 blocks (defined as cluster) contains more than 99% of the signal created by a shower. The electrons and positrons from a shower produce a cherenkov light in the lead-glass blocks. The amount of cherenkov photons is further detected by the photomultipliers, thus providing a measure of the energy of the shower. In order to discriminate between leptons and hadrons the ratio E/P is considered. Here E is the energy deposit in a cluster and P is the momentum of particle measured by means of tracking detectors. Since leptons lose almost all of their energy in the calorimeter, the average ration of E/P is typically unity. While for the hadrons, which deposit only a fraction of their energy through ionization, the E/P ratio is less than unity. The hadron rejection factor of the calorimeter was between 10 and 100, depending on the lepton energy and calorimeter threshold.

The calorimeter and preshower detectors are of special importance for the DVCS analysis, as they are the only detectors which can detect photons. The preshower detector does not provide a measure of energy or position of photons, therefore it is used for optimization of the cut imposed on cluster energy in order to improve the resolution of the photon energy measurement and for certain systematic checks. The position of the photons (leptons) in the calorimeter is reconstructed as a weighted-average of centroids of each block in a cluster with the weights $w_i = max\{0, 4.8 + ln(\frac{E_i}{\sum E_i})\}$. This reconstruction algorithm described in [Ely01], provides position reconstruction resolution of about $0.5cm$. The energy resolution of the calorimeter for leptons can be described by [Ava98]

$$\frac{\sigma(E)}{E} = \frac{5.1 \pm 1.1}{\sqrt{E}} + (2.0 \pm 0.5) + \frac{10.0 \pm 2.0}{E}. \tag{4.10}$$

For the case of photons, it is assumed that the shower development mechanism is similar to that of leptons. Investigations show [Ely02], that this is a good approximation for the photons that start showering in the preshower, like most of the leptons do.

In order to obtain good lepton/hadron identification, the responses of PID detectors are combined in a probability-based algorithm described in [Kai97]. For each PID detector a quantity $PID_i = lg(P_i^l/P_i^h)$ is defined, where $P_i^{l(h)}$ is the probability that lepton (l) or hadron (h) with the specified polar angle and momentum, gives the measured signal in the considered PID detector i (or detector module). The commonly used logarithmic probability ratios are defined for combined preshower and calorimeter response as PID_2, and respectively PID_3 and PID_5 for RICH and TRD. Further, the PID values from different detectors can be combined to achieve sufficient particle identification. As an example a typical combined PID distribution from calorimeter, preshower and TRD is shown in Figure 4.8, which indicates a clear separation between leptons and hadrons.

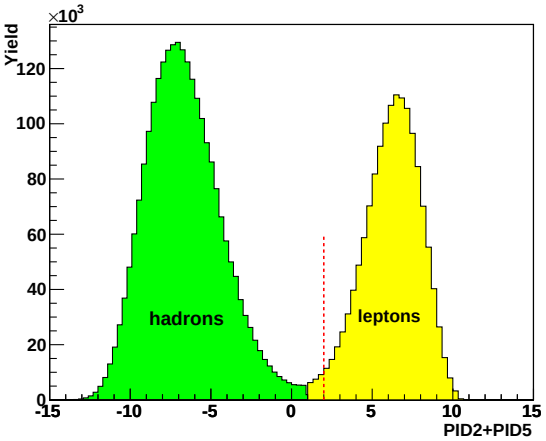

Figure 4.8: The $PID_2 + PID_5$ distribution for DIS events from 2000 data on an unpolarized deuterium.

4.3.3 The trigger system

In order to distinguish between events of specific physics interest from the background and also initiate digitization and readout of the detector signals, various trigger systems were installed at HERMES. The most important physics trigger for this analysis is the

DIS trigger (trigger-21), which indicates signals in the three hodoscopes H0, H1 and H2, together with a cluster in the calorimeter, coinciding with the HERA lepton bunch. The H0 hodoscope consists of only one $3.2\,mm$ thick scintillator paddle per detector half, read out by two photomultipliers. It was installed in front of FCs in order to suppress the trigger signals initiated by a backwards-going particles originated from a proton beam. The hodoscope H1 was constructed in the same way as H2 except the lead sheet in front of latter. It was installed in front of TRD as shown in Figure 4.6. The signal from the hodoscope H1 prevents the shower initiated by the photon in the preshower and calorimeter to be associated with the lepton. The response from the preshower was required to be above the minimum-ionizing signal, ensuring electromagnetic shower development. While the response of the calorimeter was required to be above a threshold of $1.4\,GeV$ for polarized, and above $3.5\,GeV$ for unpolarized data taking periods. The trigger decision is made in about $400\,ns$. After a trigger has been generated, all the relevant data are read out from the detectors. During that period no information can be recorded, resulting in a dead time of the spectrometer. The dead time is defined as the ratio of trigger requests which had to be rejected and the total number of readout requests. During standard running it is typically well below 10%.

4.4 Luminosity monitor

For calculation of cross sections or cross section asymmetries, the precise knowledge of absolute or relative luminosity is necessary. This is done either by counting the DIS events in data set or by using the luminosity monitor. The luminosity is the product of beam current and target density, integrated over the measurement time. Although both target density and beam current can be measured separately, more accurate determination of luminosity was achieved at HERMES by installation of luminosity monitor [Ben01]. The luminosity can be determined by comparing the measured rate of the well known process with the evaluated cross section, for example the elastic scattering processes of beam leptons off shell electrons in the target gas. In the case of positron beam, both the Bhabha scattering process ($e^+e^- \rightarrow e^+e^-$) and the annihilation processes ($e^+e^- \rightarrow \gamma\gamma$) contribute, while for the electron beam the Møller scattering processes is taken into account. For a high energetic beam the scattering angles of both leptons or photons are small and both final state particles have similar amount of energy.

The luminosity monitor consists of two small calorimeters located $7.2\,m$ downstream the target. Each calorimeter is constructed of 3×4 array of radiation resistant $NaBi(WO_4)_2$ crystals, having a $22 \times 22\,mm^2$ surface area and $200\,mm$ length. A photomultiplier tubes coupled to each crystal at the back side, provide a read out of the signal. The resulting horizontal acceptance of $4.6 - 8.9\,mrad$ sufficiently covers the detection of symmetric events from above mentioned processes. An event from desired process is selected if there is a simultaneous response in both calorimeters, each having an energy deposition greater than $4.5\,GeV$. The energy constraint reduces the dominant background from DIS scattered leptons, which has high energy deposition in only one of the calorimeter sections.

The measured absolute luminosity has a large systematic uncertainty of about 7%. It acquires due to the dependence of luminosity monitor acceptance on beam position and slopes. Nevertheless, in various asymmetry measurements only relative luminosity is essential, which has significantly lower systematic uncertainty.

4.5 Data acquisition and processing

The data production chain consists of two main parts. First data acquisition (DAQ) system realizes digitization and fast read out of the detector signals, whenever a trigger signal occurs. For digitalization of timing and analogue signals, LeCroy 1877 Multihit FastBus timetodigital converters (TDC) and LeCroy 1881M FastBus analoguetodigital converters (ADC) were used. The raw data from TDCs and ADCs are further buffered in EPIO (Experimental Physics Input Output) format on hard disks and backed up on data tapes. Later in the offline analysis the raw data were processed by the HERMES decoder (HDC), where the signals from ADCs and TDCs are translated into HERMES coordinate system using individual detector geometries and calibrations. The output of HDC is stored in DAD (Distributed ADamo) [CER93] tables. Subsequently the data are processed by HERMES reconstruction code (HRC). HRC reconstructs particle tracks by evaluating them in the front and back region of the spectrometer and joining them in the center of magnet. It also provides the charges and momenta of the particles, together with an information about PID.

In parallel to DAQ system, a slow control system reads out an information, which changes slowly and independently on triggers from the spectrometer. Those are for example beam and target polarizations, an information from luminosity monitor, detector temperature, etc.. The slow control data are read out every $10\,s$ and combined with the output of HRC into micro data summary tapes (μDST). The μDST files contain all necessary information to perform the data analysis.

The data at HERMES are specified within different time scales. The shortest time scale is *event*. It contains information about all reconstructed tracks corresponding to a single trigger signal. Events recorded within approximately $10\,s$, are grouped into a $burst$, which corresponds to a single readout of slow control data. The bursts are grouped into a run, which is defined by a size of about $450\,Mb$ of EPIO data. Runs contain data collected in a time interval of about 10 minutes. Nevertheless the time interval of a run depends on beam current, target density and luminosity. Finally the largest time scale is the $fill$, corresponding to data recorded during a HERA lepton beam fill, which has a typical time interval of 8-14 hours.

Chapter 5

Data Analysis

This chapter describes in details the procedure of data analysis. All data collected on both unpolarized and longitudinally vector polarized deuterium target until 2006 are used in the analysis. Chapter starts from the description of selection criteria for the DVCS/BH candidate events. As the recoiled particle was not detected, the missing mass technique was used to achieve exclusivity. With the optimal choice of kinematic cuts it is possible to enhance the signal and reduce the background. The extraction of asymmetry amplitudes is discussed in section 5.4 by means of maximum likelihood method. Further, the systematic studies of the detector response and the possible contributions from background processes are described using both experimental and Monte Carlo data.

5.1 Data Quality

The data used in different physics analysis, carried out at HERMES, have to satisfy various data quality requirements. Depending on the specificity of the studied physics process and considered observables the condition of the lepton beam, HERMES-target and the relevant detector components must be checked to ensure that the data are stable, free of any problems, and useful for the analysis. As was discussed in section 4.5 the combined information of the data sample from DAQ and slow control system is stored in the μDST files. The μDST files are labeled by two last digits of corresponding data taking year, by a letter denoting the version of the production, and a cypher. The first version of μDST files (a-production) is based on a calibration of the detectors on the basis of the data from a preceding years. Further, the a-production is used as an input for more precise calibrations of the detectors and reproduction of μDST files. The process of reproduction of data continues until all the calibrations and corrections are applied. Finally, the cypher indicates the number of reproductions without a new track reconstruction. For the analysis presented in this report the data productions 96d0, 97d1, 98d0, 99c0, 00d2, and 05c1 were used.

Although the μDST files contain all the information about the status of the beam, target and the detector components, a special group of experts (Data Quality Group) provided an additional information about data quality on a burst level. This information is given in a form of 32-bit hexadecimal numbers for each half of the spectrometer (top and bottom). For the DVCS analysis of the unpolarized data the list of data quality constraints is different from that of longitudinally vector polarized one, as certain bits in the bit pattern refer to a polarization status of the target and hence are not essential in the analysis of unpolarized data.

Bit	503e13dc	5dbf97fd	Description
0	–	+	Ensures that the target is in a spin state antiparallel or parallel to the beam polarization.
2	+	+	Selects the bursts with reasonable dead time.
3	+	+	Ensures that the length of the burst was reasonable.
4	+	+	Selects the bursts with a reasonable beam current.
5	–	+	Discards data with very small count rates and also data with very large fluctuations in target density.
6	+	+	Checks that the burst was not the first in an experimental run.
7	+	+	Discards all bursts with bad μDST records or last bursts in a fill.
8	+	+	Rejects any burst which has no PID values due to initialization problems or unknown Calorimeter thresholds.
9	+	+	Accepts the bursts belonging to a run marked as analyzable in the HERMES electronic logbook.
10	–	+	Rejects unpolarized data and accepts only data where the target was in the two or four state mode, respectively.
12	+	+	Specifies the case when the bit 10 was set because no data was available.
15	–	+	Discards unpolarized data according to the valve settings of the target.
16	–	+	Rejects data were the target was not properly functional.
17	+	+	Discards any burst in which at least one calorimeter block was dead.
18	+	+	Discards the burst if at least one block in the H2 Hodoscope or Luminosity Monitor was marked as dead.
19	+	+	Ensures that the TRD was operational.
20	+	+	Accepts the bursts when no high voltage trips occur in the FCs or BCs.
21	+	+	Rejects bursts belonging to a run marked as bad due to strange Calorimeter behavior or a bad RICH.
23	–	+	Accepts the burst if α_0 value is reasonable.
24	–	+	Accepts the burst if α_R value is reasonable.
26	–	+	Accepts the burst when the target is in one of the two tensor polarized states.
27	–	+	Accepts the burst when reasonable target polarization was measured.
28	+	+	Accepts the burst if the latest beam polarization measurement was taken not more than 5 minutes ago.
30	+	+	Discards the burst if the polarized data undergoes a dead time correction.

Table 5.1: List of data quality requirements and a corresponding bits.

The data quality cuts for DVCS analysis were applied according to the following 0x503e13dc and 0x5dbf97fd bit patterns respectively for unpolarized and polarized data sets, which correspond to the requirements listed in Table 5.1. Except from the cuts encoded in the bit patterns, several additional cuts were applied on a burst level. For example, the raw luminosity count rate was chosen to be reasonable, together with the lifetime of the data taking system. In a conventional variables of HERMES data acquisition system they read as $5 < g1Beam.rLumiRate < 3000$ and $0.8 < g1.DAQ.rDeadCorr21 \leq 1.0$. Also the TRD was required to be fully operational $g1Quality.rTrdDQ == 3$ and a reasonable beam polarization was available $(g1DAQ.bProdMethods\&0x00800) == 0$. Since the performed analysis contains measurements of the asymmetries with respect to the beam helicity, it was required for the fitted value of the beam polarization to be below 80% and not equal to zero. This requirements were applied in order to reject non physical values of the beam polarization, as in the experiment a polarization above 80% was never observed. For the case of polarized data an additional cut was applied on measured raw target polarization $0.5 < |g1Target.rPol| < 1.5$, which rejects data with small or illegal values of target polarization.

5.2 Event Selection

Events that pass the data quality requirements are further used for the selection of exclusive DVCS/BH sample. The measurement of an exclusive process requires exact determination of the final state, which in the case of DVCS/BH consists of three particles. As the cross section of DVCS/BH processes decreases rapidly with increasing negative four momentum transfer to the target, most of these events are produced from the kinematic range of negative four momentum transfer below 1 GeV^2. As a consequence the recoiled target particle with low momentum escapes detection by a forward spectrometer. Even though by detection of only scattered lepton and emitted photon, it is still possible to achieve exclusivity by means of restriction of the squared missing mass of the reaction $ed \rightarrow e\gamma X$ to certain kinematic range. Note that in this case it becomes impossible to separate contributions to the yield of coherent process when the deuteron stays intact $(ed \rightarrow ed\gamma)$, from that of incoherent process when it breaks up $(ed \rightarrow epn\gamma)$. In addition, their is a large contribution from the associated incoherent processes when one of the target nucleons excites to a resonance in the final state, and from a decay of neutral mesons in DIS fragmentation processes.

Due to the complications mentioned above, it is convenient to consider the event selection in three steps. As a first step the events containing exactly one electron/positron that satisfies all the DIS requirements are selected. These events are referred to as *DIS events* in the following. In a second step, within the DIS events those with exactly one photon are selected (referred to as *single photon events* in the following). Finally, in a third step the exclusive DVCS/BH events (*exclusive events* or *sample*) are selected by means of missing mass technique.

5.2.1 Selection of DIS events

The DIS events were selected first of all requiring a trigger-21 to be fired. Further, the events that contain at least one charged track reconstructed by HRC from the signals in both front and rear tracking chambers, and with certain energy deposition in the calorimeter, are selected. To be sure that the charged track did not hit the frames of the

tracking chambers and also the septum plate or the field clamps, the fiducial volume cuts were applied on the x-coordinate of the track at the front field clamp $|x_{FFC}| \leq 0.31\,cm$, y-coordinate of the track at the beginning of the septum plate $|y_{SP}| > 7cm$, and on the x and y-coordinates of the track at the rear field clamp $|x_{RFC}| \leq 100\,cm$, $|y_{RFC}| \leq 54\,cm$. In addition the impact x and y positions of the track at the surface of the calorimeter were required to be $|x_{Calo}| \leq 175\,cm$ and $30\,cm \leq |y_{Calo}| \leq 108cm$, respectively. This assures that the tracks are not incident in the outermost two-third of the outer row/column of the calorimeter blocks and the shower produced by them is entirely contained in the lead glass blocks. Further the charged track had to be identified as a lepton. As was mentioned earlier, the RICH detector was not used in this analysis for the identification of the particles, therefore the requirement on the likelihood of the combined PID detector responses of the preshower and calorimeter (PID2) and the response of the TRD (PID5) was chosen to be more than 2 (PID2+PID5>2). This means that the track is 100 times more likely a lepton than a hadron. It was also required that the track possesses the same charge as the charge of the beam in the considered data taking year.

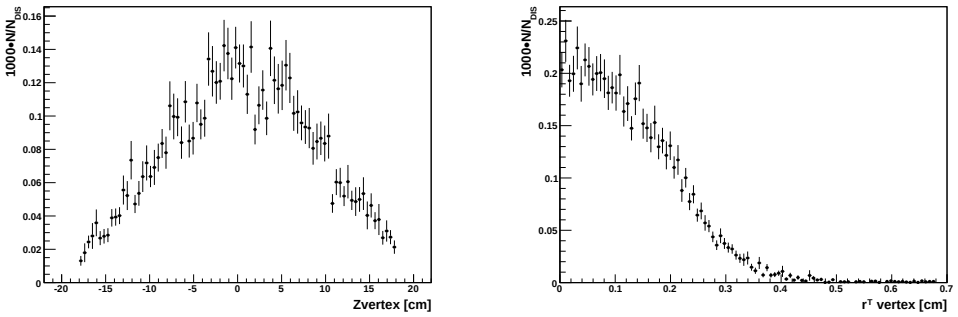

Figure 5.1: The distributions of the reconstructed longitudinal position z_{vtx} (left panel) and transverse position r^T_{vtx} (right panel) for a combined exclusive sample of events for whole unpolarized data set.

In order to assure correct vertex reconstruction by HRC, the z position of the primary interaction vertex z_{vtx} was required to be between -18 and 18 cm. Although the target cell has an extension of $\pm 20\,cm$, the choice of this restriction is caused by the resolution of the spectrometer for z_{vtx}, which is about $2\,cm$. Another cut was applied on a transverse position of the primary vertex $r^T_{vtx} = \sqrt{x^2_{vtx} + y^2_{vtx}}$, where x_{vtx} and y_{vtx} are the x and y positions of the reconstructed interaction vertex. The transverse position was required to be less than $0.75cm$ to assure that the vertex is within the elliptical cross section of the target cell. As an example, the distributions of the longitudinal and transverse positions of the reconstructed vertexes are shown in Figure 5.1 for an exclusive sample of the unpolarized data set.

On a next step, the hard leptoproduction regime of the DVCS/BH processes needs to ensured. In principle this requires for Q^2 to be much larger than the mass of the target particle. However due to the limited statistics at relatively large values of Q^2, the requirement $Q^2 > 1\,GeV^2$ was applied on the data. The squared invariant mass W^2 was required to be above $9\,GeV^2$, which excludes the data from a resonance region. For the case of DVCS process this cut does not affect the exclusive sample, as all the exclusive events satisfy to that requirement [Ell04]. The lower cut on W^2 is essential for the selection of inclusive DIS and semi-inclusive DIS processes. Especially for the semi-inclusive processes one can expect large contribution from the target remnant in the selected hadron sample

at smaller values of W^2. The choice of the cut on a W^2 was motivated by a comparison of data collected in different time periods (years) with Monte Carlo simulations. On the left upper plot of Figure 5.2 the W^2 distributions of inclusive DIS samples from different data taking years are compared with Monte Carlo prediction. One can see, that started from a value of $9\,GeV^2$ the agreement between data from different years and Monte Carlo is sufficient. It is very important to reach a good consistency between data sets collected in different data taking periods not only for exclusive samples, but also for DIS samples, as the latter is widely used for the normalization of the data. On the other hand it is important to choose an appropriate kinematic range for the investigation of various background processes, mainly the production of semi-inclusive neutral pions, which is one of the main background processes and will be discussed in details in section 5.5.5. For the same data consistency reasons, the energy transfer from the incoming lepton to the virtual photon ν was restricted to the values below $22\,GeV$. From the comparison of ν distributions from different years with Monte Carlo on the top right plot of Figure 5.2, one can see a strong inconsistency between data and Monte Carlo in the region above $22\,GeV$. On the bottom panels of Figure 5.2 the distributions in Q^2 and Bjorken variable x_N are shown for DIS sample from unpolarized data and Monte Carlo. Note that the inclusive variables W^2 and x_N were calculated using the proton mass.

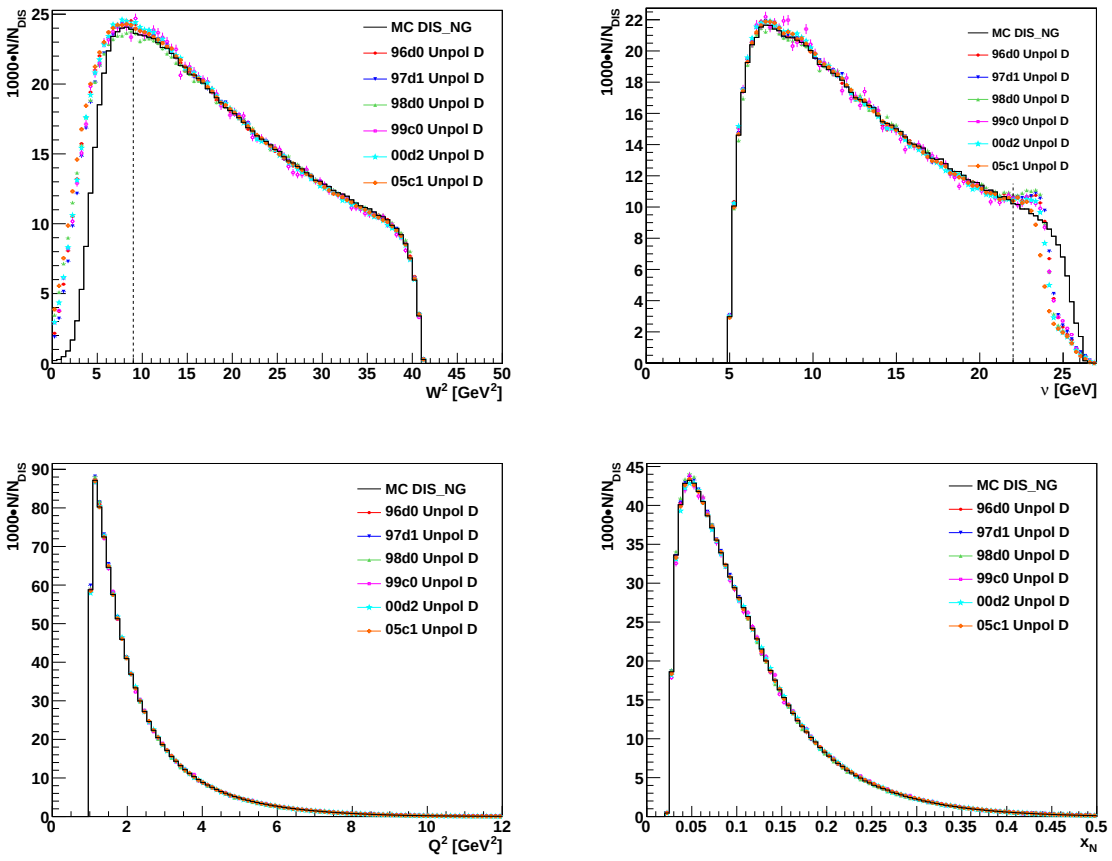

Figure 5.2: The distributions of W^2 (top left panel), ν (top right panel), Q^2 (bottom left) and nucleonic Bjorken variable x_N for the inclusive DIS samples from different data taking years on an unpolarized deuterium target . The solid line represents the Monte Carlo simulation, discussed in section 5.3

5.2.2 Selection of single photon events

The final state of DVCS/BH process, that is detected at HERMES, consists of a scattered lepton and a real photon. Hence, from the selected sample of DIS events, those need to be chosen, that contain exactly one additional uncharged cluster in the calorimeter. To be sure that the trackless cluster originates from a photon, it was required for the signal of a cluster in a preshower to be larger than $1\,MeV$. As the HERMES calorimeter was originally constructed for the detection of leptons, the photons that do not shower in the preshower were found to be miscalibrated by 15% at a photon energy of $15\,GeV$ [Ely02]. The existing difference in the probability of showering in the preshower detector by photons and leptons, leads to a wrong photon energy reconstruction in the calorimeter for those photons that do not shower in the preshower, while the shower development for the photons that start showering in the preshower detector is very similar to those originating from leptons. Nevertheless, even for the photons that start showering in the preshower, the possible differences of their shower development in the calorimeter

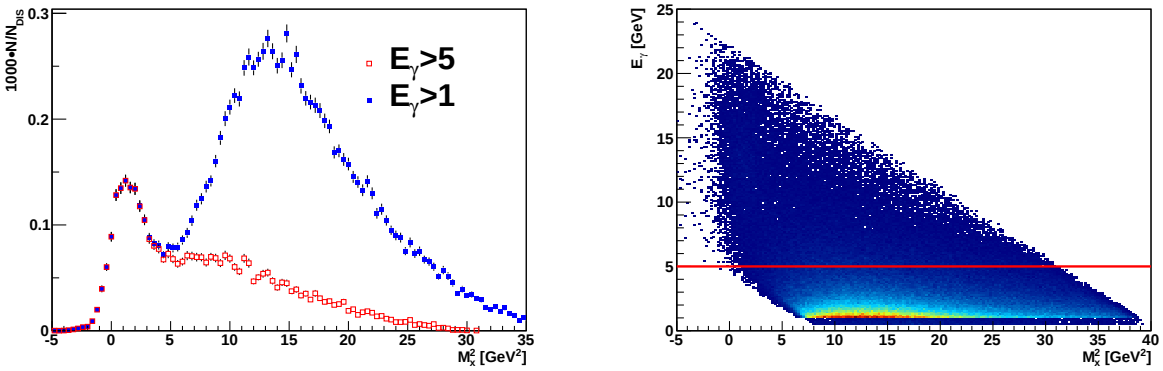

Figure 5.3: On the right side the correlation between the photon energy and squared missing mass is shown. The red horizontal line denotes the cut applied on photon energy. On the left side the comparison of squared missing mass distributions corresponding to different cuts applied on the photon energy is shown.

compared with leptons was accounted by choosing a different z-position of the cluster in the calorimeter. Based on the Monte Carlo studies the z-position of shower development in the calorimeter for the photons was found to be $z = 729\,cm$, while for leptons $z = 738\,cm$. Although the $1\,MeV$ cut on the preshower signal reduces the statistics by about 20 % [Ely02], it is essential for reliable reconstruction of photon energies.

Like in the case of DIS leptons, also for photons the fiducial volume cuts were applied, restricting the x and y positions of a cluster on a surface of the calorimeter to be $|x_{Calo}| < 125\,cm$ and $33\,cm < |y_{Calo}| < 105\,cm$. In addition, the photons were required to have an energy larger than $5\,GeV$. This cut is applied in order to improve the exclusivity of the measurement. In the left side of Figure 5.3 the squared missing mass distributions (will be defined in next section) are shown, corresponding to different cuts on photon energies. As can be seen this cut has a very small impact on the events from the exclusive region ($M_X \approx m_p$), while it significantly reduces the yield in a non-exclusive region. The non-exclusive region originates mainly from the photons of a π^0 and η decay with a typically low cluster energies. On the right side of Figure 5.3 the correlation of photon energy with the squared missing mass is shown for a single photon events from the year 2005.

5.2.3 Selection of exclusive events

As it was mentioned in section 5.2, various processes contribute in the sample of single photon events. Beside the coherent and incoherent DVCS/BH events, which are referred in the following as a signal of interest, also the associated incoherent processes with resonance excitation and semi-inclusive production of neutral mesons contribute in the single photon event sample. The latter two are referred to as a background processes. In order to maximally assure exclusivity of data sample, i.e. to select an event sample where the signal of interest will significantly dominate the contribution from the background processes, a number of requirements need to be applied on the 'exclusive' kinematic variables. One of such a variables is the opening angle between virtual and real photons, defined as

$$\theta_{\gamma^*\gamma} = arccos\left(\frac{\vec{q}\cdot\vec{q'}}{|\vec{q}||\vec{q'}|}\right). \tag{5.1}$$

For the extraction of azimuthal asymmetries, a full coverage of the acceptance in the azimuthal angle ϕ is required. Moreover, the distribution of azimuthal angle ϕ has to be uniform and independent from other kinematic variables. For these reasons an upper cut on the opening angle was applied. As can be seen from the left plot of Figure 5.4, showing the distribution of azimuthal angle ϕ versus the opening angle $\theta_{\gamma^*\gamma}$, the full coverage of ϕ acceptance can be achieved up to the values of the $\theta_{\gamma^*\gamma}$ about $0.07\,rad$. It should be noted, that not only the acceptance effects increase with the increase of the opening angle $\theta_{\gamma^*\gamma}$, but also the fractional contribution of the background processes becomes dominant at larger values of $\theta_{\gamma^*\gamma}$. This is illustrated on the right plot of Figure 5.4, where the Monte Carlo simulated fractional contributions of the signal and background processes are presented in bins of $\theta_{\gamma^*\gamma}$. An upper limit on the opening angle $\theta_{\gamma^*\gamma}$ equal to $0.045\,rad$, that suppresses the contribution from the background processes, can be determined from the same figure. Additionally, as the azimuthal angle ϕ is undefined when $\theta_{\gamma^*\gamma} = 0$, also a lower cut needs to be applied on opening angle. A Monte Carlo based investigations of smearing effects showed, that at small values of $\theta_{\gamma^*\gamma}$ the smearing of azimuthal angle significantly increases [Kra05], hence a lower cut on opening angle $\theta_{\gamma^*\gamma} > 0.005\,rad$ was

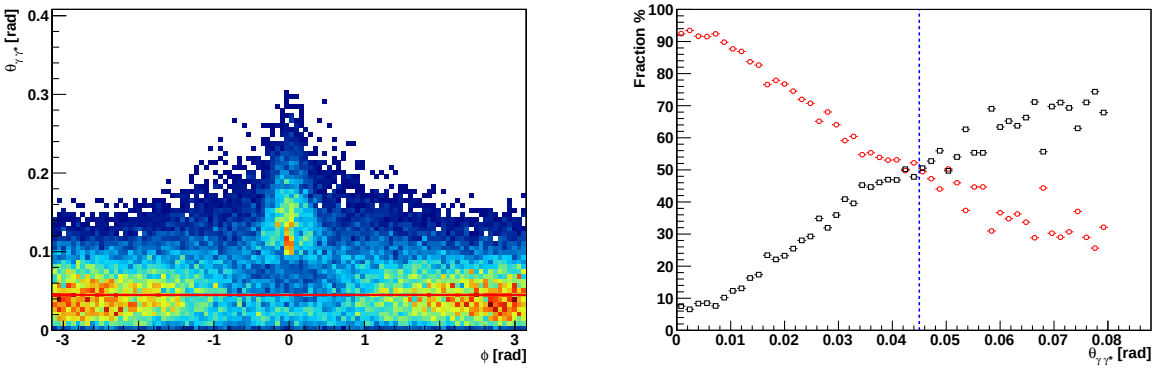

Figure 5.4: On the left side the scatter plot of the azimuthal angle ϕ versus the opening angle $\theta_{\gamma^*\gamma}$ is shown for the exclusive event sample from the year 2005 without a cut on $\theta_{\gamma^*\gamma}$. The horizontal line denotes an upper cut $\theta_{\gamma^*\gamma} = 0.045\,rad$. On the right side the fractional contributions of the signal and background processes are shown in bins of opening angle $\theta_{\gamma^*\gamma}$. The vertical line corresponds to an upper cut on $\theta_{\gamma^*\gamma}$.

determined. For further improvement of exclusivity of the event sample, an upper cut was applied on the squared four momentum transferred to the target. Direct calculation of variable t leads to

$$\begin{aligned} t &\equiv (q - q')^2 \\ &= -Q^2 - 2E_\gamma(\nu - \sqrt{\nu^2 + Q^2}\cos\theta_{\gamma^*\gamma}). \end{aligned} \tag{5.2}$$

Here, the dependence on photon energy E_γ leads to a large uncertainties in the reconstruction of t. Due to the small magnitude of t compared with Q^2 and E_γ, the resolution of E_γ, which is about a couple of percents, leads to a large resolution in t. This can be eliminated considering the constrained variable t_c instead of t. Within the assumption that the process is elastic ($M_X = m_p$, where M_X is defined in Eq. 5.4) the constraint four-momentum transfer t_c can be calculated without using the photon energy

$$t_c = \frac{-Q^2 - 2\nu(\nu - \sqrt{\nu^2 + Q^2}\cos\theta_{\gamma^*\gamma})}{1 + \frac{1}{m_p}(\nu - \sqrt{\nu^2 + Q^2}\cos\theta_{\gamma^*\gamma})}. \tag{5.3}$$

Such a definition improves the resolution of t by one order of magnitude [Ell04], even though only in the case of elastic process where the target proton/deuteron is considered as a free particle the t_c equals to t. In the case of background processes the relation between t_c and t is not obvious. Differences between t_c and t appear also for coherent and incoherent processes. The latter is expected due to the fact that the nucleons in the deuteron are not free and possess a Fermi motion. However, the Monte Carlo simulations show that for coherent and incoherent processes the t_c and t are strongly correlated, which allows to use t_c in the following analysis. This is not the case for associated processes, however the latter ones are not the main processes of interest in current analysis. On the left panel of Figure 5.5 the distribution of kinematic variable $-t$ is shown for the exclusive sample of 2005 year, and on the right panel the correlation between $-t$ and $-t_c$ is presented. The smeared distribution of $-t$ versus $-t_c$ originates from the limited resolution of the calorimeter and possible contribution of the background processes in the total measured signal.

In the data analysis an upper cut of $|t_c| < 0.7\,GeV^2$ was applied in order to suppress the background contribution. The left plot in Figure 5.6 shows the Monte Carlo simulated

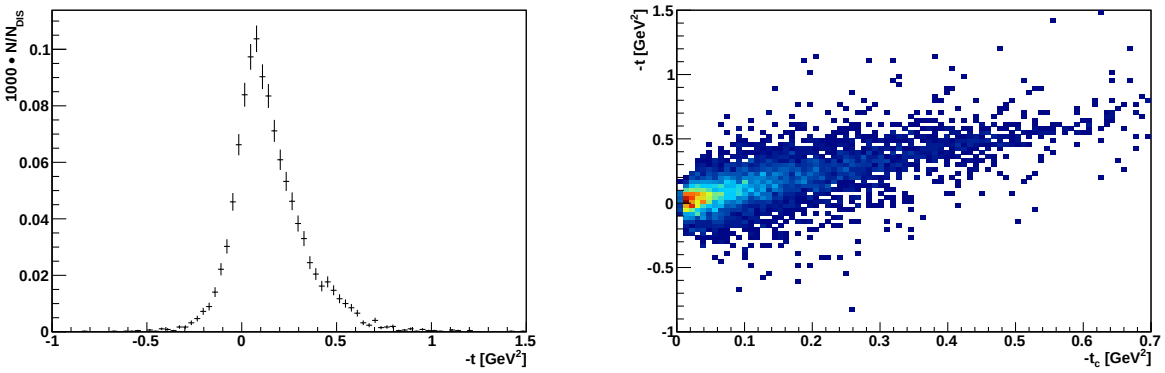

Figure 5.5: The distribution of the variable $-t$ (left panel) and the correlation between $-t$ and $-t_c$ (right panel).

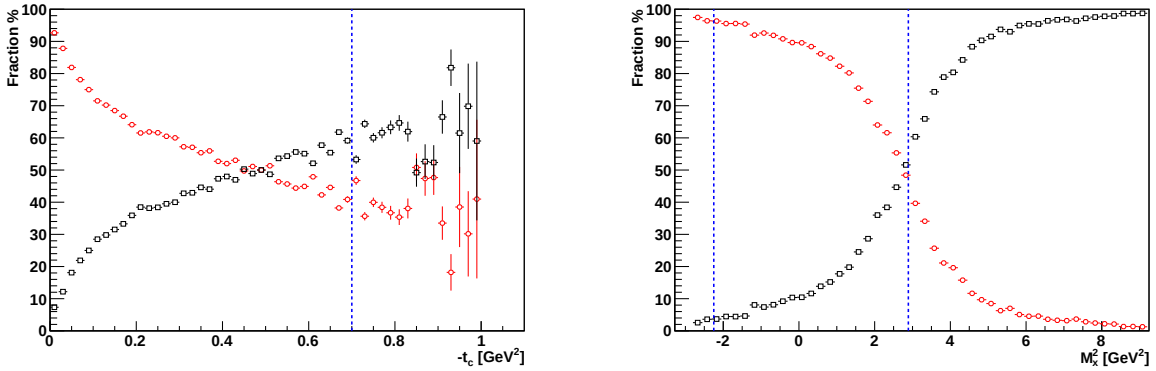

Figure 5.6: The Monte Carlo simulated fractional contributions of the signal and background processes are shown in bins of t_c (left panel) and in bins of squared missing mass M_X^2 (right panel).

fractional contributions of signal and background processes. Note that this constraint cuts a negligible amount of data, as the typical values of $-t_c$ are well below $1\,GeV^2$.

The applied constraints on opening angle $\theta_{\gamma^*\gamma}$ and t_c can not totally exclude the non-exclusive events. The further improvement of exclusivity of the data set is possible by means of missing mass technique. The squared missing mass is defined as

$$\begin{aligned} M_X^2 &= (q + p - q')^2 \\ &= m_p^2 + 2m_p(\nu - E_\gamma) + t. \end{aligned} \tag{5.4}$$

As in the case of t, the photon energy also enters in the calculation of M_X^2, resulting in a limited resolution of missing mass. As a consequence, the distribution of M_x^2 reaches negative values. In practice their is no need to consider the M_X rather than M_X^2. However in previous analysis the final exclusive sample of events was selected requiring the missing mass to be $-1.5\,GeV < M_x < 1.7\,GeV$ or respectively for the squared missing mass $-2.25\,GeV^2 < M_X^2 < 2.89\,GeV^2$. This exclusive window was obtained from a Monte Carlo studies performed in [Ely02]. In that studies the resolution of M_X^2 was estimated to be $1.840\,GeV^2$, with central value of $1.502\,GeV^2$, so the resolution in M_X was approximated according to

$$\delta M_X = \frac{d(M_X)}{d(M_X)^2}\delta M_X^2 = \frac{1}{2M_X}\delta M_X^2 \approx 0.8GeV. \tag{5.5}$$

The exclusive window was chosen as $-3\delta M_X$ below and only $+1\delta M_X$ above the proton mass, as the missing mass of the background processes is larger. In this analysis of DVCS on deuteron, the upper cut on M_X^2 distribution was studied using a Monte Carlo simulations. The result is shown on the right plot of Figure 5.6, where the fractional contributions of signal and background processes are presented versus the squared missing mass. The vertical lines on the plot represent the chosen exclusive window, which exactly indicates the point where the background starts to dominate over the signal. Finally the allowed intervals in Q^2 and x_N were limited by $Q^2 < 10\,GeV^2$ and $0.03 < x_N < 0.35$, in order to fix the kinematic coverage. This final sample of events refers to as an exclusive sample.

Note that in the above presented procedure of event selection, various kinematic variables were reconstructed using the proton mass, although in the total yield also the

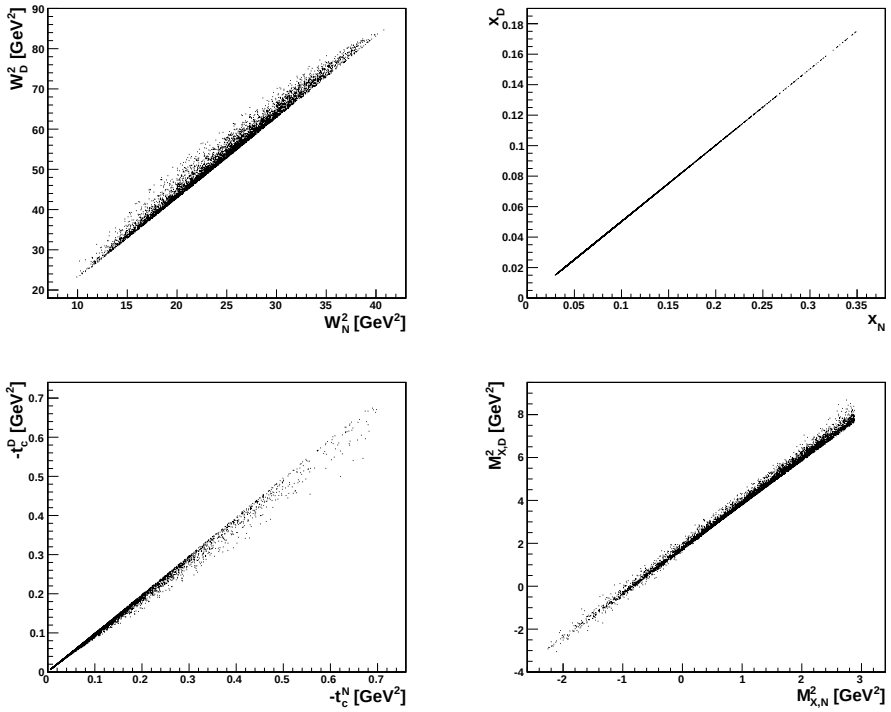

Figure 5.7: The correlations between kinematic variables calculated with proton and deuteron masses. On the top the inclusive variables W^2 and x are shown, and on the bottom the exclusive variables t_c and M_X^2.

coherent process on the deuteron contributes. Since the recoiled target particle remains undetected, one can not clearly separate the coherent and incoherent processes. Therefore, in the reconstruction of the kinematic variables either proton or deuteron mass can be chosen. However, as can be seen from Figure 5.7 both inclusive and exclusive variables defined with proton and deuteron masses are strongly correlated. Hence, changing the target mass in the calculations of certain kinematic variables, the corresponding values of kinematic cuts will be changed only.

5.2.4 Luminosity and Normalization

In the current report, the presented results of the asymmetries were extracted using the yield of DVCS/BH events, which are normalized to either time integrated luminosity or to number of DIS events. The relation between observed experimental event rate R and the cross section of the studied process is given by

$$R = \sigma \mathcal{L} \mathcal{E}. \tag{5.6}$$

Here, the $\mathcal{E}$ denotes the efficiency and receives contributions from the detector dead time, trigger and tracking efficiencies, and other effects. Hence, the normalization of measured event rate to absolute cross section requires a careful accounting for the efficiencies. From the other side, one can use the proportionality of time integrated luminosity to the rate of accepted deep inelastic scattering events for the relative normalization of the asymmetries. Therefore, assuming that the experimental setup did not changed

$$\frac{N_{DIS,1}}{N_{DIS,2}} = \frac{\int_1 dt\mathcal{L}}{\int_2 dt\mathcal{L}}. \tag{5.7}$$

Here, the indices (1,2) denote different data sets. This method of normalization is applicable only for the data collected on an unpolarized target. As the HERA lepton beam is always longitudinally polarized, the experimental yield of DIS events on a longitudinally polarized target contains a double-spin dependent contribution. This breaks the constant proportionality between the number of DIS events and time integrated luminosity. Therefor, for the normalization of the asymmetries from longitudinally polarized deuterium data the total number of DIS can not be used anymore. Instead the time integrated luminosity was used for the normalization of the asymmetries defined in section 3.4.2. Other problem with the DIS normalization occurs when combining data sets taken in different years. Due to the changes in apparatus as well as accumulated radiation damage together with possible misalignment of the detector components with respect to each other and with respect to a beam, the constant of proportionality between number of DIS events and time integrated luminosity can differ from year to year. Note, that the DIS normalization is not sensitive to dead time corrections or global tracking inefficiencies, as the DIS events as well as the DVCS events will be affected in the same way. It could be sensitive only to trigger inefficiencies. This allows to obtain precise asymmetries from the data on an unpolarized deuterium.

At HERMES the measurement of the luminosity is based on the knowledge of the cross sections of Bhabha and Moller scattering. The coincidence rate R_{LUMI} of such events, measured by the luminosity monitor, is selected as:

$$L = C\frac{A}{Z}\int dt R_{LUMI}, \tag{5.8}$$

where A denotes the number of nucleons per nucleus and Z denotes the number of protons per nucleus. The uncertainty in the measurement of the luminosity comes from the uncertainty of the determination of luminosity constant C, which is obtained from Monte Carlo simulations. As the luminosity constant depends on the beam position, slopes and also on the charge of the beam, it is provided separately for each data taking year. The values of the luminosity constants for the data collected on a longitudinally polarized deuterium are $C = 417 \pm 30\, mbarn^{-1}$ for the years 1999 and 2000, while it is reduced by a factor of about 0.6 for the year 1998 [Els02]. The uncertainty of the luminosity constant results in about 7.2% uncertainty in the measurement of integrated luminosity The integrated luminosities obtained in this way are used for the normalization of asymmetries from the data collected on a longitudinally polarized deuterium target.

5.2.5 Summary of event selection

The result of the event selection, that was described in previous sections is summarized in the Table 5.3. Here the numbers of final exclusive events, are listed for different data taking years and different configurations of beam charge, beam helicity and target spin projection. Also presented are the numbers of DIS events, together with the luminosity averaged values of beam and target polarization. The data productions used in this analysis are mentioned in the table as well. Note that from 1998 to 2000 HERMES has collected data on both unpolarized and longitudinally vector polarized deuterons.

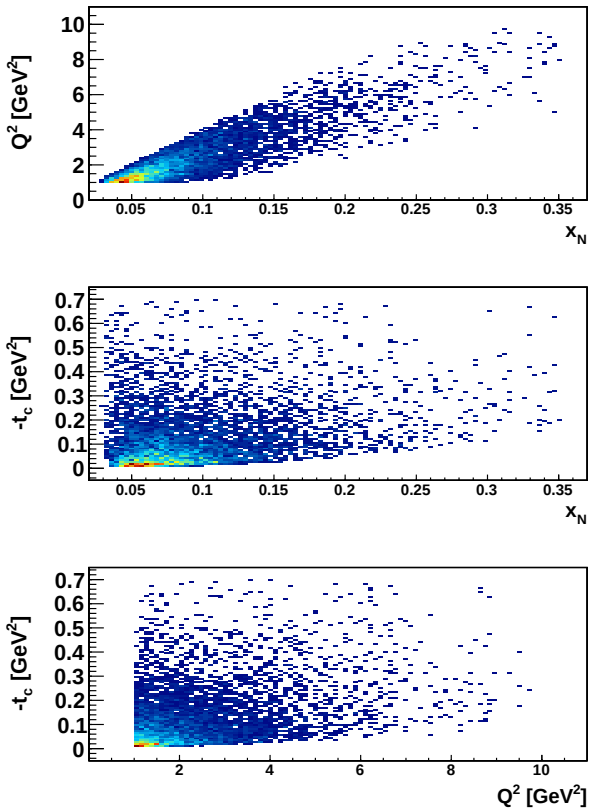

Figure 5.8: The correlations between kinematic variables Q^2, x_N and t_c.

Data with electron beam were accumulated in 1998 and in 2005. Up to 1998 the beam helicity was fixed within one year of data taking, while after that the helicity of the beam was reversed approximately every two months. The average beam polarization was typically lower for the electron data. As a consequence, in former analysis for the extraction of target spin asymmetry the beam helicity balancing cuts were applied, in order to reduce the net beam polarization. In the present report the beam balancing cuts were omitted. Instead a combined analysis was performed (described in section 5.4), that allows a simultaneous extraction of single-spin asymmetries together with double-spin asymmetry.

The final results of the asymmetries will be presented in bins of kinematic variables $-t_c$, x_N and Q^2. In Figure 5.8 the correlations between those variables are presented for

$-t_c[GeV^2]$	x_N	$Q^2[GeV^2]$
0.00-0.03	0.03-0.06	1.0-1.4
0.03-0.06	0.06-0.08	1.4-1.8
0.06-0.10	0.08-0.10	1.8-2.4
0.10-0.20	0.10-0.13	2.4-3.2
0.20-0.35	0.13-0.20	3.2-4.5
0.35-0.70	0.20-0.35	4.5-10.0

$-t_c[GeV^2]$	x_N	$Q^2[GeV^2]$
0.00-0.06	0.03-0.07	1.0-1.5
0.06-0.14	0.07-0.10	1.5-2.3
0.14-0.30	0.10-0.15	2.3-3.5
0.30-0.70	0.15-0.35	3.5-10.0

Table 5.2: The binning used in the analysis of data collected on an unpolarized deuterium is given in the left side table. In the right side the binning used in the analysis of longitudinally polarized deuterium data is given.

Year	Target State	Beam Charge	Beam Helicity	$N_{excl.}$	N_{DIS}	P_{Beam}	P_{Target}
96d0	unpol	+	+	1586	1530286	51.644 %	-
96d0	unpol	+	-	-	-	-	-
97d1	unpol	+	+	-	-	-	-
97d1	unpol	+	-	1843	1752367	-51.054 %	-
98d0	unpol	-	+	-	-	-	-
98d0	unpol	-	-	1015	920076	-30.692 %	-
99c0	unpol	+	+	193	172563	41.751 %	-
99c0	unpol	+	-	26	31592	-55.230 %	-
00d2	unpol	+	+	271	242563	55.809 %	-
00d2	unpol	+	-	1128	1058919	-58.449 %	-
05c1	unpol	-	+	2669	2348513	37.714 %	-
05c1	unpol	-	-	2606	2346854	-35.467 %	-
98d0	+	-	+	-	-	-	-
98d0	+	-	-	539	458171	-50.925 %	85.6 %
98d0	-	-	+	-	-	-	-
98d0	-	-	-	500	455906	-50.893 %	-85.6 %
99c0	+	+	+	285	252984	51.789 %	83.2 %
99c0	+	+	-	242	263712	-54.689 %	83.2 %
99c0	-	+	+	306	237930	51.817 %	-83.2 %
99c0	-	+	-	263	235358	-54.652 %	-83.2 %
00d2	+	+	+	1521	1417381	52.397 %	85.1 %
00d2	+	+	-	787	769102	-53.676 %	85.1 %
00d2	-	+	+	1625	1476289	52.467 %	-84.0 %
00d2	-	+	-	826	760053	-53.669 %	-84.0 %

Table 5.3: The numbers of exclusive and DIS events for different data taking years and different configuration of beam charge, beam helicity and target spin projection. together with luminosity averaged values of beam and target polarization.

the exclusive data sample from the year 2005. The inclusive variables x_N and Q^2 are highly correlated within the HERMES acceptance, while their is no strong correlation between those two variables with $-t_c$. In Table 5.2 the kinematic ranges (bins) of the above mentioned variables are presented that were chosen for the presentation of final results on asymmetries. The analysis of data on an unpolarized deuteron was performed in six bins for each kinematic variable, while the analysis of data on longitudinally polarized deuteron, due to lower statistics, was performed in four bins. The ranges of the bins were chosen in a way that gain approximately similar amount of events in each bin. Also it was required that the respective resolutions of the variables were smaller than the widths of the bins and the full coverage of the ϕ acceptance was ensured in each bin.

According to HERMES convention, all results need to be cross-check by independent coworkers. The cross-check of current analysis was performed in two steps. First the event selection procedure was cross-checked, i.e. the numbers of DIS and exclusive events were checked for all the analyzed data sample. In the second step the extraction procedure which is described in section 5.4 was cross-checked. The cross-check was done by G. Hill, D. Mahon (Glasgow University) and H. Marukyan (Yerevan Physics Institute), and the results can be found in [MHMM08, MM09].

5.3 Monte Carlo simulation

In this section the Monte Carlo simulation of the DVCS/BH processes, together with the simulation of background processes is considered. A precise simulation of all relevant processes is one of the essential requirements for the correct treatment of the measurements. Monte Carlo simulations are widely used for estimation of various systematic effects due to the detector response. They also provide a quantitative information about signal to background ratio in different kinematic domains and are used for motivated choice of kinematic cuts, as was discussed in previous sections.

The Monte Carlo production chain can be considered in three steps. At first, generation of various physics processes is carried out by special packages referred to as Generator of Monte Carlo (GMC). Depending on the specific type of considered process, various event generators need to be used. The output of the GMC packages does not contain any information about the geometry and the responses of certain detector components of the HERMES spectrometer. Hence, for the implementation of the acceptance and particle interaction effects , in the second step of Monte Carlo production, the generated events pass through Hermes Monte Carlo package (HMC). HMC is based on the GEANT3 package [Bru78] and contains a precise model of each component of the spectrometer and the target. The geometry and material of the different volumes can be set externally to the HMC package. This allows to take care of possible effects caused my the relative alignment of the detector components. The latter is important when combining data from different years and with different alignments. HMC tracks the particles through the detector and

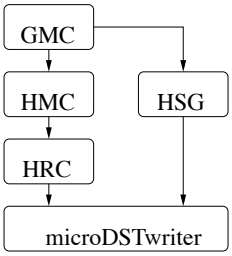

Figure 5.9: A diagram illustrating Monte Carlo Production chain at HERMES.

simulates all the possible interactions with the material in different components of the spectrometer. The output of the HMC contains all the responses of the detectors like energy depositions of the particles or signals from the wires of tracking chambers. In addition HMC output contains extra information about particle types and the kinematic parameters originally generated by the GMC, thus allowing to perform a spectrometer resolution studies. Finally the output of HMC passes through HERMES Reconstruction (HRC) package, which is used also for the production of experimental data. Here the detector responses are transferred to reconstruction of particle tracks exactly in a same way, like it was done for experimental data. Afterwards the μDSTwriter stores all the information about particle types and tracks in the μDST files, which have compatible structure with the ones from real experimental data. The above discussed steps of Monte Carlo production are illustrated in Figure 5.9. Monte Carlo productions generated in the full chain GMC+HMC+HRC referred to as fully tracked productions. Since the fully trucked production are very time consuming, an alternative procedure exists, i.e. instead of complete detector simulation the HERMES Smearing Generator (HSG) can be used. Instead of tracking the particles through detector, the HSG uses the geometry of the

spectrometer and look-up tables that contain information about possible influence of the detectors on the position and momentum of the particles. Although the HSG production contains significant approximations, it can be used for the quick estimation of kinematic smearing effects and tracking inefficiencies , in a significantly shorter time intervals. All Monte Carlo productions used in the current analysis were tracked with the full HERMES Monte Carlo production chain, i.e. GMC+HMC+HRC.

5.3.1 Monte Carlo generators

In present analysis three Monte Carlo generators *gmc_dvcs*, *gmc_dual* and *gmc_DISNG* are used for the simulation of the relevant processes.

The *gmc_dvcs* generator is used for the simulation of elastic DVCS/BH events and the BH events with excitation of resonances (associated processes). The cross sections of an unpolarized BH process are simulated based on the Mo-Tsai formalism [MT69]. The latter is applied for both nucleons and deuteron. For the calculation of unpolarized coherent BH cross section within the Mo-Tsai formalism, only two electromagnetic form factors are needed, that were taken from [Ste75]. The doubly polarized cross sections are available only for nucleons. The double spin dependent part of the cross sections is adopted from [BMK02].

The *gmc_dvcs* generator simulates also the associated BH processes with resonance excitation. The mass of the final unobserved hadronic state was generated between 1.1 and $2\,GeV$. The W dependence of the total $\gamma^* p(n)$ cross section was modeled according to Brasse parameterization [Bra76]. The individual cross sections for single-meson production channels were modeled according to MAID2000 model [DHKT99].

The simulation of elastic DVCS process on nucleons is based on the analytic expressions of the cross sections from [BMK02]. In *gmc_dvcs* generator the parameterization of GPDs is taken from [VGG99]. Within this parameterization, five different variants of the model were suggested in [KN02], where only three GPDs $H, \widetilde{H}$ and E are considered.

- The three GPDs $H, \widetilde{H}$ and E are not skewed and factorize in x and t.
- The GPDs are skewed within the double-distribution formalism from [Rad99] and the t-dependence of GPDs is factorized. The slope parameter b is set to 1.
- The same as the previous model, but with the slope parameter set to 3.
- The same as model two, but the double-distribution ansatz was expanded by adding a D-term according to the predictions of the chiral quark-soliton model. The slope parameter is set to 1.
- The same as the previous model, but with the slope parameter set to 3.

Although several GPD models exist that can be used for the simulation of coherent DVCS process on deuteron, currently non of them was precisely implemented in the generator. Instead, in the *gmc_dvcs* generator the coherent DVCS process on deuteron was simulated as modulation factor of the coherent BH cross section $\sigma_{DVCS,coh.} = \sigma_{BH,coh} \cdot (1 + \lambda A_{LU})$, where the prediction for A_{LU} was taken from [KM04]. Due to lack of information, also the associated DVCS process is not included in the generator. The incoherent DVCS/BH process is implemented according to [Ber72], where the bound state effects are taken into account. The latter is done by adding a suppression factor that modifies the electric form factor of proton [Ste75], under the assumption that the electric form factor

of neutron can be neglected. The detailed description of the *gmc_dvcs* generator can be found in [Kra05].

The *gmc_dual* generator is an alternative to *gmc_dvcs* to simulate the elastic BH/DVCS cross sections. It is based on the dual parameterization of GPDs discussed in [GT06]. The generator dose not contain any information about GPDs $\widetilde{H}$ and $\widetilde{E}$, hence it can be used only for unpolarized targets. For the deuteron target the coherent process is modeled in similar way as in *gmc_dvcs*. No suppression is applied for the incoherent channel, i.e. the nucleons in a deuteron are considered as a quasi-free particles. The generator contains both factorized and Regge ansatz's for modeling the t-dependence of GPDs. The associated processes were not implemented in the *gmc_dual* generator.

The *gmc_DISNG* generator simulates semi-inclusive DIS processes. It is one of the main generators used at HERMES. The generator is an extension of the leptoproduction generator LEPTO [Ing97] which simulates polarized DIS processes. The fragmentation and decay of the produced hadrons is simulated with JETSET [Sjo95], which in turn is based on the LUND string model [AGIS83]. The used LUND model was tuned for HERMES kinematics [Hil05]. Radiative processes are included with RADGEN [Aku99], which provides simulation of both the elastic and associated BH processes. However, in this code the simulation of the associated BH process is found to overestimate the cross section [Kra05]. Hence, in the following the *gmc_DISNG* will be used only for simulation of semi-inclusive DIS processes.

Not included in the above discussed Monte Carlo generators are the radiative corrections for DVCS process and also for BH process, i.e. higher order radiative corrections to elastic scattering, which can have a substantial impact on the simulation of the cross sections. Also one of the background processes, mainly the contribution of exclusive π^0 production was not considered in this report, as it was found that the contribution from exclusive π^0 production is less than 1% for both hydrogen [Zei09] and deuterium [Kra05] targets. The simulation of exclusive π^0 production in the above mentioned references was carried out by the *gmc_exclpion* generator, which is based on the GPD model described in [VGG99].

5.3.2 Data to Monte Carlo comparison

As it was mentioned above, the Monte Carlo events are reconstructed by HRC and stored in μDST files. This allows to analyse the Monte Carlo data in a same way as the real data, omitting only the data quality requirements, as it is assumed that in Monte Carlo the particle identification is ideal. In order to compare the experimental data with Monte Carlo, the output from different Monte Carlo generators needs to be combined. In Figure 5.10 the comparison between real data and the Monte Carlo for kinematic variables Q^2, x_N, $\theta_{\gamma\gamma*}$, ϕ, E_γ, E_{lepton}, M_x^2 and $-t_c$ are shown. In all figures except from a M_x^2 distribution, the data correspond to an exclusive sample of events. The Monte Carlo data were obtained from the combined *gmc_dvcs* and *gmc_DISNG* yield. From the *gmc_dvcs* generator the elastic/associated BH processes were chosen. The DVCS process was not included for the comparison in Figure 5.10, to avoid a model dependent uncertainties. The process of semi-inclusive production of π^0 was selected from *gmc_DISNG* production. The presented data points correspond to whole data sample collected on an unpolarized deuterium target. Also are presented the contributions of all relevant processes from Monte Carlo and the ratio of Monte Carlo and data. The latter indicates a good agreement between data and Monte Carlo. The existing differences can be caused by the missing DVCS process, which is strongly model dependent. From the other side consideration

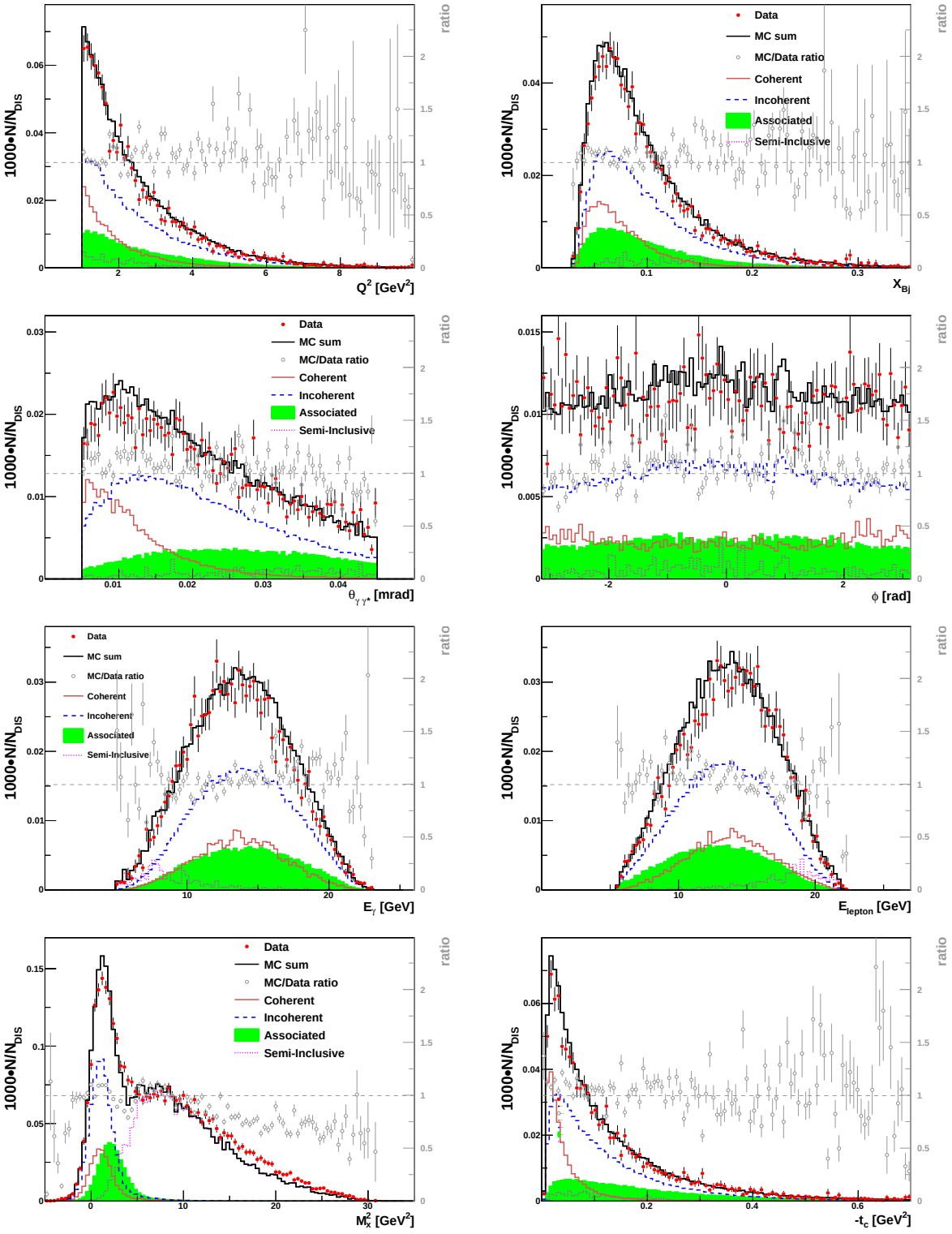

Figure 5.10: Comparison between the Monte Carlo simulation (solid lines) and the experimental data (solid points). Also shown are individual contributions from elastic coherent (solid lines), elastic incoherent (dashed -doted lines), associated BH processes (shaded area), and semi-inclusive processes (dotted line). The open points represent Monte Carlo to data ratio.

of DVCS process in the data to Monte Carlo comparison requires precise simulation of radiative corrections, which currently are not available for the HERMES kinematic conditions. Detailed comparison of data with five different Monte Carlo models can be found in [Ye07], which indicates a small influence of the DVCS process on the estimation of the fractional contributions of various processes in the measured signal.

5.3.3 Detector Resolution and Estimates for the Fractional Contributions of Relevant Processes

Since the current report contains analysis of large amount of data collected on both unpolarized and longitudinally polarized Deuterium target, it is expedient to perform the kinematic dependences of the measured asymmetries. For an appropriate choice of binning in a certain kinematic quantity, the resolutions of that quantity needs to be studied, to be sure that the chosen bin widths are larger than the measurement accuracy of the quantity.

The resolutions can be studied from a Monte Carlo simulations, comparing the generated values of the kinematic variables with reconstructed ones. They are obtained as a standard deviations from the differences between reconstructed and generated variables. While in certain cases, it is useful to consider the width obtained from a Gaussian fit to the difference between reconstructed and generated values, in order to suppress the contributions from a long tails originating from a Bremsstrahlung in the detector. The momentum and angular resolutions of DIS leptons are shown in Figure 5.11. The resolutions are obtained from a Gaussian fit and are found to be below 2.6% and 0.9 $mrad$ for momentum and scattering angle respectively. An increase of the momentum resolution for faster leptons is caused by smaller deflection due the the spectrometer magnet.

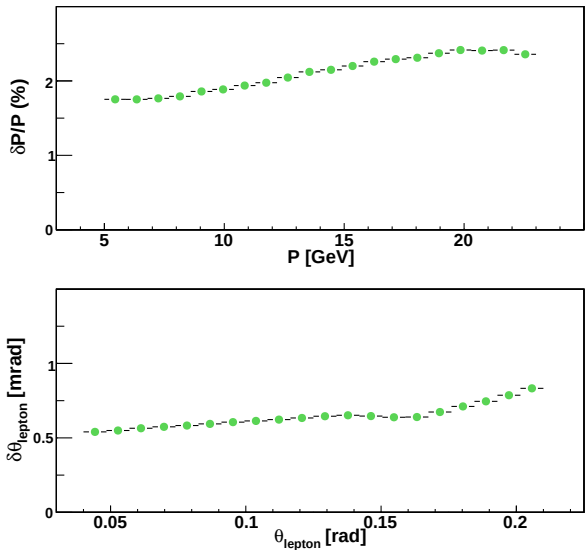

Figure 5.11: The momentum (top) and angular (bottom) resolutions of the DIS leptons obtained from a Gaussian fit.

For kinematic variables Q^2, x_N, $-t_c$, $-t$, ϕ, $\theta_{\gamma\gamma*}$, E_γ, z_{vtx}, ϕ_{lepton} the average differences between reconstructed and generated values are shown in Figure 5.12 as a function of corresponding reconstructed variable. They were derived from an exclusive Monte Carlo sample. Also are shown the mean values obtained from a fit with simple Gaussian function to the difference of reconstructed and generated variables. For the same

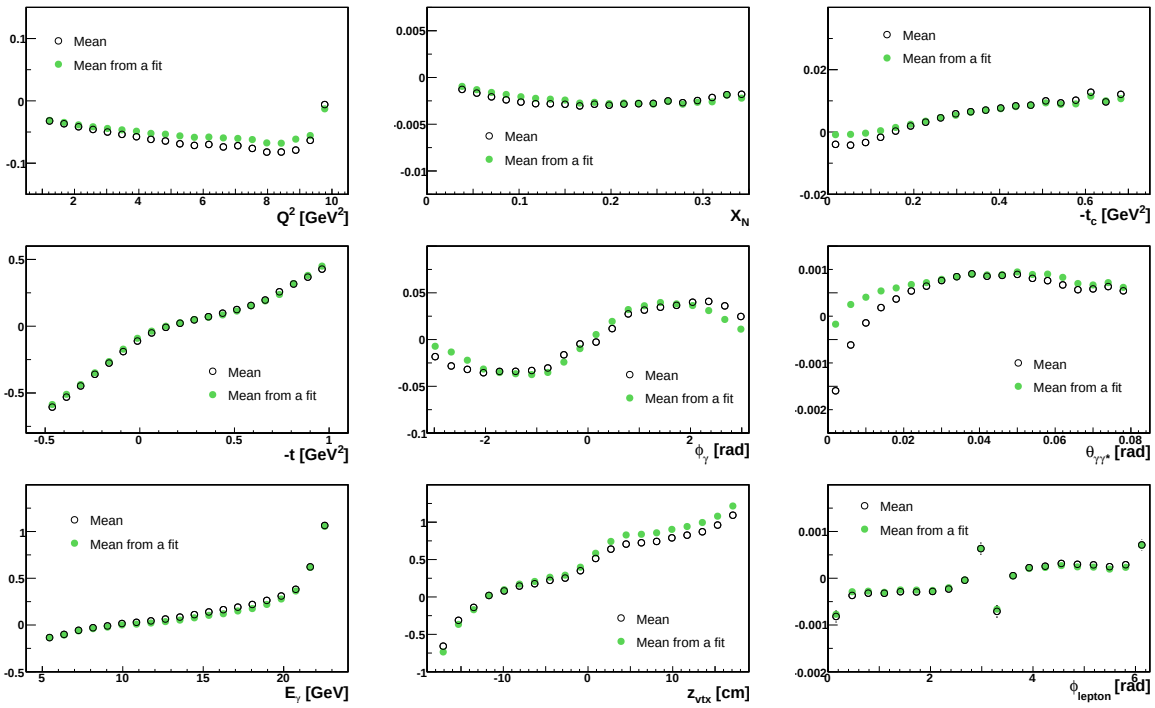

Figure 5.12: The mean of the distributions and the mean from a simple Gaussian fit to the difference between reconstructed and generated kinematic variables as a function of reconstructed variable.

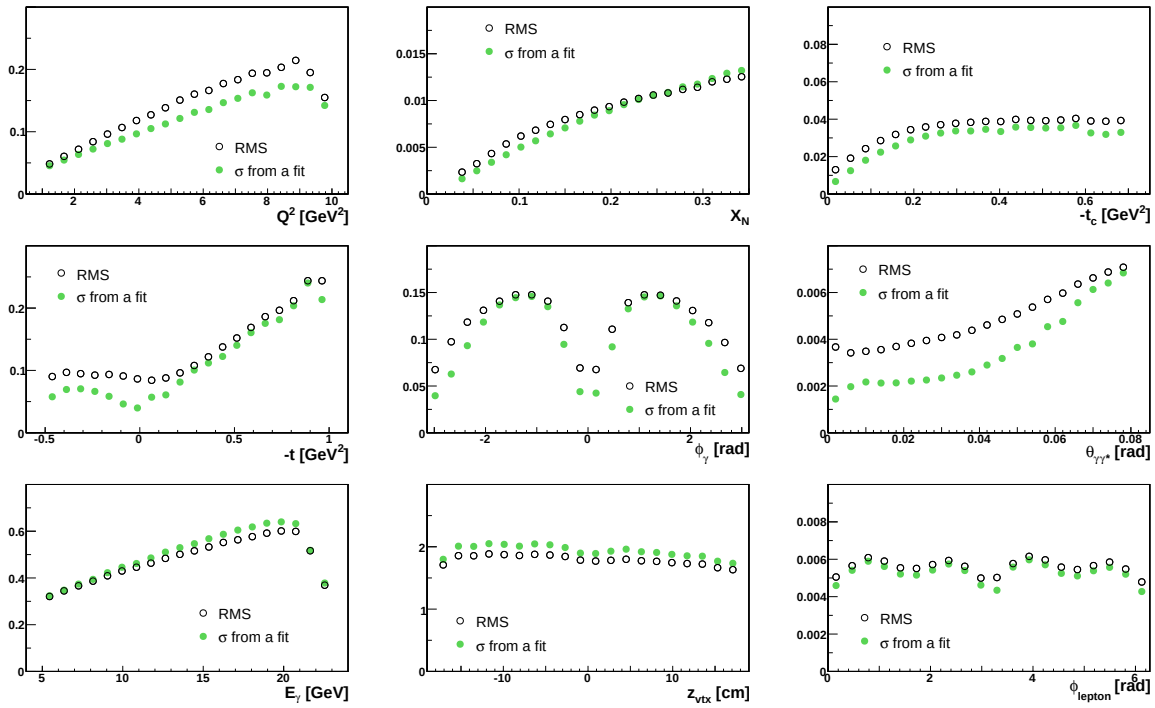

Figure 5.13: The RMS and the standard deviations from a simple Gaussian fit to the difference between reconstructed and generated kinematic variables as a function of reconstructed variable.

set of kinematic variables the resolutions and the widths of Gaussian fits are shown in Figure 5.13. Due to the specific kinematics of fixed-target experiment the Q^2 and x_N are strongly correlated and the precision of their reconstruction is sensitive to the resolution of the momentum and scattering angle. The obtained resolutions for Q^2 and x_N ensure the reasonable choice of binning given in Table 5.2. Same holds also for t_c, which has a resolution of about $0.04\,GeV^2$ for relatively large values $-t_c$, while for smaller values ($-t_c < 0.06\,GeV^2$) the resolution is about $0.01\,GeV^2$. Comparing the obtained resolutions for $-t_c$ and $-t$ one can see significant improvement of situation in the case of constrained variable $-t_c$. This is a consequence of large resolution in measurement of photon energies E_γ, which is about $500\,MeV$ for a typical energy values of the exclusive sample $15\,GeV$. As was mentioned in section 5.2.3 the choice of constrained variable t_c instead of t leads to a smearing of events for background processes toward lower values of $-t_c$. This was studied in details in [Ell04] for both associated and semi-inclusive DIS processes. The observed magnitude of the background event migration increases with increasing $-t_c$ and appears to be quit large for relatively large values of $-t_c$. While due to the decrease of the total exclusive yield at larger values of $-t_c$ and consequently also for the background

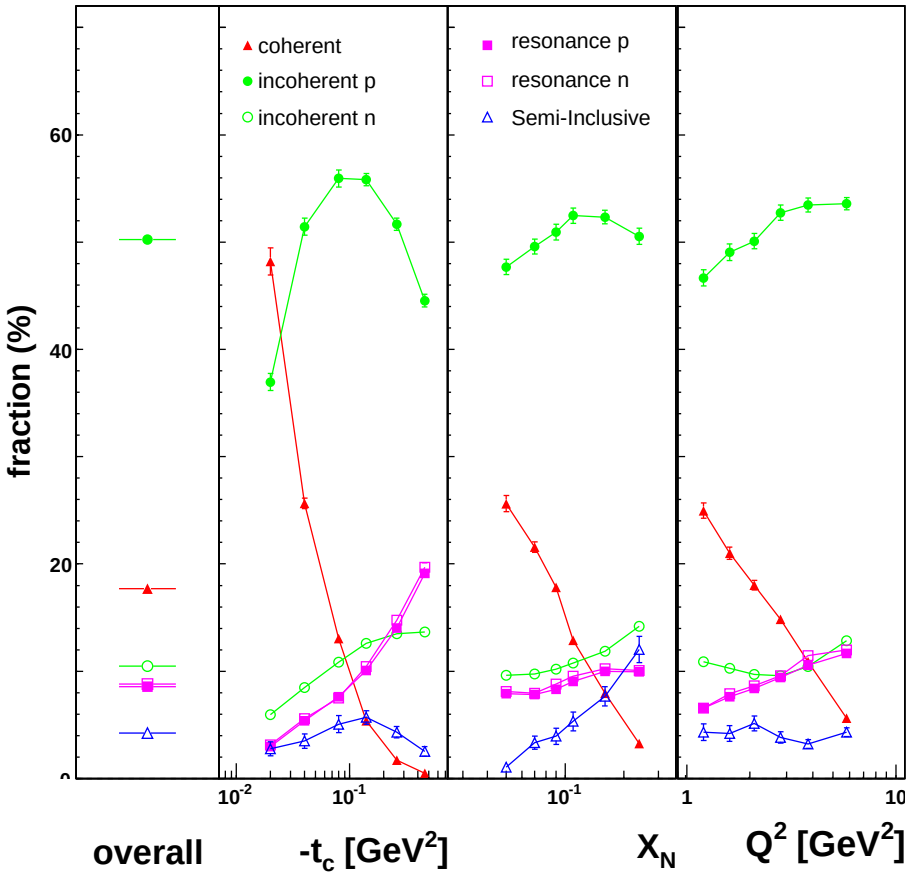

Figure 5.14: Fractional contributions in the exclusive sample of events from coherent, incoherent, associated and Semi-inclusive DIS processes for the entire HERMES kinematics (left column) and in 6 bins in $-t_c$, Q^2 and x_N, obtained from Monte Carlo. The contributions of incoherent and associated processes are shown separately for proton and neutron.

processes, the absolute size of his effect is expected to have a negligible impact on the measurement.Therefore the choice of constrained variable t_c appears to be reasonable. On the other side the migration of the background events can be accounted in the estimation of fractional contributions of relevant processes in the exclusive sample.

For the measurement of azimuthal asymmetries, the precision of the reconstruction of azimuthal angle ϕ is of special importance. It's reconstruction is based on the determination of the scattering and production planes. The scattering plane is defined by the momentum vectors of incident and scattered leptons, while the production plane is defined by the momentum vectors of virtual and real photons, $\overrightarrow{q^*}$ and $\overrightarrow{q}$ respectively. The reconstruction of virtual photon momentum vector is directly related to the reconstruction of scattered lepton momentum vector, while for the determination of real photon momentum vector the precise knowledge of the photon hit position in the calorimeter and the vertex position in the target are required. The resolution of reconstructed hit positions in the calorimeter was studied in details in [Kra05, Ely02] and was found to be of an order $0.5\,cm$. The precision of the measurement of azimuthal angle depends on measured uncertainty of polar angle $\theta_{\gamma\gamma^*}$ between virtual and real photons. The resolution of the polar angle $\theta_{\gamma\gamma^*}$ is less then $3\,mrad$ in the region $0.005\,rad < \theta_{\gamma\gamma^*} < 0.045\,rad$, while it increases with the increasing value of $\theta_{\gamma\gamma^*}$ above $45\,mrad$. Therefore, in order to obtain a reliable measurement of azimuthal angle ϕ, the lower limit on the polar angle $\theta_{\gamma\gamma^*} > 0.003\,rad$ should be applied. Nevertheless, the investigation of the resolution of azimuthal angle versus polar angle (not shown here) and also the estimates for the smearing effects indicate, that an appropriate choice of lower limit on polar angle is $0.005\,mrad$ [Kra05, Kop06].

Throughout this analysis the Monte Carlo simulations were used also for the estimation of possible contributions of the relevant processes in the measured total yield. As an example, in Figure 5.14 the fractional contributions of coherent, incoherent, associated and semi-inclusive DIS processes in the exclusive sample of events are shown. The contribution of incoherent and associated processes are shown separately for proton and neutron. The

Kinematic bin		Quasi elastic(%)	Coherent(%)	Associated(%)	Semi-inclusive(%)
overall		60.4 ± 0.3	17.7 ± 0.2	17.7 ± 0.1	4.2 ± 0.3
$-t_c$ (GeV^2)	< 0.06	51.6 ± 0.6	36.4 ± 0.6	8.8 ± 0.1	3.1 ± 0.5
	0.06 - 0.14	67.1 ± 0.7	10.7 ± 0.1	16.8 ± 0.2	5.4 ± 0.6
	0.14 - 0.30	66.6 ± 0.6	3.0 ± 0.1	25.7 ± 0.3	5.1± 0.5
	0.30 - 0.70	59.9 ± 0.6	0.6 ± 0.0	36.9 ± 0.5	2.6 ± 0.4
x_N	0.03 - 0.07	57.4 ± 0.6	24.6 ± 0.6	16.4 ± 0.2	1.6 ± 0.3
	0.07 - 0.10	62.8 ± 0.7	18.9 ± 0.3	17.2 ± 0.2	4.0 ± 0.6
	0.10 - 0.15	62.7 ± 0.7	12.3 ± 0.2	18.9 ± 0.3	6.1 ± 0.8
	0.15 - 0.35	65.4 ± 0.7	5.3 ± 0.1	20.2 ± 0.3	9.1 ± 0.8
Q^2 (GeV^2)	1.0 - 1.5	57.8 ± 0.8	24.1 ± 0.6	13.9 ± 0.2	4.2 ± 0.7
	1.5 - 2.3	59.1 ± 0.7	19.4 ± 0.4	16.9 ± 0.2	4.6 ± 0.6
	2.3 - 3.5	61.0 ± 0.7	15.1 ± 0.3	19.6 ± 0.2	4.3 ±0.5
	3.5 - 10.0	65.7 ± 0.5	8.0 ± 0.1	22.6 ± 0.3	3.7 ± 0.3

Table 5.4: The fractional contributions of various processes that contribute in the exclusive sample. The fractions are obtained from the combined Monte Carlo data sample of *gmc_dvcs* and *gmc_DISNG* generators. The latter was used only for simulation of semi-inclusive processes.The fractions are given for the entire HERMES kinematics and in four bins of $-t_c$, x_N and Q^2.

fractions are given for the entire HERMES kinematics and for 6 bins in $-t_c$, Q^2 and x_N. The numerical values of the fractions are given in Tables 5.4 and 5.5 for 4 and 6 bins in $-t_c$, Q^2 and x_N, respectively. Note that in current analysis the contribution of exclusively produced neutral pions was not considered, as it was explained in section 5.3.3.

From Figure 5.14 and Tables 5.4 - 5.5 one can see that the coherent reaction contributes mainly at very small values of the momentum transfer to the target, while the incoherent process dominates elsewhere. The largest contribution from the coherent process appears in the first $-t_c$ bin (see Table 5.5). Requiring $-t_c < 0.01\,GeV^2$ can further enhance the coherent contribution to 66%, but only at the cost of a rapidly decreasing yield. In the following the $-t_c$ bins covering the range $0.00 - 0.06\,GeV^2$ will provide a measure of coherent effects. Meanwhile at large values of $-t_c$ the contribution from associated processes significantly increases. The proton contributes about 75% of the incoherent yield and the neutron about 25%, and included in these, nucleon resonance production contributes about 22% of the incoherent yield. The incoherent reaction on a proton dominates that on a neutron because of the suppression of the Bethe -Heitler amplitude on the neutron by the small elastic electric form factor at low and moderate values of the momentum transfer to the target. This is not the case for associated processes, where the single-photon yields on proton and neutron are approximately the same.

The contribution from semi-inclusive processes varies from 1% to 12%, depending on the kinematic conditions. It contributes about 4.2% for the entire HERMES kinematics, while the largest contribution appears at large values of x_N.

Kinematic bin		Quasi elastic(%)	Coherent(%)	Associated(%)	Semi-inclusive(%)
overall		60.4 ± 0.3	17.7 ± 0.2	17.7 ± 0.1	4.2 ± 0.3
$-t_c$ (GeV^2)	< 0.03	42.7 ± 0.9	48.1 ± 1.1	6.4 ± 0.2	2.8 ± 0.7
	0.03 - 0.06	59.9 ± 0.9	25.6 ± 0.5	11.0 ± 0.2	3.5 ± 0.7
	0.06 - 0.10	66.9 ± 0.9	13.0 ± 0.2	15.0 ± 0.3	5.1 ± 0.8
	0.10 - 0.20	68.4 ± 0.7	5.3 ± 0.1	20.6 ± 0.3	5.7± 0.6
	0.20 - 0.35	65.1 ± 0.6	1.7 ± 0.0	28.9 ± 0.4	4.3 ± 0.5
	0.35 - 0.70	58.3 ± 0.7	0.5 ± 0.0	38.7 ± 0.6	2.5 ± 0.5
x_N	0.03 - 0.06	57.0 ± 0.7	25.8 ± 0.7	16.1 ± 0.3	1.1 ± 0.3
	0.06 - 0.08	59.3 ± 0.7	21.4 ± 0.5	16.0 ± 0.3	3.3 ± 0.6
	0.08 - 0.10	61.2 ± 0.8	17.6 ± 0.4	17.3 ± 0.3	3.9 ± 0.8
	0.10 - 0.13	63.6 ± 0.8	12.7 ± 0.2	18.4 ± 0.3	5.3 ± 0.8
	0.13 - 0.20	64.2 ± 0.7	7.8 ± 0.1	20.3 ± 0.3	7.7 ± 0.9
	0.20 - 0.35	65.0 ± 0.9	3.2 ± 0.1	19.8 ± 0.4	12.0 ± 1.2
Q^2 (GeV^2)	1.0 - 1.4	57.1 ± 0.8	25.3 ± 0.7	13.3 ± 0.2	4.3 ± 0.8
	1.4 - 1.8	59.5 ± 0.9	20.9 ± 0.6	15.4 ± 0.3	4.2 ± 0.7
	1.8 - 2.4	60.5 ± 0.8	17.2 ± 0.5	17.2 ± 0.3	5.1 ± 0.7
	2.4 - 3.2	61.9 ± 0.8	15.0 ± 0.4	19.3 ± 0.3	3.8 ±0.5
	3.2 - 4.5	64.0 ± 0.7	10.9 ± 0.2	21.9 ± 0.3	3.2 ± 0.4
	4.5 - 10.0	66.5 ± 0.6	5.5 ± 0.1	23.7 ± 0.3	4.3 ± 0.4

Table 5.5: The fractional contributions of various processes that contribute in the exclusive sample. The fractions are obtained from the combined Monte Carlo data sample of *gmc_dvcs* and *gmc_DISNG* generators. The latter was used only for simulation of semi-inclusive processes. The fractions are given for the entire HERMES kinematics and in six bins of $-t_c$, x_N and Q^2.

5.4 Extraction of the amplitudes of azimuthal asymmetries

In the present analysis the asymmetries in the azimuthal distributions of real photons were fitted with maximum likelihood technique, which is widely used in high-energy physics [Ams08]. An important advantage of maximum likelihood method compared with least-squares method, is that it does not need a binned distribution in azimuthal angle ϕ. From the other side, maximum likelihood method does not provide any measure of goodness of fit like χ^2. Nevertheless, the goodness of fit can be still tested by fitting a binned distribution. In this section a brief introduction to maximum likelihood method is given, and its application to the present analysis is detailed.

5.4.1 Maximum likelihood fitting method

Suppose one has N sets of independently measured quantities $x_i = y_1, y_2, ...$, which are expected to be distributed by a probability distribution function (p.d.f.) $f(x_i, \theta)$. The latter depends on a set of unknown parameters θ, that had to be determined. The likelihood function $\mathcal{L}$ for a given set of measurements is defined as a product of p.d.f.s

$$\mathcal{L} = \prod_{i=1}^{N} f(x_i, \theta). \tag{5.9}$$

Hence, the likelihood function represents a joint probability of all measurement. In this context it follows, that for the set of apriori unknown parameters θ, which provide the most sufficient description of the measured data, the likelihood function will have a maximum. So the parameters θ can be determined by maximizing the likelihood function or equivalently minimizing the negative logarithm of it. The parameters θ are the solution of the system of equations

$$\frac{\partial ln\mathcal{L}}{\partial \theta_j} = 0, \quad j = 1, 2, .. \tag{5.10}$$

The inverse covariance matrix is given by

$$(\mathcal{C}^{-1})_{ij} = -\frac{\partial^2 ln\mathcal{L}}{\partial \theta_i \partial \theta_j}. \tag{5.11}$$

The precise determination of the unknown parameters strongly depends on the normalization of the likelihood function (joint probability) or the p.d.f. $f(x_i, \theta)$. The p.d.f. $f(x_i, \theta)$ is generally normalized to unity $\int f(x_i, \theta) = 1$, whereas in the maximum likelihood method it is not necessarily to be so. Moreover, in the experimental measurements the observed number of events (yield) very often has a Poisson fluctuation around its expected actual value. In this case it is more convenient to use an extended maximum likelihood method [Bar90], where the likelihood function is extended to

$$\mathcal{L} = \frac{[\mathbb{N}(\theta)]^N e^{-\mathbb{N}(\theta)}}{N!} \prod_{i}^{N} f(x_i, (\theta)), \tag{5.12}$$

where $\mathbb{N}(\theta)$ can be interpreted as a normalization of the extended p.d.f $\mathcal{F}(x_i, (\theta)) = f(x_i, \theta)\mathbb{N}(\theta)$

$$\mathbb{N}(\theta) = \int \mathcal{F}(x_i, \theta) dx. \tag{5.13}$$

The resulting negative logarithm of extended likelihood function will be

$$-\,ln\mathcal{L}_{EML}(\theta) = -\sum_{i}^{N} ln\mathcal{F}(x_i,\theta) + \mathbb{N}(\theta), \tag{5.14}$$

while the negative logarithm of a standard likelihood function is

$$-\,ln\mathcal{L}_{SML}(\theta) = -\sum_{i}^{N} ln\mathcal{F}(x_i,\theta) + Nln\mathbb{N}(\theta). \tag{5.15}$$

A comparison of the EML and SML methods with that of least-square method, performed on an experimental data, showed that the SML method fails with the correct determination of the uncertainties of the constant terms included in the fit function [LuY07]. Meanwhile the studies based on the Monte Carlo, showed that the EML method gives much better results compared with least-square method, when reconstructing known input asymmetries [Ye07]. A detailed comparison of EML and SML methods is given also in [Hill08] and [Mah10]. The results of the fits that will be presented in the following are extracted using the EML method.

5.4.2 Combined fit to the asymmetries from an unpolarized data

The data collected on an unpolarized deuterium target with both beam polarizations and both beam charges were combined, which allowed to define three asymmetries given in Eqs. 3.34 - 3.36. The distribution of the expectation value of the yield for scattering a polarized lepton beam from an unpolarized deuterium target is given by

$$\begin{aligned}\langle\mathcal{N}\rangle(P_\ell, e_\ell, \phi) &= L(P_\ell, e_\ell)\,\epsilon(e_\ell,\phi)\,\sigma_{\rm UU}(\phi) \\ &\times \left[1 + P_\ell \mathcal{A}_{\rm LU}^{\rm DVCS}(\phi) + e_\ell \mathcal{A}_{\rm C}(\phi) + e_\ell P_\ell \mathcal{A}_{\rm LU}^{\rm I}(\phi)\right].\end{aligned} \tag{5.16}$$

Here, L denotes the integrated luminosity, P_ℓ the longitudinal beam polarization, ϵ the detection efficiency, and $\sigma_{\rm UU}(\phi)$ the cross section for an unpolarized target averaged over both beam charges and both beam helicities, which is expressed as

$$\begin{aligned}\sigma_{\rm UU} \quad (\phi) &= \frac{x_D}{32\,(2\pi)^4\,Q^4}\frac{1}{\sqrt{1+\varepsilon^2}} \\ \times \quad &\left\{\frac{K_{\rm BH}}{\mathcal{P}_1(\phi)\mathcal{P}_2(\phi)}\sum_{n=0}^{2} c_n^{\rm BH}\cos(n\phi) + K_{\rm DVCS}\sum_{n=0}^{2} c_n^{\rm DVCS}\cos(n\phi)\right\}.\end{aligned} \tag{5.17}$$

The Eq. 5.16 can be used as a p.d.f. for the EML method. To obtain a normalization or a total number of events, let us consider a number of events $d\mathcal{N}$ in a small time $d\tau$ and phase space interval $dx = \{dQ^2 dx_{Bj} d|t| d\phi\}$ for the case of 100 % detection efficiency

$$d\mathcal{N}(x) = L(\tau) d\tau dx \sigma_{UU}(x)\Big[1 + e_\ell \mathcal{A}_{\rm C}(x) + P_\ell(\tau)\mathcal{A}_{\rm LU}^{\rm DVCS} + e_\ell P_\ell(\tau)\mathcal{A}_{\rm LU}^{\rm I}\Big]. \tag{5.18}$$

It is convenient to introduce an effective polarization as a product of a beam charge and polarization $P_{e\ell} = e_\ell P_\ell$ and change the integration variable from time τ to effective

polarization $P_{e\ell}$. Integrating the Eq. 5.18 over the effective polarization one gets

$$\int_{\substack{P_\ell>0,\\ e_\ell=+1}} \frac{d\mathcal{N}(x,P_{e\ell})}{dxdP_{e\ell}}dP_{e\ell} = \tag{5.19}$$
$$\overrightarrow{N}^{+}(x) = \overrightarrow{L}^{+}\sigma_{UU}(x)\Big[1+\mathcal{A}_{\rm C}(x)+\overrightarrow{P}^{+}\mathcal{A}_{\rm LU}^{\rm DVCS}(x)+\overrightarrow{P}^{+}\mathcal{A}_{\rm LU}^{\rm I}(x)\Big]$$
$$\int_{\substack{P_\ell<0,\\ e_\ell=+1}} \frac{d\mathcal{N}(x,P_{e\ell})}{dxdP_{e\ell}}dP_{e\ell} = \tag{5.20}$$
$$\overleftarrow{N}^{+}(x) = \overleftarrow{L}^{+}\sigma_{UU}(x)\Big[1+\mathcal{A}_{\rm C}(x)+\overleftarrow{P}^{+}\mathcal{A}_{\rm LU}^{\rm DVCS}(x)+\overleftarrow{P}^{+}\mathcal{A}_{\rm LU}^{\rm I}(x)\Big]$$
$$\int_{\substack{P_\ell>0,\\ e_\ell=-1}} \frac{d\mathcal{N}(x,P_{e\ell})}{dxdP_{e\ell}}dP_{e\ell} = \tag{5.21}$$
$$\overrightarrow{N}^{-}(x) = \overrightarrow{L}^{-}\sigma_{UU}(x)\Big[1-\mathcal{A}_{\rm C}(x)+\overrightarrow{P}^{-}\mathcal{A}_{\rm LU}^{\rm DVCS}(x)-\overrightarrow{P}^{-}\mathcal{A}_{\rm LU}^{\rm I}(x)\Big]$$
$$\int_{\substack{P_\ell<0,\\ e_\ell=-1}} \frac{d\mathcal{N}(x,P_{e\ell})}{dxdP_{e\ell}}dP_{e\ell} = \tag{5.22}$$
$$\overleftarrow{N}^{-}(x) = \overleftarrow{L}^{-}\sigma_{UU}(x)\Big[1-\mathcal{A}_{\rm C}(x)+\overleftarrow{P}^{-}\mathcal{A}_{\rm LU}^{\rm DVCS}(x)-\overleftarrow{P}^{-}\mathcal{A}_{\rm LU}^{\rm I}(x)\Big].$$

where the +/- sign in the superscript denotes the charge of the beam, while $\rightarrow$ / $\leftarrow$ denotes the beam helicity. The L and P are the integrated luminosity and luminosity averaged beam polarizations respectively for each state. Resolving the system of Eqs. 5.19 - 5.22, one can express the unpolarized cross section σ_{UU} and three asymmetries through normalized yields n=N/L and average values of the beam polarization of different states. The unpolarized cross section will be

$$\sigma_{UU}(x) = \frac{1}{2}\Bigg[\frac{\overrightarrow{N}^{+}(x)}{\overrightarrow{L}^{+}(1-\overrightarrow{P}^{+}/\overleftarrow{P}^{+})}+\frac{\overrightarrow{N}^{-}(x)}{\overrightarrow{L}^{-}(1-\overrightarrow{P}^{-}/\overleftarrow{P}^{-})}+ \frac{\overleftarrow{N}^{+}(x)}{\overrightarrow{L}^{+}(1-\overleftarrow{P}^{+}/\overrightarrow{P}^{+})}+\frac{\overleftarrow{N}^{-}(x)}{\overleftarrow{L}^{-}(1-\overleftarrow{P}^{-}/\overrightarrow{P}^{-})}\Bigg], \tag{5.23}$$

while substituting the expression of σ_{UU} from Eq. 5.23 into Eqs. 5.19 - 5.22 and integrating the latter ones over the x will yield in a total number of events or normalization of the extended p.d.f..

$$\mathbb{N}(\theta) = \int dx(\overrightarrow{N}^{+}(x,\theta)+\overrightarrow{N}^{-}(x,\theta)+\overleftarrow{N}^{+}(x,\theta)+\overleftarrow{N}^{-}(x,\theta))$$
$$\approx \sum_{i=1}^{N_{obs}} K(P_i,e_i)\Big[M_1+M_2\mathcal{A}_{\rm C}(x_i,\theta)+M_3\mathcal{A}_{\rm LU}^{\rm DVCS}(x_i,\theta)+M_4\mathcal{A}_{\rm LU}^{\rm I}(x_i,\theta)\Big] \tag{5.24}$$

where

$$K(P_i,e_i) = \begin{cases} \frac{1}{2}\frac{1}{\overrightarrow{L}^{+}(1-\overrightarrow{P}^{+}/\overleftarrow{P}^{+})} & (P_i>0, e_i=+1)\\ \frac{1}{2}\frac{1}{\overrightarrow{L}^{-}(1-\overrightarrow{P}^{-}/\overleftarrow{P}^{-})} & (P_i>0, e_i=-1)\\ \frac{1}{2}\frac{1}{\overleftarrow{L}^{+}(1-\overleftarrow{P}^{+}/\overrightarrow{P}^{+})} & (P_i<0, e_i=+1)\\ \frac{1}{2}\frac{1}{\overleftarrow{L}^{-}(1-\overleftarrow{P}^{-}/\overrightarrow{P}^{-})} & (P_i<0, e_i=-1) \end{cases} \tag{5.25}$$

and

$$M_1 = \overrightarrow{L}^+ + \overrightarrow{L}^- + \overleftarrow{L}^+ + \overleftarrow{L}^- \tag{5.26}$$

$$M_2 = \overrightarrow{L}^+ - \overrightarrow{L}^- + \overleftarrow{L}^+ - \overleftarrow{L}^- \tag{5.27}$$

$$M_3 = \overrightarrow{L}^+\overrightarrow{P}^+ + \overrightarrow{L}^-\overrightarrow{P}^- + \overleftarrow{L}^+\overleftarrow{P}^+ + \overleftarrow{L}^-\overleftarrow{P}^- \tag{5.28}$$

$$M_4 = \overrightarrow{L}^+\overrightarrow{P}^+ - \overrightarrow{L}^-\overrightarrow{P}^- - \overleftarrow{L}^+\overleftarrow{P}^+ + \overleftarrow{L}^-\overleftarrow{P}^- . \tag{5.29}$$

In the evaluation of the integral from Eq. 5.24, the fallowing relations were taken into account

$$\int \mathcal{N}(x)dx \approx N_{obs.} = \sum_{i=1}^{N_{obs.}} 1 \tag{5.30}$$

$$\int \mathcal{N}(x)\mathcal{A}(x)dx \approx \sum_{i=1}^{N_{obs.}} \mathcal{A}(x_i). \tag{5.31}$$

Within the above presented normalization the possible luminosity imbalances with respect to beam charge and polarization, are accounted by the coefficients $K(P_i, e_i)$, hence their is no need to apply any balancing cuts on the data.

The asymmetries defined in section 3.4 are related to the Fourier coefficients from the azimuthal decomposition of the leptoproduction cross section of a real photon. Based on these relations, an appropriate form of the fit function can be chosen for each asymmetry. Particularly, for the asymmetries extracted from data collected on an unpolarized deuterium target $\mathcal{A}_{\rm C}, \mathcal{A}_{\rm LU}^{\rm I}$ and $\mathcal{A}_{\rm LU}^{\rm DVCS}$ the following expansion in terms of the same harmonics in ϕ as in the numerator of the corresponding asymmetries from Eqs. 3.34 - 3.36

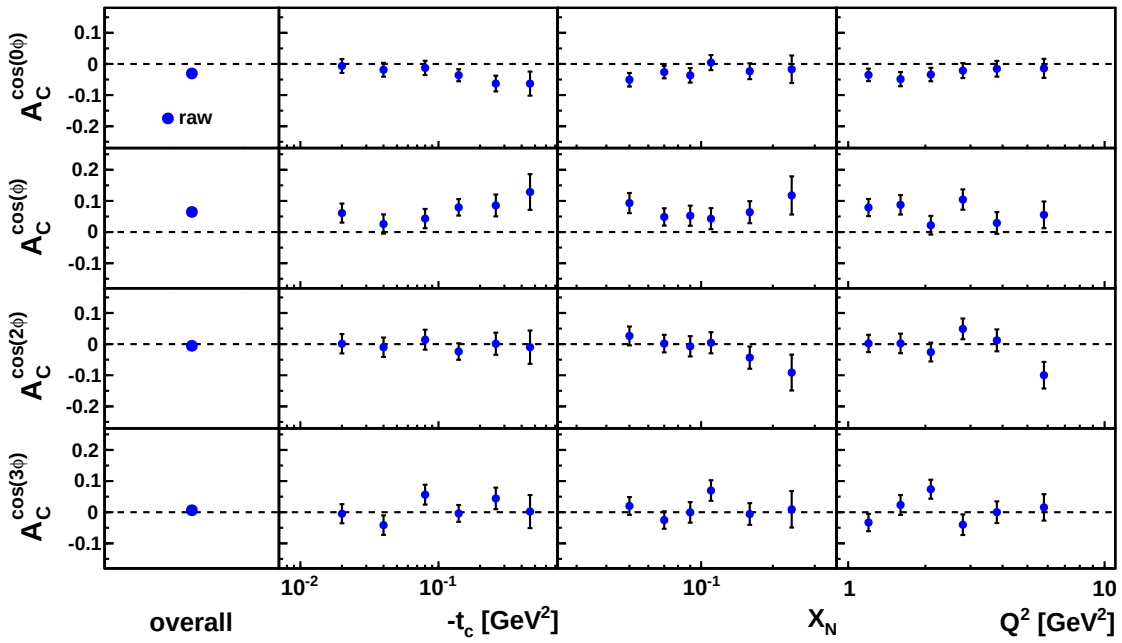

Figure 5.15: The amplitudes of beam-charge asymmetries $\mathcal{A}_{\rm C}$ for entire HERMES kinematics and in bins of $-t_c$, x_N, Q^2 extracted from raw data.

was applied.

$$\mathcal{A}_{\rm LU}^{\rm I}(\phi) \simeq \sum_{n=1}^{2} A_{\rm LU,I}^{\sin(n\phi)} \sin(n\phi) + A_{\rm LU,I}^{\cos(0\phi)} \,, \tag{5.32}$$

$$\mathcal{A}_{\rm LU}^{\rm DVCS}(\phi) \simeq A_{\rm LU,DVCS}^{\sin\phi} \sin\phi + A_{\rm LU,DVCS}^{\cos(0\phi)} \,, \tag{5.33}$$

$$\mathcal{A}_{\rm C}(\phi) \simeq \sum_{n=0}^{3} A_{\rm C}^{\cos(n\phi)} \cos(n\phi) \,. \tag{5.34}$$

Here, an additional constant amplitudes $A_{\rm LU,I}^{\cos(0\phi)}$ and $A_{\rm LU,DVCS}^{\cos(0\phi)}$ were included in a fit function as a consistency check. Due to the fact that the asymmetries $\mathcal{A}_{\rm LU}^{\rm I}$ and $\mathcal{A}_{\rm LU}^{\rm DVCS}$ are odd functions of ϕ (see Eqs. 3.34 - 3.35), their Fourier decomposition can not contain constant or even amplitudes. Same holds for the asymmetry $\mathcal{A}_{\rm C}$, while in this case the Fourier decomposition contains only even amplitudes. The extracted amplitudes of the asymmetries $\mathcal{A}_{\rm C}, \mathcal{A}_{\rm LU}^{\rm I}$ and $\mathcal{A}_{\rm LU}^{\rm DVCS}$ are shown in Figures 5.15 - 5.17. In the left column of the figures the 'overall' results of the asymmetry amplitudes corresponding to the entire HERMES kinematics are shown, while in the rest columns the results in six bins of t_c, x_N and Q^2 are presented.

As it was mentioned, in the expression of distribution in expectation value of the measured yield the detection efficiency enters linearly (see Eq. 5.16). This allows to take into account the detection inefficiencies by applying weights to corresponding events. Depending on considered inefficiency, the weight to the event can be applied according to the hit position on the surface of the detector or for the given kinematic range in certain kinematic variable or for the given time period, etc.. While in this case the sum of all weights does not coincide to total number of measured events. This should be taken into account in the propagation of statistical errors from the maximum likelihood fit. According to [Sol64] the statistical uncertainties need to be evaluated from the corrected covariance matrix $\mathcal{C}_{corr.}$, which is derived from the covariance matrix $\mathcal{C}$ obtained in the weighted maximum

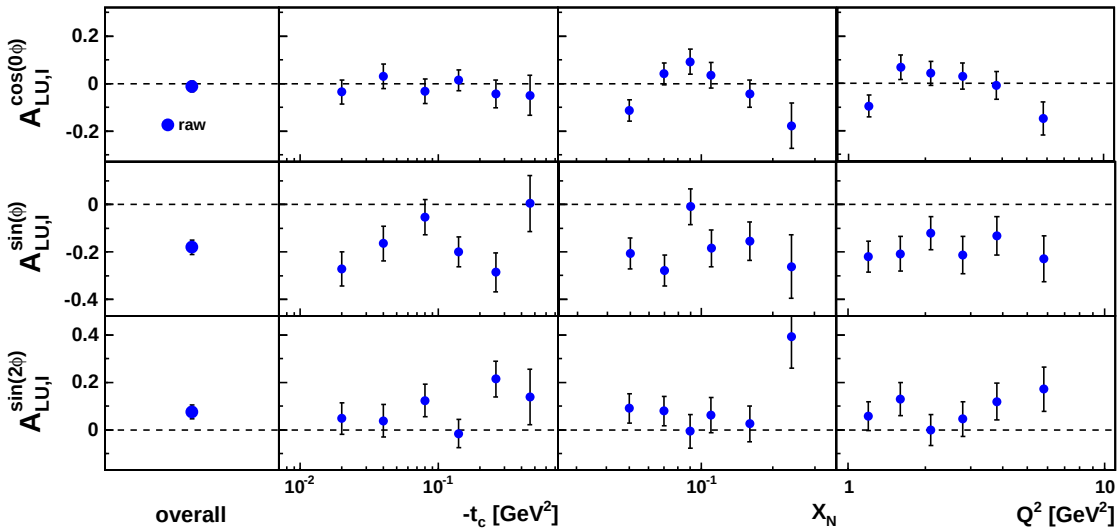

Figure 5.16: The amplitudes of combined asymmetry with respect to beam charge and beam helicity (charge-difference beam-helicity) $\mathcal{A}_{\rm LU}^{\rm I}$, extracted from raw data.

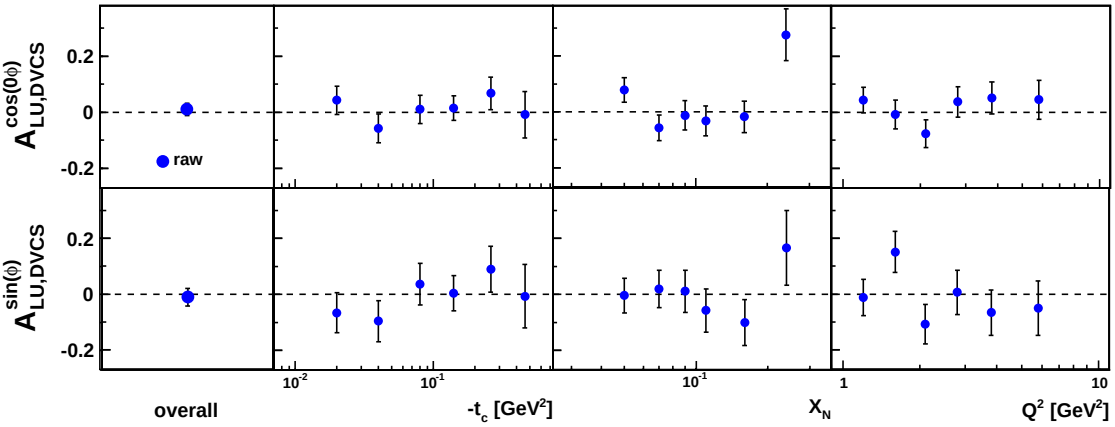

Figure 5.17: The amplitudes of the beam-helicity asymmetry (charge-averaged) $\mathcal{A}_{\rm LU}^{\rm DVCS}$, extracted from raw data.

likelihood fit and from the covariance matrix $\mathcal{C}'$ obtained in the maximum likelihood fit weighted with the squares of the weights w^2, accordingly:

$$\mathcal{C}_{corr.} = \mathcal{C} \cdot \mathcal{C}'^{-1} \cdot \mathcal{C} \tag{5.35}$$

5.4.3 Combined fit to the asymmetries from a longitudinally polarized data

The EML fit method, described in previous section, can be used to fit also the asymmetries defined in section 3.4.2 for the scattering off a longitudinally polarized deuterium target. For the extraction of single-charge asymmetries $\mathcal{A}_{\rm L\rightleftharpoons}$, $\mathcal{A}_{\rm LL}$ and $\mathcal{A}_{\rm UL}$ the distribution in the expectation value of the yield for scattering a longitudinally polarized positron beam from a longitudinally vector polarized deuterium target read as

$$\begin{aligned}\mathrm{d}\langle\mathcal{N}\rangle(e_\ell=+1,P_\ell,P_z,P_{zz},\phi) &= \mathcal{L}\,(e_\ell=+1,P_\ell,P_z,P_{zz})\,\epsilon(\phi)\\ &\times \mathrm{d}\sigma_{\rm U\rightleftharpoons}(e_\ell=+1,P_{zz},\phi)\Big[1+P_\ell\mathcal{A}_{\rm L\rightleftharpoons}(e_\ell=+1,P_{zz},\phi)\\ &+P_z\mathcal{A}_{\rm UL}(e_\ell=+1,P_{zz},\phi)+P_\ell P_z\mathcal{A}_{\rm LL}(e_\ell=+1,P_{zz},\phi)\Big]\,. \end{aligned}\tag{5.36}$$

In a close analogy with the case of unpolarized data, one can write a system of equations similar to those in Eqs. 5.19 - 5.22 in order to obtain the normalization of the corresponding EML function. In this case the cross section of the production of real photons by unpolarized positrons on a tensor-polarized deuterium target with vanishing vector polarization $\sigma_{\rm U\rightleftharpoons}$, and three asymmetries have an internal dependence on the charge of the beam (which is +1 for this particular case) and on tensor polarization of the target. The effective polarization will be defined as a product of a beam and target vector polarization $P_{\ell z} = P_\ell P_z$. Then the integration of number of events over the effective polarization yields,

$$\int_{\substack{P_\ell>0,\\ P_z>0}} \frac{d\mathcal{N}(x,P_{\ell z})}{dx dP_{\ell z}} dP_{\ell z} = \tag{5.37}$$
$$\overrightarrow{N}^{\Rightarrow}(x) = \overrightarrow{L}^{\Rightarrow}\sigma_{\mathrm{U}\leftrightarrows}(x)\Big[1 + \overrightarrow{P}_\ell^{\Rightarrow}\mathcal{A}_{\mathrm{L}\leftrightarrows}(x) + \overrightarrow{P}_z^{\Rightarrow}\mathcal{A}_{\mathrm{UL}}(x) + \overrightarrow{P}_\ell^{\Rightarrow}\overrightarrow{P}_z^{\Rightarrow}\mathcal{A}_{\mathrm{LL}}(x)\Big]$$
$$\int_{\substack{P_\ell>0,\\ P_z<0}} \frac{d\mathcal{N}(x,P_{\ell z})}{dx dP_{\ell z}} dP_{\ell z} = \tag{5.38}$$
$$\overrightarrow{N}^{\Leftarrow}(x) = \overrightarrow{L}^{\Leftarrow}\sigma_{\mathrm{U}\leftrightarrows}(x)\Big[1 + \overrightarrow{P}_\ell^{\Leftarrow}\mathcal{A}_{\mathrm{L}\leftrightarrows}(x) + \overrightarrow{P}_z^{\Leftarrow}\mathcal{A}_{\mathrm{UL}}(x) + \overrightarrow{P}_\ell^{\Leftarrow}\overrightarrow{P}_z^{\Leftarrow}\mathcal{A}_{\mathrm{LL}}(x)\Big]$$
$$\int_{\substack{P_\ell<0,\\ P_z>0}} \frac{d\mathcal{N}(x,P_{\ell z})}{dx dP_{\ell z}} dP_{\ell z} = \tag{5.39}$$
$$\overleftarrow{N}^{\Rightarrow}(x) = \overleftarrow{L}^{\Rightarrow}\sigma_{\mathrm{U}\leftrightarrows}(x)\Big[1 + \overleftarrow{P}_\ell^{\Rightarrow}\mathcal{A}_{\mathrm{L}\leftrightarrows}(x) + \overleftarrow{P}_z^{\Rightarrow}\mathcal{A}_{\mathrm{UL}}(x) + \overleftarrow{P}_\ell^{\Rightarrow}\overleftarrow{P}_z^{\Rightarrow}\mathcal{A}_{\mathrm{LL}}(x)\Big]$$
$$\int_{\substack{P_\ell<0,\\ P_z<0}} \frac{d\mathcal{N}(x,P_{\ell z})}{dx dP_{\ell z}} dP_{\ell z} = \tag{5.40}$$
$$\overleftarrow{N}^{\Leftarrow}(x) = \overleftarrow{L}^{\Leftarrow}\sigma_{\mathrm{U}\leftrightarrows}(x)\Big[1 + \overleftarrow{P}_\ell^{\Leftarrow}\mathcal{A}_{\mathrm{L}\leftrightarrows}(x) + \overleftarrow{P}_z^{\Leftarrow}\mathcal{A}_{\mathrm{UL}}(x) + \overleftarrow{P}_\ell^{\Leftarrow}\overleftarrow{P}_z^{\Leftarrow}\mathcal{A}_{\mathrm{LL}}(x)\Big]\,.$$

Here, the single and double arrows in the superscripts denote the beam and target polarization directions, respectively. In order to obtain the normalization of the p.d.f. which will account for the luminosity imbalances with respect to the beam and target polarizations, one needs to resolve the system of Eqs. 5.37 - 5.40 with respect to the unpolarized cross section $\sigma_{\mathrm{U}\leftrightarrows}$ and asymmetries $\mathcal{A}_{\mathrm{L}\leftrightarrows}, \mathcal{A}_{\mathrm{LL}}, \mathcal{A}_{\mathrm{UL}}$. Then the expression for the unpolarized cross section can be substituted in the system of Eqs. 5.37 - 5.40 and the integration over the phase-space will give the normalization of the p.d.f.. The complications in this case appear in the analytic representation of the unpolarized cross section and asymmetries through normalized yields $n = N/L$ and luminosity averaged polarizations of the beam and the target. Due to the fact that the absolute values of the beam and target polarizations can be different for each of the four states, the general expression for the unpolarized cross section becomes very complicated. Meanwhile for the extraction of the asymmetry amplitudes the analytic expressions for the coefficients $K_i(P_\ell^i, P_z^i)$ are not necessary, hence one can resolve the system of Eqs. 5.37 - 5.40 numerically and use numerical values of the coefficients in the normalization. In practice, during data taking period on longitudinally polarized deuterium target the polarization of target was stable and the existing differences of the averaged target polarization for different states are negligibly small. Hence, an average absolute value of the target polarization P_z can be used for all events. In this case the normalization can be given by

$$\mathbb{N}(\theta) \approx \sum_{i=1}^{N_{obs}} K(P_\ell^i, P_z^i)\Big[M_1 + M_2\mathcal{A}_{\mathrm{L}\leftrightarrows}(x_i,\theta) + M_3\mathcal{A}_{\mathrm{UL}}(x_i,\theta) + M_4\mathcal{A}_{\mathrm{LL}}(x_i,\theta)\Big]\,, \tag{5.41}$$

where

$$M_1 = \overrightarrow{L}^{\Rightarrow} + \overrightarrow{L}^{\Leftarrow} + \overleftarrow{L}^{\Rightarrow} + \overleftarrow{L}^{\Leftarrow} \tag{5.42}$$
$$M_2 = \overrightarrow{L}^{\Rightarrow}\overrightarrow{P}_\ell^{\Rightarrow} + \overrightarrow{L}^{\Leftarrow}\overrightarrow{P}_\ell^{\Leftarrow} + \overleftarrow{L}^{\Rightarrow}\overleftarrow{P}_\ell^{\Rightarrow} + \overleftarrow{L}^{\Leftarrow}\overleftarrow{P}_\ell^{\Leftarrow} \tag{5.43}$$
$$M_3 = \big[\overrightarrow{L}^{\Rightarrow} - \overrightarrow{L}^{\Leftarrow} + \overleftarrow{L}^{\Rightarrow} - \overleftarrow{L}^{\Leftarrow}\big]P_z \tag{5.44}$$
$$M_4 = \big[\overrightarrow{L}^{\Rightarrow}\overrightarrow{P}_\ell^{\Rightarrow} - \overrightarrow{L}^{\Leftarrow}\overrightarrow{P}_\ell^{\Leftarrow} + \overleftarrow{L}^{\Rightarrow}\overleftarrow{P}_\ell^{\Rightarrow} - \overleftarrow{L}^{\Leftarrow}\overleftarrow{P}_\ell^{\Leftarrow}]P_z\,. \tag{5.45}$$

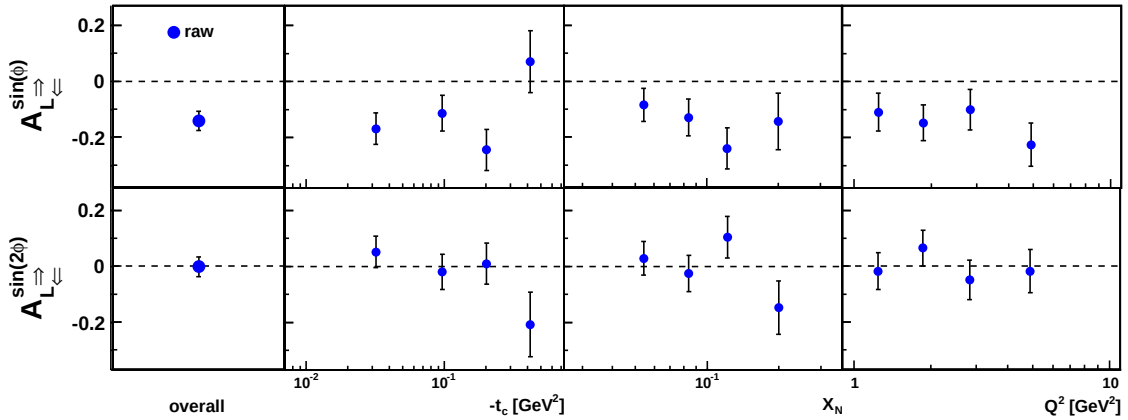

Figure 5.18: The amplitudes of the asymmetries $\mathcal{A}_{\mathrm{L}\Rightarrow}$, extracted from raw data.

Here, the coefficients $K_i(P_\ell^i, P_z^i)$ are defined in analogy to those in Eq. 5.25, interchanging the states defined by beam charge with the states defined by target polarization P_z.

The fit functions for the asymmetries $\mathcal{A}_{\mathrm{L}\Rightarrow}$, $\mathcal{A}_{\mathrm{LL}}$ and $\mathcal{A}_{\mathrm{UL}}$ are the following

$$\mathcal{A}_{\mathrm{L}\Rightarrow}(e_\ell = +1, P_{zz}, \phi) \simeq \sum_{n=1}^{2} A_{\mathrm{L}\Rightarrow}^{\sin(n\phi)}(e_\ell = +1, P_{zz}) \sin(n\phi), \tag{5.46}$$

$$\mathcal{A}_{\mathrm{UL}}(e_\ell = +1, P_{zz}, \phi) \simeq \sum_{n=1}^{3} A_{\mathrm{UL}}^{\sin(n\phi)}(e_\ell = +1, P_{zz}) \sin(n\phi), \tag{5.47}$$

$$\mathcal{A}_{\mathrm{LL}}(e_\ell = +1, P_{zz}, \phi) \simeq \sum_{n=0}^{2} A_{\mathrm{LL}}^{\cos(n\phi)}(e_\ell = +1, P_{zz}) \cos(n\phi)\,. \tag{5.48}$$

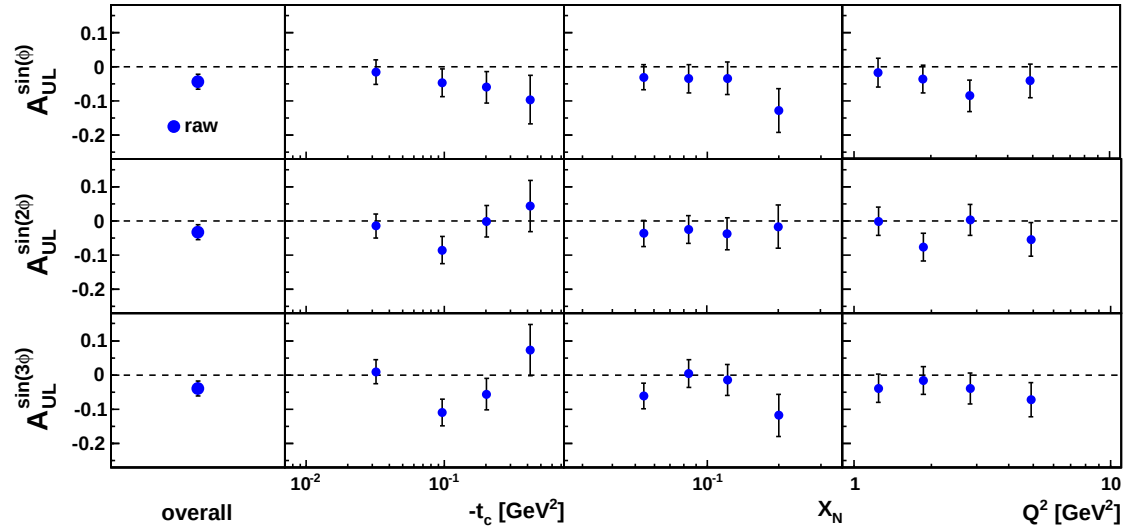

Figure 5.19: The amplitudes of target-spin asymmetry $\mathcal{A}_{\mathrm{UL}}$, extracted from raw data.

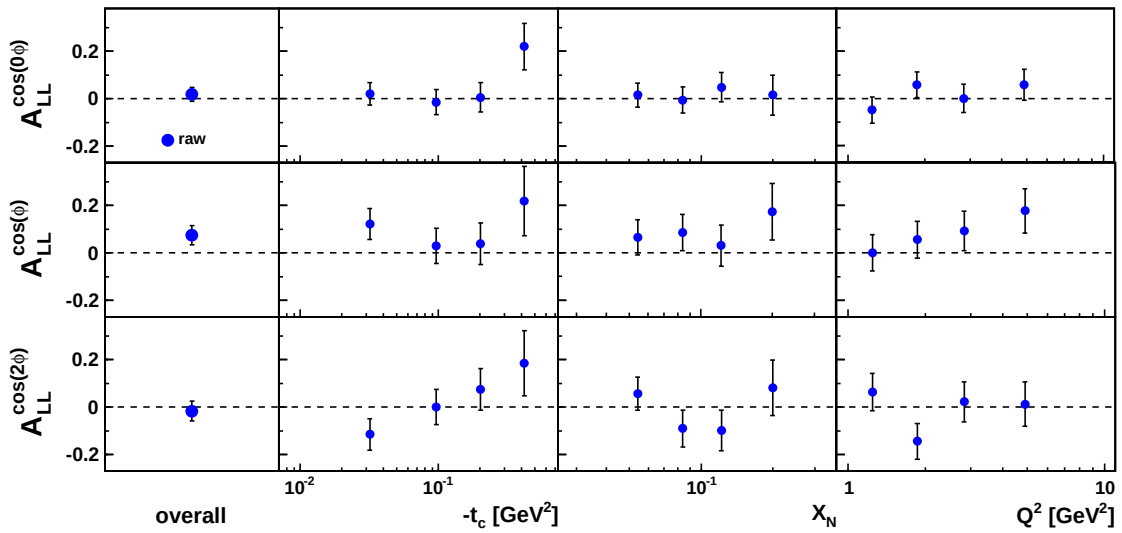

Figure 5.20: The amplitudes of double-spin asymmetry $\mathcal{A}_{\mathrm{LL}}$ extracted from raw data.

Here, the single beam-helicity or target-spin asymmetries are expanded into $\sin(n\phi)$ amplitudes, while the double-spin asymmetry was expanded in $\cos(n\phi)$ amplitudes. The amplitudes of these asymmetries are shown in Figures 5.18 - 5.20.

For the extraction of the amplitudes of single-helicity asymmetries $\mathcal{A}_{\overset{\mathrm{C}}{\leftarrow}\overset{\Leftarrow}{\Rightarrow}}$, $\mathcal{A}_{\overset{0}{\leftarrow}_{\mathrm{L}}}$ and $\mathcal{A}_{\overset{\mathrm{C}}{\leftarrow}_{\mathrm{L}}}$ the distribution in the expectation value of the yield for scattering a negatively polarized lepton beam off a longitudinally vector polarized deuterium target is parameterized as

$$\begin{aligned}\mathrm{d}\langle\mathcal{N}\rangle(e_\ell, P_\ell, P_z, P_{zz}, \phi) = \mathcal{L}\,(e_\ell, P_\ell, P_z, P_{zz})\,\epsilon(\phi)\,\mathrm{d}\sigma_{\overset{\mathrm{C}}{\leftarrow}\overset{\Leftarrow}{\Rightarrow}}(P_\ell, P_{zz}, \phi) \\ \times\left[1 + e_\ell\mathcal{A}_{\overset{\mathrm{C}}{\leftarrow}\overset{\Leftarrow}{\Rightarrow}}(P_\ell, P_{zz}, \phi) + P_z\mathcal{A}_{\overset{0}{\leftarrow}_{\mathrm{L}}}(P_\ell, P_{zz}, \phi) + e_\ell P_z\mathcal{A}_{\overset{\mathrm{C}}{\leftarrow}_{\mathrm{L}}}(P_\ell, P_{zz}, \phi)\right], \quad (5.49)\end{aligned}$$

And the asymmetries were decomposed in a following way

$$\mathcal{A}_{\overset{\mathrm{C}}{\leftarrow}\overset{\Leftarrow}{\Rightarrow}}(P_\ell, P_{zz}, \phi) \simeq \sum_{n=0}^{3} A_{\overset{\mathrm{C}}{\leftarrow}\overset{\Leftarrow}{\Rightarrow}}^{\cos(n\phi)}(P_{zz})\cos(n\phi) + P_\ell\sum_{n=1}^{2} A_{\overset{\mathrm{C}}{\leftarrow}\overset{\Leftarrow}{\Rightarrow}}^{\sin(n\phi)}(P_{zz})\sin(n\phi)\,, \quad (5.50)$$

$$\mathcal{A}_{\overset{0}{\leftarrow}_{\mathrm{L}}}(P_\ell, P_{zz}, \phi) \simeq P_\ell\sum_{n=0}^{1} A_{\overset{0}{\leftarrow}_{\mathrm{L}}}^{\cos(n\phi)}(P_{zz})\cos(n\phi) + \sum_{n=1}^{2} A_{\overset{0}{\leftarrow}_{\mathrm{L}}}^{\sin(n\phi)}(P_{zz})\sin(n\phi)\,, \quad (5.51)$$

$$\mathcal{A}_{\overset{\mathrm{C}}{\leftarrow}_{\mathrm{L}}}(P_\ell, P_{zz}, \phi) \simeq P_\ell\sum_{n=0}^{2} A_{\overset{\mathrm{C}}{\leftarrow}_{\mathrm{L}}}^{\cos(n\phi)}(P_{zz})\cos(n\phi) + \sum_{n=1}^{3} A_{\overset{\mathrm{C}}{\leftarrow}_{\mathrm{L}}}^{\sin(n\phi)}(P_{zz})\sin(n\phi)\,. \quad (5.52)$$

The results for the leading amplitudes are given in Figure 5.21

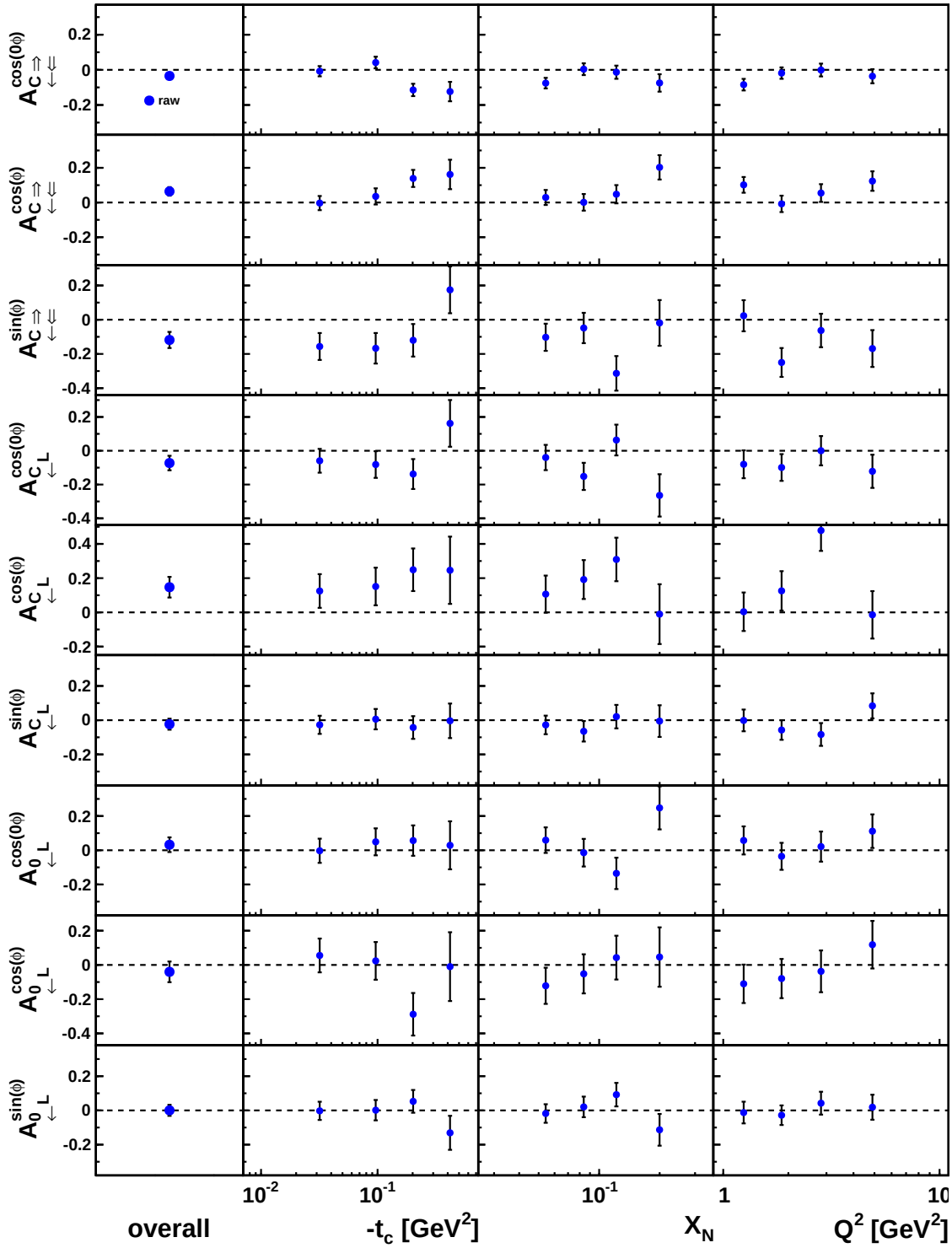

Figure 5.21: The leading amplitudes of the asymmetries $\mathcal{A}_{\overleftarrow{C}\Leftrightarrow}$, $\mathcal{A}_{\overleftarrow{C}_L}$ and $\mathcal{A}_{\overleftarrow{0}_L}$ extracted from raw data.

5.5 Systematic studies

The extracted amplitudes of the asymmetries are influenced by various systematic effects. This section describes in details the systematic studies performed to ensure the stability of the results, a number of corrections that were applied on the extracted amplitudes and the methods to estimate the impact of various systematic effects on the final results. The considered systematic effects are listed below:

- Fit stability.
- Year-by-year comparison
- Miscalibration of the calorimeter and the shift of the mean values of M_X^2 distribution
- Background correction
- Acceptance effects
- Misalignment of the detector components and the beam
- Kinematic smearing
- An impact of finite-bin-width or bin centering effects
- Detection inefficiency
- Normalization uncertainty
- Scale uncertainties due to beam and target polarization measurement
- QED radiative corrections
- Contribution from transverse component of target polarization

5.5.1 Fit stability

The considered observables that were defined in section 3.4 do not provide a clear access to Fourier coefficients from the leptoproduction cross section in Eqs. 3.14 - 3.16. They rather encompass a complicated azimuthal dependence, and moreover, only the moments of the asymmetries, i.e. asymmetry amplitudes, can be extracted from the fit. Thereby, the choice of the fit function plays an important role in the treatment of the measurement. The asymmetries were expanded into truncated harmonics in azimuthal angle ϕ. The amount of harmonics (amplitudes) in the expansion of the asymmetries or of the fit function was taken to be the same as the amount of Fourier coefficients entering the numerator of the corresponding asymmetries. This choice of the fit function does not warranty that the higher amplitudes do not exist. They could appear due to the ϕ dependence of the denominator of the asymmetries or due to the ϕ dependence of lepton propagators. However, it is assumed that the additional non-zero amplitudes do not change the magnitudes of the amplitudes of interest. Note that if the asymmetry is an even (odd) function in ϕ, then its Fourier expansion should contain only even (odd) harmonics. Hence, as an example the constant moments of the asymmetries $\mathcal{A}_{\mathrm{LU}}^{\mathrm{I}}$ and $\mathcal{A}_{\mathrm{LU}}^{\mathrm{DVCS}}$ should be consistent with zero. The stability of the extracted amplitudes to the choice of the fit function is illustrated in Figure 5.22, where the leading amplitudes of

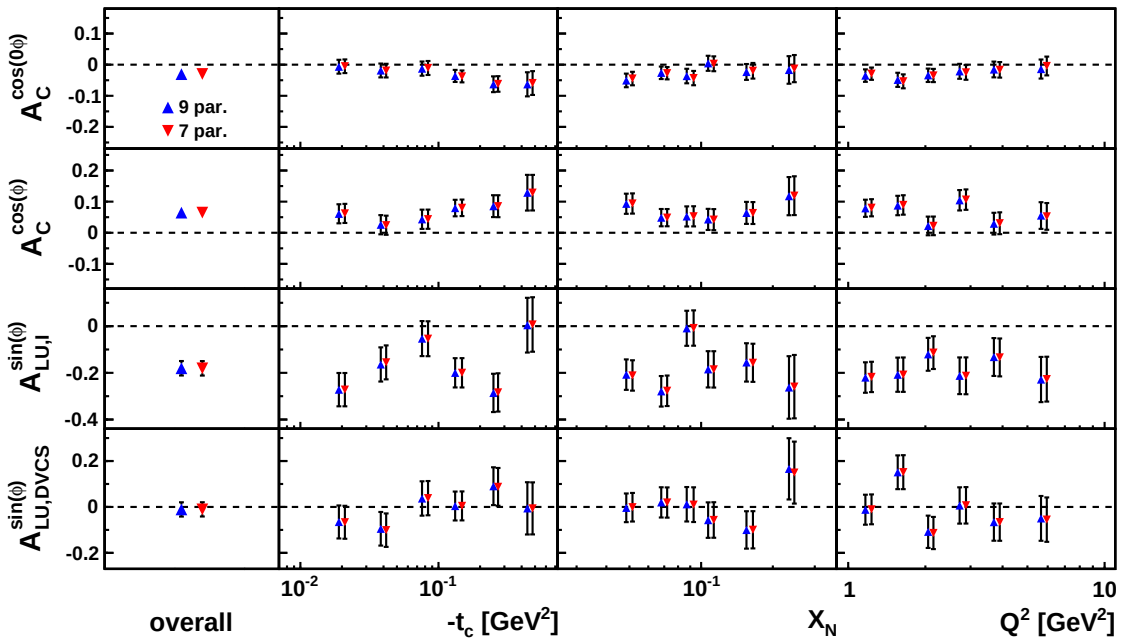

Figure 5.22: The leading amplitudes of the asymmetries $\mathcal{A}_{\rm C}, \mathcal{A}_{\rm LU}^{\rm I}$ and $\mathcal{A}_{\rm LU}^{\rm DVCS}$ extracted with 7 or 9 parameter fit .

the asymmetries $\mathcal{A}_{\rm C}, \mathcal{A}_{\rm LU}^{\rm I}$ and $\mathcal{A}_{\rm LU}^{\rm DVCS}$ are shown, extracted either with 7 or 9 parameter fit functions. In the case of 7 parameter fit function the additional constant amplitudes of the asymmetries $\mathcal{A}_{\rm LU}^{\rm I}$ and $\mathcal{A}_{\rm LU}^{\rm DVCS}$ were excluded. As can be seen from this figure, the impact of the additional amplitudes on the leading ones is negligible. Hence, no systematic uncertainty was applied due to the choice of the fit function. Similar checks were performed for the other asymmetries.

5.5.2 Year-by-year comparison

The results obtained from a combined analysis of the data collected during several years might be influenced by the possible effects, that lead to an inconsistency or internal differences of the data samples accumulated during large time interval. These effects can be caused by replacement of different detector components or due to the changes from positron to electron beam. Therefore, the consistency of the data sets needs to be ensured, which can be done by comparing the distributions of the kinematic variables from different data sets. As an example on the top plots of Figure 5.23 the ratios of normalized yield of DIS events in Q^2 and x_B for different data sets of polarized data are compared. The kinematic distributions of the DIS samples agree very well, which can be seen also in Figure 5.2, where the distributions of W^2, Q^2, x_N and ν are compared for all unpolarized data taking years. For the DVCS analysis the most important distributions are the squared missing mass and the $-t_c$ distributions. In the bottom plots of Figure 5.23 the ratios of M_X^2 and $-t_c$ distributions from exclusive sample of different unpolarized data sets are presented. Apart from a small differences at large $-t_c$ and small M_X^2, the exclusive samples from different data taking periods also agree very well. Nevertheless, more detailed comparison of the M_X^2 distributions from different years indicate a small

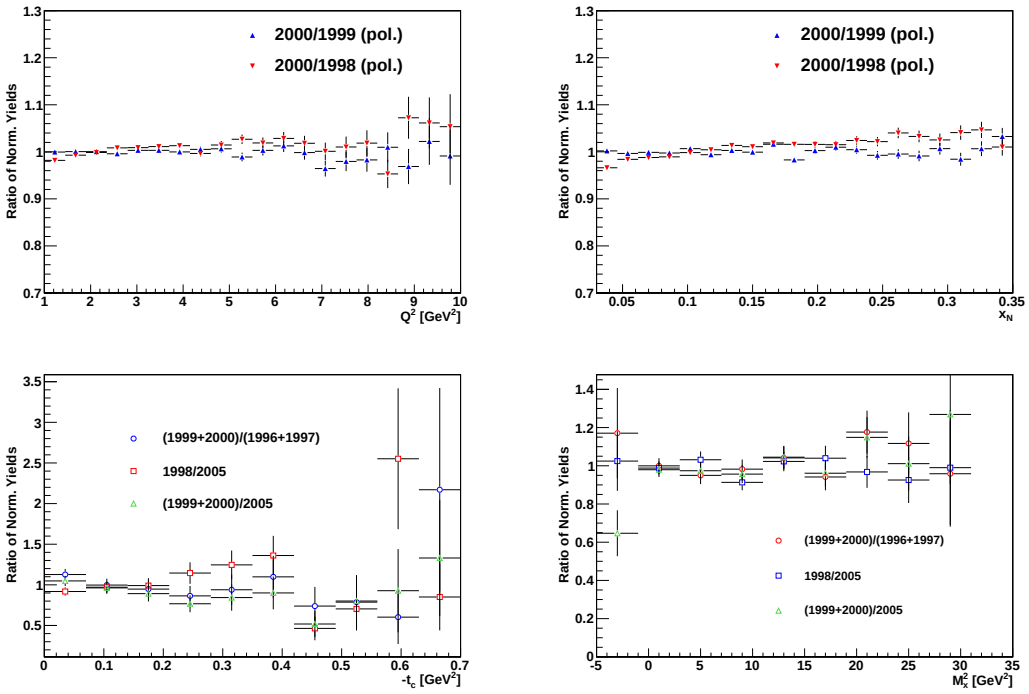

Figure 5.23: The plots on the top show the ratio of normalized distributions of Q^2 and x_N from different data sets. The plots on the bottom show the ratio of normalized distributions of t_c and M_X^2 from different data sets.

shift in the position of the exclusive peak. This will be discussed in details in the next section.

Together with the direct comparison of the kinematic distributions of data from different years, the consistency between data sets was checked on a level of the extracted asymmetry amplitudes. In Figure 5.24 the leading amplitudes of the asymmetries $\mathcal{A}_{\rm C}, \mathcal{A}_{\rm LU}^{\rm I}$ and $\mathcal{A}_{\rm LU}^{\rm DVCS}$, extracted from a different combinations of the data collected on an unpolarized deuterium target for the entire HERMES kinematic acceptance, are presented. The results are in good agreement. The largest deviations appear for the $A_C^{\cos(0\phi)}$ amplitude, which do not exceed one standard deviation. Similar consistence holds also for the amplitudes extracted in bins of $-t_c$, x_N and Q^2, that are not presented here.

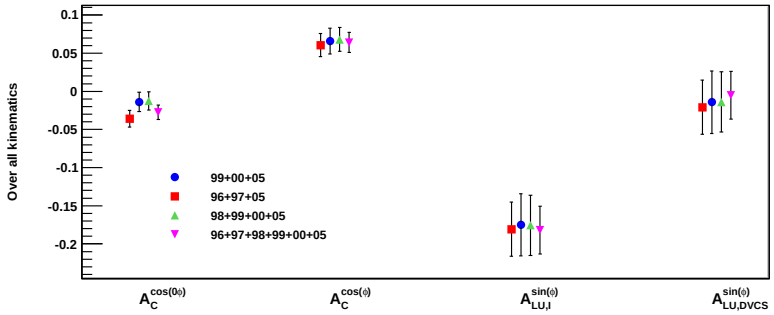

Figure 5.24: Comparison of the leading amplitudes of the asymmetries $\mathcal{A}_{\rm C}, \mathcal{A}_{\rm LU}^{\rm I}$ and $\mathcal{A}_{\rm LU}^{\rm DVCS}$ extracted from different data sets. The amplitudes are presented for the entire HERMES kinematics.

Another possible check for the consistency of the data from different years was provided by the inclusion of non physical constant amplitudes $A_{\mathrm{LU,I}}^{\cos(0\phi)}$ and $A_{\mathrm{LU,DVCS}}^{\cos(0\phi)}$ in the fit functions of the $\mathcal{A}_{\mathrm{LU}}^{\mathrm{I}}$ and $\mathcal{A}_{\mathrm{LU}}^{\mathrm{DVCS}}$ asymmetries, since mainly the constant amplitudes are sensitive to the relative normalization. As can be seen from the Figures 5.16 - 5.17, these amplitudes are consistent with zero. Non physical constant amplitudes were extracted also for the $\mathcal{A}_{\mathrm{UL}}$ and $\mathcal{A}_{\mathrm{L}\overleftrightarrow{}}$ asymmetries, while for the beam-charge $\mathcal{A}_{\mathrm{C}}$ and double-spin $\mathcal{A}_{\mathrm{LL}}$ asymmetries an even amplitudes ($\sin\phi$) were introduced in the fit functions (not shown here), that were found to be compatible with zero.

The above mentioned consistency checks and many other investigations of the internal differences between data sets carried out in [Kra05, Kop06, Ell04] did not reveal an essential differences between data sets except from a slight shift in the missing mass peak position, which will be discussed in the next section. Hence, no systematic uncertainty was applied on the results presented in this report due to the year dependence.

5.5.3 Miscalibration of the calorimeter and the shift of M_X^2 peak position.

As was mentioned in previous section, when comparing the spectra of the missing mass distributions from several data taking periods, a shift in the mean value of the distributions in an exclusive region is observed. Based on the observed shift the data collected on an unpolarized deuteron were split into four time periods, divided into positron or electron data and data taken before and after installation of RICH detector in 1998. In the latter case the shift is caused by changes in the momentum resolution of the DIS leptons due to the RICH detector. For the above mentioned four periods the mean values of the M_X^2 distributions in the exclusive region were obtained. The new exclusive windows were determined according to the differences in these values for different periods. The

Running period	Mean $[GeV^2]$	Shift $[GeV^2]$	Window $[GeV^2]$
e^+ (1996+1997)	1.153	0.028	[-2.02,2.81]
e^- (1998)	1.000	-0.125	[-2.38,2.77]
e^+ (1999+2000)	1.125	0.000	[-2.25,2.89]
e^- (2005)	1.043	-0.082	[-2.33,2.81]

Table 5.6: The mean values of the M_X^2 distributions in the standard exclusive region, the relative shifts of the mean values and the adjusted exclusive windows for different running periods on an unpolarized deuterium target.

exclusive windows were adjusted with respect to the 1999/2000 data taking year. The mean values of the squared missing mass distributions in an exclusive region, the shifts and the obtained new exclusive windows for different data taking periods are given in Table 5.6. Note that for the data set taken before the installation of the RICH, the width of the exclusive peak in the M_X^2 distribution was decreased by approximately 6%. Therefore, the width of the window for these period was decreased accordingly. Finally, the adjusted exclusive M_X^2 widows were used for the selection of exclusive event sample. The numbers of exclusive events obtained from the adjusted exclusive windows are given in Table 5.7 for whole unpolarized data sample.

In Figure 5.25 the leading amplitudes of the asymmetries $\mathcal{A}_{\mathrm{C}}$, $\mathcal{A}_{\mathrm{LU}}^{\mathrm{I}}$ and $\mathcal{A}_{\mathrm{LU}}^{\mathrm{DVCS}}$ are shown extracted after applying a shift on the exclusive region of M_X^2 distribution in comparison with the amplitudes extracted from the data using standard exclusive window.

Beam Charge	Beam Helicity	$N_{excl.}$
+1	+1	2022
+1	-1	2959
-1	+1	2613
-1	-1	3556

Table 5.7: The final statistics after applying the shift on the exclusive window of the missing mass distributions.

One can see that the size of the correction is small. Nevertheless, a systematic uncertainty was applied to the final results equal to one quarter of the difference between amplitudes obtained with standard and shifted exclusive windows.

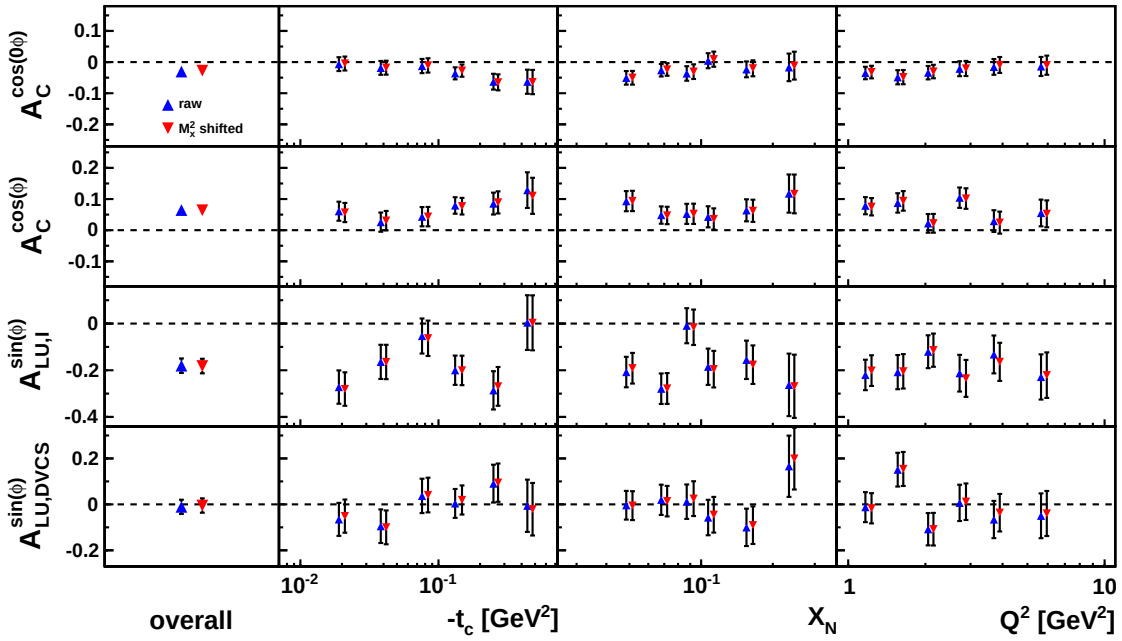

Figure 5.25: The leading amplitudes of the asymmetries $\mathcal{A}_{\rm C}, \mathcal{A}_{\rm LU}^{\rm I}$ and $\mathcal{A}_{\rm LU}^{\rm DVCS}$ extracted with the standard exclusive window in comparisons with amplitudes extracted with the shifted exclusive window.

The above described procedure of the correction of the results due to the shift of missing mass distributions was applied only for the asymmetry amplitudes from the unpolarized data, i.e $\mathcal{A}_{\rm C}$, $\mathcal{A}_{\rm LU}^{\rm I}$ and $\mathcal{A}_{\rm LU}^{\rm DVCS}$. For the polarized data, a more detailed analysis of the possible reasons of the shift was performed and an alternative approach was taken. Particularly, as the missing mass is the only kinematic variable, among the variables used this analysis, which is reconstructed from the photon energy, it is natural to refer the effect of the shift to miscalibration of the calorimeter. For the calibration of the calorimeter the ratio of the energy E measured by the calorimeter to the reconstructed momentum P of the DIS sample of leptons is considered. In Figure 5.26 the E/P ratio is shown for polarized data. The distributions are fitted to the function of the form

$$f(x) = p_0 \cdot \left\{ p_1 + p_2 \cdot x + exp\left[-\frac{(x-p_3)^2}{2 \cdot p_4^2} \right] \right\}. \tag{5.53}$$

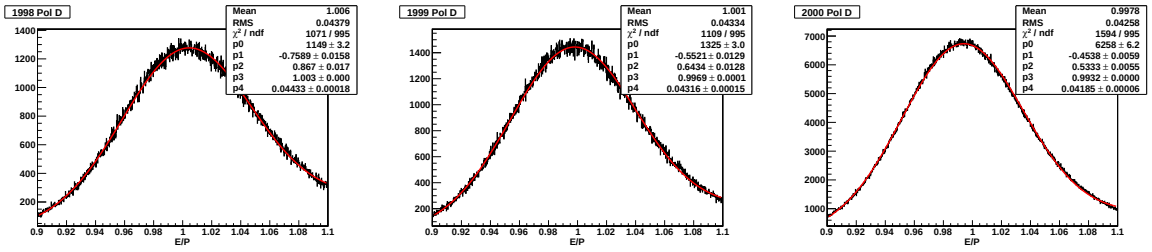

Figure 5.26: The E/P ratio for sample of DIS leptons from a different polarized data taking years. Also results of the fit are given on the plots.

Comparing the mean values obtained from a fit, one can see that the relative difference of the E/P ratio between electrons (1998) and positrons (1999, 2000) is approximately 1%. Although the mean values of the E/P ratio were obtained for leptons, they can be applied also for the correction of energies for those photons, which produce a signal in the preshower detector (see section 5.2.2). In order to provide a more precise calibration of the calorimeter, the momentum dependence of the E/P ratio was studied. A similar fits like in Figure 5.26 were done in fixed bins of the lepton momentum. The obtained momentum dependence of the E/P ratio for polarized data is shown in Figure 5.27, with the maximum relative shift of about 2% between 1998 and 2000 data at low momentum. The mean values obtained from the fit were used for the energy dependent correction

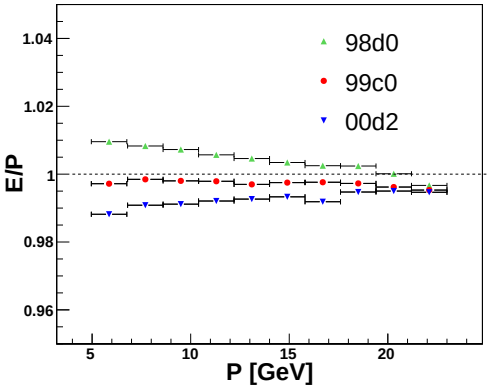

Figure 5.27: Momentum dependence of the E/P ratio for DIS leptons from polarized data.

of the photon energies. To see the impact of this correction on the M_X^2 distribution, the mean values of a simple Gaussian fits to squared missing mass spectra before and after applying the correction on photon energy for each data taking year are compared in

data set	before corr.	after corr.
1998	1.221 ± 0.075	1.342 ± 0.077
1999	1.371 ± 0.067	1.304 ± 0.065
2000	1.514 ± 0.034	1.369 ± 0.032

Table 5.8: The mean values of the Gaussian fit to the squared missing mass spectra before and after applying the photon energy correction.

Table 5.8. Within the uncertainties of the fit one can see that the Gaussian means of the three spectra become consistent. Also the mean values of the M_x^2 distributions, that are not given in the table agree within their uncertainties. The numbers of exclusive events obtained on longitudinally vector polarized deuterium target after applying the described correction on photon energy, are summarized in Table 5.9 for different data sets.

Beam Charge	Beam Helicity	Target Pol.	$N_{excl.}$
+1	+1	+	1870
+1	+1	-	1991
+1	-1	+	1032
+1	-1	-	1133
-1	+1	+	532
-1	+1	-	494
-1	-1	+	-
-1	-1	-	-

Table 5.9: The numbers of exclusive events for all combinations of beam charge, beam helicity and target polarization, obtained after applying an energy correction for photons.

The resulting leading amplitudes of the asymmetries $\mathcal{A}_{\Leftrightarrows}$, $\mathcal{A}_{\mathrm{LL}}$ and $\mathcal{A}_{\mathrm{UL}}$ are shown in Figure 5.28, in comparison with the amplitudes extracted without the photon energy correction. Note that this second approach for the correction of the photon energies was applied only on polarized data sets, which compensates the shifts in M_X^2 distributions. Therefore, in this case no systematic uncertainty from this effect was assigned to the final results.

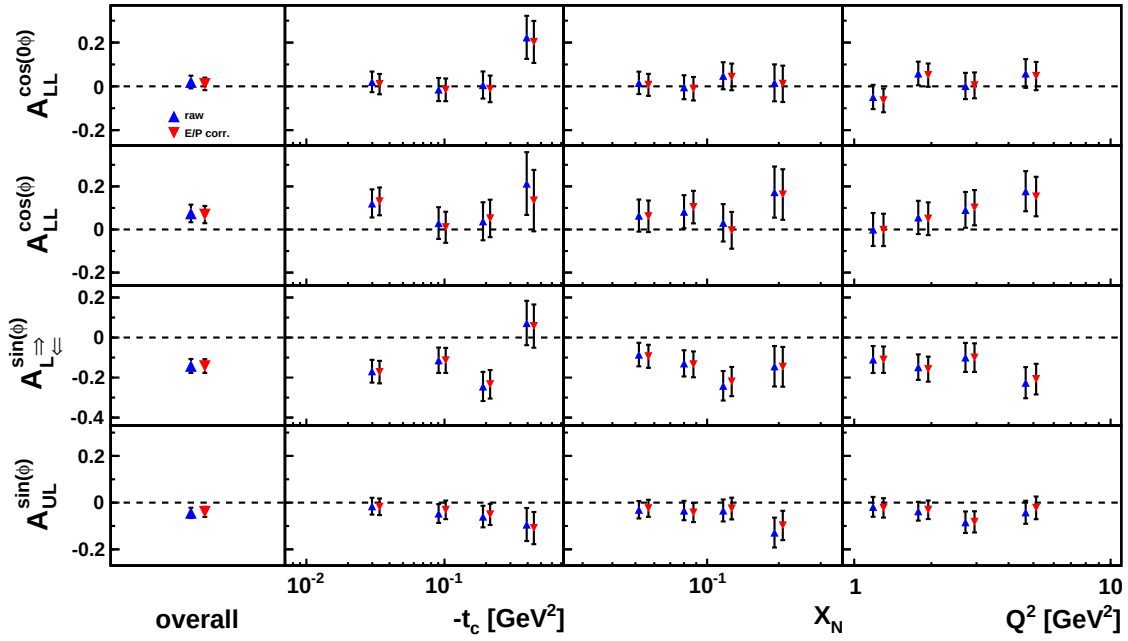

Figure 5.28: The leading amplitudes of the asymmetries $\mathcal{A}_{\Leftrightarrows}$, $\mathcal{A}_{\mathrm{LL}}$ and $\mathcal{A}_{\mathrm{UL}}$ extracted from the data with corrected photon energies in comparison with the amplitudes extracted without applying a photon energy correction.

5.5.4 Detection efficiency

An inefficiencies in the detection can cause a strong dilution of the extracted asymmetry amplitudes, especially in the case when results are obtained from data collected during extended time periods, when the inefficiencies can be non-uniform and time dependent. In this case the inefficiencies can introduce false asymmetries, since they will have a non-uniform impact on the kinematic distributions of the selected events. The asymmetry amplitudes discussed in this report can particularly be sensitive to the trigger inefficiency, tracking inefficiency, and to the inefficiency of calorimeter in photon detection.

As was mentioned in section 5.2 the main physics trigger used at HERMES is trigger 21, which is formed from a combined responses of three hodoscopes H0, H1, H2 and calorimeter. In order to estimate the possible influence of the trigger efficiency on the measured asymmetries, the inefficiencies of all components of the trigger-21 need to be obtained. This is done considering the triggers 17, 18, 19 and 20[1]. Those are formed from a combined responses of the three detectors eliminating respectively the signal from Calo., H0, H1 and H2 hodoscope

$$\begin{aligned} Trig.17 &= (H0\&H1\&H2)_{top} + ()_{bot} \\ Trig.18 &= (H1\&H2\&Calo)_{top} + ()_{bot} \\ Trig.19 &= (H0\&H2\&Calo)_{top} + ()_{bot} \\ Trig.20 &= (H0\&H1\&Calo)_{top} + ()_{bot}\,. \end{aligned}$$

The efficiencies of individual detector component were obtained as a ratio of the count rate of events firing the trigger i over the number of events firing both trigger i and trigger 21, $\epsilon(i) = N_i/N_{i\wedge 21}$.

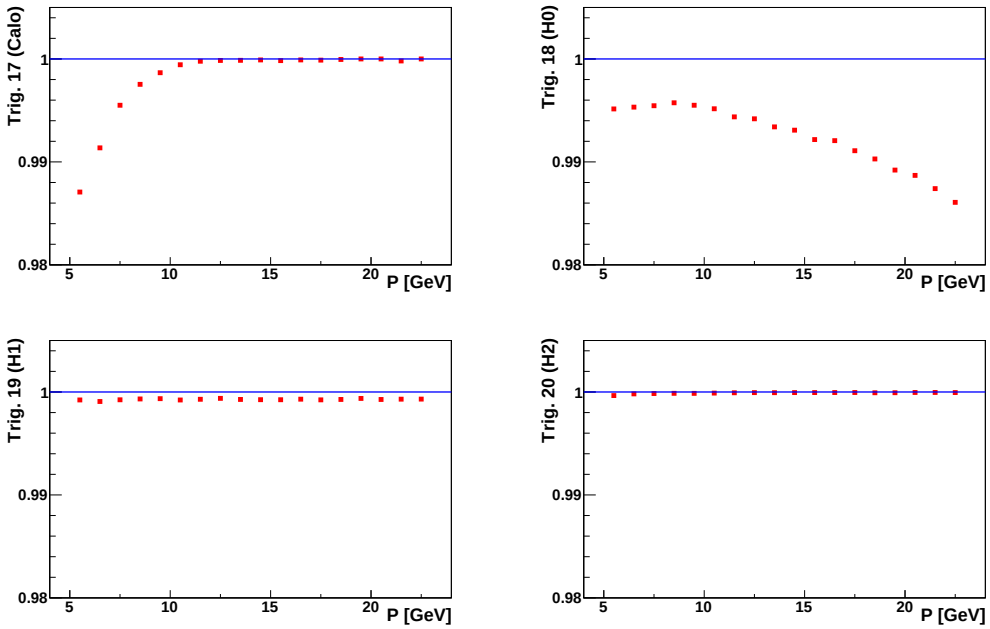

Figure 5.29: The efficiencies of H0, H1, H2 hodoscopes and the calorimeter versus the momentum of lepton track.

[1] Note that the naming convention for various triggers was changing from year to year. Here for simplicity the triggers are defined according to their definition during 1996 data taking year.

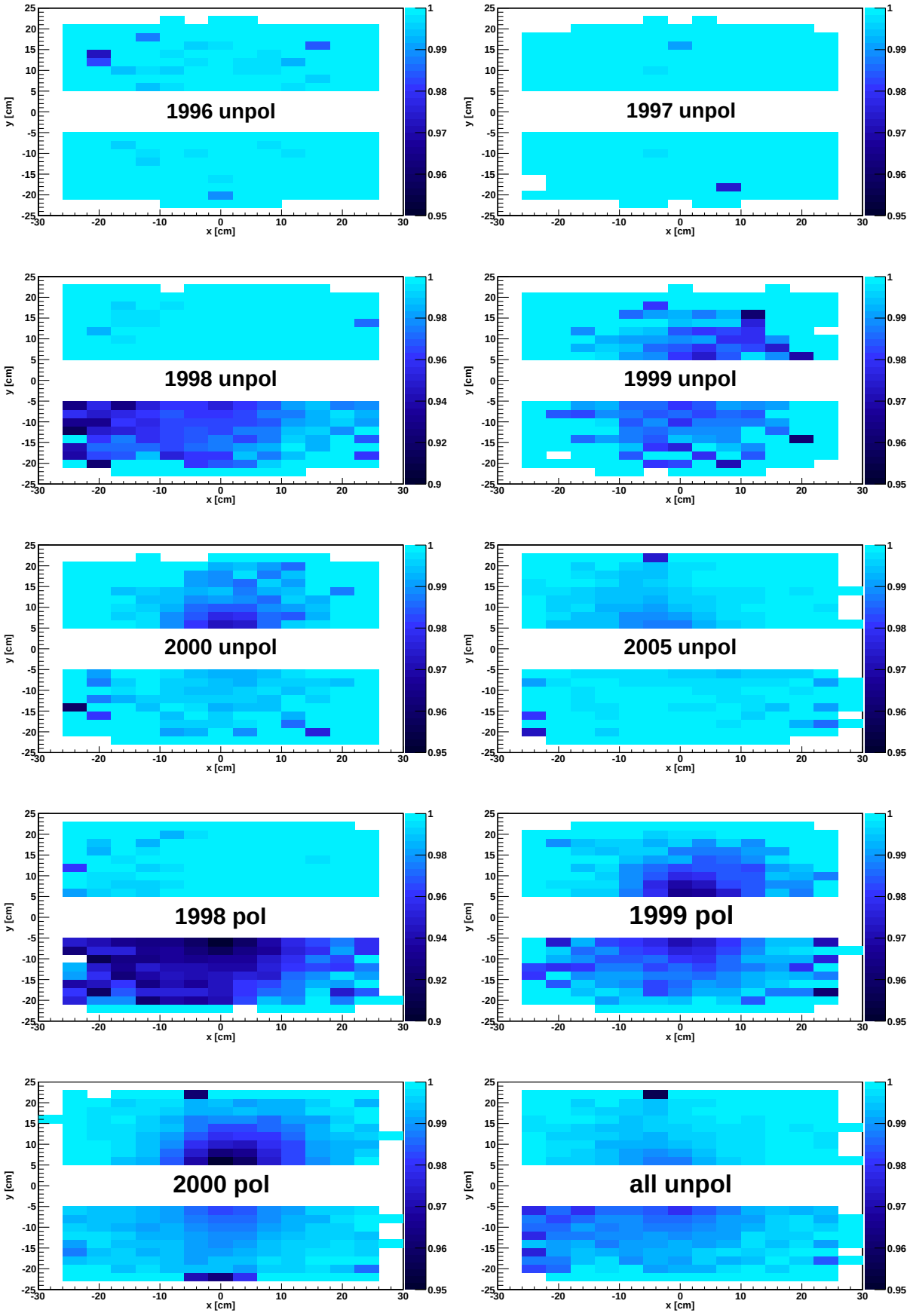

Figure 5.30: The efficiencies of the H0 hodoscope versus hit position on its surface for all analyzed data sample.

The efficiencies for the hodoscopes and the calorimeter are shown in Figure 5.29 versus momentum of the considered lepton. The efficiencies shown in this figure were obtained for the DIS leptons from all data collected on an unpolarized deuterium. As can be seen from Figure 5.29 the H1 and H2 hodoscopes were operating with approximately constant and very high efficiency, while the efficiency of the calorimeter decreases at low momentum of leptons. Nevertheless, since the typical energies of the leptons and photons for exclusive sample of DVCS events are about 15 GeV (see Figure 5.10), the drop of efficiency of the calorimeter at low energies can not affect current results. On the other side the photons that start showering in the preshower detector are expected to have very similar behavior to that of the leptons, hence the efficiency of the calorimeter in the detection of emitted photons is expected to be similar to the trigger efficiency of the calorimeter, shown in Figure 5.29. Therefore, the detection efficiency of the calorimeter also can not have a sizable influence on the measured asymmetries.

Figure 5.29 shows, that the dominant contribution to the total inefficiency of trigger 21 arises from H0 hodoscope. Therefore, in current analysis it was studied in more details. Since the changes in the inefficiency of the H0 hodoscope are caused by local radiation damage, it is reasonable to study the efficiency versus hit position of the leptons on its surface. The surface of the hodoscope was divided into a grid of cells with dimensions $4cm \times 2cm$, and for each cell the efficiency was derived. The obtained efficiencies are shown in Figure 5.30 for all analyzed data from different years and for combined unpolarized data sample separately. As can be seen, the H0 efficiency was quit stable over its surface area for all data taking years, while problems appeared only in 1998 when, the efficiency decreased up to 90% in the bottom half of the hodoscope. In order to account for the possible influence of H0 efficiency on the extracted asymmetry amplitudes, the inverse of

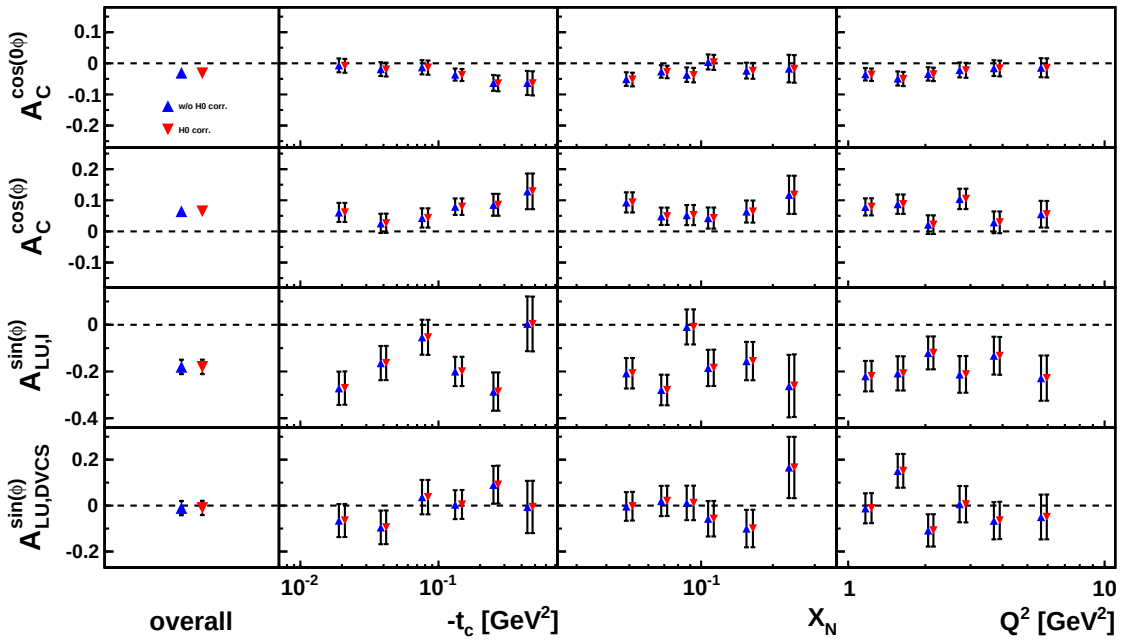

Figure 5.31: The comparison of leading amplitudes of the asymmetries $\mathcal{A}_{\rm C}$, $\mathcal{A}_{\rm LU}^{\rm I}$ and $\mathcal{A}_{\rm LU}^{\rm DVCS}$ extracted with and without applying a correction due to the H0 inefficiency.

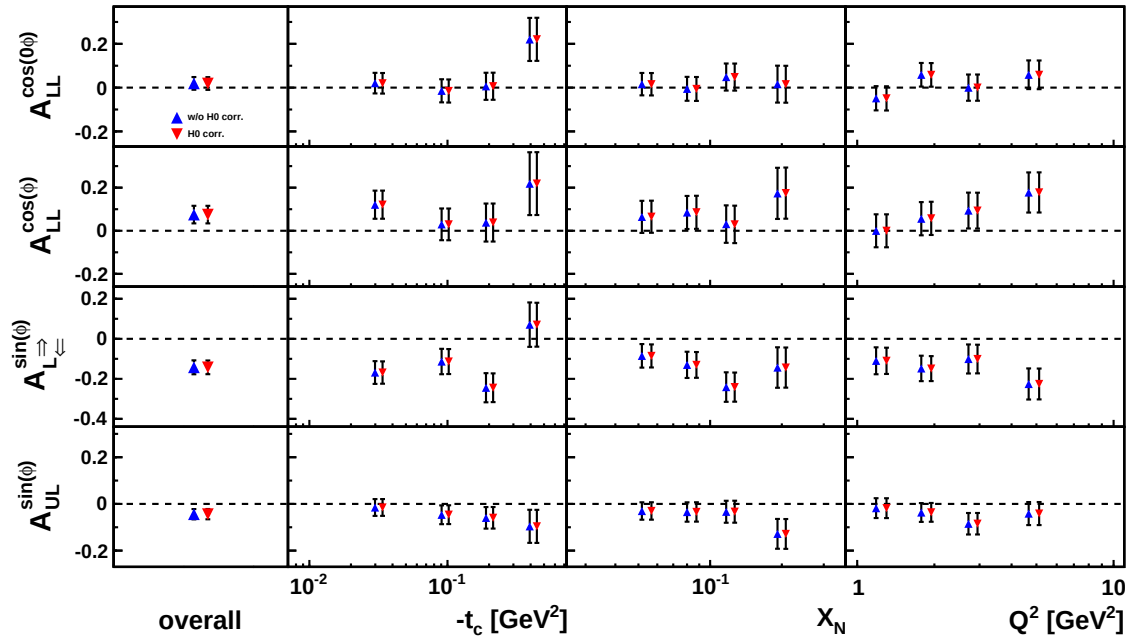

Figure 5.32: The comparison of leading amplitudes of the asymmetries $\mathcal{A}_{\mathrm{LL}}$, $\mathcal{A}_{\mathrm{L}\leftrightarrows}$ and $\mathcal{A}_{\mathrm{UL}}$ extracted with and without applying a correction due to the H0 inefficiency.

the efficiency ϵ^{-1} for each cell on the surface was assigned as a weight to each exclusive DVCS event according to the hit position of corresponding DIS lepton. Further the asymmetry amplitudes were extracted from a weighted event sample with the method described in section 5.4. The results of the efficiency correction for leading amplitudes of the asymmetries $\mathcal{A}_{\mathrm{C}}, \mathcal{A}_{\mathrm{LU}}^{\mathrm{I}}, \mathcal{A}_{\mathrm{LU}}^{\mathrm{DVCS}}$ and $\mathcal{A}_{\mathrm{LL}}, \mathcal{A}_{\mathrm{L}\leftrightarrows}, \mathcal{A}_{\mathrm{UL}}$ are shown in Figures 5.31 - 5.32 respectively, where they are compared with the amplitudes extracted without correcting

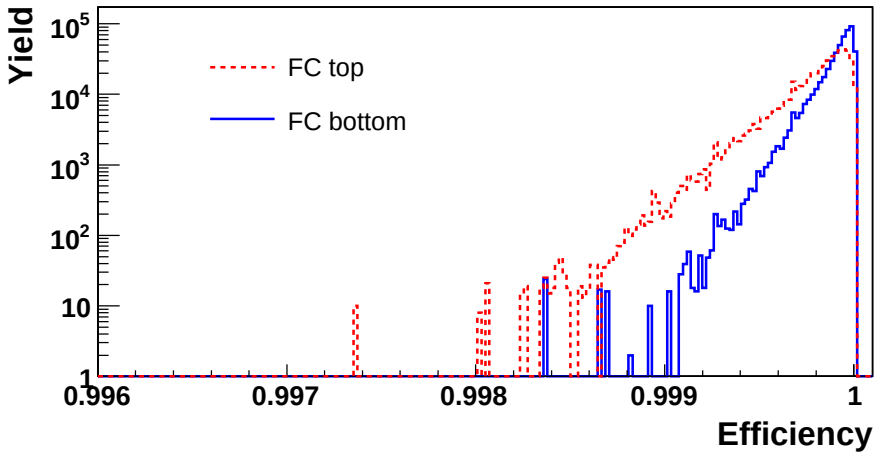

Figure 5.33: The distribution of plane efficiencies of top and bottom halves of forward chambers from the data taking year 2000 with polarized deuterons.

for the H0 efficiency. The comparison in Figures 5.31 - 5.32 indicate that the influence of H0 efficiency on the extracted asymmetry amplitudes is negligible.

Remaining sources of the detection inefficiencies that is relevant for current analysis are the tracking inefficiencies. They are caused by the ability of HRC to reconstruct the tracks from the hits in the tracking chambers. The efficiencies are defined for a single tracking plane ('plane efficiency') as a ratio of number of tracks which have a hit in the given detector plane to the number of reconstructed tracks without considering the selected plane [Due95]. Further the plane efficiencies are combined and the global plane efficiencies are given separately for each half of the forward and backward chambers. As an example the plane efficiencies of the forward chambers are shown in Figure 5.33 for the data collected on polarized deuterium in the year 2000. The average efficiencies for both halves of the detector are larger than 99%. High efficiencies for the FC's were obtained also for all other years, while the efficiencies of BC's were always higher then that of FC's.

As a conclusion, the influence of detection inefficiencies on the extracted asymmetry amplitudes were found to be negligible. Therefore, the data were not corrected for the detection inefficiencies, and no systematic uncertainty due to these inefficiencies was assigned to the final results.

5.5.5 Background correction

It has been discussed in a previous sections that the exclusive sample that is used for the extraction of asymmetry amplitudes from the data collected on the deuterium target originates from different processes. Beside the coherent and incoherent DVCS/BH processes, which are the main signals of interest, also the background processes contribute in the exclusive sample of events. Among the background processes the ones, whose contribution in the exclusive sample exceeds 1% are the associated DVCS/BH processes and semi-inclusive production of neutral mesons, mainly pions. The background itself is dominated by the associated DVCS/BH processes. In present analysis without a detection of recoiled target particle, the associated process can not be separated and remains as a part of signal. The contribution in the semi-inclusive background originates mainly from π^0 production, which significantly dominates over the production of η meson. These processes contribute in the single photon sample, when one of the decay photons remains undetected by a spectrometer or unresolved by the calorimeter. Beside above mentioned processes, their is also a contribution from the exclusive production of neutral pions in the measured yield. As was mentioned in section 5.3.3, the fractional contribution of this process in the exclusive sample of DVCS events was estimated from Monte Carlo and was found to be less than 0.7% [Kra05, Zei09]. Meanwhile the correction for exclusive pion production was carried out in the analysis of DVCS asymmetries on hydrogen target [Zei09, Ye07, Mah10], resulting in a negligibly small contribution compared with semi-inclusive pion production. Therefore, in the current analysis no correction was applied on the measured amplitudes due to the exclusive pion production, and it was not included also in the Monte Carlo simulations

In order to correct the extracted asymmetry amplitudes for the background processes, the asymmetries of the background processes A_{bg} need to be known, together with fractional contributions of each process f_{bg} in the exclusive sample. Further, the correction can be done according to

$$A_{ela.} = \frac{1}{1 - \sum_i f_{bg}^i} (A_{meas.} - \sum_i f_{bg}^i A_{bg}^i) \,, \tag{5.54}$$

where the $A_{ela.}$ is the corrected asymmetry of the elastic process and $A_{meas.}$ is the measured asymmetry. The sum goes over all background process. As was mentioned above, among the background processes the resonance production has the largest contribution, while the asymmetries in current analysis were not corrected for the associated background process, since not to much is known about the transition GPDs that govern the dynamics of the associated DVCS processes and can produce azimuthal asymmetries.

The only process that was corrected for, is the semi-inclusive production of neutral mesons. The fractional contributions of semi-inclusive processes were estimated from Monte Carlo and are given in Tables 5.4 and 5.5 for each kinematic bin in $-t_c$, Q^2 and x_N. The semi-inclusive production of neutral mesons is dominated mainly by neutral pions (about 80%) , therefore in the determination of the background asymmetries only neutral pions will be considered. The asymmetries of semi-inclusive pions can be determined from the experimental data accumulated at HERMES. For this purpose the so-called two-photon analysis was performed. The following requirements were applied for the selection of exclusive two-photon event sample.

- Same Data Quality Requirements as for DVCS analysis (see section 5.1).
- Same DIS cuts on the scattered lepton as in the case of DVCS analysis (see section 5.2.1).
- Two uncharged clusters in the calorimeter.
  - Both photons pass the fiducial volume cuts.
  - Both photons leave a signal in the preshower.
  - The leading photon deposits an energy above $5\,GeV$ and the non-leading one above $1\,GeV$.
- The invariant mass of reconstructed π^0 was required to be $0.1\,GeV < m_{\gamma\gamma} < 0.17\,GeV$.
- Same exclusive cut as in the case of DVCS analysis, except from the cut on squared missing mass.

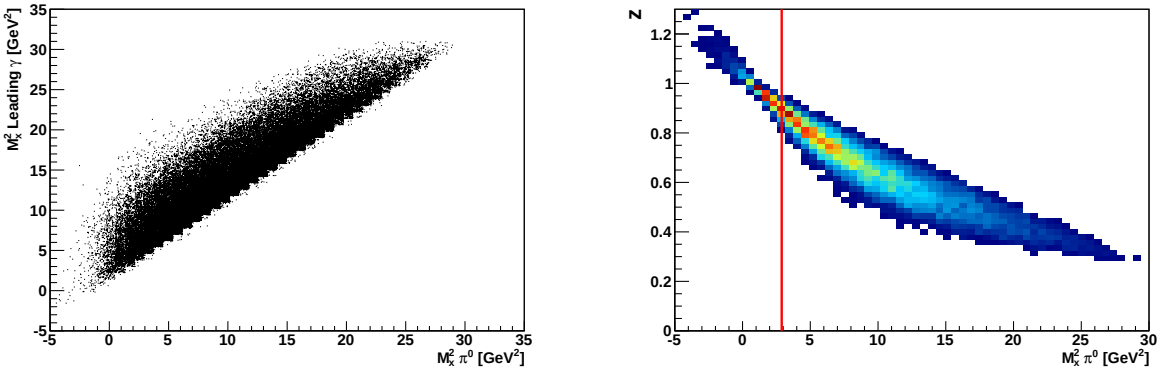

Figure 5.34: On the left side the correlation of M_x^2 variable calculated either for reconstructed pion or for leading photon kinematics is shown. On the right side the correlation between the fractional energy z and M_x^2 calculated for reconstructed pions is shown. The vertical line shows an upper boundary of the exclusive window $M_x^2 = 2.89\,GeV^2$.

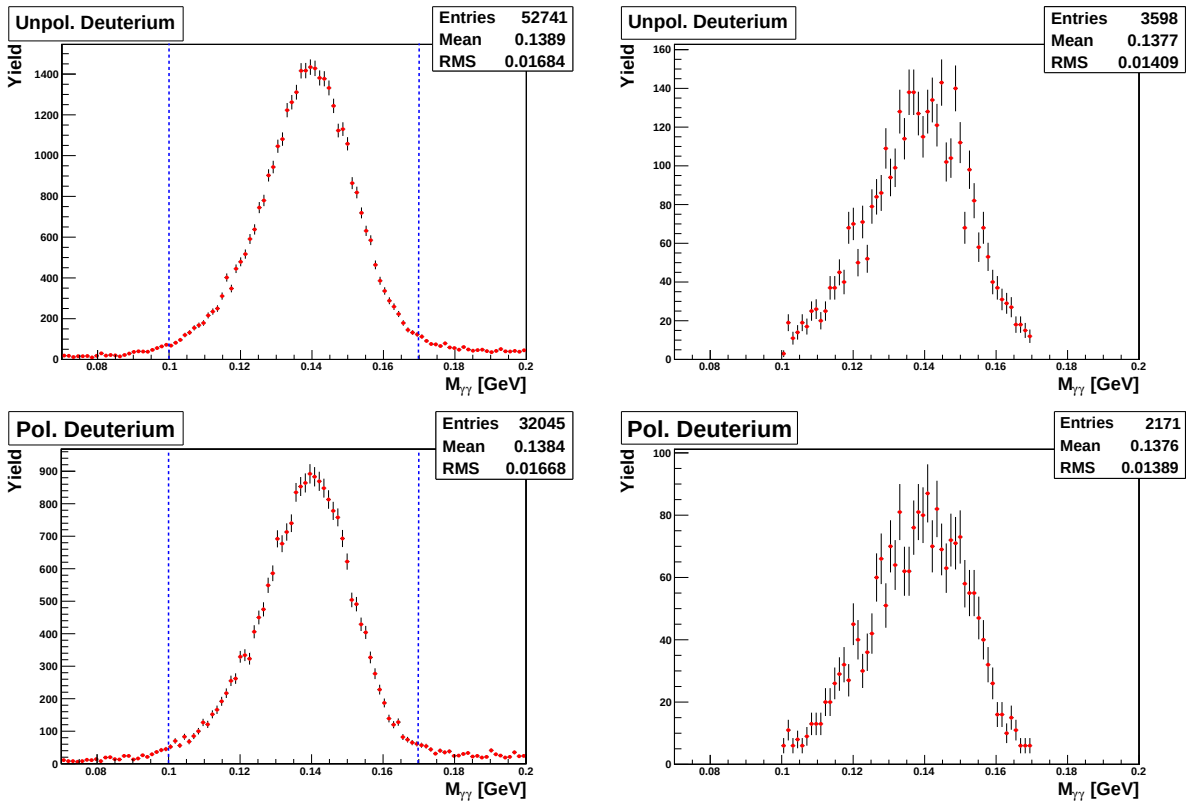

Figure 5.35: The distributions of invariant mass of reconstructed π^0 before (left) and after (right) applying an exclusive cuts. The distributions were obtained from all unpolarized (top) and longitudinally polarized (bottom) data sample.

- The fractional energy $z = E_{\pi^0}/\nu$ was required to be larger than 0.8.

In the selection criteria of two-photon sample that can contribute in the exclusive region of DVCS/BH sample, two alternative approaches can be applied. One can calculate the kinematics either with respect to reconstructed neutral pion or with respect to leading photon originated from the decay of π^0. Since the exclusive DVCS/BH sample contains only single cluster events, it is reasonable to consider the background asymmetries with respect to the leading photon. While in this case a problem arises with the cut on M_x^2. As can be seen from the left side plot of Figure 5.34, where the correlation of M_x^2 is shown, calculated either using the leading photon or using the reconstructed pion kinematics, the yield of two photon events in the exclusive region $-2.25\,GeV^2 < M_x^2 < 2.89\,GeV^2$ is quit low for the case when M_x^2 is calculated using the leading photon kinematics. On the other hand, from the correlation between pion fractional energy z and M_x^2 calculated from the pion kinematics, shown on the right side plot of Figure 5.34, one can see that mainly pions with fractional energies $z > 0.8$ contribute in the exclusive region. Hence, for the selection of semi-inclusive background sample, the exclusive kinematic variables were calculated using the kinematics of leading photon from two-photon data sample that satisfy a requirement $z > 0.8$.

In Figure 5.35 the reconstructed π^0 invariant mass distributions are shown for the two-photon event sample before and after applying the exclusive cuts. Figure contains all data collected on an unpolarized (top) and longitudinally polarized (bottom) deuterium target. The selected sample of two-photon events is used for the extraction of asymmetry

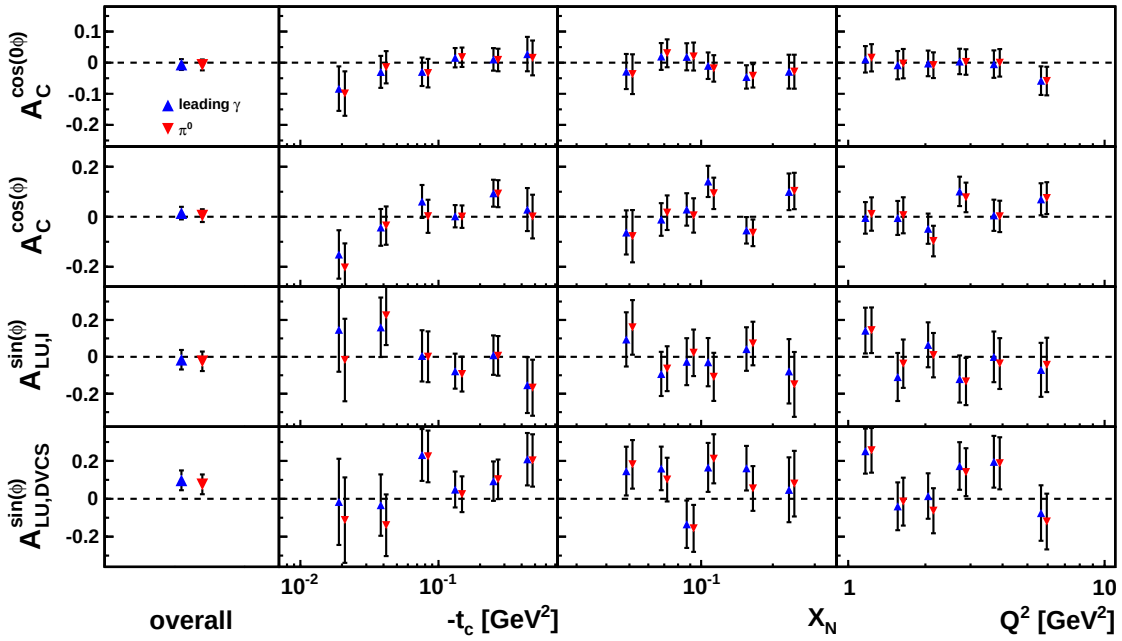

Figure 5.36: The leading amplitudes of the asymmetries $\mathcal{A}_{\rm C}$, $\mathcal{A}_{\rm LU}^{\rm I}$ and $\mathcal{A}_{\rm LU}^{\rm DVCS}$ extracted from the two-photon analysis, with respect to leading photon and reconstructed pion.

amplitudes of semi-inclusive neutral pion production. The results of the amplitudes of the asymmetries $\mathcal{A}_{\rm C}$, $\mathcal{A}_{\rm LU}^{\rm I}$ and $\mathcal{A}_{\rm LU}^{\rm DVCS}$ from semi-inclusive π^0 sample are shown in Figure 5.36. The asymmetry amplitudes obtained from a calculation of kinematics with respect to the leading photons are compared with the amplitudes corresponding to the kinematics of reconstructed pions. The comparison indicates that the asymmetry of neutral pions is mostly carried by the leading photons. This feature was also studied in details using Monte Carlo simulations [Ye07]. Note that the amplitudes of the asymmetries which are defined with respect to the beam charge, i.e. the amplitudes of the asymmetries $\mathcal{A}_{\rm C}$ and $\mathcal{A}_{\rm LU}^{\rm I}$, are compatible with zero. This is expected, as the beam-charge related asymmetries can not appear in the semi-inclusive pion production within one photon exchange approximation. Hence, the extracted zero valued amplitudes indicate a self consistence of the data and a precise calibration of the detectors. Meanwhile the charge-averaged beam-helicity asymmetry $\mathcal{A}_{\rm LU}^{\rm DVCS}$ shows a non-zero value (bottom raw of Figure 5.36). In Figure 5.37 the amplitudes of the asymmetries $\mathcal{A}_{\rightleftarrows}$, $\mathcal{A}_{\rm UL}$ and $\mathcal{A}_{\rm LL}$ are shown, extracted with respect to the leading photons from decay of π^0 in comparison with the ones extracted with respect to the reconstructed pions.

With the knowledge of the fractional contributions f_{SIDIS} and the asymmetry amplitudes A_{SIDIS} of the semi-inclusive neutral meson production, the background correction can be applied according to the following formula:

$$A_{corr.} = \frac{1}{1 - f_{SIDIS}}(A_{meas.} - f_{SIDIS}A_{SIDIS}). \tag{5.55}$$

Here $A_{meas.}$ is the extracted asymmetry amplitude and $A_{corr.}$ is the corrected one. The statistical uncertainty of the corrected amplitudes were propagated accordingly:

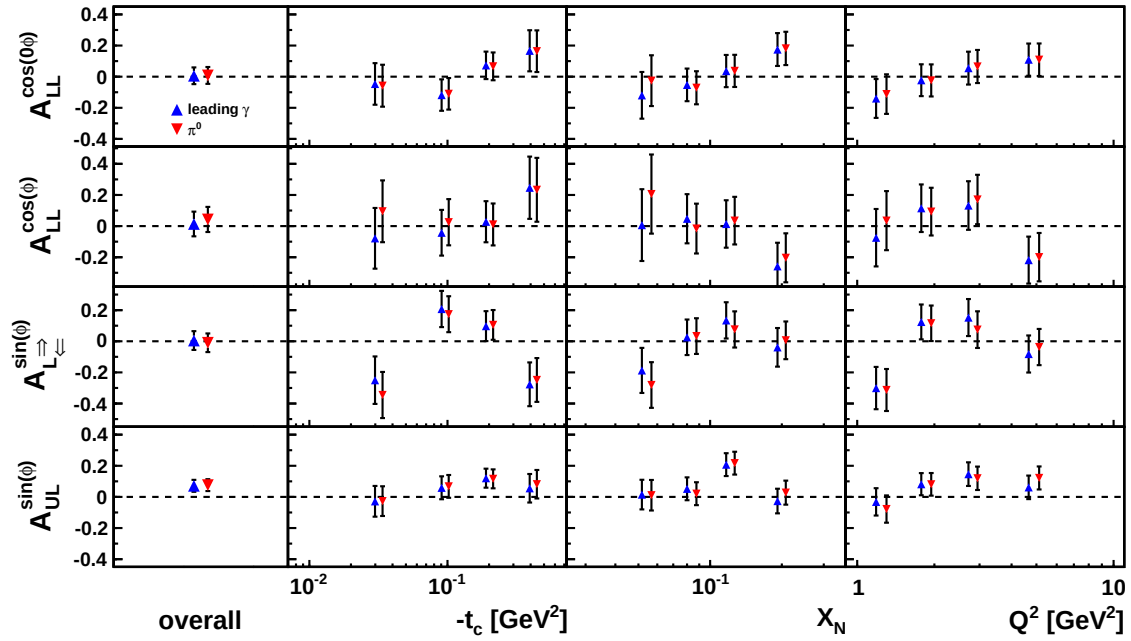

Figure 5.37: The leading amplitudes of the asymmetries $\mathcal{A}_{\Leftrightarrow}$, $\mathcal{A}_{\rm UL}$ and $\mathcal{A}_{\rm LL}$ extracted from the two-photon analysis, with respect to leading photon and reconstructed pion.

$$\delta_{A_{meas}} = \frac{1}{1-f_{SIDIS}} dA_{meas} \tag{5.56}$$

$$\delta_{A_{SIDIS}} = -\frac{f_{SIDIS}}{1-f_{SIDIS}} dA_{SIDIS} \tag{5.57}$$

$$\delta_{f_{SIDIS}} = \frac{A_{meas}-A_{SIDIS}}{(1-f_{SIDIS})^2} df_{SIDIS} \tag{5.58}$$

$$dA_{corr} = \sqrt{\delta^2_{A_{meas}} + \delta^2_{A_{SIDIS}} + \delta^2_{f_{SIDIS}}}\,. \tag{5.59}$$

Note that the beam-charge related asymmetries $\mathcal{A}_{\rm C}$, $\mathcal{A}^{\rm I}_{\rm LU}$, $\mathcal{A}_{\underset{\Rightarrow}{\rm C}\Leftarrow}$ and $\mathcal{A}_{\underset{\leftarrow}{\rm C}_{\rm L}}$ were corrected for a semi-inclusive background as dilutions, i.e the background asymmetry was taken to be $A_{SIDIS}=0$ and $dA_{SIDIS}=0$. The results of the semi-inclusive background correction for leading amplitudes of the asymmetries $\mathcal{A}_{\rm C}$, $\mathcal{A}^{\rm I}_{\rm LU}$, $\mathcal{A}^{\rm DVCS}_{\rm LU}$ and $\mathcal{A}_{\Leftrightarrow}$, $\mathcal{A}_{\rm UL}$, $\mathcal{A}_{\rm LL}$ are shown in Figures 5.38 - 5.39 respectively, where they are compared with the amplitudes before applying background correction.

Apart from the above described correction, also a systematic uncertainty was assigned to the final results due to background correction. The systematic uncertainty was taken as a half of correction size, with an additional contributions due to the statistical uncertainties of the measured background asymmetry and simulated fractions of the background process. The resulting systematic uncertainty was assigned as

$$Syst.Uncertainty = \sqrt{(\frac{A_{corr}-A_{meas}}{2})^2 + \delta^2_{A_{SIDIS}} + \delta^2_{f_{SIDIS}}}\,.$$

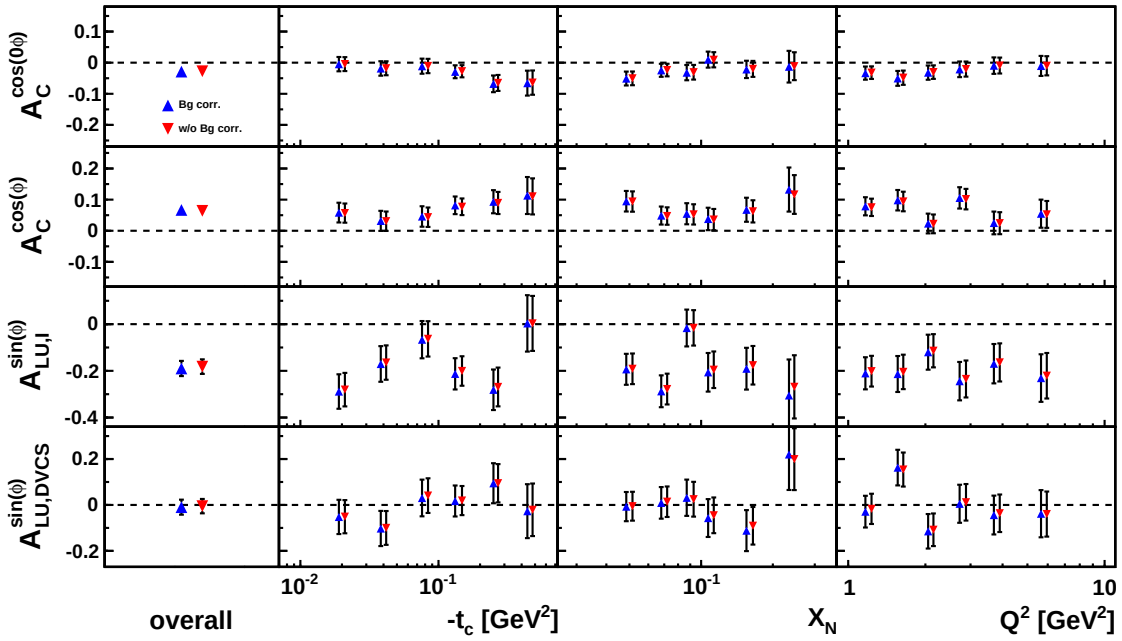

Figure 5.38: Comparison of leading amplitudes of the asymmetries $\mathcal{A}_{\mathrm{C}}$, $\mathcal{A}_{\mathrm{LU}}^{\mathrm{I}}$ and $\mathcal{A}_{\mathrm{LU}}^{\mathrm{DVCS}}$ before and after background correction.

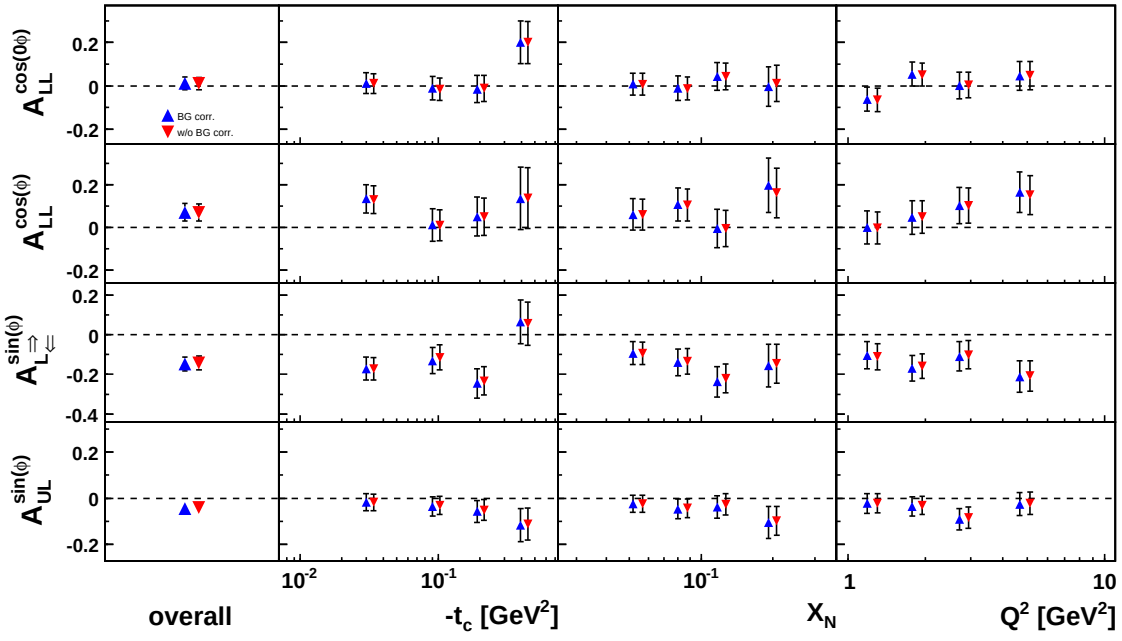

Figure 5.39: Comparison of leading amplitudes of the asymmetries $\mathcal{A}_{\Leftrightarrows}$, $\mathcal{A}_{\mathrm{UL}}$ and $\mathcal{A}_{\mathrm{LL}}$ before and after background correction.

5.5.6 Four - in - one method

An estimate of possible influences on the extracted asymmetry amplitudes from the acceptance, smearing, finite bin width, and misalignment of detector components with respect to each other and with respect to the beam are discussed in this section.

The acceptance of HERMES spectrometer allows to measure the desired quantities in a limited geometric region. In addition, to ensure the reliability of any measurement, various kinematic requirements and limitations need to be satisfied. Given these circumstances, the measurement can be performed in a fixed phase space, specific for the given experiment. For the comparison with other experimental measurements and also with theoretical predictions, the results need to interpreted in 4π geometry and presented in fixed kinematic point. This requires precise estimation of the possible difference between asymmetries measured in the acceptance and in the 4π, $\langle A(x)\rangle_{4\pi} - \langle A(x)\rangle_{HERMES}$. Moreover, since the theoretical predictions for the asymmetries are given for fixed kinematics, also the experimental results, extracted from certain kinematic range, should be presented for averaged kinematics. Therefore, the bias introduced from averaging over finite bin width (bin centering effect) should be estimate, $\langle A(x)\rangle - A(\langle x\rangle)$. The complications with the estimation of acceptance and finite-bin-width effects arise due to the fact that the measured asymmetries are a priori unknown. The only knowledge about measured asymmetries is available either from the experimental measurement which are almost affected by the acceptance or binning effects or from a theoretical predictions, which are a subject of model dependence. A Monte Carlo based investigations [Kra05, Ely02, Ell04] indicate that the acceptance effects are mainly sensitive to the absolute values of the true asymmetries, while the finite bin with effect has a strong dependence on the internal kinematic dependences of the asymmetries. The latter does not allow to correctly esti-

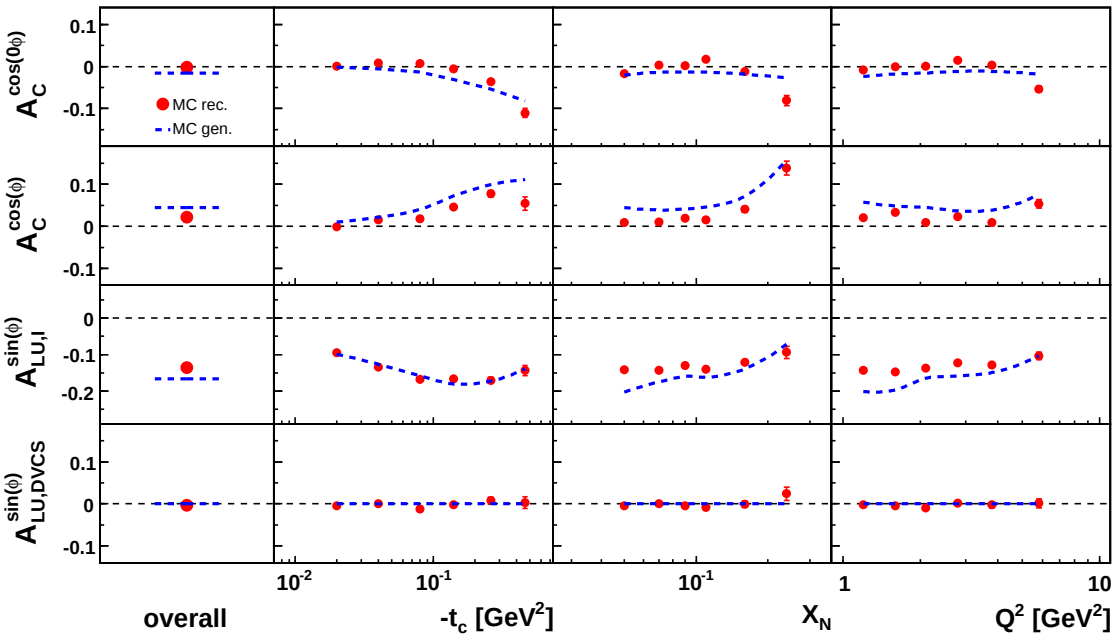

Figure 5.40: Reconstructed and generated leading amplitudes of the asymmetries $\mathcal{A}_{\rm C}$, $\mathcal{A}_{\rm LU}^{\rm I}$ and $\mathcal{A}_{\rm LU}^{\rm DVCS}$ obtained from *gmc_dual* generator.

mate the finite bin width effect by introducing a constant asymmetry in the Monte Carlo generator. Apart from the above mentioned effects also the smearing of reconstructed kinematic variables due the limited resolution of the detectors can cause a bias in the measured asymmetries compared with the true ones. This effect is also sensitive to the internal kinematic dependences of the asymmetries. Finally, the detector components of the spectrometer were found to be slightly tilted or shifted from their designed positions, also the HERA lepton beam was found to be tilted with respect to the z-axis. These misalignment effects can also influence the reconstruction of kinematic variables.

The combined contribution of the above mentioned effects to the systematic uncertainties was estimated from a Monte Carlo simulation. The Monte Carlo data were simulated according to the full simulation chain described in section 5.3 and including an information about the misalignment of the detector and the beam. The asymmetry amplitudes were extracted in a same way as those from experimental data. These reconstructed asymmetry amplitudes were compared with the amplitudes generated at the mean kinematics in 4π with the corresponding model. The difference between generated and reconstructed amplitudes provides a measure of systematic uncertainty.

For the asymmetries from an unpolarized deuterium target the *gmc_dual* generator was used for the estimation of four-in-one systematic uncertainties, while for the polarized data the *gmc_dvcs* generator was used. In the latter case only incoherent process was considered and the resulting systematic uncertainties were determined as root mean square of the differences between generated and reconstructed amplitudes obtained from five available models. The comparison between reconstructed and generated amplitudes are shown in Figure 5.40 obtained from *gmc_dual* generator and in Figures 5.41 - 5.42 from models one and five of *gmc_dvcs* generator.

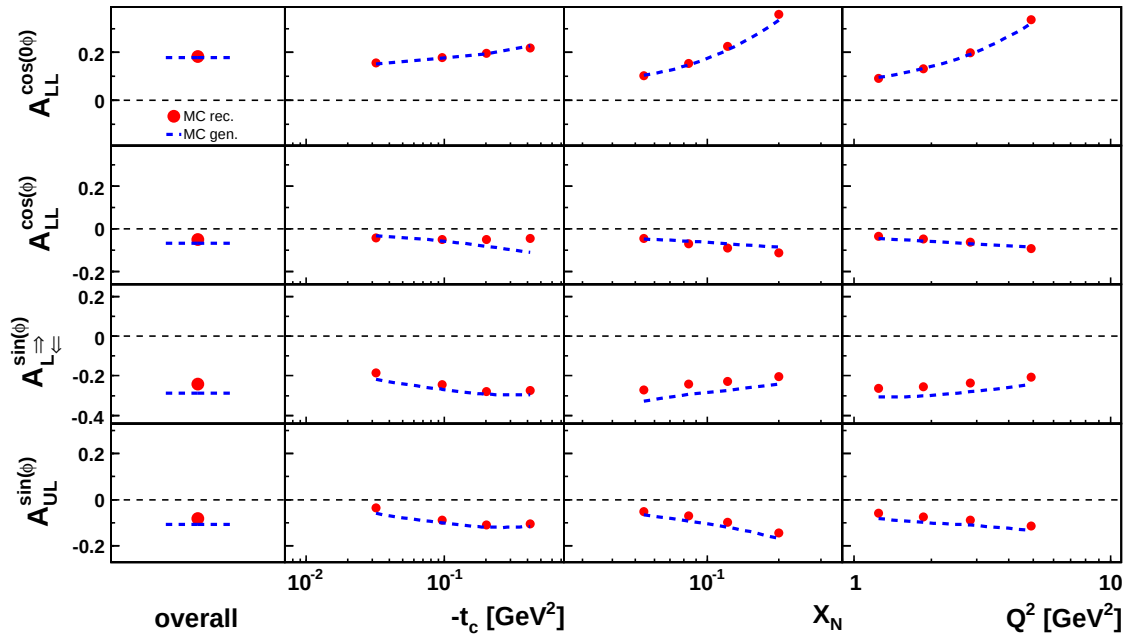

Figure 5.41: Reconstructed and generated leading amplitudes of the asymmetries $\mathcal{A}_{\Leftrightarrow}$, $\mathcal{A}_{\mathrm{UL}}$ and $\mathcal{A}_{\mathrm{LL}}$ obtained from model one of *gmc_dvcs* generator.

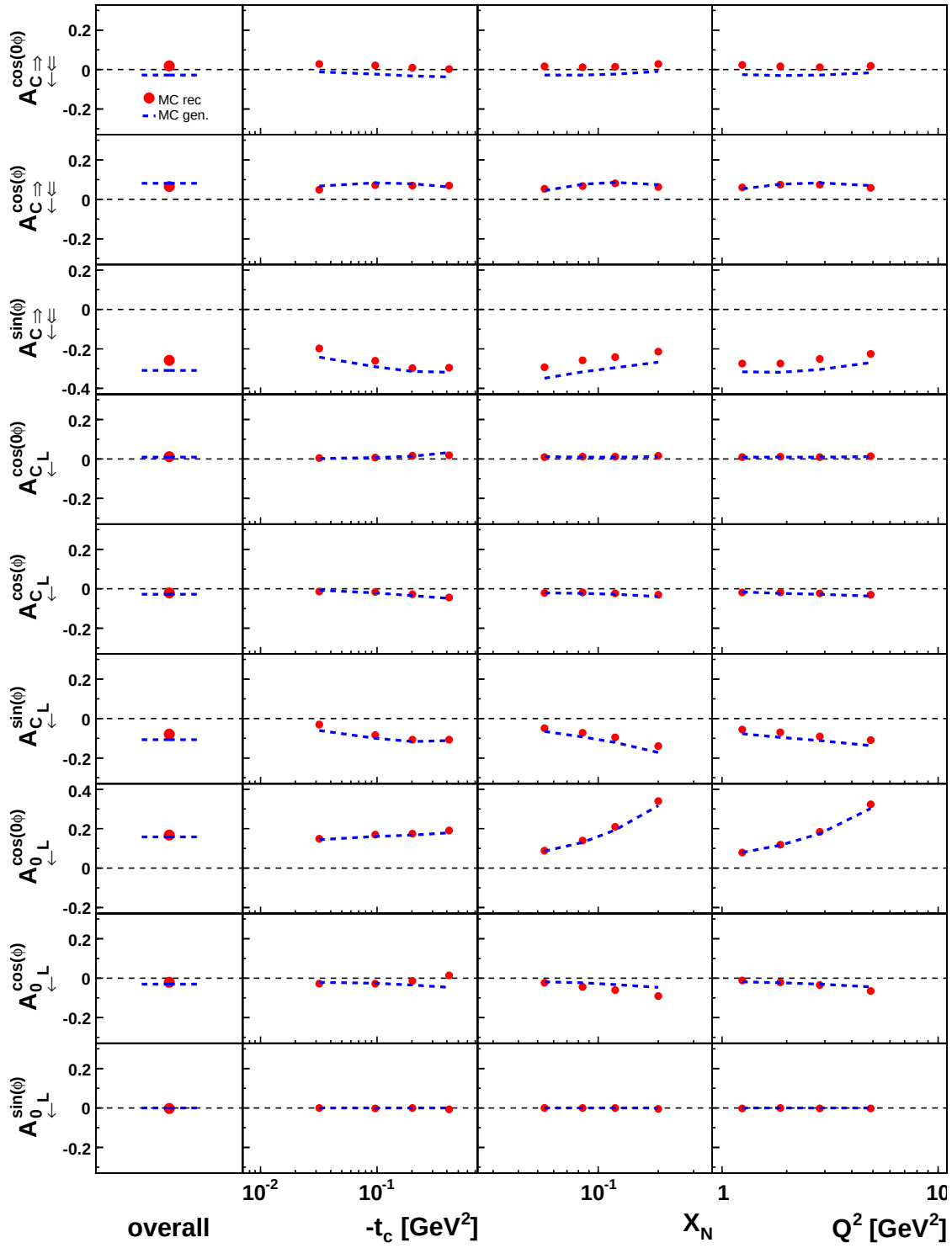

Figure 5.42: Reconstructed and generated leading amplitudes of the asymmetries $\mathcal{A}_{\overleftarrow{\Leftrightarrow}}$, $\mathcal{A}_{\overleftarrow{0}_{\mathrm{L}}}$ and $\mathcal{A}_{\overleftarrow{\mathrm{C}}_{\mathrm{L}}}$ obtained from model five of *gmc_dvcs* generator.

5.5.7 Normalization uncertainty

As was mentioned in section 5.2.4 the asymmetries discussed in current report can be normalized to either integrated luminosity or to number of DIS events. Both normalization methods have certain disadvantages and advantages, that were discussed in section 5.2.4. The results obtained from data collected on an unpolarized deuterium were normalized to DIS. The uncertainties arising from DIS normalization can be caused by the trigger inefficiency, by differences in the acceptance for different data taking years or by the charge symmetric background. The mentioned uncertainties are expected to affect mainly the constant amplitude of the beam-charge asymmetry $A_C^{\cos(0\phi)}$. An influence of position dependent trigger inefficiency was studied in section 5.5.4, for exclusive sample of DVCS/BH events, and was found to be negligible. In the case of DIS counting, their is no need to consider position dependent correction, therefore the correction to DIS numbers will be less than 1%. The count rate of the DIS numbers were not corrected also for the charge symmetric background. The latter is usually done by counting the number of oppositely charged leptons that satisfy to all DIS requirements. This effect was found to be of an order of 1%, while its variation for data collected in different years is even less. Since the mentioned 1% effects refer to a count rate of the DIS number, their contribution in the asymmetries is expected to be much smaller. Therefore, no systematic uncertainty was applied to the final results due to the uncertainty of DIS normalization.

The situation is more complicated with luminosity normalization. The latter was used in the extraction of asymmetry amplitudes from data collected on a longitudinally polarized deuterium. As was mentioned in section 5.2.4, the uncertainty of integrated luminosity measurement is about 7.2% for these data. For the normalization of single-charge asymmetries $\mathcal{A}_{\mathrm{LL}}$, $\mathcal{A}_{\mathrm{L}\overleftrightarrow{}}$ and $\mathcal{A}_{\mathrm{UL}}$, the raw luminosity count rate can be used instead of integrated luminosity. As the luminosity constant for the data collected in 1999 and 2000 is the same. On the other hand since the luminosity measurement does not depend on the target polarization, and the latter flips rapidly compared to changes in luminosity, the uncertainty of measured luminosity can not affect the target-spin related asymmetries. Therefore, no systematic uncertainty was applied due the luminosity normalization also to the asymmetries extracted from the longitudinally polarized data set.

5.5.8 Radiative corrections

The results presented in current report are not corrected for QED radiative effects. Substantial contributions to the BH and DVCS cross section originates from a soft photon emission processes and from a first order one-loop corrections, that include vertex, lepton self-energy, and vacuum polarization corrections. Although these corrections are expected to be suppressed by one order of $\alpha_{em} = 1/137$, they can still have a non-negligible contribution at certain kinematic regions. The radiative corrections to BH and DVCS processes have been estimated for JLAB kinematic conditions [Van00], where they lead to a reduction of BH and DVCS cross section by about $\approx 20\%$. The same calculations for a single beam-spin asymmetry at JLAB kinematics $E_{beam} = 6\,GeV$, $Q^2 = 2\,GeV^2$ and $x_{Bj} = 0.3$ suggest a reduction of asymmetry by about 5%. Since the radiative corrections are inversely proportional to the beam energy, they can be expected to have much smaller contribution at HERMES. While the contribution of radiative corrections strongly depends on the resolution of the detector. The calculations in [Van00] were done for the soft photon energies up to $0.1\,GeV$, assuming that soft photon emission with photon energies above $0.1\,GeV$ can be distinguished from a single photon events by the spectrometer.

The latter is not the case for HERMES. Therefore the estimates from [Van00] can not be directly propagated to the results presented in this report. Other estimates of radiative corrections have been carried out in [Afa06]. Here the single beam and target -spin asymmetries were calculated, originating from radiative corrections only to BH process. The estimated asymmetries for HERMES kinematic conditions were found to be negligibly small. Presently no estimates exist for radiative corrections to beam-charge asymmetry.

As a conclusion no systematic uncertainty was assigned to the asymmetries presented in current report due to the radiative corrections.

5.5.9 Scale uncertainty

The polarization of HERA lepton beam was measured by two independent polarimeters LPOL and TPOL, that were discussed in section 4.1. In parallel with polarization measurement various systematic investigations were performed by group of experts to ensure the stability and reliability of these measurements. The polarization measurement is detailed in [Bar93, Bec02] for TPOL and LPOL respectively, where also the possible sources of systematic uncertainties are discussed and the total scale uncertainty is given for the polarization measurement. They are listed in Table 5.10 separately for both polarimeters and for different data taking years. Note that during operation the polarization measurement was not always carried out by both polarimeters. For some fills only measurements from one of the polarimeters were provided. Table 5.10 summarizes the collected integrated luminosities during the operation of each polarimeter in each data taking year. Whenever measurements were available from both polarimeters, they are combined with LPOL measurements, since its systematic uncertainty is smaller from that of TPOL. From Table 5.10 the scale uncertainties were derived for each of the asymmetries, sensitive to the beam polarization measurement. They were obtained by luminosity weighted averaging uncertainties from different data taking years. For the asymmetries that are sensitive to the target polarization measurement, the scale uncertainties were derived from Table 4.1, while for the double-spin asymmetries, the scale uncertainties from beam and target polarization measurement were combined in quadrature. The exact numbers will be given in section 5.5.11.

Data set	$Lumi_{TPOL}$ $[pb^{-1}]$	$Lumi_{LPOL}$ $[pb^{-1}]$	$Syst_{TPOL}$	$Syst_{LPOL}$
96d0	43.9	-	3.26 %	-
97d1	53.1	-	3.26 %	-
98d0	10.6	13.5	3.26 %	1.6 %
99c0	-	6.1	3.26 %	1.6 %
00d2	1.3	37.4	3.26 %	1.6 %
05c1	14.8	117.2	3.26 %	2.0 %
98d0 pol.	23.0	3.6	3.26 %	1.6 %
99c0 pol.	2.5	27.2	3.26 %	1.6 %
00d2 pol.	27.6	98.2	3.26 %	1.6 %

Table 5.10: The integrated luminosities of each data set used in current analysis. The collected luminosities for each data taking year are given separately for a time periods, when each of the polarimeters was operating. Also given are the systematic uncertainties of the beam polarization measurement for each data taking year and each polarimeter.

5.5.10 Contribution from transverse component of target polarization

In the extraction of asymmetry amplitudes with respect to longitudinal vector polarization of the target it was assumed that the target is polarized along the virtual photon direction. Based on this assumption an appropriate decomposition of Fourier coefficients from the BH/DVCS cross section was introduced in Eqs. 3.20 - 3.21, respectively for spin-1/2 and spin-1 targets and also the azimuthal dependencies of each term of the cross section in Eqs. 3.42 - 3.44. While in the real experimental situation the target was polarized with respect to the lepton beam. Therefore the polarization vector is rotated with respect to the virtual photon direction by an angle $\theta_{\gamma*}$. This is illustrated on the left plot of Figure 5.43[2]. The above mentioned effect leads to a non-vanishing transverse

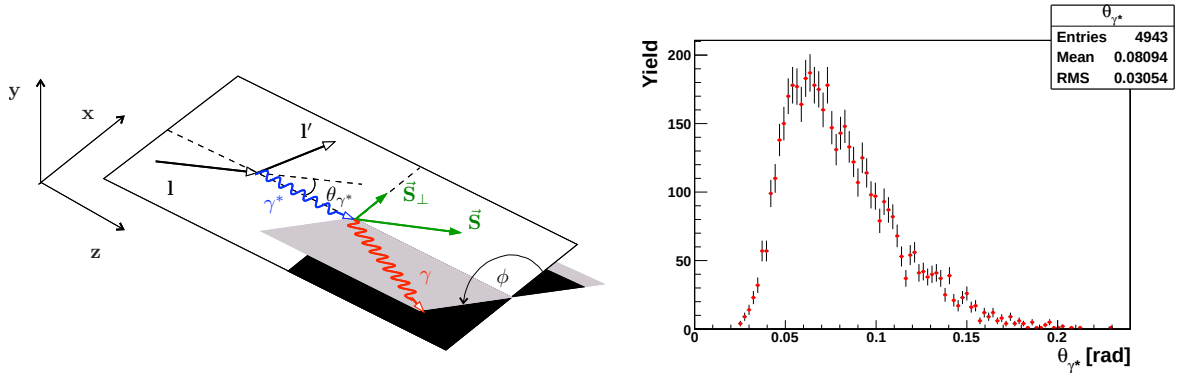

Figure 5.43: On the left side the orientation of target polarization vector with respect to the virtual photon and lepton beam is shown. On the right side the distribution of the angle between lepton beam and virtual photons is shown from data collected with longitudinally polarized deuterium target during the year 2000.

polarization component of the target and meanwhile introduces a depolarization of the longitudinal component. In order to estimate a possible contribution of this effect on the extracted asymmetries, the knowledge of transverse single target-spin and double-spin asymmetries is necessary. The latter are unknown for the coherent process on deuterium, and it is expected that they do not differ much from that on hydrogen target. The leading amplitudes of transverse single and double-spin asymmetries on hydrogen are sensitive to the Fourier coefficients from the azimuthal decomposition of the interference term of the BH/DVCS cross section on transversely polarized target. The latter reads as [BMK02]:

$$
\begin{aligned}
I \;=\; & -\frac{K_I e_\ell}{\mathcal{P}_1(\phi)\mathcal{P}_1(\phi)}\Big[\sum_{n=0}^{3} c^I_{n,unp}\cos(n\phi) + P_\ell\Big[\sum_{n=1}^{2} s^I_{n,unp}\sin(n\phi)\Big] + \\
& S_T\Big[\sum_{n=0}^{3} c^I_{n,TP-}\sin(\phi-\phi_s)\cos(n\phi) + \sum_{n=1}^{3} s^I_{n,TP+}\cos(\phi-\phi_s)\sin(n\phi)\Big] + \\
& P_\ell S_T\Big[\sum_{n=0}^{2} c^I_{n,TP+}\cos(\phi-\phi_s)\cos(n\phi) + \sum_{n=1}^{2} s^I_{n,TP-}\sin(\phi-\phi_s)\sin(n\phi)\Big]\Big],
\end{aligned}
\tag{5.60}
$$

[2]Note that the coordinate system shown in the figure is also rotated with respect to the HERMES coordinate system by an angle $\theta_{\gamma*}$.

where ϕ_s is the angle between lepton scattering plane and transverse component of target polarization. Since the target is polarized in the lepton scattering plane, the angle ϕ_s has fixed values of 0 and π for positive and negative target polarization respectively. These allows to distinguish between coefficients from Eq. 5.60 that can contribute either in $\sin(\phi)$ or $\sin(2\phi)$ amplitude of longitudinal target-spin asymmetry A_{UL}, and respectively in $\cos(0\phi)$ or $\cos(\phi)$ amplitude of longitudinal double-spin asymmetry A_{LL}

The extracted longitudinal target-spin asymmetry amplitudes $A_{UL}^{\sin(\phi)}$ and $A_{UL}^{\sin(2\phi)}$ can be related to the true values of the same amplitudes $A_{UL}^{*\sin(\phi)}$ and $A_{UL}^{*\sin(2\phi)}$ as

$$\begin{aligned} A_{\mathrm{UL}}^{\sin(\phi)} &= \cos(\theta_{\gamma*}) A_{\mathrm{UL}}^{*\sin(\phi)} - \frac{1}{2}\sin(\theta_{\gamma*})\Big[2A_{UT,I}^{\sin(\phi-\phi_s)} \\ &\quad - A_{UT,I}^{\sin(\phi-\phi_s)\cos(2\phi)} + A_{UT,I}^{\cos(\phi-\phi_s)\sin(2\phi)} \Big]_{\phi_s=0} \end{aligned} \tag{5.61}$$

$$\begin{aligned} A_{\mathrm{UL}}^{\sin(2\phi)} &= \cos(\theta_{\gamma*}) A_{\mathrm{UL}}^{*\sin(2\phi)} - \frac{1}{2}\sin(\theta_{\gamma*})\Big[A_{UT,I}^{\sin(\phi-\phi_s)\cos(\phi)} \\ &\quad + A_{UT,I}^{\cos(\phi-\phi_s)\sin(\phi)} - A_{UT,I}^{\sin(\phi-\phi_s)\cos(3\phi)} + A_{UT,I}^{\cos(\phi-\phi_s)\sin(3\phi)} \Big]_{\phi_s=0} \end{aligned} \tag{5.62}$$

The estimates for the depolarization effect can be done based on the reconstructed values of the angle $\theta_{e\gamma*}$, that is shown on the right plot of Figure 5.43 and has an average value of about $0.08\,rad$. Hence, the depolarization effects that are proportional to the $\langle\cos(\theta_{e\gamma*})\rangle$ are less than 1%. The absolute size of the contribution from transverse target-spin asymmetry are estimated from the values of corresponding asymmetry amplitudes extracted at HERMES [Air08]. Since the largest amplitude of transverse target-spin was measured to be $A_{UT}^{\sin(\phi-\phi_s)\cos(\phi)} = -0.164 \pm 0.039(stat.) \pm 0.023(\mathrm{syst.})$, therefore the absolute size of this effect does not exceed the value of 0.008. And in addition it mainly contributes to the $A_{UL}^{\sin(2\phi)}$ amplitude.

The estimates of depolarization effects hold also for the case of double-spin asymmetry amplitudes. For the estimation of the contribution from transverse double-spin asymmetry A_{LT}, one can write the relations between measured amplitudes $A_{\mathrm{LL}}^{\cos(0\phi)}$ and $A_{\mathrm{LL}}^{\cos(\phi)}$ and their true values as:

$$\begin{aligned} A_{\mathrm{LL}}^{\cos(0\phi)} &= \cos(\theta_{\gamma*}) A_{\mathrm{LL}}^{*\cos(0\phi)} - \frac{1}{2}\sin(\theta_{\gamma*})\Big[A_{LT,I}^{\cos(\phi-\phi_s)\cos(\phi)} \\ &\quad + A_{LT,I}^{\sin(\phi-\phi_s)\sin(\phi)} \Big]_{\phi_s=0} \end{aligned} \tag{5.63}$$

$$\begin{aligned} A_{\mathrm{LL}}^{\cos(\phi)} &= \cos(\theta_{\gamma*}) A_{\mathrm{LL}}^{*\cos(\phi)} - \frac{1}{2}\sin(\theta_{\gamma*})\Big[2A_{LT,I}^{\cos(\phi-\phi_s)} \\ &\quad + A_{LT,I}^{\cos(\phi-\phi_s)\cos(2\phi)} + A_{LT,I}^{\sin(\phi-\phi_s)\sin(2\phi)} \Big]_{\phi_s=0} \end{aligned} \tag{5.64}$$

The preliminary HERMES results of the transverse double-spin asymmetry suggest even smaller contribution, then that for single target spin asymmetry.

Based on the above discussed estimates of contribution from transverse polarization component of the target and also of the depolarization effects, no correction and no systematic uncertainty were assigned from these sources to the final results.

5.5.11 Summary of Systematic Uncertainties

Among various sources of systematic uncertainties that were discussed in previous sections, the ones that were found to make a sizable contributions were accounted for the total systematic uncertainty. Those are the uncertainties caused by the measurement of beam and target polarization, background correction, the shift of missing mass distribution, and by the combined influence of acceptance, finite-bin-width, smearing and misalignment effects. The individual contributions of these uncertainties are given in Table 5.11 for the leading asymmetry amplitudes, corresponding to the entire HERMES kinematics. The total uncertainty was obtained by quadratically adding all the contributions, except from the scale uncertainty. The systematic uncertainties were estimated for each kinematic bin separately.

Asymmetry Amplitude	δM_x^2 shift	δ BG. corr.	δ 4-in-1	Scale Uncertainty
$A_C^{\cos(0\phi)}$	0.001	0.001	0.014	-
$A_C^{\cos(\phi)}$	< 0.001	0.002	0.023	-
$A_{LU,I}^{\sin(\phi)}$	< 0.001	0.004	0.031	2.4%
$A_{LU,DVCS}^{\sin(\phi)}$	0.002	0.006	0.003	2.4%
$A_{LL}^{\cos(0\phi)}$	-	0.002	0.004	4.4 %
$A_{LL}^{\cos(\phi)}$	-	0.003	0.019	4.4 %
$A_{UL}^{\sin(\phi)}$	-	0.002	0.029	4.0 %
$A_{\mathrm{L}\overleftrightarrows}^{\sin(\phi)}$	-	0.004	0.057	1.9 %
$A_{\mathrm{C}\overleftrightarrows}^{\cos(0\phi)}$	-	< 0.001	0.034	-
$A_{\mathrm{C}\overleftrightarrows}^{\cos(\phi)}$	-	0.001	0.008	-
$A_{\mathrm{C}\overleftrightarrows}^{\sin(\phi)}$	-	0.001	0.057	2.2 %
$A_{\underset{\mathrm{L}}{\mathrm{C}}}^{\cos(0\phi)}$	-	< 0.001	0.002	5.7 %
$A_{\underset{\mathrm{L}}{\mathrm{C}}}^{\cos(\phi)}$	-	0.003	0.006	5.7 %
$A_{\underset{\mathrm{L}}{\mathrm{C}}}^{\sin(\phi)}$	-	< 0.001	0.028	5.3 %
$A_{\underset{\mathrm{L}}{0}}^{\cos(0\phi)}$	-	0.003	0.009	5.7 %
$A_{\underset{\mathrm{L}}{0}}^{\cos(\phi)}$	-	0.005	0.009	5.7 %
$A_{\underset{\mathrm{L}}{0}}^{\sin(\phi)}$	-	0.001	0.002	5.3 %

Table 5.11: Individual contributions of different sources of systematic uncertainties to the leading amplitudes of the asymmetries for entire HERMES kinematics.

Chapter 6

Results

In this chapter the final results of the asymmetry amplitudes are presented. The obtained asymmetry amplitudes from the analysis of the data collected on an unpolarized and longitudinally vector polarized deuterium targets are compared with the model predictions. Also a comparison of the results obtained on a deuterium target, with the similar ones extracted from a hydrogen data at HERMES is given.

6.1 Results on beam-charge and beam-helicity asymmetries for an unpolarized deuterium target

The final results of the asymmetry amplitudes extracted from a data collected on an unpolarized deuterium target are shown in Figures 6.1 - 6.3 as a function of $-t$, x_N, or Q^2. Note that in the following t will stand for a constrained variable t_c. While the variable x_D would be the appropriate choice when presenting experimental results for pure coherent scattering, the nucleonic Bjorken variable x_N is the practical choice in this case where incoherent scattering dominates over most of the kinematic range. The 'overall' results in the left columns correspond to the entire HERMES kinematic acceptance. Figure 6.1 shows the amplitudes of beam-charge asymmetry $A_{\rm C}^{\cos(n\phi)}$, and Figure 6.2 shows the amplitude of charge averaged beam-helcity asymmetry $A_{\rm LU,DVCS}^{\sin\phi}$, and the amplitudes of charge difference beam-helicity asymmetry $A_{\rm LU,I}^{\sin(n\phi)}$. All amplitudes are listed in Table 6.1 with the mean kinematic values of each bin[1], together with the statistical and systematic uncertainties.

In the case of beam-charge asymmetry, of special interest is the amplitude $A_{\rm C}^{\cos\phi}$. In the HERMES kinematic conditions the latter is sensitive to the GPD H_1 for coherent and GPD H for the incoherent process. The amplitude $A_{\rm C}^{\cos\phi}$ shows a positive value by 2.4 standard deviations from total experimental uncertainty. Moreover the present data indicates that this amplitude increases with increasing $-t$. The amplitude $A_{\rm C}^{\cos(0\phi)}$ in Figure 6.1, which is expected to relate to the same combination of GPDs as does $A_{\rm C}^{\cos\phi}$, shows similar behaviour but with opposite sign, as expected [BMK02]. The dependences of the amplitudes $A_{\rm C}^{0\cos\phi}$ and $A_{\rm C}^{\cos\phi}$ on x_N and Q^2 are flat, while possibly a small decrease of the amplitude $A_{\rm C}^{0\cos\phi}$ at smaller values of x_N can be seen. The other two amplitudes $A_{\rm C}^{\cos(2\phi)}$ and $A_{\rm C}^{\cos(3\phi)}$, related to twist-3 GPDs and the gluon transversity operator, respectively , are consistent with zero.

[1] The results of the amplitudes extracted in four bins in $-t\,, x_N$ and Q^2, i.e. a binning used for the extraction of the asymmetry amplitudes from polarized data given in Table 5.2, are available in the Durham database.

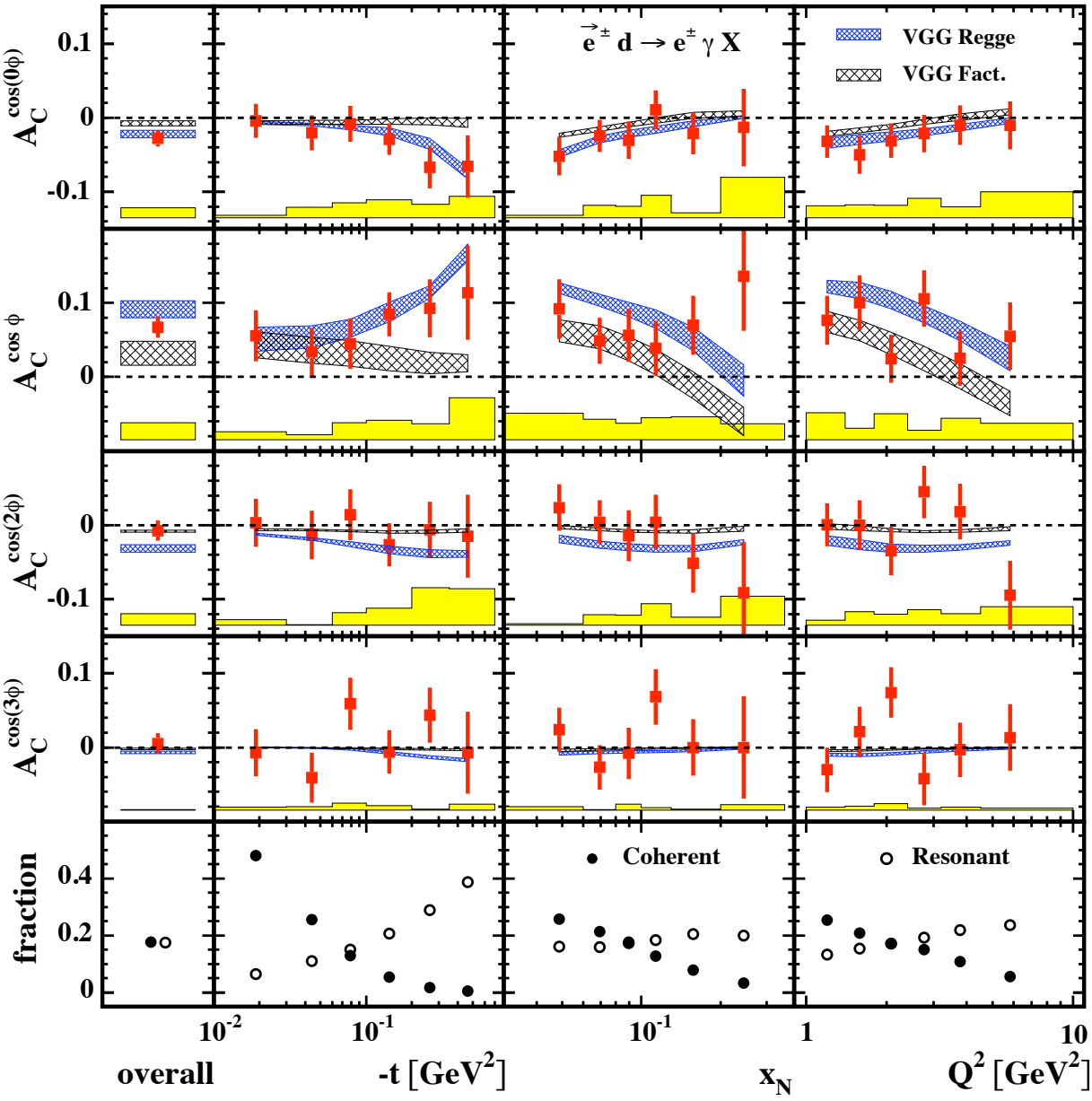

Figure 6.1: Amplitudes of the beam-charge asymmetry, which are sensitive to the interference term, in bins of $-t$, x_N, or Q^2. The squares represent the results from the present work. The error bars (bands) represent the statistical (systematic) uncertainties. The finely (coarsely) hatched bands are theoretical calculations for incoherently combined proton and neutron targets, using variants of a double-distribution model [VGG99, Rad99, GPV01] with the VGG Regge (VGG Factorized) ansatz for GPDs. The lowest panel shows the simulated fractions of coherent and resonant production.

The fractional contributions to the yield from the coherent processes and from processes with excitation of resonant final states are presented in the bottom row of Figure 6.1. Note that these fractional contributions that are given also in Table 5.5, are subject to considerable model dependence.

Figure 6.2 shows amplitudes of beam-helicity asymmetries, with the charge-averaged case related to the squared DVCS term in the upper row and the charge-difference case

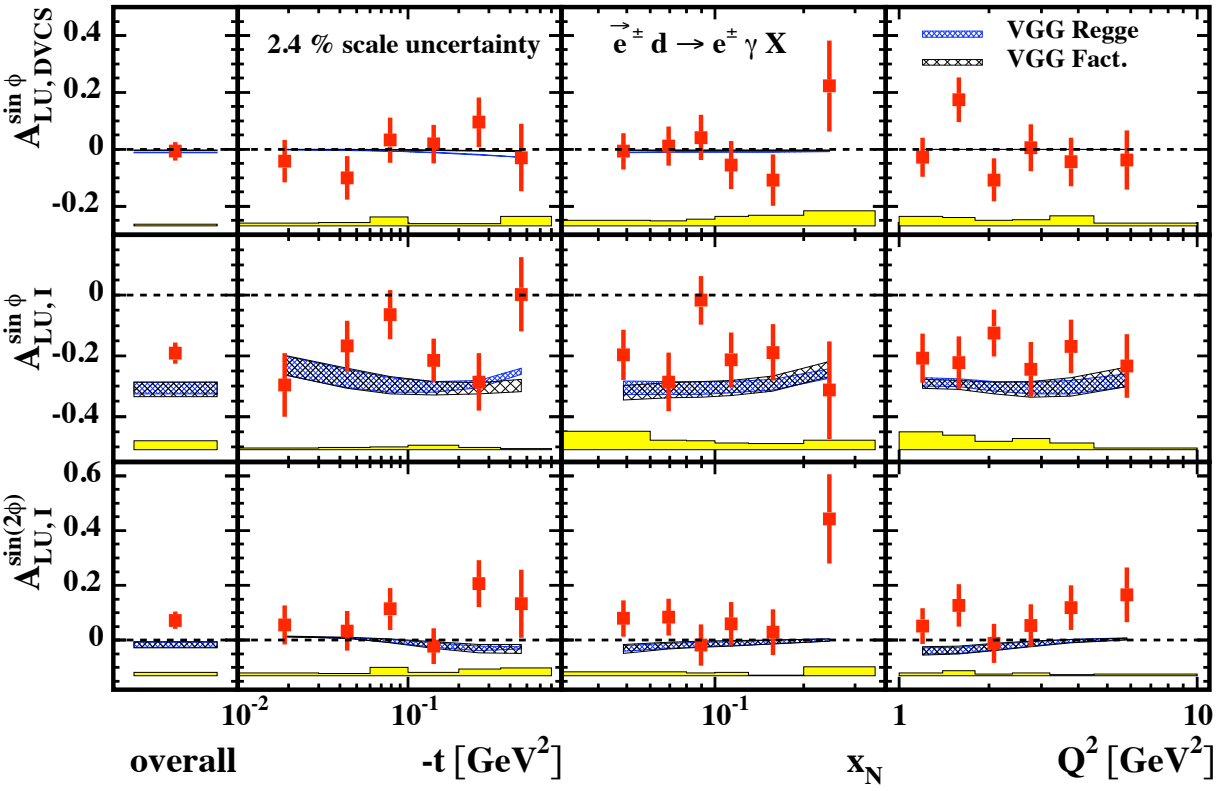

Figure 6.2: The first row shows the $\sin\phi$ amplitude of the charge averaged beam-helicity asymmetry that is sensitive to the squared DVCS term, in bins of $-t$, x_N, or Q^2. Correspondingly, the second (third) row shows the $\sin\phi$ ($\sin 2\phi$) amplitude of the charge difference beam-helicity asymmetry sensitive to the interference term. All symbols are defined as in Figure 6.1. There is an overall 2.4% scale uncertainty arising from the uncertainty in the measurement of the beam polarization.

related to the interference term in the other rows. The amplitude $A_{\mathrm{LU,DVCS}}^{\sin\phi}$, which is related to twist-3 GPDs, is found to be consistent with zero. Like the amplitude $A_{\mathrm{C}}^{\cos\phi}$, the amplitude $A_{\mathrm{LU,I}}^{\sin\phi}$ is also sensitive to the GPD H_1 [H] for the coherent [incoherent] process, although these two asymmetries reveal different aspects of the (real) GPD, selected by different convolutions with (complex) hard scattering amplitudes. While the amplitude $A_{\mathrm{C}}^{\cos\phi}$ is related to the real part of the CFF $\mathcal{H}_1$ [$\mathcal{H}$], the $A_{\mathrm{LU,I}}^{\sin\phi}$ amplitude is proportional to the imaginary part and shows significant negative values. The amplitude $A_{\mathrm{LU,I}}^{\sin(2\phi)}$ appears at twist-3 level, but nevertheless it shows a value which is non-zero and positive by 1.7 standard deviations of the total experimental uncertainty. Figure 6.3 shows the amplitudes that are forbidden by parity conservation but were included in the fit as a consistency test. They are consistent with zero.

The two hatched bands in Figures 6.1 and 6.2 are theoretical calculations for the incoherent process, based on two different ansätze for modeling GPDs [GPV01] in the VGG model [VGG01] (the coherent process will be considered in Section 6.3). In this model, a GPD is written as a double distribution [Mul94, Rad96] complemented by a D-term:

- In the 'factorized ansatz' (VGG Fact.), the dependences on t and (x, ξ) are uncorrelated. The t dependence is written in accordance with proton elastic form factors.

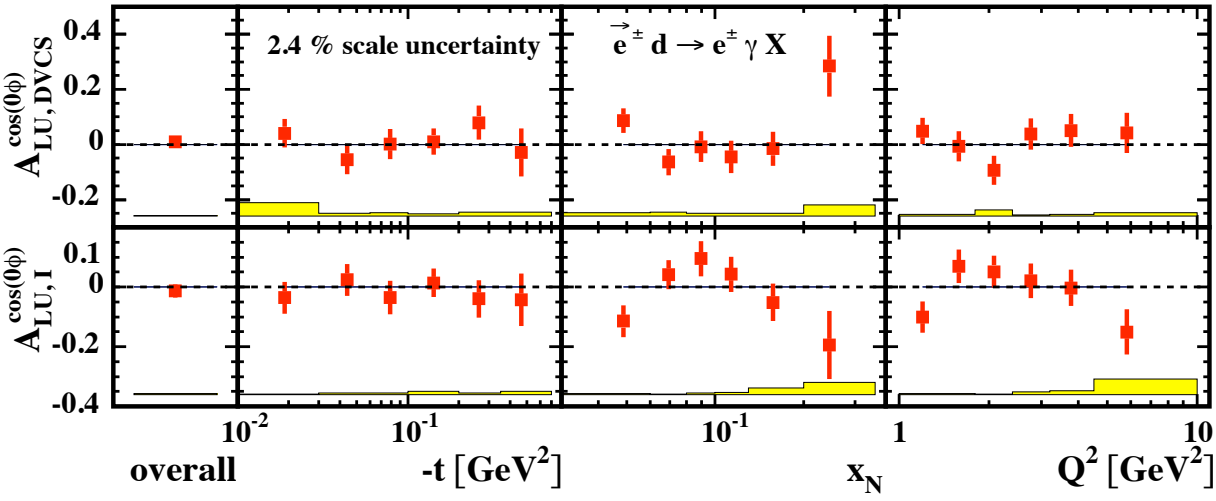

Figure 6.3: The $\cos(0\phi)$ amplitudes (constant terms) that are included as a consistency test in the fit function. All symbols are defined as in Figure 6.1. There is an overall 2.4% scale uncertainty arising from the uncertainty in the measurement of the beam polarization.

The (x, ξ) dependence is based on double distributions [Mul94] constructed from ordinary PDFs complemented with a profile function that characterizes the strength of the ξ dependence; in the limit $b \to \infty$ of the profile parameter b, the GPD is independent of ξ [Rad99]. Note that b is a free parameter to be experimentally determined independently for valence and sea quarks.

- The 'Regge ansatz' (VGG Regge) implements entanglement of the t dependence of the GPD with its dependence on x and ξ. This feature is inspired by the traditional interpretation of measurements of elastic diffractive processes in terms of Regge phenomenology [GPV01], and finds further support in more recent phenomenological considerations [DFJK05]. This ansatz for GPDs hence uses for the t dependence of the double distributions a soft Regge-type parameterization $\propto |\xi|^{-\alpha(0)+\alpha' |t|}$ with $\alpha' = 0.8\,\mathrm{GeV}^{-2} \ldots 0.9\,\mathrm{GeV}^{-2}$ for quarks.

Both theoretical calculations are averaged at the cross section level over incoherent processes on the proton and neutron in each kinematic bin. In both calculations the D-term is assigned the value zero. Earlier, it was found that inclusion of a D-term with any significant magnitude in the double-distribution model of reference [VGG01] employing several variants of Regge or factorized ansätze with any choice of profile parameters fails to describe the beam-charge asymmetry amplitudes measured at HERMES on a hydrogen target [Air08, Air09]. The theoretical bands in Figures 6.1 and 6.2 correspond to the range of values of the asymmetry amplitudes obtained by varying the profile parameters b_{val} and b_{sea} between unity and infinity. The theoretical calculations based on the factorized ansatz fail to describe the t dependence of $A_{\mathrm{C}}^{\cos(0\phi)}$ and $A_{\mathrm{C}}^{\cos\phi}$ as seen in Figure 6.1. The calculations based on the Regge ansatz for GPDs are in good agreement with the t dependence of the measured asymmetry amplitudes with respect to the beam charge $A_{\mathrm{C}}^{\cos(n\phi)}$. Both ansätze predict that $A_{\mathrm{C}}^{\cos\phi}$ decreases with increasing x_N, which is not seen in the data. Both ansätze undershoot the asymmetry amplitudes with respect to the beam helicity $A_{\mathrm{LU,I}}^{\sin(n\phi)}$.

kinematic bin		$\langle -t \rangle$ [GeV^2]	$\langle x_N \rangle$	$\langle Q^2 \rangle$ [GeV^2]	$A_C^{\cos(0\phi)}$ $\pm\delta_{\text{stat}} \pm \delta_{\text{syst}}$	$A_C^{\cos\phi}$ $\pm\delta_{\text{stat}} \pm \delta_{\text{syst}}$
overall		0.13	0.10	2.5	$-0.028 \pm 0.010 \pm 0.014$	$0.067 \pm 0.015 \pm 0.023$
$-t$[GeV^2]	0.00-0.03	0.02	0.07	1.7	$-0.004 \pm 0.023 \pm 0.003$	$0.056 \pm 0.035 \pm 0.011$
	0.03-0.06	0.04	0.09	2.2	$-0.020 \pm 0.024 \pm 0.014$	$0.034 \pm 0.033 \pm 0.007$
	0.06-0.10	0.08	0.10	2.4	$-0.008 \pm 0.024 \pm 0.020$	$0.045 \pm 0.034 \pm 0.023$
	0.10-0.20	0.14	0.11	2.7	$-0.029 \pm 0.021 \pm 0.024$	$0.085 \pm 0.030 \pm 0.027$
	0.20-0.35	0.26	0.12	3.1	$-0.067 \pm 0.028 \pm 0.018$	$0.093 \pm 0.039 \pm 0.022$
	0.35-0.70	0.46	0.11	3.5	$-0.066 \pm 0.042 \pm 0.029$	$0.114 \pm 0.064 \pm 0.057$
x_N	0.03-0.06	0.12	0.05	1.3	$-0.052 \pm 0.026 \pm 0.003$	$0.092 \pm 0.040 \pm 0.036$
	0.06-0.08	0.10	0.07	1.8	$-0.024 \pm 0.022 \pm 0.017$	$0.049 \pm 0.031 \pm 0.028$
	0.08-0.10	0.11	0.09	2.3	$-0.030 \pm 0.025 \pm 0.016$	$0.056 \pm 0.036 \pm 0.023$
	0.10-0.13	0.13	0.11	2.9	$0.011 \pm 0.026 \pm 0.030$	$0.039 \pm 0.037 \pm 0.030$
	0.13-0.20	0.17	0.16	4.0	$-0.021 \pm 0.028 \pm 0.007$	$0.070 \pm 0.040 \pm 0.031$
	0.20-0.35	0.23	0.24	6.1	$-0.013 \pm 0.052 \pm 0.055$	$0.136 \pm 0.074 \pm 0.022$
Q^2[GeV^2]	1.0-1.4	0.09	0.05	1.2	$-0.032 \pm 0.022 \pm 0.016$	$0.077 \pm 0.033 \pm 0.037$
	1.4-1.8	0.10	0.07	1.6	$-0.050 \pm 0.026 \pm 0.017$	$0.100 \pm 0.037 \pm 0.016$
	1.8-2.4	0.12	0.09	2.1	$-0.031 \pm 0.023 \pm 0.017$	$0.025 \pm 0.032 \pm 0.035$
	2.4-3.2	0.14	0.11	2.8	$-0.021 \pm 0.024 \pm 0.026$	$0.106 \pm 0.038 \pm 0.013$
	3.2-4.5	0.16	0.14	3.8	$-0.010 \pm 0.027 \pm 0.014$	$0.026 \pm 0.037 \pm 0.029$
	4.5-10.0	0.23	0.20	5.8	$-0.010 \pm 0.032 \pm 0.035$	$0.055 \pm 0.046 \pm 0.023$

kinematic bin		$\langle -t \rangle$ [GeV^2]	$\langle x_N \rangle$	$\langle Q^2 \rangle$ [GeV^2]	$A_C^{\cos(2\phi)}$ $\pm\delta_{\text{stat}} \pm \delta_{\text{syst}}$	$A_C^{\cos(3\phi)}$ $\pm\delta_{\text{stat}} \pm \delta_{\text{syst}}$
overall		0.13	0.10	2.5	$-0.007 \pm 0.014 \pm 0.016$	$0.005 \pm 0.014 \pm 0.001$
$-t$[GeV^2]	0.00-0.03	0.02	0.07	1.7	$0.003 \pm 0.032 \pm 0.008$	$-0.007 \pm 0.032 \pm 0.004$
	0.03-0.06	0.04	0.09	2.2	$-0.013 \pm 0.033 \pm 0.001$	$-0.041 \pm 0.034 \pm 0.005$
	0.06-0.10	0.08	0.10	2.4	$0.014 \pm 0.035 \pm 0.017$	$0.059 \pm 0.035 \pm 0.010$
	0.10-0.20	0.14	0.11	2.7	$-0.026 \pm 0.029 \pm 0.023$	$-0.006 \pm 0.029 \pm 0.006$
	0.20-0.35	0.26	0.12	3.1	$-0.006 \pm 0.038 \pm 0.050$	$0.044 \pm 0.037 \pm 0.002$
	0.35-0.70	0.46	0.11	3.5	$-0.015 \pm 0.056 \pm 0.049$	$-0.007 \pm 0.055 \pm 0.008$
x_N	0.03-0.06	0.12	0.05	1.3	$0.024 \pm 0.031 \pm 0.002$	$0.024 \pm 0.030 \pm 0.005$
	0.06-0.08	0.10	0.07	1.8	$0.004 \pm 0.029 \pm 0.014$	$-0.027 \pm 0.030 \pm 0.001$
	0.08-0.10	0.11	0.09	2.3	$-0.014 \pm 0.035 \pm 0.013$	$-0.008 \pm 0.035 \pm 0.008$
	0.10-0.13	0.13	0.11	2.9	$0.004 \pm 0.037 \pm 0.029$	$0.068 \pm 0.037 \pm 0.004$
	0.13-0.20	0.17	0.16	4.0	$-0.051 \pm 0.040 \pm 0.011$	$0.000 \pm 0.038 \pm 0.002$
	0.20-0.35	0.23	0.24	6.1	$-0.091 \pm 0.069 \pm 0.039$	$0.000 \pm 0.069 \pm 0.008$
Q^2[GeV^2]	1.0-1.4	0.09	0.05	1.2	$0.000 \pm 0.029 \pm 0.007$	$-0.030 \pm 0.030 \pm 0.004$
	1.4-1.8	0.10	0.07	1.6	$0.000 \pm 0.034 \pm 0.018$	$0.021 \pm 0.034 \pm 0.006$
	1.8-2.4	0.12	0.09	2.1	$-0.035 \pm 0.033 \pm 0.015$	$0.074 \pm 0.034 \pm 0.009$
	2.4-3.2	0.14	0.11	2.8	$0.045 \pm 0.036 \pm 0.021$	$-0.042 \pm 0.035 \pm 0.003$
	3.2-4.5	0.16	0.14	3.8	$0.018 \pm 0.037 \pm 0.015$	$-0.003 \pm 0.037 \pm 0.004$
	4.5-10.0	0.23	0.20	5.8	$-0.095 \pm 0.046 \pm 0.025$	$0.013 \pm 0.045 \pm 0.003$

kinematic bin		$\langle -t \rangle$ [GeV^2]	$\langle x_N \rangle$	$\langle Q^2 \rangle$ [GeV^2]	$A_{\text{LU,DVCS}}^{\sin\phi}$ $\pm\delta_{\text{stat}} \pm \delta_{\text{syst}}$	$A_{\text{LU,I}}^{\sin\phi}$ $\pm\delta_{\text{stat}} \pm \delta_{\text{syst}}$	$A_{\text{LU,I}}^{\sin(2\phi)}$ $\pm\delta_{\text{stat}} \pm \delta_{\text{syst}}$
overall		0.13	0.10	2.5	$-0.007 \pm 0.033 \pm 0.007$	$-0.192 \pm 0.035 \pm 0.031$	$0.073 \pm 0.031 \pm 0.012$
$-t$[GeV^2]	0.00-0.03	0.02	0.07	1.7	$-0.042 \pm 0.074 \pm 0.011$	$-0.296 \pm 0.104 \pm 0.006$	$0.056 \pm 0.071 \pm 0.011$
	0.03-0.06	0.04	0.09	2.2	$-0.101 \pm 0.077 \pm 0.013$	$-0.167 \pm 0.084 \pm 0.008$	$0.034 \pm 0.072 \pm 0.009$
	0.06-0.10	0.08	0.10	2.4	$0.032 \pm 0.080 \pm 0.032$	$-0.064 \pm 0.081 \pm 0.010$	$0.114 \pm 0.076 \pm 0.032$
	0.10-0.20	0.14	0.11	2.7	$0.018 \pm 0.068 \pm 0.009$	$-0.215 \pm 0.071 \pm 0.016$	$-0.022 \pm 0.065 \pm 0.013$
	0.20-0.35	0.26	0.12	3.1	$0.095 \pm 0.087 \pm 0.009$	$-0.286 \pm 0.095 \pm 0.008$	$0.206 \pm 0.085 \pm 0.024$
	0.35-0.70	0.46	0.11	3.5	$-0.029 \pm 0.118 \pm 0.035$	$0.003 \pm 0.122 \pm 0.005$	$0.133 \pm 0.124 \pm 0.030$
x_N	0.03-0.06	0.12	0.05	1.3	$-0.007 \pm 0.064 \pm 0.021$	$-0.197 \pm 0.083 \pm 0.061$	$0.080 \pm 0.066 \pm 0.015$
	0.06-0.08	0.10	0.07	1.8	$0.012 \pm 0.069 \pm 0.018$	$-0.286 \pm 0.096 \pm 0.032$	$0.084 \pm 0.067 \pm 0.014$
	0.08-0.10	0.11	0.09	2.3	$0.041 \pm 0.080 \pm 0.025$	$-0.017 \pm 0.080 \pm 0.031$	$-0.018 \pm 0.075 \pm 0.010$
	0.10-0.13	0.13	0.11	2.9	$-0.056 \pm 0.084 \pm 0.033$	$-0.212 \pm 0.090 \pm 0.023$	$0.060 \pm 0.080 \pm 0.013$
	0.13-0.20	0.17	0.16	4.0	$-0.109 \pm 0.090 \pm 0.037$	$-0.189 \pm 0.093 \pm 0.020$	$0.029 \pm 0.083 \pm 0.002$
	0.20-0.35	0.23	0.24	6.1	$0.222 \pm 0.160 \pm 0.053$	$-0.313 \pm 0.161 \pm 0.032$	$0.444 \pm 0.163 \pm 0.032$
Q^2[GeV^2]	1.0-1.4	0.09	0.05	1.2	$-0.028 \pm 0.068 \pm 0.035$	$-0.208 \pm 0.082 \pm 0.060$	$0.052 \pm 0.065 \pm 0.011$
	1.4-1.8	0.10	0.07	1.6	$0.175 \pm 0.079 \pm 0.030$	$-0.222 \pm 0.087 \pm 0.049$	$0.127 \pm 0.077 \pm 0.019$
	1.8-2.4	0.12	0.09	2.1	$-0.108 \pm 0.076 \pm 0.020$	$-0.124 \pm 0.077 \pm 0.029$	$-0.011 \pm 0.071 \pm 0.007$
	2.4-3.2	0.14	0.11	2.8	$0.005 \pm 0.083 \pm 0.023$	$-0.244 \pm 0.091 \pm 0.037$	$0.054 \pm 0.077 \pm 0.010$
	3.2-4.5	0.16	0.14	3.8	$-0.045 \pm 0.086 \pm 0.037$	$-0.169 \pm 0.088 \pm 0.022$	$0.119 \pm 0.082 \pm 0.005$
	4.5-10.0	0.23	0.20	5.8	$-0.038 \pm 0.104 \pm 0.010$	$-0.233 \pm 0.105 \pm 0.006$	$0.166 \pm 0.100 \pm 0.006$

Table 6.1: Results for azimuthal Fourier amplitudes of the beam-charge and beam-helicity asymmetries extracted from an unpolarized deuteron.

6.2 Comparison of the deuteron results with the HERMES results on beam-charge and beam-helicity asymmetries on the proton

In Figures 6.4 - 6.6 the overall asymmetry amplitudes as well as their $-t$, x_N, and Q^2 dependences, measured for the unpolarized deuterium target, are compared with the analogous results obtained from HERMES data on the proton [Air09]. The analysis of the data and the extraction of the asymmetry amplitudes on Hydrogen target is discussed in details in [Zei09]. The deuteron data include the coherent process $\vec{e}^{\pm}\, d \rightarrow e^{\pm}\, d\, \gamma$, and the incoherent process $\vec{e}^{\pm}\, d \rightarrow e^{\pm}\, p\, n\, \gamma$, where a nucleon may be excited to a resonance. The proton data include only $\vec{e}^{\pm}\, p \rightarrow e^{\pm}\, p\, \gamma$ and the case with resonance excitation. Any difference that appears at small values of $-t$ (coherent-enriched data sample) may be due to the coherent process.

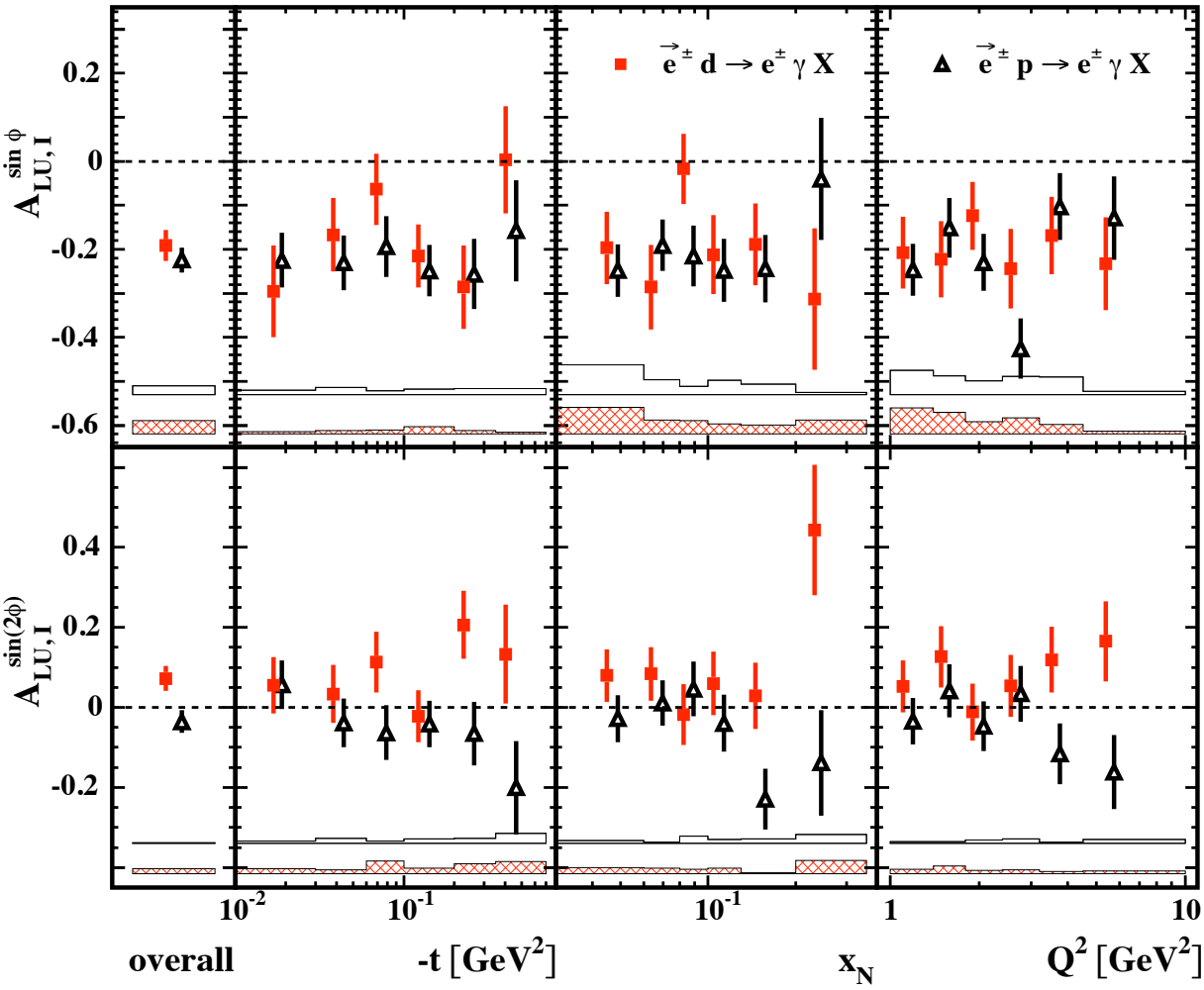

Figure 6.4: Fourier amplitudes of the beam-helicity asymmetry that are sensitive to the interference term, in bins of $-t$, x_N, or Q^2, extracted from deuteron data (squares) and from proton data (triangles). The error bars (bands) represent the statistical (systematic) uncertainties, which include all sources apart from the 2.4% (2.8%) scale uncertainty for the deuteron (proton) data due to the beam polarization. The hatched band is for the deuterium target.

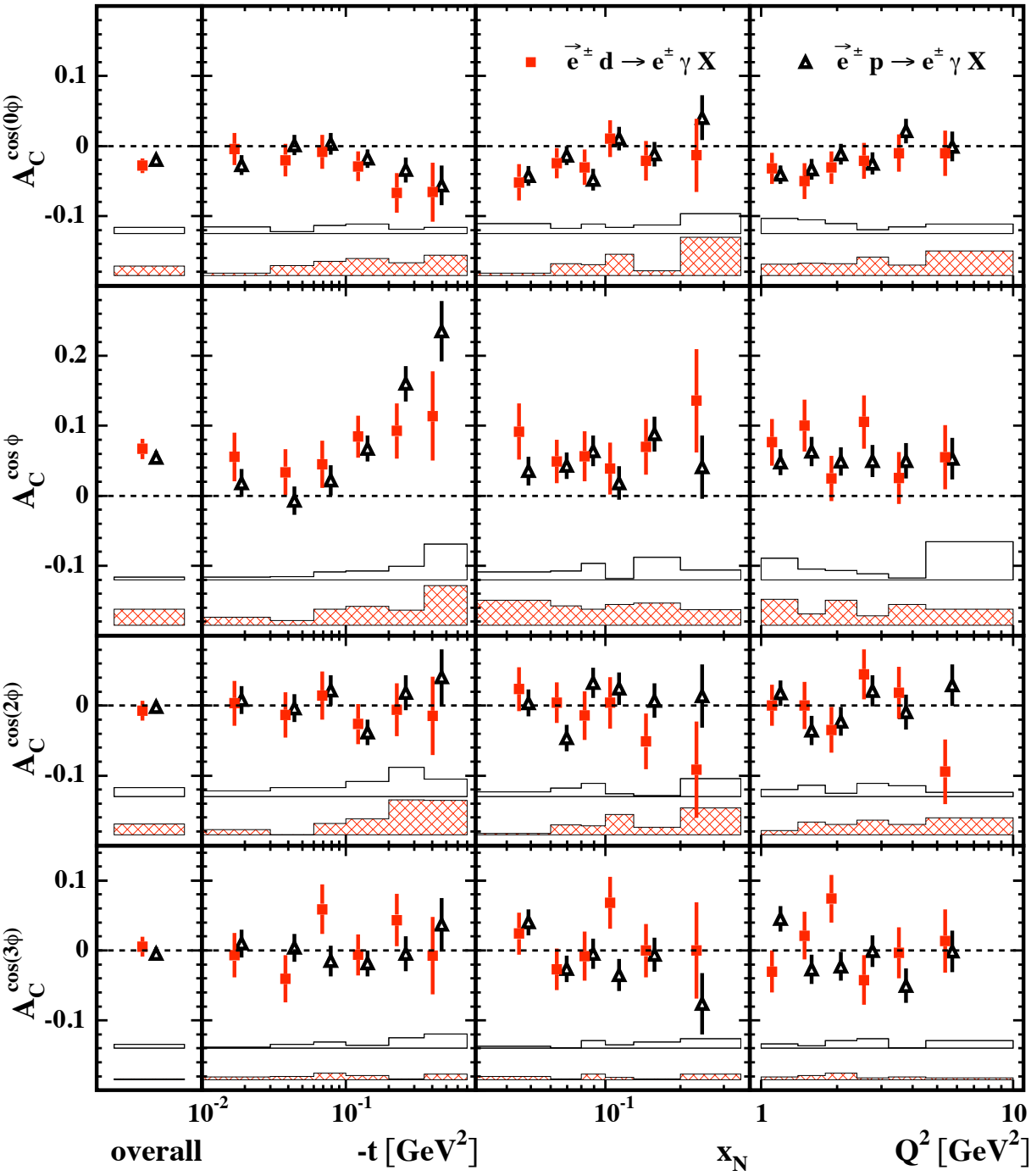

Figure 6.5: Fourier amplitudes of the beam-charge asymmetry, which are sensitive to the interference term, in bins of $-t$, x_N, or Q^2, extracted from deuteron data (squares) and from proton data (triangles). The points for deuterium are slightly shifted along the x-axis for visibility. The error bars (bands) represent the statistical (systematic) uncertainties. The hatched band is for the deuterium target.

Monte Carlo simulations described in section 5.3 indicate that the incoherent process dominates for $0.06\,\mathrm{GeV}^2 < -t < 0.7\,\mathrm{GeV}^2$ (incoherent-enriched data sample). Meanwhile the contribution of proton to the incoherent process dominates over that from neutron. Therefore, one could expect similar results on both targets for intermediate values of $-t$.

And indeed, as shown in Figures 6.4 - 6.6, the deuteron and proton results are found to be consistent in most kinematic regions. A possible difference in the last two $-t$ bins of the amplitude $A_{\mathrm{C}}^{\cos\phi}$, shown in Figure 6.5, may be due to the contributions of the neutron and its resonances. The proton and deuteron results for the amplitude $A_{\mathrm{LU,I}}^{\sin(\phi)}$ in Figure 6.4, agree very well for both coherent and incoherent-enriched data samples, and do not show any significant dependence on kinematic variables $-t$, Q^2 and x_N. The proton and deuteron results for the amplitude $A_{\mathrm{LU,I}}^{\sin(2\phi)}$ in Figure 6.4, integrated over the acceptance differ by 2.5 times the total experimental uncertainties. This possible discrepancy is most evident at large $-t$ and large x_N (or Q^2). Such a discrepancy would have no obvious explanation. The results for the amplitude $A_{\mathrm{LU,DVCS}}^{\sin(\phi)}$ of charge-averaged beam helicity asymmetry, shown in Figure 6.6 for both proton and deuteron targets, also agree over the whole kinematic range.

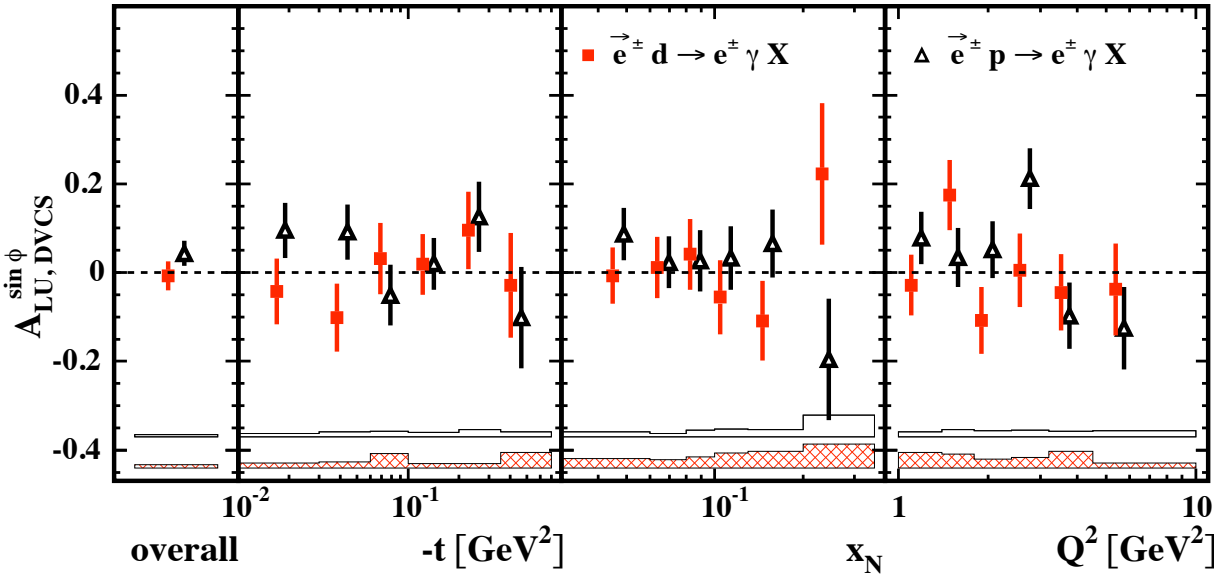

Figure 6.6: Fourier amplitudes of the beam-helicity asymmetry that are sensitive to the squared DVCS term, in bins of $-t$, x_N, or Q^2, extracted from deuteron data (squares) and from proton data (triangles). The error bars (bands) represent the statistical (systematic) uncertainties, which include all sources apart from the 2.4% (2.8%) scale uncertainty for the deuteron (proton) data due to the beam polarization. The hatched band is for the deuterium target.

6.3 Estimates of the asymmetries from coherent scattering

Estimates of the asymmetries for coherent scattering in the range $-t < 0.06\,\mathrm{GeV}^2$, corresponding to the first two bins, were derived by correcting for the incoherent contributions of the proton and its resonances using the simulated fractional coherent contributions from Table 5.5, under the assumption that the asymmetries for these contributions are the same as those on the free proton. The simulated contribution of approximately 7% from the process $\vec{e}^{\pm}\,n \rightarrow e^{\pm}\,n\,\gamma$ is estimated to have an effect on the asymmetries of less than 0.01. The extracted coherent asymmetries $A_{\mathrm{C,coh}}^{\cos\phi}$ and $A_{\mathrm{LU,I,coh}}^{\sin\phi}$ are found to be

	Exp. value	Model						
	value $\pm\,\delta_{\rm stat} \pm \delta_{\rm syst}$	A	B	B_0	$\widehat{B}$	B'	C	[CP04]
$A_{\rm LU,I,coh}^{\sin\phi}$	$-0.29 \pm 0.18 \pm 0.03$	-0.44	-0.38	-0.16	-0.37	-0.39	-0.58	-0.36
$A_{\rm C,coh}^{\cos\phi}$	$0.11 \pm 0.07 \pm 0.03$	0.10	0.09	-0.17	0.09	0.09	0.22	-0.15

Table 6.2: Experimental and theoretical values of the beam-helicity and beam-charge asymmetries for the coherent process on the deuteron. The theoretical predictions are for variants of the models of [BMK02, KM04] and a model from [CP04]. The experimental uncertainties do not account for the model dependence of the simulated fractional contributions of coherent and incoherent processes.

deuteron H_1 GPD	Model			
Model parameters	A	B (B', $\widehat{B}$)	B_0	C
$b_{\rm val}$	1	∞	∞	1
$b_{\rm sea}$	∞	∞	–	1
$B_{\rm sea}$ [GeV^{-2}]	20	20	–	15

Table 6.3: Model parameter sets for the GPD H_1 of the deuteron [BMK02, KM04]. The t slope parameter $B_{\rm sea}$ is used mainly to change the normalization of the sea quark GPD H_1.

0.11 ± 0.07 (stat.) $\pm\, 0.03$ (syst.) and -0.29 ± 0.18 (stat.) $\pm\, 0.03$ (syst.), respectively, at the average kinematic values $\langle -t \rangle = 0.03$ GeV^2, $\langle x_D \rangle = 0.04$, and $\langle Q^2 \rangle = 1.9$ GeV^2.

These results for the coherent asymmetries are compared in Table 6.2 with model estimates using the models A, B, B_0, $\widehat{B}$, B', and C of references [BMK02, KM04], the main parameters of which are listed in Table 6.3. The model estimates are based on the double distribution ansatz [Rad99] for nucleonic GPDs, combined with a factorized t dependence, and with the D-term set to zero. The nucleonic GPDs are combined using the impulse approximation. The contribution of sea quarks is neglected in model B_0, while it is enhanced in model C by a choice of a smaller value of the parameter $b_{\rm sea}$, which increases the absolute value of the beam-helicity asymmetry amplitude $A_{\rm LU,I,coh}^{\sin\phi}$ compared to model A. In model B' ($\widehat{B}$), the GPD H_3 (H_5) is taken into account by arbitrarily equating it with H_1 ($H_1(x) - H_1(-x)$). All other GPDs are kinematically suppressed and are set to zero. The models B_0 and C were previously ruled out by the beam-helicity and beam-charge asymmetry measurements on the hydrogen target [Air01, Step01, Air08, Air07b, Air09]. Table 6.2 also includes model predictions from [CP04], that was discussed in section 2.8.

All models are consistent within two standard deviations in the total experimental uncertainty with the extracted results for $A_{\rm LU,I,coh}^{\sin\phi}$ and $A_{\rm C,coh}^{\cos\phi}$, except for models B_0 and that of [CP04], which disagree with the results of $A_{\rm C,coh}^{\cos\phi}$ by about 3.5 standard deviations. Here, it should be noted that predictions for the real part of the CFFs are subject to delicate cancellations [BMK02] and hence are extremely sensitive to assumptions.

6.4 Single- and double-spin asymmetries

The results for the Fourier amplitudes of the single-charge asymmetries $\mathcal{A}_{\mathrm{L}\leftrightarrows}(e_\ell = +1, P_{zz}, \phi)$, $\mathcal{A}_{\mathrm{UL}}(e_\ell = +1, P_{zz}, \phi)$ and $\mathcal{A}_{\mathrm{LL}}(e_\ell = +1, P_{zz}, \phi)$ are presented in Figures 6.7–6.9 as a function of $-t$, x_N, or Q^2 and are also given in Table 6.4. Figure 6.7 shows the amplitudes $A_{\mathrm{L}\leftrightarrows}^{\sin(n\phi)}$ related to beam helicity only, while Figures 6.8 and 6.9 show the amplitudes $A_{\mathrm{UL}}^{\sin(n\phi)}$, which relate to target vector polarization only, and the amplitudes $A_{\mathrm{LL}}^{\cos(n\phi)}$, which relate to the product of beam helicity and target vector polarization.

The values for the $\sin\phi$ amplitude of the asymmetry $\mathcal{A}_{\mathrm{L}\leftrightarrows}$ in Figure 6.7 are found to

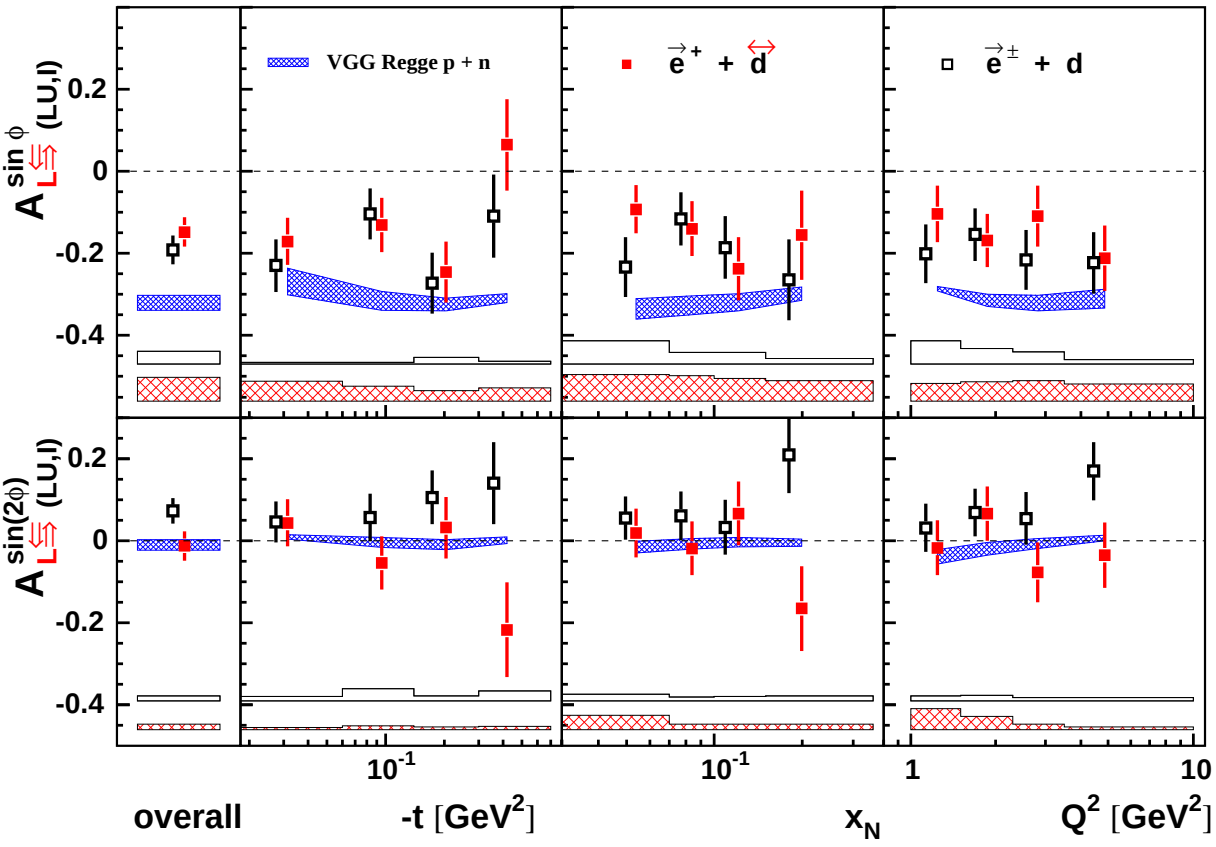

Figure 6.7: Results in red filled squares represent single-charge beam-helicity asymmetry amplitudes $A_{\mathrm{L}\leftrightarrows}^{\sin(n\phi)}$ describing the dependence of the sum of squared DVCS and interference terms on the beam helicity, for a tensor polarization of $P_{zz} = 0.827$ (indicated by the symbol $\leftrightarrow$). The black open squares represent charge-difference amplitudes $A_{\mathrm{LU,I}}^{\sin(n\phi)}$ from only the interference term, extracted from unpolarized deuterium data. The error bars represent the statistical uncertainties, while the coarsely hatched (open) bands represent the systematic uncertainties of the filled (opened) squares. There is an additional overall 1.9% (2.4%) scale uncertainty arising from the uncertainty in the measurement of the beam polarization in the case of polarized (unpolarized) deuterium data. The points for unpolarized deuterium data are slightly shifted to the left for better visibility. The finely hatched band shows the results of theoretical calculations for the combination of incoherent scattering on proton and neutron, using variants of the VGG double-distribution model [VGG99, VGG01] with a Regge ansatz for modeling the t dependence of GPDs [GPV01].

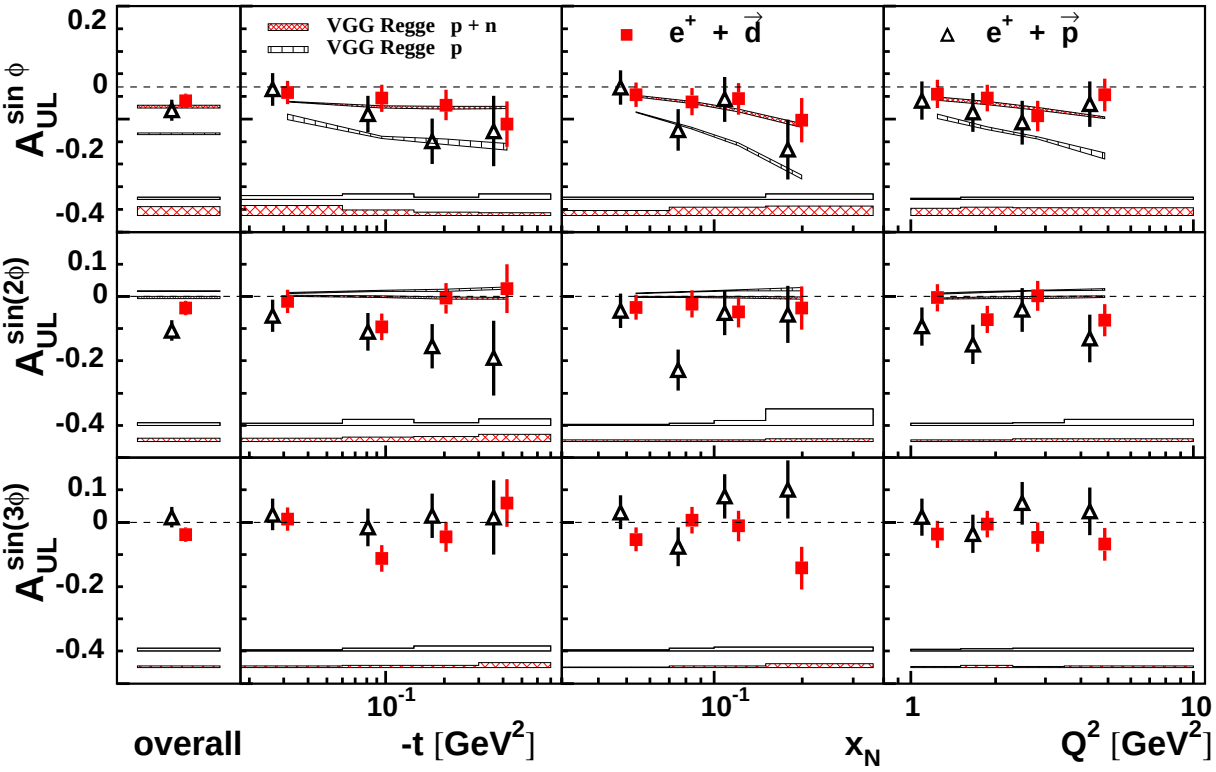

Figure 6.8: Single-charge target-spin asymmetry amplitudes describing the dependence of the sum of squared DVCS and interference terms on the target vector polarization, for a tensor polarization of $P_{zz} = 0.827$. The squares represent the results from the present work. The triangles denote the corresponding amplitudes extracted from longitudinally polarized hydrogen data [Air10a]. The error bars (bands) represent the statistical (systematic) uncertainties. The finely hatched bands have the same meaning as in Figure 6.7. There is an additional overall 5.0% (5.2%) scale uncertainty arising from the uncertainty in the measurement of the target polarization in the case of deuterium (hydrogen). The points for hydrogen are slightly shifted to the left for better visibility.

be significantly negative, while the $\sin(2\phi)$ amplitude is found to be consistent with zero. Figure 6.7 also presents for comparison the amplitudes of the charge-difference asymmetry $\mathcal{A}^{\mathrm{I}}_{\mathrm{LU}}$ extracted from an unpolarized deuterons. $\mathcal{A}_{\mathrm{L}\leftrightarrows}$ is expected to differ from $\mathcal{A}^{\mathrm{I}}_{\mathrm{LU}}$ (only if $P_{zz} \neq 0$) due only to a term involving the CFF $\mathcal{H}_5$. Figure 6.7 shows that these two asymmetries are found to be consistent in most kinematic regions, except possibly for the last $-t$ or x_N bin in the case of $\sin(2\phi)$. (The overall results differ by only 1.7 standard deviations in the total experimental uncertainties. The consistency in the first $-t$ bin, where the contribution from coherent scattering is significant, suggests that there is no distinctive contribution from $\mathcal{H}_5$, as was observed in the case of corresponding forward limit [Air05, Air07a].

In the first $-t$ bin, the asymmetry amplitude $A^{\sin\phi}_{\mathrm{L}\leftrightarrows,\mathrm{coh}}$ for pure coherent scattering on a polarized deuterium target was estimated from the measured asymmetry by correcting for the incoherent contributions of the proton and neutron and their resonances . This correction is based on the assumption that for the incoherent contribution of the proton, $A^{\sin\phi}_{\mathrm{L}\leftrightarrows}(P_{zz} = 0.827) \approx A^{\sin\phi}_{\mathrm{LU,I}}$ where the latter was measured on a hydrogen target [Air09]. The fractional contributions and the asymmetry for incoherent scattering from the neutron was taken from the Monte Carlo calculation described in section 5.3, with uncertainties

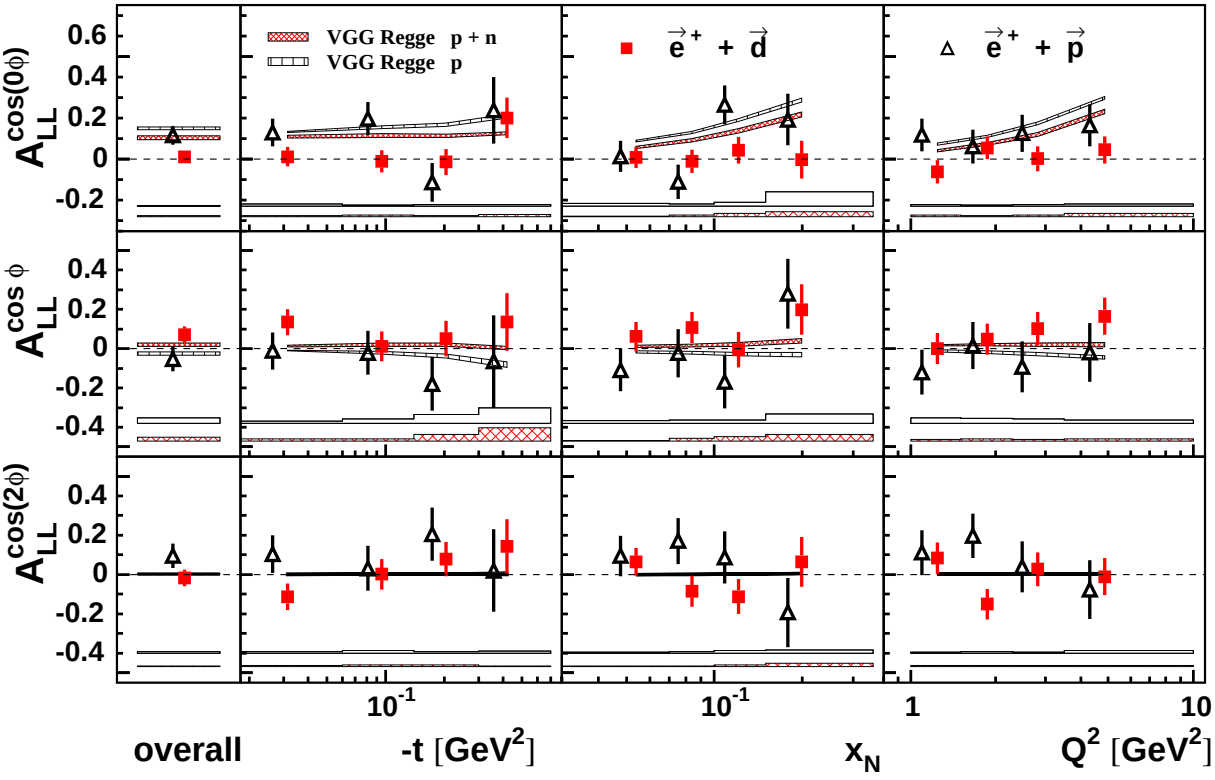

Figure 6.9: Single-charge double-spin asymmetry amplitudes describing the dependence of the sum of Bethe-Heitler, squared DVCS and interference terms on the product of the beam helicity and target vector polarization, for a tensor polarization of $P_{zz} = 0.827$. The plotted symbols and bands have the same meaning as in Figure 6.8. There is an additional overall 5.4% (5.3%) scale uncertainty arising from the uncertainties in the measurement of the beam and target polarizations in the case of deuterium (hydrogen) data.

equal to their magnitude. The result for the asymmetry amplitude $A^{\sin\phi}_{\mathrm{L}\overleftrightarrows,\mathrm{coh}}(P_{zz} = 0.827)$ is estimated to be $-0.12 \pm 0.17(\mathrm{stat.}) \pm 0.14(\mathrm{syst.}) \pm 0.02(\mathrm{model})$, where the systematic uncertainty is propagated from only the corresponding experimental uncertainties. Within the uncertainties there is no evidence of a difference between this value and the value for the asymmetry amplitude $A^{\sin\phi}_{\mathrm{LU,I,coh}} = -0.29 \pm 0.18(\mathrm{stat.}) \pm 0.03(\mathrm{syst.})$ previously estimated for coherent scattering on an unpolarized deuterium target, using a disjoint HERMES data set for an unpolarized deuterium target, but using the same data set for a hydrogen target.

The extracted values for the $\sin\phi$ and $\sin(2\phi)$ amplitudes of the single-charge asymmetry $\mathcal{A}_{\mathrm{UL}}$ measured on a longitudinally polarized deuterium target are shown in Figure 6.8. The 'overall' values are slightly negative by less than 1.5 standard deviations of the total experimental uncertainty. For coherent scattering on the deuteron, the amplitude $A^{\sin\phi}_{\mathrm{UL}}$ is sensitive to the imaginary part of a deuteron CFFs $\widetilde{\mathcal{H}}_1$. For comparison, the same amplitudes measured on a longitudinally polarized hydrogen target [Air10a] are also shown in Figure 6.8. The analysis of the data and the extraction of the asymmetry amplitudes on longitudinally polarized hydrogen target are discussed in details in [Mah10]. The $\sin\phi$ amplitude shows consistency between deuterium and hydrogen data both for the 'overall' result and the kinematic projections on $-t$, x_N, and Q^2. In this comparison, no account was taken of the 7.5% depolarization of nucleons in the deuteron due to the 5% admix-

Kinematic bin		$\langle -t \rangle$ [GeV^2]	$\langle x_N \rangle$	$\langle Q^2 \rangle$ [GeV^2]	$A_{\mathrm{L}\overleftrightarrow{\mathrm{S}}}^{\sin\phi}$ $\pm\delta_{\mathrm{stat}} \pm \delta_{\mathrm{syst}}$	$A_{\mathrm{L}\overleftrightarrow{\mathrm{S}}}^{\sin(2\phi)}$ $\pm\delta_{\mathrm{stat}} \pm \delta_{\mathrm{syst}}$
Overall		0.13	0.10	2.5	$-0.148 \pm 0.036 \pm 0.058$	$-0.012 \pm 0.035 \pm 0.013$
$-t$[GeV^2]	0.00-0.06	0.03	0.08	1.9	$-0.171 \pm 0.058 \pm 0.049$	$0.043 \pm 0.057 \pm 0.005$
	0.06-0.14	0.10	0.10	2.5	$-0.131 \pm 0.066 \pm 0.037$	$-0.053 \pm 0.065 \pm 0.010$
	0.14-0.30	0.20	0.11	2.9	$-0.246 \pm 0.074 \pm 0.025$	$0.032 \pm 0.075 \pm 0.007$
	0.30-0.70	0.42	0.12	3.5	$0.064 \pm 0.111 \pm 0.032$	$-0.217 \pm 0.115 \pm 0.008$
x_N	0.03-0.07	0.11	0.05	1.4	$-0.093 \pm 0.058 \pm 0.064$	$0.018 \pm 0.060 \pm 0.035$
	0.07-0.10	0.11	0.08	2.1	$-0.140 \pm 0.067 \pm 0.062$	$-0.019 \pm 0.066 \pm 0.013$
	0.10-0.15	0.14	0.12	3.1	$-0.238 \pm 0.077 \pm 0.055$	$0.066 \pm 0.077 \pm 0.014$
	0.15-0.35	0.20	0.20	5.0	$-0.156 \pm 0.109 \pm 0.049$	$-0.165 \pm 0.103 \pm 0.013$
Q^2[GeV^2]	1.0-1.5	0.09	0.06	1.2	$-0.103 \pm 0.068 \pm 0.043$	$-0.017 \pm 0.067 \pm 0.051$
	1.5-2.3	0.11	0.08	1.9	$-0.169 \pm 0.065 \pm 0.047$	$0.065 \pm 0.066 \pm 0.032$
	2.3-3.5	0.14	0.11	2.8	$-0.110 \pm 0.074 \pm 0.050$	$-0.077 \pm 0.073 \pm 0.014$
	3.5-10.0	0.20	0.17	4.9	$-0.212 \pm 0.079 \pm 0.042$	$-0.036 \pm 0.080 \pm 0.006$

Kinematic bin		$\langle -t \rangle$ [GeV^2]	$\langle x_N \rangle$	$\langle Q^2 \rangle$ [GeV^2]	$A_{\mathrm{UL}}^{\sin\phi}$ $\pm\delta_{\mathrm{stat}} \pm \delta_{\mathrm{syst}}$	$A_{\mathrm{UL}}^{\sin(2\phi)}$ $\pm\delta_{\mathrm{stat}} \pm \delta_{\mathrm{syst}}$	$A_{\mathrm{UL}}^{\sin(3\phi)}$ $\pm\delta_{\mathrm{stat}} \pm \delta_{\mathrm{syst}}$
Overall		0.13	0.10	2.5	$-0.044 \pm 0.023 \pm 0.029$	$-0.037 \pm 0.022 \pm 0.010$	$-0.039 \pm 0.022 \pm 0.004$
$-t$[GeV^2]	0.00-0.06	0.03	0.08	1.9	$-0.018 \pm 0.037 \pm 0.031$	$-0.015 \pm 0.036 \pm 0.010$	$0.009 \pm 0.036 \pm 0.005$
	0.06-0.14	0.10	0.10	2.5	$-0.036 \pm 0.042 \pm 0.018$	$-0.094 \pm 0.041 \pm 0.013$	$-0.112 \pm 0.041 \pm 0.006$
	0.14-0.30	0.20	0.11	2.9	$-0.057 \pm 0.047 \pm 0.012$	$-0.006 \pm 0.048 \pm 0.015$	$-0.045 \pm 0.047 \pm 0.006$
	0.30-0.70	0.42	0.12	3.5	$-0.116 \pm 0.071 \pm 0.009$	$0.024 \pm 0.075 \pm 0.023$	$0.060 \pm 0.074 \pm 0.014$
x_N	0.03-0.07	0.11	0.05	1.4	$-0.025 \pm 0.037 \pm 0.016$	$-0.034 \pm 0.038 \pm 0.005$	$-0.053 \pm 0.038 \pm 0.002$
	0.07-0.10	0.11	0.08	2.1	$-0.046 \pm 0.042 \pm 0.026$	$-0.023 \pm 0.042 \pm 0.006$	$0.006 \pm 0.041 \pm 0.004$
	0.10-0.15	0.14	0.12	3.1	$-0.037 \pm 0.049 \pm 0.026$	$-0.048 \pm 0.049 \pm 0.006$	$-0.011 \pm 0.047 \pm 0.004$
	0.15-0.35	0.20	0.20	5.0	$-0.104 \pm 0.069 \pm 0.030$	$-0.036 \pm 0.068 \pm 0.009$	$-0.142 \pm 0.066 \pm 0.011$
Q^2[GeV^2]	1.0-1.5	0.09	0.06	1.2	$-0.022 \pm 0.043 \pm 0.023$	$-0.004 \pm 0.042 \pm 0.005$	$-0.037 \pm 0.042 \pm 0.004$
	1.5-2.3	0.11	0.08	1.9	$-0.035 \pm 0.041 \pm 0.026$	$-0.071 \pm 0.042 \pm 0.006$	$-0.006 \pm 0.041 \pm 0.006$
	2.3-3.5	0.14	0.11	2.8	$-0.091 \pm 0.047 \pm 0.026$	$-0.002 \pm 0.046 \pm 0.008$	$-0.047 \pm 0.046 \pm 0.003$
	3.5-10.0	0.20	0.17	4.9	$-0.025 \pm 0.050 \pm 0.024$	$-0.073 \pm 0.050 \pm 0.008$	$-0.069 \pm 0.050 \pm 0.005$

Kinematic bin		$\langle -t \rangle$ [GeV^2]	$\langle x_N \rangle$	$\langle Q^2 \rangle$ [GeV^2]	$A_{\mathrm{LL}}^{\cos(0\phi)}$ $\pm\delta_{\mathrm{stat}} \pm \delta_{\mathrm{syst}}$	$A_{\mathrm{LL}}^{\cos\phi}$ $\pm\delta_{\mathrm{stat}} \pm \delta_{\mathrm{syst}}$	$A_{\mathrm{LL}}^{\cos(2\phi)}$ $\pm\delta_{\mathrm{stat}} \pm \delta_{\mathrm{syst}}$
Overall		0.13	0.10	2.5	$0.011 \pm 0.029 \pm 0.004$	$0.072 \pm 0.042 \pm 0.019$	$-0.017 \pm 0.042 \pm 0.005$
$-t$[GeV^2]	0.00-0.06	0.03	0.08	1.9	$0.012 \pm 0.048 \pm 0.005$	$0.136 \pm 0.066 \pm 0.010$	$-0.115 \pm 0.068 \pm 0.008$
	0.06-0.14	0.10	0.10	2.5	$-0.011 \pm 0.055 \pm 0.007$	$0.013 \pm 0.076 \pm 0.011$	$0.002 \pm 0.077 \pm 0.009$
	0.14-0.30	0.20	0.11	2.9	$-0.015 \pm 0.063 \pm 0.005$	$0.052 \pm 0.090 \pm 0.034$	$0.078 \pm 0.089 \pm 0.009$
	0.30-0.70	0.42	0.12	3.5	$0.200 \pm 0.099 \pm 0.010$	$0.136 \pm 0.147 \pm 0.068$	$0.143 \pm 0.139 \pm 0.005$
x_N	0.03-0.07	0.11	0.05	1.4	$0.008 \pm 0.051 \pm 0.003$	$0.062 \pm 0.074 \pm 0.003$	$0.064 \pm 0.070 \pm 0.003$
	0.07-0.10	0.11	0.08	2.1	$-0.011 \pm 0.056 \pm 0.007$	$0.108 \pm 0.078 \pm 0.014$	$-0.085 \pm 0.079 \pm 0.005$
	0.10-0.15	0.14	0.12	3.1	$0.043 \pm 0.064 \pm 0.014$	$-0.004 \pm 0.090 \pm 0.021$	$-0.112 \pm 0.088 \pm 0.009$
	0.15-0.35	0.20	0.20	5.0	$-0.003 \pm 0.091 \pm 0.024$	$0.199 \pm 0.128 \pm 0.034$	$0.065 \pm 0.126 \pm 0.017$
Q^2[GeV^2]	1.0-1.5	0.09	0.06	1.2	$-0.062 \pm 0.056 \pm 0.006$	$0.008 \pm 0.078 \pm 0.009$	$0.083 \pm 0.080 \pm 0.007$
	1.5-2.3	0.11	0.08	1.9	$0.054 \pm 0.055 \pm 0.005$	$0.047 \pm 0.079 \pm 0.010$	$-0.150 \pm 0.078 \pm 0.007$
	2.3-3.5	0.14	0.11	2.8	$0.001 \pm 0.061 \pm 0.006$	$0.103 \pm 0.085 \pm 0.007$	$0.027 \pm 0.086 \pm 0.007$
	3.5-10.0	0.20	0.17	4.9	$0.045 \pm 0.067 \pm 0.016$	$0.166 \pm 0.095 \pm 0.010$	$-0.011 \pm 0.095 \pm 0.007$

Table 6.4: Results for azimuthal Fourier amplitudes of the single-charge asymmetries $\mathcal{A}_{\mathrm{L}\overleftrightarrow{\mathrm{S}}}$, $\mathcal{A}_{\mathrm{UL}}$ and $\mathcal{A}_{\mathrm{LL}}$, extracted from longitudinally polarized deuteron data, for a tensor polarization of $P_{zz} = 0.827$. Not included are the 1.9%, 4.0% and 4.4% scale uncertainties for corresponding asymmetry amplitudes arising from the uncertainties in the measurement of the beam, target, beam and target polarizations, respectively.

ture of the D-state. The 'overall' results on the $\sin(2\phi)$ amplitude differ between the two targets by 1.5 standard deviations of the total experimental uncertainties, mainly due to the region of large $-t$, but in only one x_N bin. The 'overall' result on the asymmetry amplitude $A_{\rm UL}^{\sin(3\phi)}$ is slightly negative by less than 1.7 standard deviation of the total experimental uncertainty. The $\sin(3\phi)$ amplitude shows consistency between deuterium and hydrogen data, accounting for the total experimental uncertainties of the corresponding measurements, except possibly for the highest x_N bin.

The $A_{\rm LL}^{\cos(n\phi)}$ amplitudes of the single-charge double-spin asymmetry measured using longitudinally polarized deuteron data and presented in Figure 6.9 are found to be compatible with zero, although the $A_{\rm LL}^{\cos\phi}$ amplitude is positive by 1.6 standard deviations of the total experimental uncertainty. Within the uncertainties, these asymmetry amplitudes do not show significant differences from those measured on a longitudinally polarized hydrogen target [Air10a], except possibly for the overall result for the amplitude $A_{\rm LL}^{\cos(0\phi)}$, where there is observed a discrepancy of 1.9 standard deviations in the total experimental uncertainties.

The model calculations predict a magnitude of the $\sin\phi$ harmonic of the single-charge beam-helicity asymmetry that exceeds that of the data by about a factor of two, a situation similar to that found in the case of a hydrogen target [Air10a]. On the other hand the predictions are in good agreement with data for single-charge target-spin asymmetries. A large difference appears between the predictions for the $\sin\phi$ harmonic of this asymmetry on the deuteron and proton targets, arising entirely from the contributions of the neutron. The data are consistent with this difference, but lack the precision to confirm the large positive prediction of the neutron asymmetry by this model. The predictions are in good agreement with the single-charge double-spin asymmetry amplitudes, aside from the $\cos(0\phi)$ harmonic. Here the theoretical predictions for both the deuteron and proton, which are dominated by the BH contribution, are significantly positive, in agreement with the proton data, while the more precise deuteron data are consistent with zero. The small contribution of coherent scattering to the overall result, with a predicted negative asymmetry [KM04], is expected to slightly reduce this asymmetry amplitude for the deuteron.

6.5 The single-helicity asymmetries

The results for the Fourier amplitudes of the single-beam-helicity asymmetries are presented in Figures. 6.10 - 6.12. More specifically, Figures. 6.10, 6.11, and 6.12 show the $\cos(n\phi)$ and $\sin(n\phi)$ harmonics of the asymmetry $\mathcal{A}_{\substack{\rm C\\ \leftarrow\\ \Rightarrow}}(P_\ell, P_{zz}, \phi)$, $\mathcal{A}_{\substack{0\\ \leftarrow\\ \rm L}}(P_\ell, P_{zz}, \phi)$ and $\mathcal{A}_{\substack{\rm C\\ \leftarrow\\ \rm L}}(P_\ell, P_{zz}, \phi)$, respectively (see also Tables 6.5 - 6.7), for $P_\ell = -0.530 \pm 0.012$ and $P_{zz} = 0.827 \pm 0.027$.

The only overall results for the asymmetry $\mathcal{A}_{\substack{\rm C\\ \leftarrow\\ \Rightarrow}}$ in Figure 6.10 that are found to be significantly non-zero are the $\cos\phi$ and $\sin\phi$ amplitudes. The theoretical calculations for incoherent scattering predict that the results for the amplitudes $A_{\substack{\rm C\\ \leftarrow\\ \Rightarrow}}^{\cos(n\phi)}$ should strongly resemble those for the amplitudes $A_{\rm C}^{\cos(n\phi)}$ measured with an unpolarized beam on an unpolarized deuterium target . The data confirm this resemblance, even in the first $-t$ bin where coherent scattering contributes about 40% of the yield. This is another indication that the CFF $\mathcal{H}_5$ [KM04], in this case its real part, makes no distinctive contribution to coherent scattering off deuterons, similar to the case of $A_{\substack{\rm L\\ \leftarrow\\ \Rightarrow}}^{\sin\phi}$.

The numerators of the $A_{\substack{\rm C\\ \leftarrow\\ \Rightarrow}}^{\sin(n\phi)}$ amplitudes shown in Figure 6.10 differ from those of

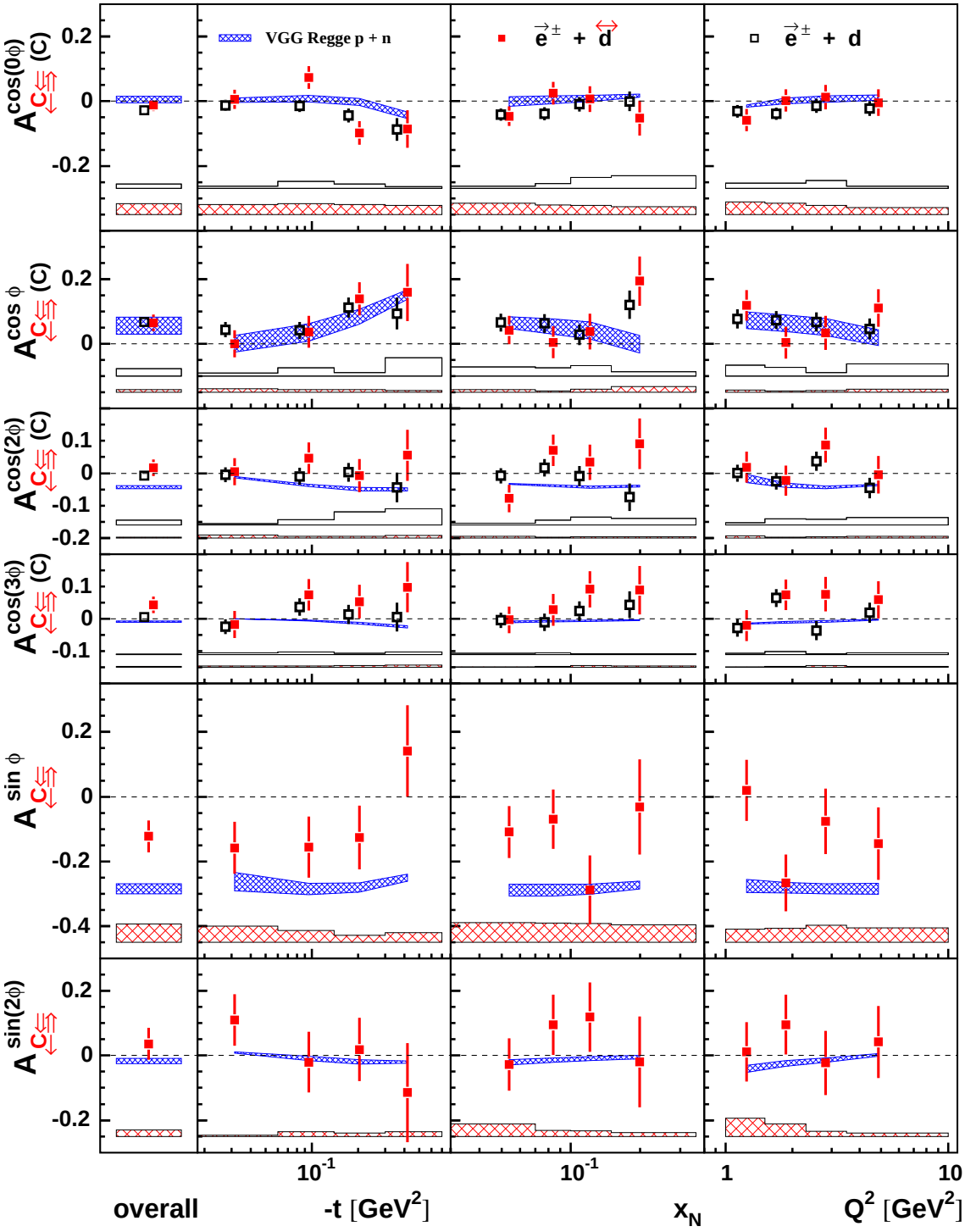

Figure 6.10: Results in red filled squares represent single-beam-helicity beam-charge asymmetry amplitudes $A_{C\overleftrightarrows}^{\cos(n\phi)}$ and $A_{C\overleftrightarrows}^{\sin(n\phi)}$, for $P_\ell = -0.530$ and a tensor polarization of $P_{zz} = 0.827$ (indicated by the symbol $\leftrightarrow$). The black open squares are $A_{C}^{\cos(n\phi)}$ amplitudes extracted from data recorded with an unpolarized deuterium target. The error bars and bands and finely hatched bands have the same meaning as in Figure 6.7. The points for unpolarized deuterium data are slightly shifted to the left for better visibility. There is an additional overall 2.2% scale uncertainty for the $A_{C\overleftrightarrows}^{\sin(n\phi)}$ amplitudes arising from the uncertainty in the measurement of the beam polarization.

the $\sin(n\phi)$ amplitudes of the $\mathcal{A}_{\mathrm{L}\overleftrightarrows}$ asymmetry shown in Figure 6.7 only by squared DVCS terms. Furthermore, the cross sections $\mathrm{d}\sigma_{\mathrm{U}\overleftrightarrows}$ and $\mathrm{d}\sigma_{\underset{\leftarrow}{\mathrm{C}}\overleftrightarrows}$ in the denominators of these two asymmetries should be similar because they are dominated by Bethe-Heitler contributions. Hence, these asymmetry amplitudes are expected to be similar, and within the statistical accuracy this is indeed found to be the case.

The $\cos(n\phi)$ amplitudes of the asymmetry $\mathcal{A}_{\underset{\leftarrow}{0}_{\mathrm{L}}}$ in Figure 6.11 contain a sum of BH and squared DVCS even harmonics, and relate to the longitudinal vector polarization of the target. However, even where the BH contribution dominates the numerator of

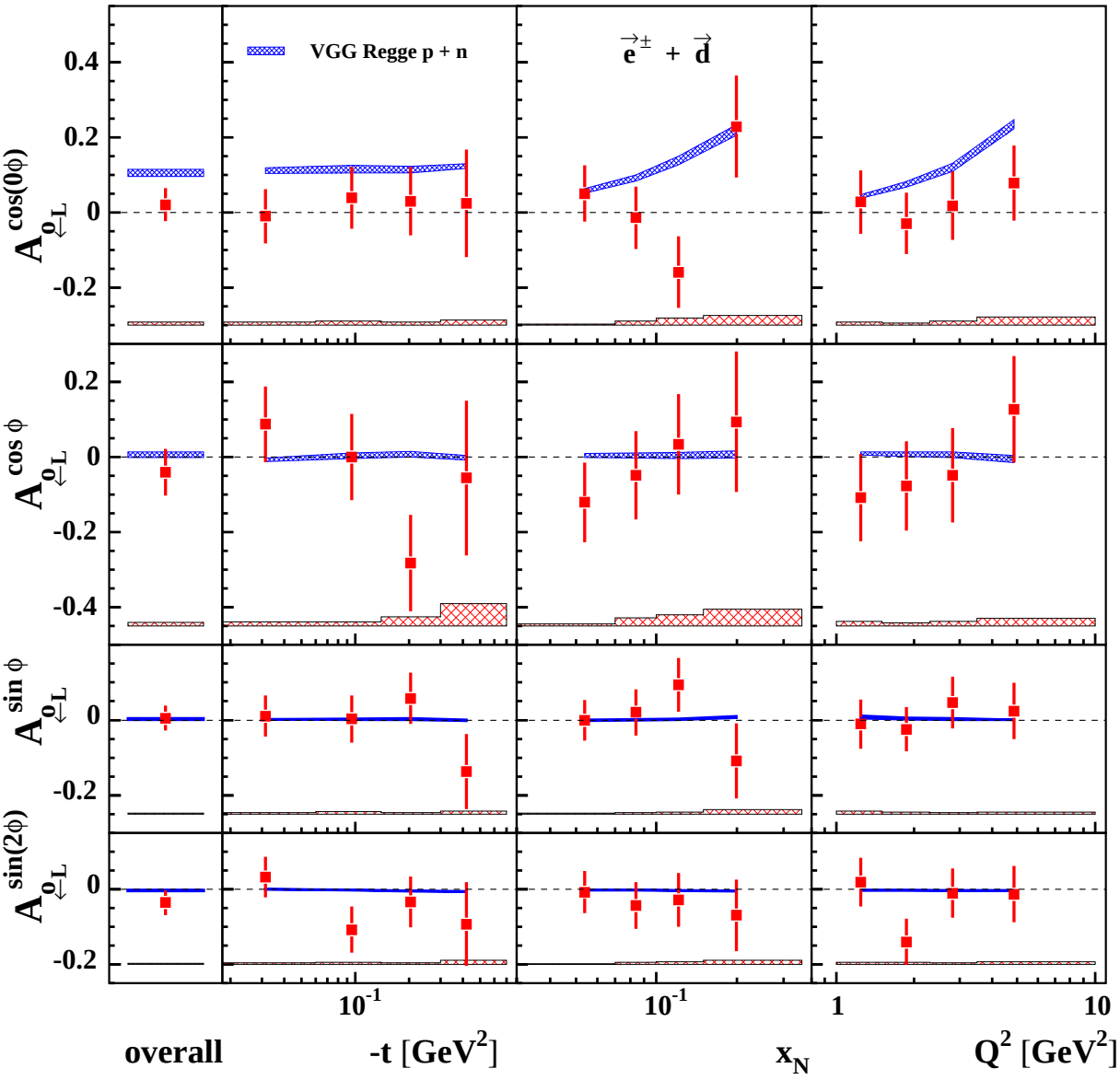

Figure 6.11: Kinematic dependence of the charge-averaged single-beam-helicity target-spin asymmetry amplitudes $A_{\underset{\leftarrow}{0}_{\mathrm{L}}}^{\cos(n\phi)}$ and $A_{\underset{\leftarrow}{0}_{\mathrm{L}}}^{\sin(n\phi)}$, for $P_\ell = -0.530$ and a tensor polarization of $P_{zz} = 0.827$. The plotted symbols and bands have the same meaning as in Figure 6.10. There is an additional overall 5.3% (5.7%) scale uncertainty for the extracted $A_{\underset{\leftarrow}{0}_{\mathrm{L}}}^{\sin(n\phi)}$ $\left(A_{\underset{\leftarrow}{0}_{\mathrm{L}}}^{\cos(n\phi)}\right)$ amplitudes arising from the uncertainties in the measurement of the target (beam and target) polarizations.

the asymmetry amplitude $A_{\underset{\leftarrow}{0}_{\mathrm{L}}}^{\cos(0\phi)}$ for incoherent scattering at not small $-t$, the data are found to be consistent with zero, and differing by 1.7 standard deviations in the total experimental uncertainty from the positive prediction for the overall result. The $\sin(n\phi)$ amplitudes of the asymmetry $\mathcal{A}_{\underset{\leftarrow}{0}_{\mathrm{L}}}$ in Figure 6.11 receive contributions from the pure squared DVCS harmonics only, and are found to be consistent with zero.

Of particular interest are the $A_{\underset{\leftarrow}{\mathrm{C}}_{\mathrm{L}}}^{\cos(n\phi)}$ and $A_{\underset{\leftarrow}{\mathrm{C}}_{\mathrm{L}}}^{\sin(n\phi)}$ amplitudes shown in Figure 6.12, which represent respectively the even and odd vector-polarization related harmonics of the interference term only, receiving no contribution from pure BH and DVCS terms. The theoretical predictions for the $\cos(n\phi)$ harmonics are negligibly small, while the data differ from zero by about two standard deviations for the first two harmonics. As expected and observed in the case of unpolarized hydrogen and deuterium targets, the $\cos(0\phi)$ and $\cos\phi$ harmonics are found to have opposite signs.

Like the asymmetry amplitude $A_{\mathrm{UL}}^{\sin(\phi)}$, in the first $-t$ bin the asymmetry amplitude $A_{\underset{\leftarrow}{\mathrm{C}}_{\mathrm{L}}}^{\sin\phi}$ is sensitive to the imaginary part of the deuteron CFF $\widetilde{\mathcal{H}}_1$. Within their statistical accuracies, they are found to be consistent, although $A_{\mathrm{UL}}^{\sin\phi}$ receives also a contribution

Kinematic bin		$\langle -t\rangle$ [GeV^2]	$\langle x_N\rangle$	$\langle Q^2\rangle$ [GeV^2]	$A_{\underset{\leftarrow}{\mathrm{C}}\Leftarrow}^{\cos(0\phi)}$ $\pm\delta_{\mathrm{stat}}\pm\delta_{\mathrm{syst}}$	$A_{\underset{\leftarrow}{\mathrm{C}}\Leftarrow}^{\cos\phi}$ $\pm\delta_{\mathrm{stat}}\pm\delta_{\mathrm{syst}}$	$A_{\underset{\leftarrow}{\mathrm{C}}\Leftarrow}^{\cos(2\phi)}$ $\pm\delta_{\mathrm{stat}}\pm\delta_{\mathrm{syst}}$
Overall		0.13	0.10	2.5	$-0.012\pm0.018\pm0.034$	$0.065\pm0.026\pm0.009$	$0.017\pm0.026\pm0.003$
$-t$[GeV^2]	0.00-0.06	0.03	0.08	1.9	$0.006\pm0.030\pm0.031$	$0.001\pm0.041\pm0.012$	$0.005\pm0.042\pm0.009$
	0.06-0.14	0.10	0.10	2.5	$0.074\pm0.035\pm0.034$	$0.037\pm0.049\pm0.008$	$0.046\pm0.049\pm0.006$
	0.14-0.30	0.20	0.11	2.9	$-0.098\pm0.036\pm0.031$	$0.139\pm0.052\pm0.008$	$-0.007\pm0.051\pm0.005$
	0.30-0.70	0.42	0.12	3.5	$-0.086\pm0.058\pm0.028$	$0.159\pm0.088\pm0.007$	$0.056\pm0.079\pm0.008$
x_N	0.03-0.07	0.11	0.05	1.4	$-0.046\pm0.031\pm0.035$	$0.042\pm0.044\pm0.009$	$-0.078\pm0.043\pm0.005$
	0.07-0.10	0.11	0.08	2.1	$0.025\pm0.035\pm0.030$	$0.005\pm0.050\pm0.005$	$0.071\pm0.048\pm0.003$
	0.10-0.15	0.14	0.12	3.1	$0.007\pm0.040\pm0.028$	$0.038\pm0.055\pm0.010$	$0.034\pm0.055\pm0.004$
	0.15-0.35	0.20	0.20	5.0	$-0.052\pm0.054\pm0.024$	$0.194\pm0.077\pm0.018$	$0.091\pm0.079\pm0.004$
Q^2[GeV^2]	1.0-1.5	0.09	0.06	1.2	$-0.059\pm0.034\pm0.039$	$0.119\pm0.047\pm0.007$	$0.019\pm0.049\pm0.006$
	1.5-2.3	0.11	0.08	1.9	$0.002\pm0.034\pm0.034$	$0.004\pm0.049\pm0.004$	$-0.023\pm0.047\pm0.002$
	2.3-3.5	0.14	0.11	2.8	$0.012\pm0.038\pm0.028$	$0.034\pm0.053\pm0.005$	$0.087\pm0.054\pm0.004$
	3.5-10.0	0.20	0.17	4.9	$-0.005\pm0.041\pm0.022$	$0.111\pm0.058\pm0.010$	$-0.004\pm0.058\pm0.005$

Kinematic bin		$\langle -t\rangle$ [GeV^2]	$\langle x_N\rangle$	$\langle Q^2\rangle$ [GeV^2]	$A_{\underset{\leftarrow}{\mathrm{C}}\Leftarrow}^{\cos(3\phi)}$ $\pm\delta_{\mathrm{stat}}\pm\delta_{\mathrm{syst}}$	$A_{\underset{\leftarrow}{\mathrm{C}}\Leftarrow}^{\sin\phi}$ $\pm\delta_{\mathrm{stat}}\pm\delta_{\mathrm{syst}}$	$A_{\underset{\leftarrow}{\mathrm{C}}\Leftarrow}^{\sin(2\phi)}$ $\pm\delta_{\mathrm{stat}}\pm\delta_{\mathrm{syst}}$
Overall		0.13	0.10	2.5	$0.044\pm0.026\pm0.003$	$-0.123\pm0.049\pm0.057$	$0.036\pm0.049\pm0.020$
$-t$[GeV^2]	0.00-0.06	0.03	0.08	1.9	$-0.018\pm0.042\pm0.004$	$-0.158\pm0.081\pm0.050$	$0.109\pm0.080\pm0.005$
	0.06-0.14	0.10	0.10	2.5	$0.075\pm0.049\pm0.004$	$-0.156\pm0.095\pm0.036$	$-0.021\pm0.094\pm0.015$
	0.14-0.30	0.20	0.11	2.9	$0.053\pm0.052\pm0.005$	$-0.126\pm0.098\pm0.021$	$0.018\pm0.099\pm0.011$
	0.30-0.70	0.42	0.12	3.5	$0.098\pm0.077\pm0.007$	$0.141\pm0.142\pm0.029$	$-0.015\pm0.153\pm0.015$
x_N	0.03-0.07	0.11	0.05	1.4	$-0.002\pm0.041\pm0.002$	$-0.109\pm0.080\pm0.060$	$-0.028\pm0.081\pm0.039$
	0.07-0.10	0.11	0.08	2.1	$0.028\pm0.049\pm0.003$	$-0.069\pm0.092\pm0.059$	$0.095\pm0.094\pm0.018$
	0.10-0.15	0.14	0.12	3.1	$0.091\pm0.056\pm0.006$	$-0.288\pm0.107\pm0.058$	$0.119\pm0.107\pm0.018$
	0.15-0.35	0.20	0.20	5.0	$0.089\pm0.075\pm0.005$	$-0.032\pm0.147\pm0.054$	$-0.020\pm0.141\pm0.011$
Q^2[GeV^2]	1.0-1.5	0.09	0.06	1.2	$-0.020\pm0.048\pm0.002$	$0.020\pm0.095\pm0.041$	$0.011\pm0.092\pm0.056$
	1.5-2.3	0.11	0.08	1.9	$0.074\pm0.047\pm0.003$	$-0.266\pm0.087\pm0.043$	$0.095\pm0.092\pm0.038$
	2.3-3.5	0.14	0.11	2.8	$0.076\pm0.053\pm0.006$	$-0.076\pm0.101\pm0.053$	$-0.023\pm0.099\pm0.016$
	3.5-10.0	0.20	0.17	4.9	$0.059\pm0.058\pm0.003$	$-0.145\pm0.112\pm0.044$	$0.042\pm0.112\pm0.011$

Table 6.5: Results for azimuthal Fourier amplitudes of the single-beam-helicity charge asymmetry $\mathcal{A}_{\underset{\leftarrow}{\mathrm{C}}\Leftarrow}$, extracted from longitudinally polarized deuteron data, for $P_\ell = -0.530$ and a tensor polarization of $P_{zz} = 0.827$. Not included is the 2.2% scale uncertainty for $\sin(n\phi)$ asymmetry amplitudes arising from the uncertainty in the measurement of the beam polarization.

from the squared DVCS term . The asymmetry amplitude $A_{\overleftarrow{C}_L}^{\cos\phi}$ is sensitive to the real part of the deuteron CFF $\widetilde{\mathcal{H}}_1$. Unlike the corresponding harmonic $A_{LL}^{\cos\phi}$, it does not receive a contribution from the Bethe-Heitler term. The $\sin(n\phi)$ harmonics are found to be consistent with zero and also with the small negative prediction in the case of the $\sin\phi$ harmonic.

From the definitions of the asymmetries $\mathcal{A}_{UL}$, $\mathcal{A}_{LL}$, $\mathcal{A}_{\overleftarrow{0}_L}$ and $\mathcal{A}_{\overleftarrow{C}_L}$ in Eqs. 3.46, 3.47, 3.54, and 3.55, and also from examination of Table 3.1, it can be seen that they are related. In the case of approximate equality of $d\sigma_{U\overleftrightarrows}$ and $d\sigma_{\overleftarrow{C}\overleftrightarrows}$, the following relations

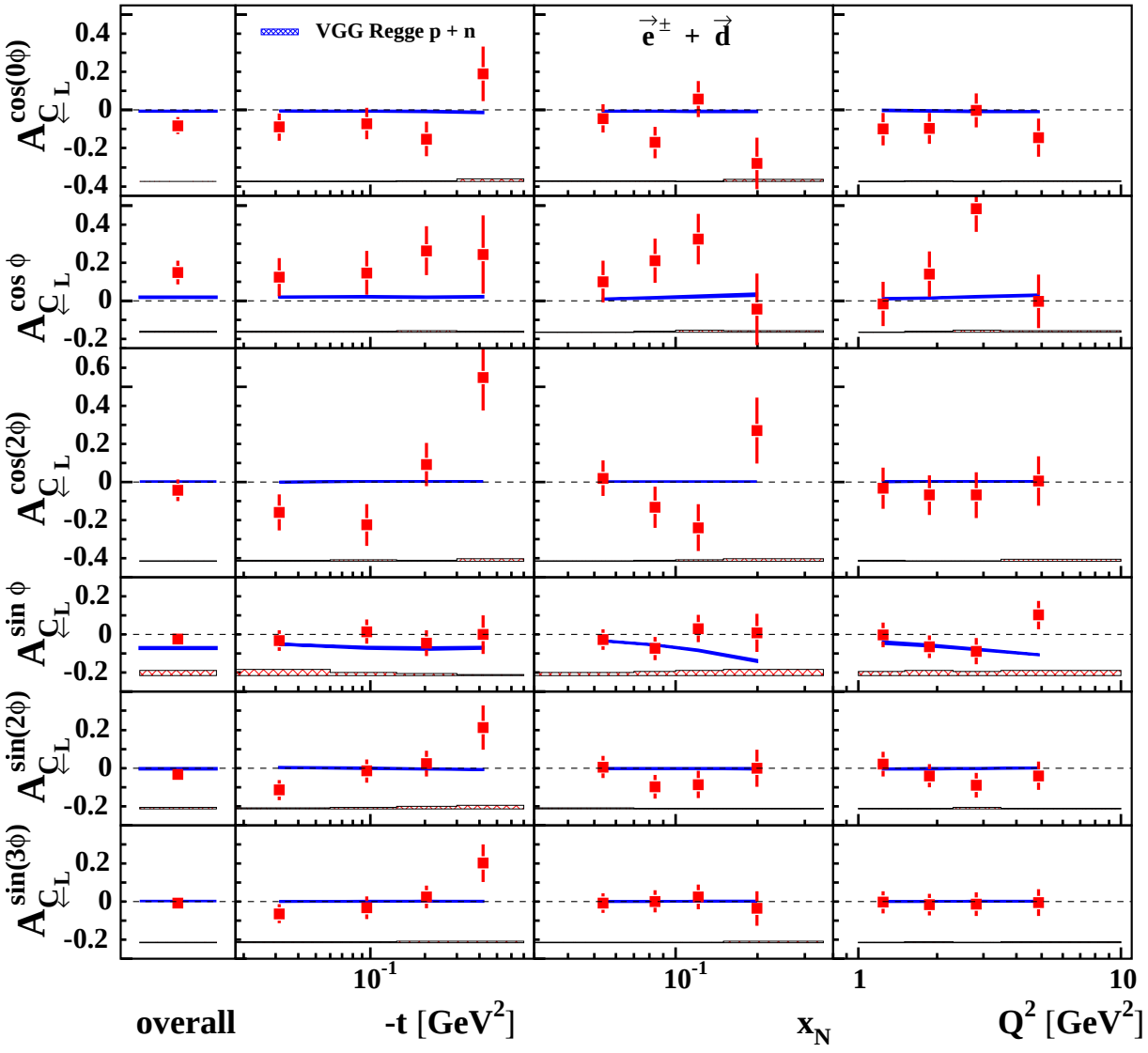

Figure 6.12: Kinematic dependence of the single-beam-helicity charge-difference target-spin asymmetry amplitudes $A_{\overleftarrow{C}_L}^{\cos(n\phi)}$ and $A_{\overleftarrow{C}_L}^{\sin(n\phi)}$, for $P_\ell = -0.530$ and a tensor polarization of $P_{zz} = 0.827$. The plotted symbols and bands have the same meaning as in Figure 6.10. There is an additional overall 5.3% (5.7%) scale uncertainty for the extracted $A_{\overleftarrow{C}_L}^{\sin(n\phi)}$ $\left(A_{\overleftarrow{C}_L}^{\cos(n\phi)}\right)$ amplitudes arising from the uncertainties in the measurement of the target (beam and target)
polarizations.

hold between the asymmetry amplitudes:

$$A_{\mathrm{UL}}^{\sin(n\phi)} \simeq A_{\overleftarrow{0}_{\mathrm{L}}}^{\sin(n\phi)} + A_{\overleftarrow{\mathrm{C}}_{\mathrm{L}}}^{\sin(n\phi)}, \quad n = 1, 2\,, \tag{6.1}$$

$$A_{\mathrm{LL}}^{\cos(n\phi)} \simeq A_{\overleftarrow{0}_{\mathrm{L}}}^{\cos(n\phi)} + A_{\overleftarrow{\mathrm{C}}_{\mathrm{L}}}^{\cos(n\phi)}, \quad n = 0, 1\,. \tag{6.2}$$

For most of the kinematic points, the differences between left and right hand sides of Eqs. 6.1 and 6.2 are found below 1.2 standard deviations of the total experimental uncertainties, while for the remaining six points they are between 1.5 and 2.0. Note that here the correlations between two asymmetries from the right hand sides are taken into account.

The correlation coefficients between extracted asymmetry amplitudes are given in the appendix, separately for the amplitudes of the asymmetries from unpolarized deuterium target, for the amplitudes of singe-beam-charge asymmetries, and for the single-beam-helicity asymmetries.

Kinematic bin		$\langle -t \rangle$ [GeV^2]	$\langle x_N \rangle$	$\langle Q^2 \rangle$ [GeV^2]	$A_{\overleftarrow{0}_{\mathrm{L}}}^{\cos(0\phi)}$ $\pm\delta_{\mathrm{stat}} \pm \delta_{\mathrm{syst}}$	$A_{\overleftarrow{0}_{\mathrm{L}}}^{\cos\phi}$ $\pm\delta_{\mathrm{stat}} \pm \delta_{\mathrm{syst}}$
Overall		0.13	0.10	2.5	$0.021 \pm 0.044 \pm 0.009$	$-0.041 \pm 0.062 \pm 0.010$
$-t$[GeV^2]	0.00-0.06	0.03	0.08	1.9	$-0.009 \pm 0.072 \pm 0.008$	$0.087 \pm 0.101 \pm 0.011$
	0.06-0.14	0.10	0.10	2.5	$0.039 \pm 0.083 \pm 0.012$	$-0.005 \pm 0.115 \pm 0.011$
	0.14-0.30	0.20	0.11	2.9	$0.030 \pm 0.091 \pm 0.008$	$-0.282 \pm 0.128 \pm 0.024$
	0.30-0.70	0.42	0.12	3.5	$0.024 \pm 0.142 \pm 0.014$	$-0.056 \pm 0.206 \pm 0.059$
x_N	0.03-0.07	0.11	0.05	1.4	$0.051 \pm 0.075 \pm 0.004$	$-0.121 \pm 0.106 \pm 0.005$
	0.07-0.10	0.11	0.08	2.1	$-0.014 \pm 0.083 \pm 0.012$	$-0.049 \pm 0.117 \pm 0.021$
	0.10-0.15	0.14	0.12	3.1	$-0.158 \pm 0.095 \pm 0.019$	$0.033 \pm 0.133 \pm 0.030$
	0.15-0.35	0.20	0.20	5.0	$0.228 \pm 0.135 \pm 0.027$	$0.093 \pm 0.187 \pm 0.044$
Q^2[GeV^2]	1.0-1.5	0.09	0.06	1.2	$0.028 \pm 0.085 \pm 0.009$	$-0.108 \pm 0.116 \pm 0.013$
	1.5-2.3	0.11	0.08	1.9	$-0.029 \pm 0.082 \pm 0.006$	$-0.077 \pm 0.119 \pm 0.009$
	2.3-3.5	0.14	0.11	2.8	$0.018 \pm 0.091 \pm 0.012$	$-0.049 \pm 0.125 \pm 0.013$
	3.5-10.0	0.20	0.17	4.9	$0.078 \pm 0.100 \pm 0.022$	$0.127 \pm 0.142 \pm 0.020$

Kinematic bin		$\langle -t \rangle$ [GeV^2]	$\langle x_N \rangle$	$\langle Q^2 \rangle$ [GeV^2]	$A_{\overleftarrow{0}_{\mathrm{L}}}^{\sin\phi}$ $\pm\delta_{\mathrm{stat}} \pm \delta_{\mathrm{syst}}$	$A_{\overleftarrow{0}_{\mathrm{L}}}^{\sin(2\phi)}$ $\pm\delta_{\mathrm{stat}} \pm \delta_{\mathrm{syst}}$
Overall		0.13	0.10	2.5	$0.005 \pm 0.033 \pm 0.003$	$-0.036 \pm 0.033 \pm 0.003$
$-t$[GeV^2]	0.00-0.06	0.03	0.08	1.9	$0.011 \pm 0.054 \pm 0.004$	$0.033 \pm 0.054 \pm 0.005$
	0.06-0.14	0.10	0.10	2.5	$0.003 \pm 0.063 \pm 0.006$	$-0.108 \pm 0.062 \pm 0.006$
	0.14-0.30	0.20	0.11	2.9	$0.058 \pm 0.068 \pm 0.003$	$-0.034 \pm 0.068 \pm 0.005$
	0.30-0.70	0.42	0.12	3.5	$-0.137 \pm 0.100 \pm 0.008$	$-0.093 \pm 0.111 \pm 0.011$
x_N	0.03-0.07	0.11	0.05	1.4	$-0.001 \pm 0.054 \pm 0.002$	$-0.008 \pm 0.056 \pm 0.002$
	0.07-0.10	0.11	0.08	2.1	$0.020 \pm 0.062 \pm 0.004$	$-0.043 \pm 0.062 \pm 0.006$
	0.10-0.15	0.14	0.12	3.1	$0.093 \pm 0.072 \pm 0.006$	$-0.029 \pm 0.071 \pm 0.006$
	0.15-0.35	0.20	0.20	5.0	$-0.108 \pm 0.100 \pm 0.011$	$-0.069 \pm 0.095 \pm 0.011$
Q^2[GeV^2]	1.0-1.5	0.09	0.06	1.2	$-0.011 \pm 0.065 \pm 0.008$	$0.019 \pm 0.065 \pm 0.005$
	1.5-2.3	0.11	0.08	1.9	$-0.025 \pm 0.059 \pm 0.005$	$-0.140 \pm 0.061 \pm 0.005$
	2.3-3.5	0.14	0.11	2.8	$0.047 \pm 0.069 \pm 0.004$	$-0.011 \pm 0.066 \pm 0.005$
	3.5-10.0	0.20	0.17	4.9	$0.024 \pm 0.075 \pm 0.005$	$-0.013 \pm 0.075 \pm 0.007$

Table 6.6: Results for azimuthal Fourier amplitudes of the single-beam-helicity charge-averaged target-spin asymmetry $\mathcal{A}_{\overleftarrow{0}_{\mathrm{L}}}$, extracted from longitudinally polarized deuteron data, for $P_\ell = -0.530$ and a tensor polarization of $P_{zz} = 0.827$. Not included is the 5.3% (5.7%) scale uncertainty for the $\sin(n\phi)$ ($\cos(n\phi)$) asymmetry amplitudes arising from the uncertainties in the measurement of the target (beam and target) polarizations.

Kinematic bin		$\langle -t \rangle$ [GeV^2]	$\langle x_N \rangle$	$\langle Q^2 \rangle$ [GeV^2]	$A_{\overleftarrow{\mathrm{C}}_\mathrm{L}}^{\cos(0\phi)}$ $\pm\delta_{\mathrm{stat}} \pm \delta_{\mathrm{syst}}$	$A_{\overleftarrow{\mathrm{C}}_\mathrm{L}}^{\cos\phi}$ $\pm\delta_{\mathrm{stat}} \pm \delta_{\mathrm{syst}}$	$A_{\overleftarrow{\mathrm{C}}_\mathrm{L}}^{\cos(2\phi)}$ $\pm\delta_{\mathrm{stat}} \pm \delta_{\mathrm{syst}}$
Overall		0.13	0.10	2.5	$-0.082 \pm 0.044 \pm 0.002$	$0.148 \pm 0.062 \pm 0.007$	$-0.044 \pm 0.057 \pm 0.002$
$-t$[GeV^2]	0.00-0.06	0.03	0.08	1.9	$-0.089 \pm 0.072 \pm 0.002$	$0.124 \pm 0.100 \pm 0.006$	$-0.161 \pm 0.095 \pm 0.003$
	0.06-0.14	0.10	0.10	2.5	$-0.071 \pm 0.082 \pm 0.002$	$0.147 \pm 0.114 \pm 0.007$	$-0.225 \pm 0.110 \pm 0.006$
	0.14-0.30	0.20	0.11	2.9	$-0.152 \pm 0.091 \pm 0.003$	$0.262 \pm 0.127 \pm 0.008$	$0.092 \pm 0.114 \pm 0.005$
	0.30-0.70	0.42	0.12	3.5	$0.190 \pm 0.142 \pm 0.014$	$0.244 \pm 0.205 \pm 0.006$	$0.547 \pm 0.172 \pm 0.014$
x_N	0.03-0.07	0.11	0.05	1.4	$-0.044 \pm 0.075 \pm 0.003$	$0.101 \pm 0.109 \pm 0.001$	$0.019 \pm 0.093 \pm 0.003$
	0.07-0.10	0.11	0.08	2.1	$-0.170 \pm 0.082 \pm 0.004$	$0.210 \pm 0.116 \pm 0.006$	$-0.132 \pm 0.108 \pm 0.003$
	0.10-0.15	0.14	0.12	3.1	$0.058 \pm 0.095 \pm 0.002$	$0.323 \pm 0.132 \pm 0.010$	$-0.239 \pm 0.123 \pm 0.007$
	0.15-0.35	0.20	0.20	5.0	$-0.281 \pm 0.135 \pm 0.012$	$-0.045 \pm 0.188 \pm 0.009$	$0.269 \pm 0.173 \pm 0.012$
Q^2[GeV^2]	1.0-1.5	0.09	0.06	1.2	$-0.100 \pm 0.085 \pm 0.002$	$-0.016 \pm 0.116 \pm 0.001$	$-0.032 \pm 0.108 \pm 0.005$
	1.5-2.3	0.11	0.08	1.9	$-0.097 \pm 0.082 \pm 0.002$	$0.140 \pm 0.119 \pm 0.005$	$-0.069 \pm 0.104 \pm 0.003$
	2.3-3.5	0.14	0.11	2.8	$-0.002 \pm 0.089 \pm 0.001$	$0.483 \pm 0.123 \pm 0.010$	$-0.068 \pm 0.120 \pm 0.002$
	3.5-10.0	0.20	0.17	4.9	$-0.145 \pm 0.100 \pm 0.003$	$-0.003 \pm 0.141 \pm 0.008$	$0.005 \pm 0.131 \pm 0.009$

Kinematic bin		$\langle -t \rangle$ [GeV^2]	$\langle x_N \rangle$	$\langle Q^2 \rangle$ [GeV^2]	$A_{\overleftarrow{\mathrm{C}}_\mathrm{L}}^{\sin\phi}$ $\pm\delta_{\mathrm{stat}} \pm \delta_{\mathrm{syst}}$	$A_{\overleftarrow{\mathrm{C}}_\mathrm{L}}^{\sin(2\phi)}$ $\pm\delta_{\mathrm{stat}} \pm \delta_{\mathrm{syst}}$	$A_{\overleftarrow{\mathrm{C}}_\mathrm{L}}^{\sin(3\phi)}$ $\pm\delta_{\mathrm{stat}} \pm \delta_{\mathrm{syst}}$
Overall		0.13	0.10	2.5	$-0.023 \pm 0.033 \pm 0.028$	$-0.035 \pm 0.033 \pm 0.008$	$-0.009 \pm 0.030 \pm 0.003$
$-t$[GeV^2]	0.00-0.06	0.03	0.08	1.9	$-0.032 \pm 0.054 \pm 0.033$	$-0.116 \pm 0.053 \pm 0.007$	$-0.064 \pm 0.050 \pm 0.004$
	0.06-0.14	0.10	0.10	2.5	$0.016 \pm 0.062 \pm 0.016$	$-0.016 \pm 0.062 \pm 0.009$	$-0.033 \pm 0.059 \pm 0.005$
	0.14-0.30	0.20	0.11	2.9	$-0.045 \pm 0.068 \pm 0.010$	$0.024 \pm 0.067 \pm 0.015$	$0.025 \pm 0.060 \pm 0.008$
	0.30-0.70	0.42	0.12	3.5	$-0.001 \pm 0.102 \pm 0.005$	$0.212 \pm 0.115 \pm 0.020$	$0.201 \pm 0.099 \pm 0.008$
x_N	0.03-0.07	0.11	0.05	1.4	$-0.027 \pm 0.054 \pm 0.015$	$0.006 \pm 0.058 \pm 0.005$	$-0.007 \pm 0.051 \pm 0.001$
	0.07-0.10	0.11	0.08	2.1	$-0.073 \pm 0.061 \pm 0.023$	$-0.098 \pm 0.062 \pm 0.004$	$0.001 \pm 0.057 \pm 0.003$
	0.10-0.15	0.14	0.12	3.1	$0.031 \pm 0.072 \pm 0.026$	$-0.087 \pm 0.072 \pm 0.003$	$0.025 \pm 0.065 \pm 0.003$
	0.15-0.35	0.20	0.20	5.0	$0.009 \pm 0.100 \pm 0.031$	$-0.001 \pm 0.097 \pm 0.002$	$-0.036 \pm 0.090 \pm 0.006$
Q^2[GeV^2]	1.0-1.5	0.09	0.06	1.2	$-0.003 \pm 0.065 \pm 0.022$	$0.020 \pm 0.065 \pm 0.003$	$-0.003 \pm 0.058 \pm 0.001$
	1.5-2.3	0.11	0.08	1.9	$-0.064 \pm 0.059 \pm 0.026$	$-0.041 \pm 0.061 \pm 0.004$	$-0.017 \pm 0.057 \pm 0.005$
	2.3-3.5	0.14	0.11	2.8	$-0.087 \pm 0.068 \pm 0.021$	$-0.090 \pm 0.065 \pm 0.008$	$-0.014 \pm 0.062 \pm 0.001$
	3.5-10.0	0.20	0.17	4.9	$0.102 \pm 0.075 \pm 0.027$	$-0.040 \pm 0.075 \pm 0.005$	$-0.004 \pm 0.070 \pm 0.004$

Table 6.7: Results for azimuthal Fourier amplitudes of the single-beam-helicity charge-difference target-spin asymmetry $\mathcal{A}_{\overleftarrow{\mathrm{C}}_\mathrm{L}}$, extracted from longitudinally polarized deuteron data, for $P_\ell = -0.530$ and a tensor polarization of $P_{zz} = 0.827$. Not included is the 5.3% (5.7%) scale uncertainty for the $\sin(n\phi)$ ($\cos(n\phi)$) asymmetry amplitudes arising from the uncertainties in the measurement of the target (beam and target) polarizations.

Chapter 7

Summary and Conclusion

Deeply virtual Compton scattering is studied in this report, using all data collected at the HERMES experiment from 1996 to 2005. Azimuthal asymmetries with respect to beam-helicity, beam-charge and target polarization alone and also to their different combinations for hard exclusive electroproduction of real photons in deep-inelastic scattering from a both unpolarized and longitudinally polarized deuterium targets are measured. The asymmetries are attributed to the interference between the deeply virtual Compton scattering and Bethe–Heitler processes. The asymmetries are observed in the exclusive region $-(1.5)^2\,\mathrm{GeV}^2 < M_X^2 < (1.7)^2\,\mathrm{GeV}^2$ of the squared missing mass. The dependences of these asymmetries on $-t$, x_N, or Q^2 are investigated. The results include the coherent process $e\,d \to e\,d\,\gamma$ and the incoherent process $e\,d \to e\,p\,n\,\gamma$ where in addition a nucleon may be excited to a resonance.

For an unpolarized deuterium target, the leading Fourier amplitude of the beam-helicity asymmetry that is sensitive to the interference term is found to be substantial, but no significant t dependence is observed. The leading amplitude of the beam-charge asymmetry is substantial at large $-t$, but becomes small at small values of $-t$. The amplitudes of the beam-helicity asymmetry that are sensitive to the squared DVCS term are found to be consistent with zero. The data are able to discriminate among various GPD models.

The measured asymmetry amplitudes from unpolarized deuteron and proton [Air09, Air10b] targets are consistent in most kinematic regions, except possibly for the leading amplitude of the beam-charge asymmetry in the last two $-t$ bins, and the 'overall' value of $A_{\mathrm{LU}}^{sin(2\phi)}$.

The beam-charge and beam-helicity asymmetry amplitudes for coherent scattering from the deuteron are extracted from the asymmetry amplitudes measured on unpolarized deuteron and proton targets. When compared to the GPD models of [BMK02, KM04], the results disfavor a large sea quark contribution while favoring a non-zero contribution. The results disfavor the variants of the model of [BMK02, KM04] that omit sea quark contributions, and also the model of [CP04].

Within the total experimental uncertainties, the results of the sinusoidal (cosinusoidal) amplitudes of the asymmetry $\mathcal{A}_{\mathrm{L}\overleftrightarrows}$ ($\mathcal{A}_{\mathrm{C}\underset{\rightleftarrows}{\leftarrow}}$) extracted from a longitudinally polarized data set with $P_{zz} = 0.827$ (corresponding to a small population for the $\Lambda = 0$ state) resemble those for the amplitudes extracted from unpolarized deuterium data. Therefore, no indication of effects of tensor polarization was found at small values of $-t$, in particular in the first $-t$ bin where the coherent process contributes up to 40%. Neither the $\mathcal{A}_{\mathrm{UL}}^{\sin(n\phi)}$ nor $\mathcal{A}_{\mathrm{LL}}^{\cos(n\phi)}$ amplitudes measured on longitudinally polarized deuterons show significant differences compared with those extracted from longitudinally polarized protons, consid-

ering the total experimental uncertainties. (Statistically marginal differences are observed for $\mathcal{A}_{\rm UL}^{\sin(2\phi)}$ and $\mathcal{A}_{\rm LL}^{\cos(0\phi)}$).

The differences between the leading amplitudes of the asymmetries $\mathcal{A}_{\rm LU}^{\rm I}$ and $\mathcal{A}_{\rm L\overleftrightarrows}$ for coherent scattering from unpolarized and longitudinally polarized deuterium targets, respectively, is expected to be small. Indeed, within the total experimental uncertainties, no difference is seen between the reconstructed values of the asymmetry amplitudes $A_{\rm L\overleftrightarrows,coh}^{\sin\phi}$ and $A_{\rm LU,I,coh}^{\sin\phi}$.

In conclusion, even in the first $-t$ bin where the coherent process contributes about 40%, all asymmetries on deuterium that have (approximate) counterparts for hydrogen are found to be compatible with them. The data are unable to reveal any evidence of the influence of the Compton form factor $\mathcal{H}_5$ or features of the deuteron Compton form factors $\mathcal{H}_1$ and $\widetilde{\mathcal{H}}_1$ that distinguish them from the counterparts for the proton. Hence, coherent scattering presents no obvious signature in these data. The deuteron Compton form factor $\mathcal{H}_1$ appears to have a similar behavior as $\mathcal{H}$ of the proton. The data were compared with theoretical calculations for only incoherent scattering, based on a well-known GPD model. Those asymmetries that are expected to resemble counterparts for a hydrogen target reveal the same shortcomings of the model calculations that appeared in comparisons with the hydrogen data.

Appendix: Correlation Matrices

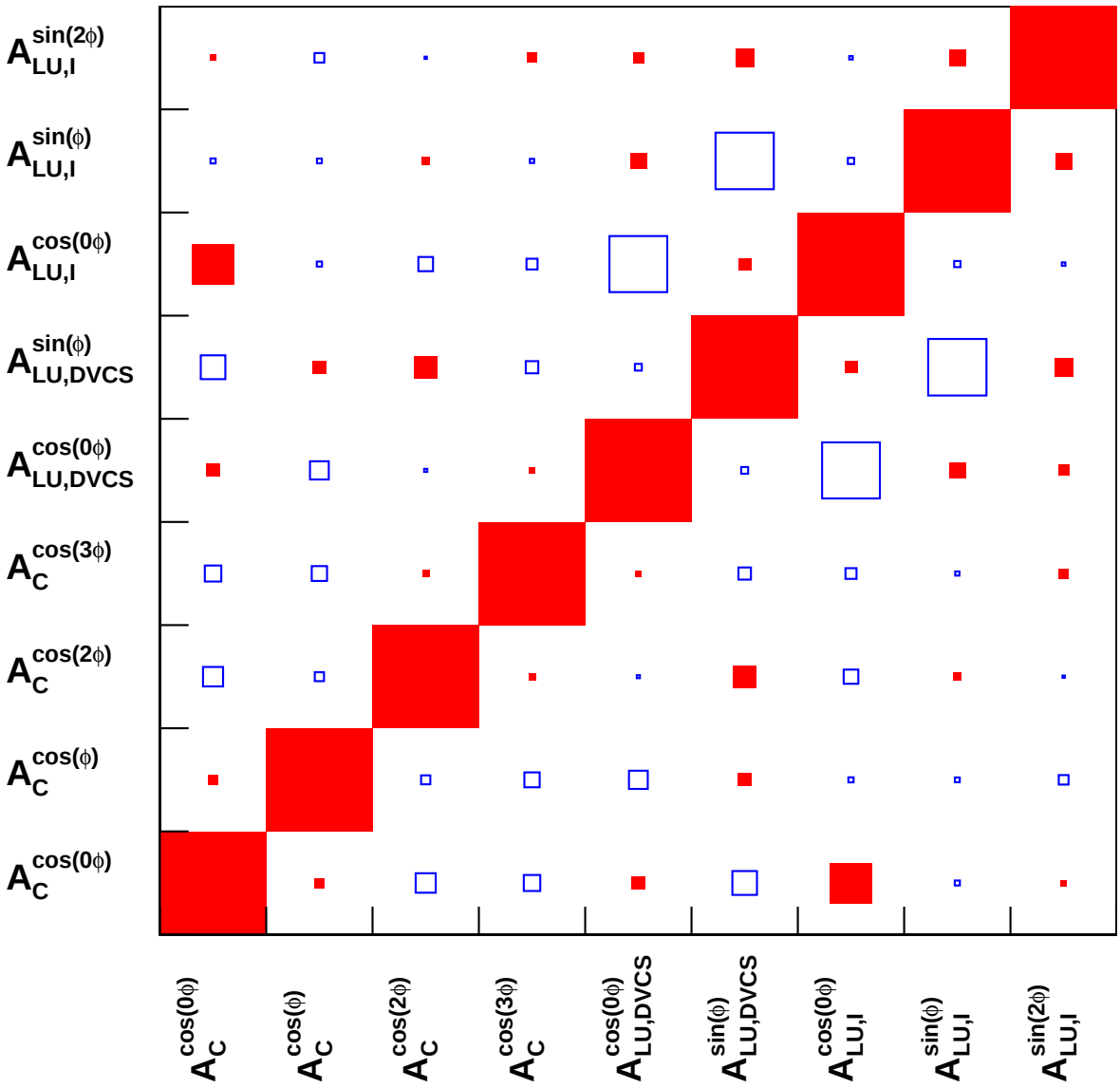

Figure 7.1: Correlation coefficients between the amplitudes of the asymmetries $\mathcal{A}_{\rm C}$, $\mathcal{A}_{\rm LU}^{\rm I}$ and $\mathcal{A}_{\rm LU}^{\rm DVCS}$ from an unpolarized data. The area of the symbols represents the size of the correlation. Filled and open squares represent positive and negative values respectively.

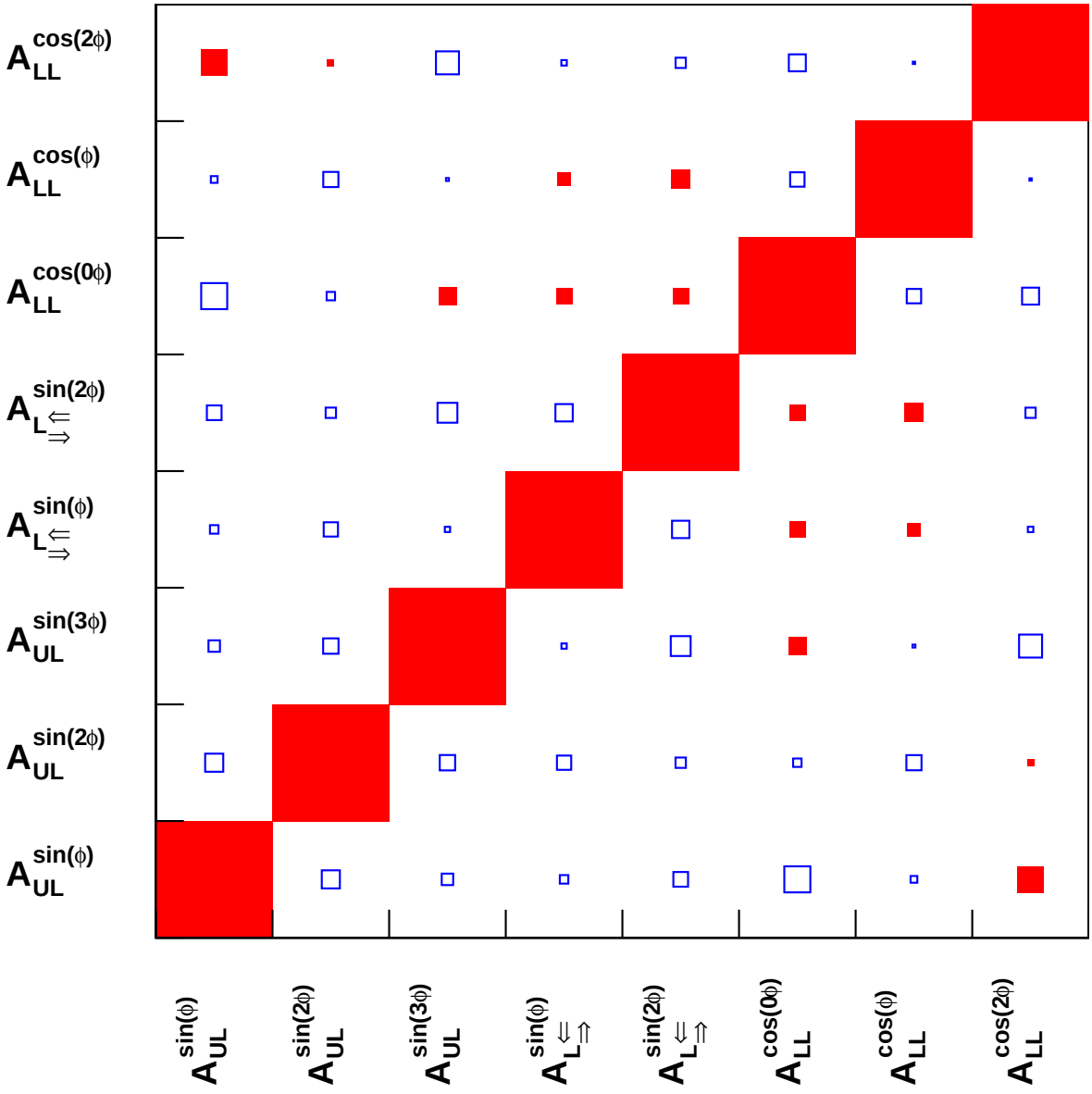

Figure 7.2: Correlation coefficients between the amplitudes of the sigle-charge asymmetries $\mathcal{A}_{\mathrm{L}\leftrightarrows}$, $\mathcal{A}_{\mathrm{UL}}$ and $\mathcal{A}_{\mathrm{LL}}$. The area of the symbols represents the size of the correlation. Filled and open squares represent positive and negative values respectively.

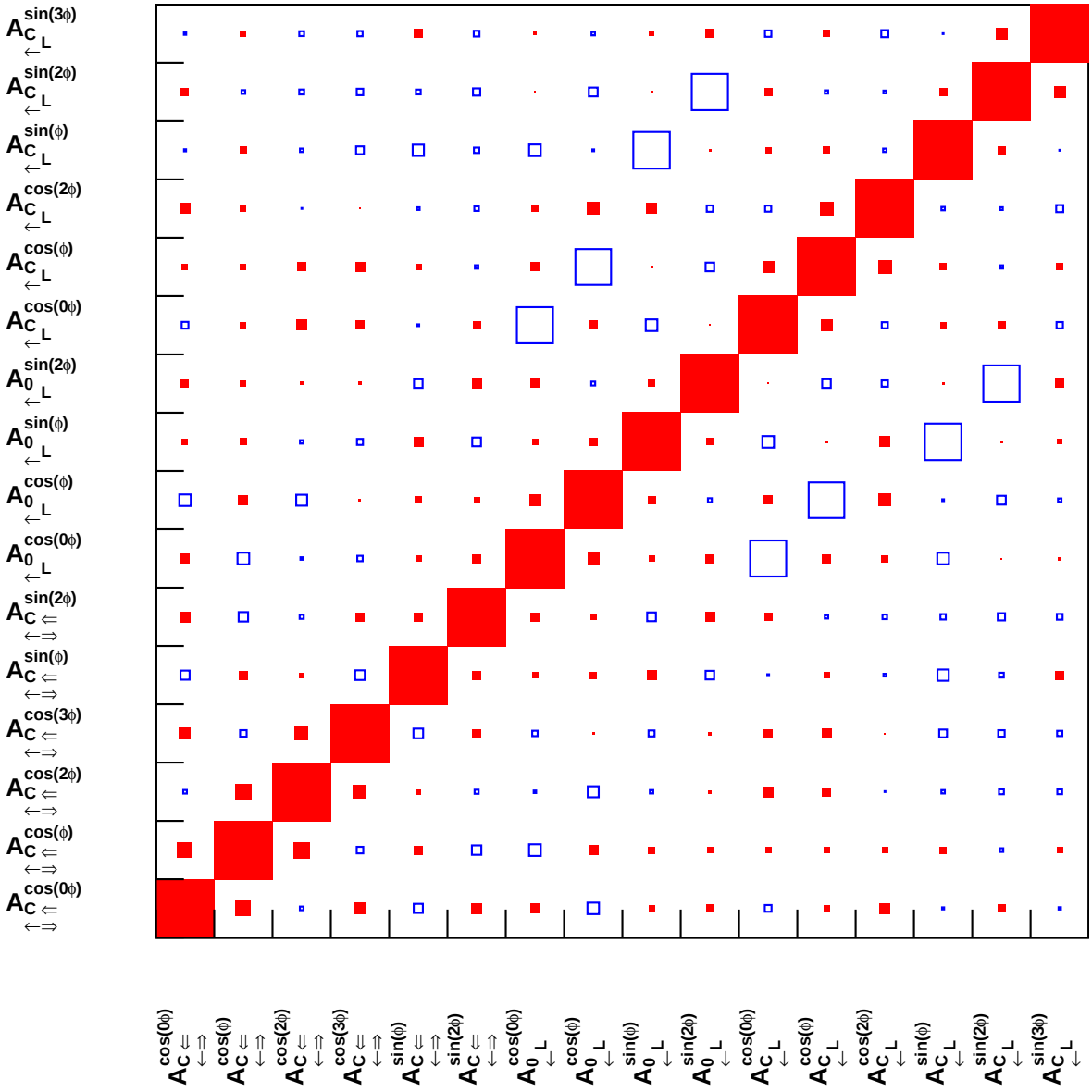

Figure 7.3: Correlation coefficients between the amplitudes of the sigle-beam-helicity asymmetries $\mathcal{A}_{\underset{\leftarrow\Rightarrow}{C}}$, $\mathcal{A}_{\underset{\leftarrow L}{0}}$ and $\mathcal{A}_{\underset{\leftarrow L}{C}}$. The area of the symbols represents the size of the correlation. Filled and open squares represent positive and negative values respectively.

Bibliography

[Abb00] D. Abbott et al., "Phenomenology of the deuteron electromagnetic form-factors", Eur. Phys. J. A7 (2000) 421, nucl-ex/0002003.

[Ack98] K. Ackerstaff et al., "The HERMES spectrometer", Nucl. Instrum. Meth. A417 (1998) 230, hep-ex/9806008.

[Adl03] C. Adloff et al., "Measurement and QCD analysis of neutral and charged current cross-sections at HERA", Eur. Phys. J. C 30 (2003) 1,hep-ex/0304003.

[Afa06] A.V. Afanasev, M.I. Konchatnij, N.P. Merenkov, " Single-spin asymmetries in the Bethe-Heitler process $e^- + p \to e^- + \gamma + p$ from QED radiative corrections", J. Exp. Theor. Phys. 102 (2006) 220.

[AGIS83] B. Andersson, G. Gustafson, G. Ingelman, T. Sjostrand, "Parton fragmentation and string dynamics", Phys. Rept. 97 (1983) 31.

[Air01] A. Airapetian et al., "Measurement of the beam spin azimuthal asymmetry associated with deeply-virtual Compton scattering", Phys. Rev. Lett. 87 (2001) 182001, hep-ex/0107043.

[Air05] A. Airapetian et al., "Measurement of the tensor structure function b_1 of deuteron", Phys. Rev. Lett. 95 (2005) 242001, hep-ex/0506018.

[Air05a] A. Airapetian et al., "The HERMES polarized hydrogen and deuterium gas target in the HERA electron storage ring", Nucl. Instr. Meth. A540 (2005) 68.

[Air07a] A. Airapetian et al., "Precise determination of the spin structure function g_1 of the proton, deuteron and neutron", Phys. Rev. D 75 (2007) 012007, hep-ex/0609039.

[Air07b] A. Airapetian et al., "The beam-charge azimuthal asymmetry and deeply virtual Compton scattering", Phys. Rev. D75 (2007) 011103, hep-ex/0605108.

[Air08] A. Airapetian et al.,"Measurement of azimuthal asymmetries with respect to both beam charge and transverse target polarization in exclusive electroproduction of real photons", JHEP 0806 (2008) 066.

[Air09] A. Airapetian et al., "Separation of contributions from deeply virtual Compton scattering and its interference with the Bethe-Heitler process in measurements on a hydrogen target" JHEP 0911 (2009) 083.

[Air10a] A. Airapetian et al., "Exclusive leptoproduction of real photons on a longitudinally polarised hydrogen target", JHEP 1006 (2010) 019.

[Air10b] A. Airapetian et al., "Measurement of azimuthal asymmetries associated with deeply virtual Compton scattering on an unpolarized deuterium target", Nucl. Phys. B829 (2010) 1.

[Akt05] A. Aktas et al.,"Measurement of deeply virtual compton scattering at HERA", Eur. Phys. J. C44 (2005) 1. hep-ph/0505061

[Aku97] I. Akushevich, A. Ilichev, N. Shumeiko, A. Soroko, A. Tolkachev, "POLRAD 2.0: FORTRAN code for the radiative corrections calculation to deep inelastic scattering of polarized particles", Comput. Phys. Commun. 104 (1997) 201.

[Aku99] I. Akushevich, H. Bottcher, D. Ryckbosch, "RADGEN 1.0: Monte Carlo generator for radiative events in DIS on polarized and unpolarized targets", Talk at the workshop "Monte Carlo generators for HERA physics, Hamburg (1999), hep-ph/9906408.

[AlPa77] G. Altarelli, G. Parisi, "Asymptotic Freedom in Parton Language", Nucl. Phys. B126 (1977) 298.

[Ams08] C. Amsler et al., "Particle Data Group". Phys. Lett. B667 (2008) 1.

[Ans95] M. Anselmino, A. Efremov, E. Leader, "The Theory and phenomenology of polarized deep inelastic scattering", Phys. Rept. 261 (1995) 1.

[Ant03] P.L. Anthony et al, "Precision measurement of the proton and deutron spin structure functions g_2 and asymmetries A_2", Phys. Lett. B553 (2003) 18.

[Ash88] J. Ashman et al., "A measurement of the spin asymmetry and determination of the structure function g_1 in deep inelastic muon proton scattering", Phys. Lett. B206 (1988) 364.

[Ava98] H. Avakian et al., "Performance of the electromagnetic calorimeter of the HERMES experiment", Nucl. Instr. and Meth. A 417 (1998) 69.

[Bar93] D.P. Barber et al., "The HERA polarimeter and the first observation of electron spin polarization at HERA", Nucl. Instr. and Meth. A 329 (1993) 79.

[Bar90] R.J. Barlow, "Extended maximum likelihood", Nucl. Instr. and Meth. A297 (1990) 496.

[Bau02] C. Baumgarten et al., "An atomic beam polarimeter to measure the nuclear polarization in the HERMES gaseous polarized hydrogen and deuterium target", Nucl. Instr. and Meth. A 482 (2002) 606.

[Bau03] C. Baumgarten et al., "The storage cell of the polarized internal H/D gas target of the HERMES experiment at HERA", Nucl. Instr. and Meth. A 496 (2003) 277.

[Bau03a] C. Baumgarten et al., "A gas analyzer for the internal polarized target of the HERMES experiment", Nucl. Instr. and Meth. A508 (2003) 268.

[Bec02] M. Beckmann et al., "The longitudinal polarimeter at HERA", Nucl. Instr. and Meth. A479 (2002) 334.

[Bel00a] A. V. Belitsky, A. Freund, D. Muller, "NLO evolution kernels for skewed transversity distributions", Phys. Lett. B493 (2000) 341, hep-ph/0008005.

[Bel00b] A. V. Belitsky, D. Muller, L. Niedermeier, A. Schafer, "Deeply virtual Compton scattering in next-to leading order", Phys. Lett. B474 (2000) 163, hep-ph/9908337.

[Bel98] A. V. Belitsky, D. Muller, "Predictions from conformal algebra for the deeply virtual Compton scattering", Phys. Lett. B417 (1998) 129, hep-ph/9709379.

[BelR05] A. V. Belitsky, A. V. Radyushkin, "Unraveling hadron structure with generalized parton distributions", JLAB-THY-04-34 (2005), hep-ph/0504030.

[Ben01] T. Benisch et al., "The luminosity monitor of the HERMES experiment at DESY", Nucl. Instr. and Meth. A 471 (2001) 314.

[Ber01] E.R. Berger, F. Cano, M. Diehl, B. Pire, "Generalized parton distributions in the deuteron", Phys. Rev. Lett. 87 (2001) 142302.

[Ber72] J. Bernabeu, "Quasielastic electron and neutrino interactions and the exclusion effects", Nucl. Phys. B49 (1972) 1972.

[Bjo69a] J.D. Bjorken, "Asymptotic sum rules at infinite momentum", Phys. Rev. 179 (1969) 1547.

[Bjo69b] J.D. Bjorken, E.A. Paschos, "Inelastic electron-proton and γ-proton scattering and the structure of the nucleon", Phys. Rev. 185 (1969) 1975.

[BMK02] A. V. Belitsky, D. Muller, A. Kirchner, "Theory of deeply virtual Compton scattering on the nucleon", Nucl. Phys. B629 (2002) 323.

[Bra76] F.W. Brasse et al.,"Parametrization of the Q^2 depedence of virtual gamma p total cross-section in the resonance region", Nucl. Phys. B110 (1976) 413.

[Bru78] R. Brun et al.,"GEANT: Simulation Program for Particle Physics Experiments. Users Guide and Reference Manual", CERN-DD-78-2-REV (1978).

[Bur00] M. Burkardt, "Impact parameter dependent parton distributions and off-forward parton distributions for $z \to 0$", Phys. Rev. D62 (2000) 071503. Phys. Rev. D66 (2002) 119903, Erratum.

[Cam06] C.M. Camacho et al., "Scaling tests of the cross section for deeply virtual Compton scattering", Phys. Rev. Lett. 97 (2006) 262002, nucl-ex/0607029

[CER93] CERN Programming Techniques Group, ADAMO reference manual version 3.3 (1993); ADAMO Entity-relationship Programming System, Users Guide version 3.3 (1993)

[CF99] J.C. Collins, A. Freund, "Proof of factorization for deeply virtual compton scattering in QCD", Phys. Rev. D59 (1999) 074009, hep-ph/9801262.

[Che01] S. Chekanov et al., "Measurement of the neutral current cross-section and F(2) structure function for deep inelastic e + p scattering at HERA", Eur. Phys. J. C 21 (2001) 443.

[Che03] S. Chekanov et al., "Measurement of deeply virtual compton scattering at HERA", Phys. Lett. B573 (2003) 46. hep-ex/0305028

[Chen06] S. Chen et al., "Measurement of deeply virtual Compton scattering with a polarized proton target", Phys. Rev. Lett. 97 (2006) 072002. hep-ex/0605012

[Cho93] S. Choi et al., "Axial and pseudoscalar nucleon form-factors from low-energy pion electroproduction", Phys. Rev. Lett. 71 (993) 3927.

[Col88] J.C. Collins, D.E. Soper, G. Sterman, "Factorization of hard processes in QCD", Adv. Ser. Direct. High Energy Phys. 5 (1988) 1.

[Col77] P.D.B. Collins, "An introduction to Regge theory and high-energy physics", Cambridge University Press (1977).

[CP03] F. Cano, B.Pire, "Deeply virtual Compton scattering on Spin one nuclei", Nucl. Phys. A721 (2003) 789, hep-ph/0211444

[CP04] F. Cano, B.Pire, "Deep electroproduction of photons and mesons on the deuteron", Eur. Phys. J. A19 (2004) 423.

[DFJK99] M. Diehl, T. Feldman, R. Jakob, P. Kroll, "Linking parton distributions to form-factors and Compton scattering", Eur. Phys. J. C8 (1999) 409.

[DFJK05] M. Diehl, T. Feldman, R. Jakob, P. Kroll, "Generalized parton distributions from nucleon form-factor data", Eur. Phys. J. C39 (2005) 1.

[DGPR97] M. Diehl, T. Gousset, B. Pire, J.P. Ralston, "Testing the handbag contribution to exclusive virtual Compton scattering", Phys. Lett. B411 (1997) 193, peh-ph/9706344.

[DHKT99] D. Drechsel, O. Hanstein, S.S. Kamalov, L. Tiator, "The unitary isobar model for pion photo- and electroproduction on the proton up to $1\,GeV$", Nucl. Phys. A645 (1999) 145, nucl-th/9807001.

[Dok77] Yu.L. Dokshitzer, "Calculation of the Structure Functions for Deep Inelastic Scattering and e+ e- Annihilation by Perturbation Theory in Quantum Chromodynamics", Sov. Phys. JETP 46 (1977) 641.

[Due95] M. Dueren, "The HERMES Experiment: From the Design to the First Results". DESY-THESIS-1995-002.

[EfRa80] A.V. Efremov, A.V. Radyushkin,"Factorization and Asymptotical Behavior of Pion Form-Factor in QCD", Phys. Lett. B94 (1980) 245.

[Ell04] F. Ellinghaus, "Beam charge and beam spin azimuthal asymmetries in deeply virtual Compton scattering". DESY-THESIS-2004-005.

[Els02] U. Elschenbroich, "Analysis of Luminosity Monitor Data for Different Years", HERMES internal report 02-013 (2002).

[Ely01] J. Ely, "HERMES calorimeter position reconstruction study", HERMES internal report 01-056 (2001).

[Ely02] J. Ely, "Measurement of the single spin azimuthal asymmetry int the predominantly exclusive electroproduction of photons from the proton". DESY-THESIS-2002-014.

[Ent01] R. Ent et al., "Radiative corrections for $(e, e'p)$ reactions at GeV energies", Phys. Rev. C64 (2001) 054610.

[Fey69] R. Feynman, "Very high-energy collisions of hadrons", Phys. Rev. Lett. 23 (1969) 1415.

[Fox74] D.J. Fox et al., "Test of scale invariance at high-energy muon scattering", Phys. Rev. Lett. 33 (1974) 1504.

[Gav09] G. Gavalian et al., "Beam Spin Asymmetries in DVCS with CLAS at $4.8\,GeV$", Phys. Rev. C80 (2009) 035206.

[Gel64] M. Gell-Mann, "A schematic model of baryons and mesons", Phys. Lett. 8 (1964) 214.

[Gir08] F.X. Girod et al., "Deeply Virtual Compton Scattering Beam-Spin Asymmetries", Phys. Rev. Lett. 100 (2008) 162002.

[GPV01] K. Goeke, M. Polyakov, M. Vanderhaeghen, "Hard exclusive reactions and the structure of hadrons" Prog. Part. Nucl. Phys. 47 (2001) 401. hep-ph/0106012

[GrLi72] V.N. Gribov, L.N. Lipatov, "e+ e- pair annihilation and deep inelastic e p scattering in perturbation theory", Sov. J. Nucl. Phys. 15 (1972) 675.

[GT06] V. Guzey, T. Teckentrup, "The dual parameterization of the proton generalized parton distribution functions H and E and description of the DVCS cross sections and asymmetries" Phys. Rev. D74 (2006) 054027, hep-ph/0607099.

[GT09] V. Guzey, T. Teckentrup, "On the mistake in the implementation of the minimal model of the dual parameterization and resulting inability to describe the highenergy DVCS data" Phys. Rev. D79 (2009) 017501. arXiv:0810.3899

[Gui98] P.A.M. Guichon, M. Vanderhaeghen, "Virtual Compton Scattering off the Nucleon", Prog. Part. Nucl. Phys. 41 (1998) 125.

[Hil05] A. Hillenbrand, "Measurement and simulation of the fragmentation process at HERMES". DESY-THESIS-2005-035.

[Hill08] G. Hill, "Deeply virtual Compton scattering off unpolarized deuterium at HERMES". DESY-THESIS-2008-035.

[Hoo89] P. Hoodbhoy, R.L Jaffe, A. Manohar, "Novel effects in deep inelastic scattering from spin-one hadrons", Nucl. Phys. B312 (1989) 571.

[Ing97] G. Ingelman, A. Edin, J Rathsman, "LEPTO 6.5 - A Monte Carlo generator for deep inelastic lepton-nucleon scattering", Comput. Phys. Commun. 101 (1997) 108. hep-ph/9605286

[Jaf96] R.L. Jaffe, "Spin, twist and hadron structure in deep inelastic processes", (1996) . hep-ph/9602236

[Ji97a] X.-D. Ji, "Deeply-virtual compton scattering", Phys. Rev. D55 (1997) 7114. hep-ph/9609381

[Ji97b] X.-D. Ji, "Gauge invariant decomposition of nucleon spin", Phys. Rev. Lett. 78 (1997) 610. hep-ph/9603249

[Ji98] X.-D. Ji, "Off-forward parton distributions", J. Phys. G24 (1998) 1181. hep-ph/9807258

[JiO98] X.-D. Ji, J. Osborne, "One-loop corrections and all order factorization in deeply-virtual compton scattering", Phys. Rev. D58 (1998) 094018. hep-ph/9801260

[Kai97] R. Kaiser, "Particle identification at HERMES", HERMES internal report 97-025 (1997).

[KM04] A. Kirchner, D. Muller, "Deeply virtual compton scattering off nuclei", Eur. Phys. J. C32 (2004) 347.

[KN02] V. Korotkov, W.D. Nowak, "Future measurements of deeply virtual compton scattering at HERMES", Eur. Phys. J. C23 (2002) 455.

[Kob95] A.P. Kobushkin, A.I. Syamtomov, "Deuteron electromagnetic form-factors in the transitional region between nucleon - meson and quark - gluon pictures", Phys. Atom. Nucl. 58 (1995) 1477. hep-ph/9409411

[Kop06] M. Kopytin, "Longitudinal target-spin azimuthal asymmetry in deeply- virtual Compton scattering", DESY-TGESIS-2006-100.

[KPV01] N. Kivel, M.V. Polyakov, M. Vanderhaeghen, "DVCS on the nucleon: Study of the twist - three effects", Phys. Rev. D63 (2001) 114014.

[Kra05] B. Krauss, "Deeply virtual Compton scattering and the HERMES recoil-detector". DESY-THESIS-2005-008.

[Lac81] M. Lacombe et al., "Parametrization of the deuteron wave function of the Paris n-n potential", Phys. Lett. B101 (1981) 139.

[LeBr79] G.P. Lepage, S.J. Brodsky, "Exclusive Processes in Quantum Chromodynamics: Evolution Equations for Hadronic Wave Functions and the Form-Factors of Mesons", Phys. Lett. B87 (1979) 359.

[Lip75] L.N. Lipatov, "The parton model and perturbation theory", Sov. J. Nucl. Phys. 20 (1975) 94.

[LuY07] X.G. Lu, Z. Ye, "Simultaneous Extraction of the BSAs and the BCA Associated with DVCS with the Extended Maximum Likelihood Method", HERMES internal report 07-001 (2007).

[Mah10] D. Mahon, "Deeply Virtual Compton Scattering off Longitudinally Polarised Protons at HERMES", DESY-THESIS-2010-005.

[MHMM08] H. Marukyan, G. Hill, C.A. Miller, A. Movsisyan, "DVCS off a longitudinally polarized deuterium target.", HERMES release report (unpublished) 2009.

[MM09] H. Marukyan, A. Movsisyan, "DVCS analysis on unpolarized Deuterium", HERMES release report (unpublished) 2008.

[MT69] L.W. Mo, Y.S. Tsai, "Radiative corrections to elastic and inelastic ep and μp scattering", Rev. Mod. Phys. 41 (1969) 205.

[MRST98] A.D. Martin, R.G. Roberts, W.J. Stirling, R.S. Thorne "Parton distributions: a new global analysis", Eur. Phys. J. C4 (1998) 463. hep-ph/9803445.

[Mul94] D. Muller, D. Robaschik, B. Geyer, F.M. Dittes, J. Horejsi, "Wave functions, evolution equations and evolution kernels from light-ray operators of QCD", Fortsch. Phys. 42 (1994) 101, hep-ph/9812448.

[Mul94] D. Muller, D. Robaschik, B. Geyer, F.M. Dittes, J. Horejsi, "Wave functions, evolution equations and evolution kernels from light-ray operators of QCD", Fortsch. Phys. 42 (1994) 101, hep-ph/9812448.

[Nas03] A. Nass et al., "The HERMES polarized atomic beam source", Nucl. Instr. and Meth. A505 (2003) 633.

[Pet98] V. Y. Petrov et al., " Off-forward quark distributions of the nucleon in the large N_C limit", Phys. Rev. D57 (1998) 4325.

[PS02] M. V. Polyakov, A.G. Shuvaev, "On dual parameterization of generalized parton distributions", (2002) , hep-ph/0207153.

[Rad96] A. V. Radyushkin, "Scaling limit of deeply virtual compton scattering", Phys. Lett. B380 (1996) 417, hep-ph/9604317.

[Rad98] A. V. Radyushkin, Phys. Rev. D58 (1998) 114008.

[Rad99] A. V. Radyushkin, "Double distributions and evolution equations", Phys. Rev. D59 (1999) 014030, hep-ph/9805342.

[Rad01] A. V. Radyushkin, "Generalized Parton Distributions", (2001), hep-ph/0101225.

[Roc00] J. Roche et al., "First Determination of Generalized Polarizabilities of the proton by a Virtual Compton Scattering Experiment", Phys. Rev. Lett. 85 (2000) 708.

[Sjo95] T. Sjostrand, "PYTHIA 5.7 and JETSET 7.4", Physics and manual, (1995) hep-ph/9508391.

[Sol64] F.T. Solmitz, "Analysis of experiments in particle physics", Ann. Rev. Nucl. Part. Sci. 14 (1964) 375.

[ST64] A.A. Sokolov, I.M. Ternov, "On polarization and spin effects in the theory of synchrotron radiation", Sov. Phys. Doklady 8 (1964) 1203.

[Ste00] J..J.M Steijger, "The HERMES Silicon Project", Nucl. Instr. and Meth. A447 (2000) 55.

[Ste75] S. Stein et al, "Electron scattering at 4-degrees with energies of 4.5 GeV-20GeV", Phys. Rev. D12 (1975) 1884.

[Step01] S. Stepanyan et al., "First observation of exclusive deeply virtual Compton scattering in polarized electron beam asymmetry measurements", Phys. Rev. Lett. 87 (2001) 182002, hep-ex/0107043.

[Van06] A. Vandenbroucke, "Exclusive π^0 Production at HERMES: Detection - Simulation - Analysis", DESY-THESIS-2006-110.

[Van00] M. Vanderhaeghen et al., "QED radiative corrections to virtual Compton scattering", Phys. Rev. C62 (2000) 025501.

[VGG99] M. Vanderhaeghen, P. A. M. Guichon, and M. Guidal, "Deeply virtual electroproduction of photons and mesons on the nucleon: Leading order amplitudes and power corrections" Phys. Rev. D60 (1999) 094017, hep-ph/9905372.

[VGG01] M. Vanderhaeghen, P. A. M. Guichon, and M. Guidal, " Computer code for the calculation of DVCS and BH processes in the reaction $ep \to ep\gamma$, private communication, (2001).

[Whi90a] L.W. Whitlow et al, "Precise extraction of $R = \sigma_L/\sigma_T$ from a global analysis of the SLAC deep inelastic e-p and e-d scattering cross-sections", Phys. Lett. B250 (1990) 193.

[Whi90b] L.W. Whitlow et al., Phys. Lett. B282 (1992) 475; L.W. Whitlow, Dissertation, Stanford University, SLAC Report 357 (1990)

[WW77] S. Wandzura, F. Wilczek, "Sum Rules for Spin Dependent Electroproduction: Test of Relativistic Constituent Quarks", Phys. Lett. B72 (1977) 195.

[Yao06] W.-M. Yao et al., "The Review of Particle Physics". Journal of Physics, G 33 (2006) 1.

[Ye07] Z. Ye, "Transverse target-spin asymmetry associated with deeply virtual Compton scattering on the proton and a resulting model-dependent constraint on the total angular momentum of quarks in the nucleon", DESY-THESIS-2007-005.

[Zei09] D. Zeiler, "Deeply Virtual Compton Scattering off an Unpolarized Hydrogen Target at the HERMES Experiment", DESY-THESIS-2009-024.

[Zwe64] G. Zweig,"An SU(3) model for strong interaction symmetry and its breaking", CERN preprints TH-401, TH-412 (1964).

Acknowledgments

This thesis would not have been possible without the contributions and help of many people.

First of all I would like to thank my supervisor Hrachya Marukyan for providing me an opportunity to work on the HERMES experiment with such an interesting topic, and of course for his support, encouragement and patience throughout this work. His guidance over the many years of my work on this thesis was always very wise and friendly.

I am greatly appreciative of HERMES management and members of HERMES DVCS group. In particular I would like to thank Caroline Riedl, Sergey Yaschenko, Gunar Schnell, Eduard Avetisyan, Dietmar Zeiler, Armine Rostomyan and Charlotte van Hulse for useful discussions during our subgroup meetings. Thanks also to David Mahon, Gordon Hill and Hongxue Ye for their assistance with the data analysis. I would like to thank also Wolf-Dieter Nowak, Andy Miller and other members of our DVCS drafting committee for the exchange of ideas during many meetings and the elegant solutions of complicated problems, which helped and inspired me a lot.

I am much obliged to Prof. N. Akopov, group leader of YerPhI group at HERMES, and to all members of Yerevan group G. Elbakyan, L. Grigoryan, G. Karyan, A. Avetissian, S. Taroyan, Z. Akopoff, A. Petrosyan and R. Avakian for their continuous help, support and friendly working atmosphere.

I also sincerely appreciate Inna Aznauryan and Hamlet Mkrtchyan for detailed proofreading of this thesis and for their constructive and felicitous remarks. Special thanks to Mareta Hakobyan for her great support at the ending phase of this work.

Finally, I thank my family and friends for their help and support during all these years.